

Search for Electron Anti-Neutrinos from the Sun using the
KamLAND Large Volume Liquid Scintillator Detector

Hiroshi Ogawa
Doctor Thesis
Tohoku University

October 6, 2003

Abstract

An exposure of 0.28 kt-yr by the KamLAND experiment has been used to search for $\bar{\nu}_e$'s in the energy range $8.3 \leq E_{\bar{\nu}_e} \leq 14.8$ MeV. No candidates were found. Assuming that $\bar{\nu}_e$'s have the same dependence on energy as ${}^8\text{B}$ ν_e 's according to the Standard Solar Model (SSM) with no oscillations, An upper limit of $5.81 \times 10^2 \text{cm}^{-2} \text{s}^{-1}$ (90% C.L.) is obtained on the $\bar{\nu}_e$ flux. This limit corresponds to 0.038% of the SSM ${}^8\text{B}$ ν_e flux (no oscillation). Also the framework of spin-flavor precession and neutrino decay models are interpreted to this limit.

Acknowledgements

First of all, I must thank Professor Atsuto Suzuki, the spokesman of the KamLAND experiment. He leaded me to the neutrino physics since I had been graduate student and this exciting experiment - KamLAND. Also I must thank Asst. Prof. Junpei Shirai, Fumihiko Suekane and Kunio Inoue. They gave me many advices which help me to make this study.

I would like to thank the KamLAND collaborators for the detector construction and operation. Many thanks to Dr. Masayuki Koga, Dr. Shuichiro Hatakeyama, Dr. Tadao Mitsui, Dr. Kenji Ishihara, Dr. Kengo Nakamura, Dr. Masakazu Motoki, Dr. Jesse Goldman, Dr. Yasuhiro Kishimoto, Dr. Koichiro Furuno for many advices, discussions and comments for this study. Also I perceived the various preparations as the experimental physicist through their working.

I would like to thank all people of Research Center for Neutrino Science (RCNS) at Tohoku University. Many thanks to Professor Toshio Kitagaki, Professor Koya Abe, Professor Akira Yamaguchi, Professor Hitoshi Yamamoto, Asst. Prof. Tomoki Hayashino, Dr. Takuya Hasegawa, Dr. Tadashi Nagamine. Also many thanks to Technical Staff Tomoaki Takayama, Hiromitsu Hanada, Takashi Nakajima, Minoru Nakajima, Kyoko Tamae.

Many thanks to RCNS students with my fruitful study. Thanks to Toshiyuki Iwamoto, Sanshiro Enomoto, Osamu Tajima, Hideki Watanabe, Haruo Ikeda, Yoshihito Gando, Fumiaki Handa, Itaru Higuchi, Kyo Nakajima.

Finally, I thank my parents, Yoshihisa and Aiko Ogawa for their many supports in my study and life.

Contents

1	Introduction	11
2	Solar neutrino and neutrino oscillation	13
2.1	Neutrino	13
2.2	Solar neutrino problem	14
2.2.1	Solar neutrinos	14
2.2.2	The energy spectrum of ^8B neutrinos	17
2.2.3	Observation of solar neutrinos - I Homestake, Kamiokande, SAGE and GALLEX	17
2.2.4	Observation of solar neutrinos - II SuperKamiokande and SNO	20
2.3	Neutrino oscillation	20
2.3.1	Neutrino oscillation in vacuum	21
2.3.2	Neutrino oscillation in matter	22
2.4	Neutrino oscillation analysis for solar neutrino problem	25
3	Neutrino magnetic moment and neutrino decay	29
3.1	Neutrino magnetic moment	29
3.1.1	Experimental limit for neutrino magnetic moment	29
3.1.2	Phenomenological limit for neutrino magnetic moment	30
3.1.3	Progress of neutrino event rate and RSFP	31
3.1.4	Hybrid model (RSFP+MSW) and anti-electron neutrino production . . .	31
3.2	Neutrino decay	32
3.2.1	The limit for neutrino lifetime	32
3.2.2	Anti-neutrino production by neutrino decay	33
3.3	Search for the solar anti-neutrino in KamLAND	34
4	KamLAND Detector	36
4.1	The Site	36
4.2	The detector Design	36
4.2.1	Overview	36
4.2.2	The Liquid Scintillator and buffer oil	38
4.2.3	The Scintillator Purification System	39
4.2.4	The Photomultiplier	43

4.2.5	The Front-end Electronics (FEE)	46
4.2.6	Trigger	46
4.2.7	Data acquisition system	48
4.3	Detection principle for electron anti-neutrino	49
5	Event Reconstruction	52
5.1	Vertex Reconstruction	52
5.2	Energy Reconstruction	53
5.2.1	Gain correction	53
5.2.2	Bad channel cut	55
5.2.3	Energy fitter tuning	58
5.3	Muon Reconstruction	61
5.4	Trigger efficiency	65
5.5	Charge efficiency	65
6	Calibration	67
6.1	Calibration support system structure	67
6.2	Gain calibration	67
6.3	Timing calibration	68
6.4	Energy & vertex calibration by radioactive sources	72
6.4.1	Radioactive isotopes	72
6.4.2	Energy spectrum	72
6.4.3	Energy scale	75
6.4.4	Vertex distribution	77
6.4.5	Detector stability	78
6.5	Calibration for delayed coincidence	78
6.5.1	Neutron capture time and neutron capture length by Am/Be source	80
6.6	Neutron events after muon	83
6.6.1	Energy distribution	85
6.6.2	Vertex distribution	85
6.6.3	Neutron capture time	86
6.7	Neutrons captured by carbon	87
6.8	Spallation events	87
6.8.1	Energy distribution	87
6.8.2	Vertex distribution	88
7	Data Reduction	91
7.1	Bad runs selection	91
7.2	Selection of low energy events	92
7.2.1	Rejection of muon events	92
7.2.2	Rejection of noise events	93
7.2.3	Flasher event cut	94
7.2.4	Muon 2ms cut	94
7.2.5	summary	97

7.3	Fiducial cut	97
7.4	Selection of the delayed coincidence events	98
7.4.1	dt and dL cut	101
7.4.2	Energy cut	101
7.5	Spallation event cut	104
7.6	Final samples	105
8	Analysis	108
8.1	Livetime calculation	108
8.2	Detection efficiency	109
8.3	Systematic errors	112
8.4	Background	113
8.4.1	Reactor anti-neutrino	113
8.4.2	Atmospheric neutrino	113
8.4.3	Spallation	114
8.4.4	Fast neutron	115
8.4.5	Accidental background	118
8.4.6	background summary	118
8.5	Limit calculation	120
9	Interpretation and Discussions	121
9.1	Neutrino magnetic moment	121
9.1.1	Input parameter and solar magnetic field	121
9.1.2	Neutrino propagation	124
9.1.3	Average probability and expected flux	125
9.1.4	Analysis region for oscillation parameter	130
9.1.5	RSFP analysis	131
9.1.6	Compare the survival probability ν_e between RSFP+MSW and MSW only	133
9.2	Neutrino Decay	140
9.2.1	Neutrino decay process	140
9.2.2	Neutrino decay analysis	141
10	Conclusion	143
A	Neutrons after the muon and the spallation events	144
A.1	Neutrons after the muon	144
A.2	Spallation events	145
A.2.1	${}^9\text{Li}$, ${}^8\text{He}$	148
A.2.2	Event selection criteria for other spallation events	149
A.2.3	${}^8\text{Li}+{}^8\text{B}$, ${}^9\text{C}$ and ${}^{12}\text{B}+{}^{12}\text{N}$	153

List of Tables

2.1	Solar neutrino flux on the earth predicted by the standard solar model BP2000 .	16
6.1	The list of radioactive calibration source	72
7.1	The summary of event reduction	106
8.1	The neutron capture fraction and emitted energy	111
8.2	The summary of detection efficiency	111
8.3	Summary of the systematic errors	113
8.4	The summary of background events estimation	120
9.1	the $\mu_{11}B_{max}$ limit obtained for the four magnetic field profiles and LMA region .	133
A.1	The list of spallation nuclei produced after the cosmic ray muons	147
A.2	The efficiency for the selection of ^9Li and ^8He samples.	151
A.3	The results of estimation for the spallation events	154

List of Figures

2.1	Solar neutrino pp-chain	15
2.2	Solar neutrino CNO-cycle	15
2.3	Solar neutrino spectrum predicted by the standard solar model	16
2.4	Neutrino production point distribution as a function of solar radius	17
2.5	Energy levels of decay chains of ${}^8\text{B}(\beta^+){}^8\text{Be}(2\alpha)$ and the energy spectrum of 2α .	18
2.6	Neutrino spectrum of Ortiz et.al. and Bahcall's work (top) and ratio of the two spectra (bottom)	18
2.7	Flux of ${}^8\text{B}$ neutrinos which are μ or τ flavor vs flux of electron neutrino for SNO	21
2.8	Feynman diagrams for neutrino scattering for electron and neutron	23
2.9	The radial dependence of electron and neutron density in the sun	25
2.10	Solar neutrino survival probability in six solutions	26
2.11	Oscillation parameter plot for solar neutrino analysis	27
2.12	Oscillation parameter plot for solar + KamLAND result	28
3.1	The progress of neutrino event rate and sunspot number	31
3.2	The energy spectrum of reactor neutrino and anti-neutrino from solar ${}^8\text{B}$ neutrino	35
3.3	The detector sensitivity for the solar anti-neutrino	35
4.1	The location of KamLAND in Japan	37
4.2	The whole view of KamLAND detector and the laboratory area	37
4.3	The picture of KamLAND main detector	38
4.4	The view of the water extraction tower	40
4.5	The test of LS light output and transparency stability by water contamination .	40
4.6	The nitrogen gas circulation of the LS nitrogen purge system	41
4.7	The oxygen dependence of the LS's light output and the nitrogen purge performance	42
4.8	The result of small beaker experiment to check the Rn rejection	42
4.9	The works for the film coating and the nylon pipes	43
4.10	The purification and circulation system	44
4.11	The view of 17" PMT	45
4.12	The comparison of the performances between 17" and 20" PMT	45
4.13	Quantum efficiency of 17" PMT	46
4.14	The FEE board with ATWD circuits	47
4.15	A sample KamLAND waveform showing two PMT pulses	47
4.16	The block diagram of the ATWD board	48

4.17	KamLAND DAQ system structure	49
4.18	Total cross section for $\bar{\nu}_e + p \rightarrow e^+ + n$ energy dependence	51
5.1	The effective speed of light as a function of z position	53
5.2	The time offset of cable 0-B	54
5.3	The all cable's T_{offset} for one run	54
5.4	The appearance of time distribution by vertex reconstruction process	55
5.5	The criteria of event selection for gain correction.	56
5.6	The typical 1 p.e. charge distribution of one PMT in a low energy event sample .	56
5.7	The 1 p.e. mean charge distribution for all channel	57
5.8	The time variation of average 1 p.e. for all PMTs	57
5.9	The time variation of the number of bad channels	58
5.10	Time distribution of the hit PMTs to the trigger signal in ^{65}Zn calibration	59
5.11	Normalized total charges ratio before and after shadow correction	60
5.12	The total charges ratio after missing PMTs correction	60
5.13	KamLAND event display for the muon event	62
5.14	Inner charge distribution and time distribution for muon events	63
5.15	Muon event time and charge distribution	63
5.16	Track length vs. charge distribution	64
5.17	Track length vs. charge and the charge per unit track length	64
5.18	Trigger efficiency	65
5.19	Charge efficiency	66
6.1	The view of the glove box	68
6.2	LED calibration setup	69
6.3	The 1 p.e. distribution of a typical 17 inch PMT	69
6.4	The 1 p.e. peak position before and after the HV adjustment for all 17" PMTs .	70
6.5	The laser calibration system setup	70
6.6	The typical TQ-map	71
6.7	The result of the timing calibration	71
6.8	The devices of calibration source box	73
6.9	Zn energy spectrum for all volume and only z-axis	73
6.10	The energy spectrum for ^{68}Ge , ^{65}Zn and ^{60}Co source at Z=0 cm	74
6.11	The ^{65}Zn energy distribution and energy resolution	75
6.12	The calibration data points and fitting result	77
6.13	The fractional difference of the reconstructed γ energy	78
6.14	^{65}Zn vertex distribution plot for xz-axis	79
6.15	The vertex distribution at (0,0,0) for ^{65}Zn	79
6.16	The vertex distribution at (0,0,0) for ^{60}Co	80
6.17	The vertex deviation for ^{68}Ge , ^{65}Zn , ^{60}Co and Am/Be	81
6.18	The vertex resolution for ^{65}Zn and ^{60}Co	81
6.19	The time variation for Zn and Co mean energy distribution	82
6.20	The energy spectrum for Am/Be	82
6.21	the energy spectrum of Am/Be delayed coincidence	83

6.22	The time difference between Am/Be prompt events and delayed events	84
6.23	The neutron capture length from Am/Be	84
6.24	The energy spectrum and the R dependence of energy difference for neutron events	85
6.25	R^3 distribution of neutrons after the muon	86
6.26	Time distribution of the neutrons after the muon	87
6.27	The energy spectrum for neutron captured by carbon	88
6.28	Spallation events from ^{12}B and ^{12}N spectrum	89
6.29	The energy scale for ^{12}B and ^{12}N	89
6.30	^3R distribution spallation ^{12}B and ^{12}N	90
7.1	Running time of the normal data taking	92
7.2	The total charge distribution of the inner detector.	93
7.3	The event display of the typical noise event	94
7.4	The time distribution of the typical low energy event and the noise event	95
7.5	The N_{100ns} vs. N_{hit} distribution	95
7.6	The event display of the typical flasher event	96
7.7	The flasher event charge distribution	96
7.8	The energy spectrum of low energy events each reduction process	97
7.9	The energy spectrum in the various fiducial cuts	98
7.10	The R distribution of low energy events	99
7.11	The vertex distribution of the low energy events (1)	99
7.12	The vertex distribution of the low energy events (2)	100
7.13	The vertex distribution of the low energy events (3)	100
7.14	The neutron dL distribution by Geant4 simulation	101
7.15	The dt vs. delayed energy distribution	102
7.16	The dL distribution vs. delayed energy distribution	102
7.17	The prompt energy distribution before and after the cut on dt and dL	103
7.18	The delayed energy distribution before and after the cut on dt and dL	103
7.19	The energy distribution for prompt and delayed energy(1)	104
7.20	The prompt energy spectrum before and after the spallation cut	105
7.21	The vertex distribution for prompt and delayed events	106
7.22	The sample distribution between prompt/delayed energy and dt/dL	107
7.23	The final samples distribution for E_{prompt} and $E_{delayed}$	107
8.1	The dead volume along the muon track as a function of the distance of the muon track from the detector center.	109
8.2	The simulation result of radius distribution for generated prompt and delayed events	110
8.3	Visible energy spectra of reactor anti-neutrino and the solar anti-neutrino	114
8.4	Energy distribution of atmospheric neutrino flux calculation	115
8.5	An illustration of the fast neutron events	116
8.6	The time distribution for fast neutron samples	117
8.7	The energy distribution of delayed and prompt events for fast neutron samples	117
8.8	The radial distribution for fast neutron samples	118

8.9	The time and the vertex distribution for the accidental background events	119
8.10	The time distribution of the accidental events collected from the whole data . . .	119
9.1	The radial dependence of the solar magnetic field (1)	123
9.2	The radial dependence of the solar magnetic field (2)	124
9.3	The radial dependence of neutrino probability for profile (1)	126
9.4	The radial dependence of neutrino probability for profile (2)	127
9.5	The radial dependence of neutrino probability for profile (3)	128
9.6	The radial dependence of neutrino probability for profile MHD	129
9.7	The energy distribution of average $\bar{\nu}_e$ probability	130
9.8	Total $\bar{\nu}_e$ probability depending to the neutrino transition magnetic moment . . .	131
9.9	Exclude and allowed region for KamLAND reactor neutrino analysis	132
9.10	The total $\bar{\nu}_e$ probability at LMA whole	134
9.11	The total $\bar{\nu}_e$ probability at region(B)	135
9.12	The total $\bar{\nu}_e$ probability at region(C)	136
9.13	The example of difference between RSFP+MSW and MSW	137
9.14	The energy dependence between MSW and RSFP for each magnetic field profiles and each $\mu_{11}B_{max}$ limit	138
9.15	the Δm^2 dependence of total ν_e survival probability	139
9.16	The energy spectrum for ^8B and decay neutrino spectrum	140
9.17	The $\bar{\nu}_e$ conversion probability vs τ_0	142
A.1	Nsum and Nhit distribution at the time dT after the muon	145
A.2	Time distribution for neutron after muon	146
A.3	Ratio of the good neutron events over all the neutron events	146
A.4	Neutron background subtraction	147
A.5	$^9\text{Li}/^8\text{He}$ prompt and delayed energy distribution	149
A.6	χ^2 distribution for $^8\text{He}/(^9\text{Li}+^8\text{He})$	150
A.7	^9Li dt distribution	150
A.8	The distance of the neutrons from the muons in the spallation neutron samples for non-energetic muons.	151
A.9	The decay time distribution of the events whose distance from the non-energetic muon track is larger than 300cm.	152
A.10	The time distribution of the spallation events for the short range and the long range after the muon	153
A.11	The energy spectrum for the spallation events	154
A.12	The decay time fitting result for the spallation events	155
A.13	The spallation energy spectrum for ^8B , ^8Li , ^{12}B and ^{12}N	155

Chapter 1

Introduction

The observed deficit of solar neutrinos compared to the the expectations based on the standard solar model is explained with non-standard neutrino properties. In 2002, Sudbury Neutrino Observatory (SNO) Collaboration has demonstrated that significant fraction of solar ν_e is changed to other active neutrino (ν_μ , $\bar{\nu}_\mu$, ν_τ or $\bar{\nu}_\tau$) [1]. The most promising and common explanation of solar neutrino deficit is now the neutrino oscillation including the matter enhanced in the solar interior. Also, the recent observation of reactor $\bar{\nu}_e$ disappearance by KamLAND [2] indicates that the oscillation parameters lies in the MSW Large Mixing Angle (LMA) region.

Nonetheless, the limited precision of the current measurements allows the possibility that other mechanisms play a subdominant role, the detection of which would be important to further understanding the nature of neutrinos and the properties of the Sun. Toward that end, we report in this thesis **the search for $\bar{\nu}_e$ from the Sun**. There are several conceivable mechanisms which would produce a $\bar{\nu}_e$ component in the solar flux incident on Earth. For example, if neutrinos are Majorana particles with nonzero transition magnetic moments, electron neutrinos produced in the Sun could evolve into electron anti-neutrino by the neutrino spin-flavor precession due to the interaction of neutrino transition magnetic moments with the solar magnetic field and the neutrino oscillation by the LMA solution. Another example of the subdominant mechanism is neutrino decay, which includes the possibility of the heavier neutrino mass eigenstate decaying into a lighter anti-neutrino mass eigenstate.

The KamLAND (Kamioka Liquid scintillator Anti-Neutrino Detector) has large potential for the low energy $\bar{\nu}_e$ detection. In this experiment, the electron anti-neutrinos are detected by the inverse beta decay process $\bar{\nu}_e p \rightarrow e^+ n$ using the 1000 ton liquid scintillator detector which is the largest volume of the liquid scintillator in the world. The experiment had been started at January, 2002 and the deficit of the reactor anti-neutrino is firstly observed.

The purpose of this thesis is to present, **the result of search for electron anti-neutrino from the sun using the KamLAND detector**. The contents are as follows ;

In Chapter 2, the summary of the solar neutrino problem is presented. In Chapter 3, the motivation of solar anti-neutrino search, which is the spin-flavor precession and the neutrino decay are discussed. In Chapter 4, a description of KamLAND detector is presented. In Chapter 5, the method of event reconstruction is presented. In Chapter 6, the calibration results using the radioactive sources and the spallation events are given. Chapter 7 gives the process of data

reduction. Chapter 8 gives the systematic errors, the background and the estimated upper limit of the solar $\bar{\nu}_e$. In Chapter 9, the physics interpretation for neutrino magnetic moment and neutrino decay using the solar $\bar{\nu}_e$ limit is presented. The conclusion is presented at Chapter 10.

Chapter 2

Solar neutrino and neutrino oscillation

2.1 Neutrino

The first postulation of neutrino was made by W.Pauli in 1930 [3] as a massless and a neutral particle with spin 1/2 to explain the missing momentum in a nuclear beta decay. The existence of the neutrino was confirmed by F.Rines and C.Cowan in 1956 [4]. The detection of the electron anti-neutrino from nuclear reactor was made by inverse beta decay process :

$$\bar{\nu}_e + p \rightarrow e^+ + n \quad (2.1)$$

In 1962, another type of neutrino, ν_μ , was identified. In 1975, the tau lepton was discovered by M.Pertl et. al. [5], and the observation of the decay properties implied the existence of ν_τ . More recently the precise measurements of the decay width of Z have shown that just three neutrino flavors participate in the weak interaction [6]. In 2001, existence of ν_τ was directly confirmed by a neutrino beam experiment [7].

The neutrinos are organized to constitute elementary particles of the Standard Model. These fermion particles have spin 1/2 and are combined in each generation :

$$\begin{pmatrix} u \\ d \end{pmatrix} \begin{pmatrix} c \\ s \end{pmatrix} \begin{pmatrix} t \\ b \end{pmatrix} \quad \begin{pmatrix} \nu_e \\ e \end{pmatrix} \begin{pmatrix} \nu_\mu \\ \mu \end{pmatrix} \begin{pmatrix} \nu_\tau \\ \tau \end{pmatrix} \quad (2.2)$$

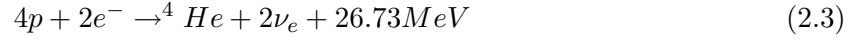
While our knowledge of the neutrino properties are still limited, these particles have been used as tools to understand the physics phenomena. The first step of application to the solar physics phenomena began thirty years ago when Davis and his collaborators detected neutrinos from the sun [8]. Neutrino astronomy was opened by the observation of the neutrino burst from the supernova 1987A [9].

These observations suggested of new neutrino properties, for example, ‘neutrino mass’. In the next section, the problem of the solar neutrino deficit is discussed.

2.2 Solar neutrino problem

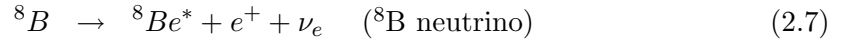
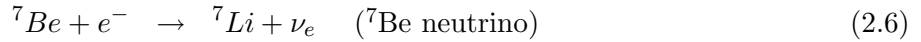
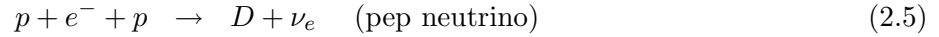
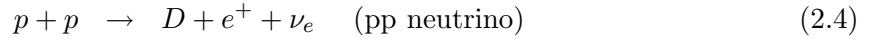
2.2.1 Solar neutrinos

The generation of the solar neutrinos is explained by the Standard Solar Model (SSM) [10]. It is generally believed that the stellar energy is provided by thermonuclear reactions. In the main sequence stars like our sun, the reactions result in a fusion of hydrogen into helium:

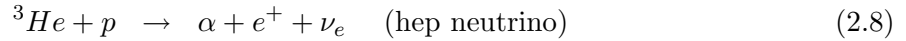


In the sun, the net reaction occurs in two kinds of processes, the so-called proton-proton chain (pp-chain) and the carbon-nitrogen-oxygen cycle (CNO-cycle). The main reaction chain is the pp-chain, as shown Figure 2.1 which produces 98.5% of the solar energy. Also the CNO-cycle is given Figure 2.2.

The reactions that generate electron neutrinos in the pp-chain are:



In addition to those reactions, there is another reaction which generates neutrinos called hep neutrino,



and the total solar neutrino flux are shown in table 2.1.

As shown in the table 2.1, the flux of pp neutrinos accounts for about 90% of the total solar neutrino flux. But the endpoint energy of pp neutrinos is very small, about 0.420 MeV. So far the pp neutrino has been detected by experiments using ${}^{71}\text{Ga}$ detector only.

The reaction (2.5) emits a 1.4 MeV neutrino but this flux is comparatively small. The reaction (2.6) generates monochromatic lines of 0.861 MeV and 0.383 MeV. The higher line can be detected by ${}^{37}\text{Cl}$ experiment.

The reaction (2.7) generates ${}^8\text{B}$ neutrinos. These neutrino have been detected by several experiment (${}^{37}\text{Cl}$, Kamiokande, SuperKamiokande, SNO). These neutrino have high energy endpoint about 15 MeV. The rate of this reaction in the sun is determined by the reaction:



The cross section of this reaction has larger uncertainly than other reaction and is about 20 %. The reaction (2.8) in the pp-chain generates the highest energy neutrino with 18.77 MeV endpoint. But the flux of these neutrinos is very small and about 10^{-3} of ${}^8\text{B}$ neutrinos.

Figure 2.3 shows the energy spectrum predicted by the standard solar model. And the production rate of the ${}^8\text{B}$, ${}^7\text{Be}$ and pp neutrinos as a function of the solar radius are shown in Figure 2.4.

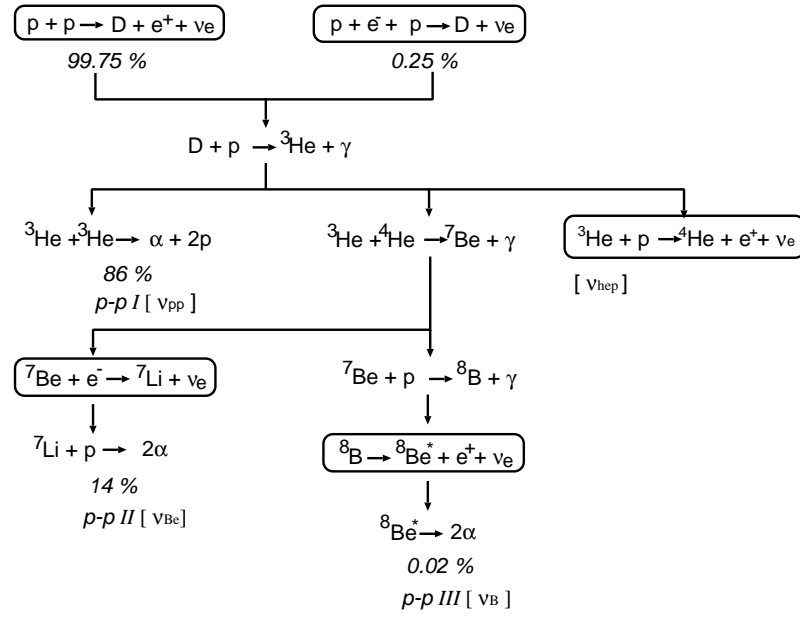


Figure 2.1: Solar neutrino pp-chain

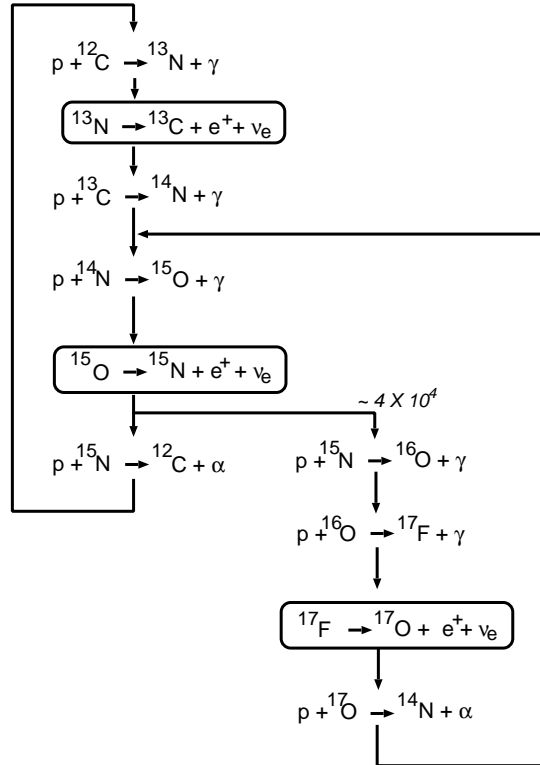


Figure 2.2: Solar neutrino CNO-cycle

Type of neutrino	Flux($\text{cm}^{-2}\text{s}^{-1}$)	fraction(%)
pp	$5.95(1.00 \pm 0.01) \times 10^{10}$	90.1
pep	$1.40(1.00 \pm 0.015) \times 10^8$	0.21
${}^7\text{Be}$	$4.77(1.00 \pm 0.10) \times 10^9$	7.9
${}^8\text{B}$	$5.05(1.00^{+0.20}_{-0.16}) \times 10^6$	0.01
hep	9.3×10^3	1.8×10^{-6}
${}^{13}\text{N}$	$5.48(1.00^{+0.21}_{-0.17}) \times 10^8$	0.94
${}^{15}\text{O}$	$4.80(1.00^{+0.25}_{-0.19}) \times 10^8$	0.83
${}^{13}\text{F}$	$5.63(1.00^{+0.25}_{-0.25}) \times 10^6$	0.01

Table 2.1: Solar neutrino flux on the earth predicted by the standard solar model BP2000 [10]

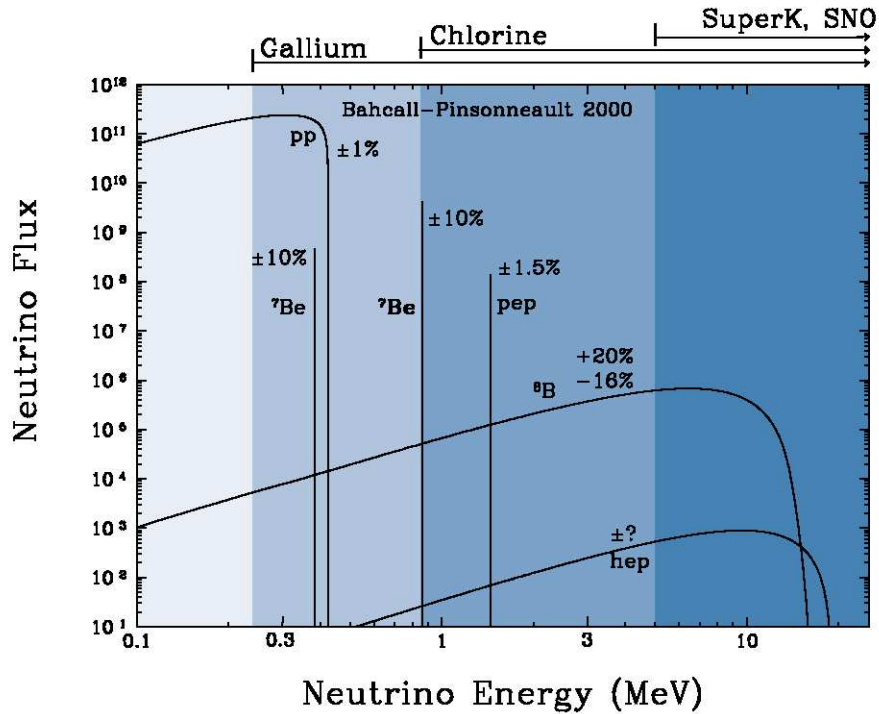


Figure 2.3: Solar neutrino spectrum predicted by the standard solar model

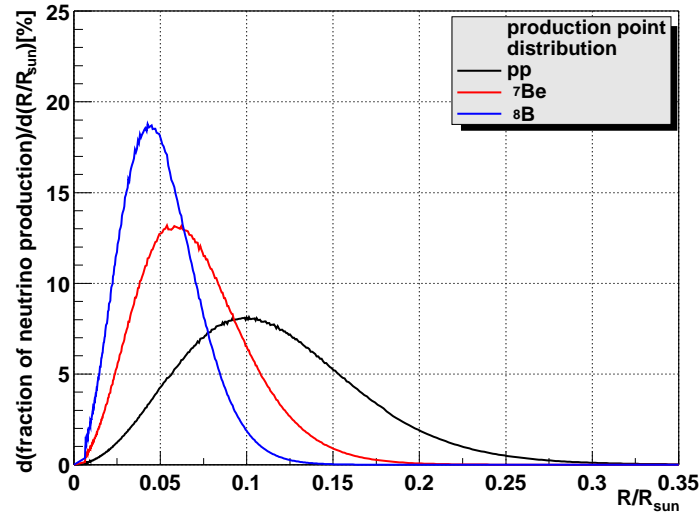


Figure 2.4: Neutrino production point distribution as a function of solar radius

2.2.2 The energy spectrum of ^8B neutrinos

It is important for the estimation of the limit of the solar anti-neutrino flux which is the main motivation of this thesis to understand the shape of the ^8B neutrino spectrum.

The ^8B neutrinos are generated in the β decay of reaction (2.7) and $^8\text{Be}^*$ decay to 2α . The energy level are shown in the left picture of the Figure 2.5. The 2α 's energy distribution affect the β decay spectrum. In the BP2000, the subsequent decay of the excited state into 2α particles had been determined to the monochromatic line of 3.04 MeV.

However, C.E.Ortiz et al. measured the these 2α spectrum strictly [11] (see the right picture of Figure 2.5). In this work, the neutrino energy spectrum is reflected by a broad distribution of 2α . The ^8B neutrino energy spectrum and ratio between [10] and [11] is shown in Figure 2.6. Approximately 10-20% more neutrinos are found in the high energy end of the spectrum according to Ortiz et al.

In this thesis, the work of Ortiz et al. is adopted as the ^8B neutrino spectrum.

2.2.3 Observation of solar neutrinos - I Homestake, Kamiokande, SAGE and GALLEX

In this subsection, solar neutrino observations by four experiments are described.

The first experiment of the solar neutrino detection by Davis and his collaborators is the Homestake chlorine experiment. It is based on the reaction :



The radioactive argon atoms produced in this reaction are extracted using chemical methods and counted in proportional counters. The threshold energy of $E_{th} = 0.814\text{MeV}$ permits the

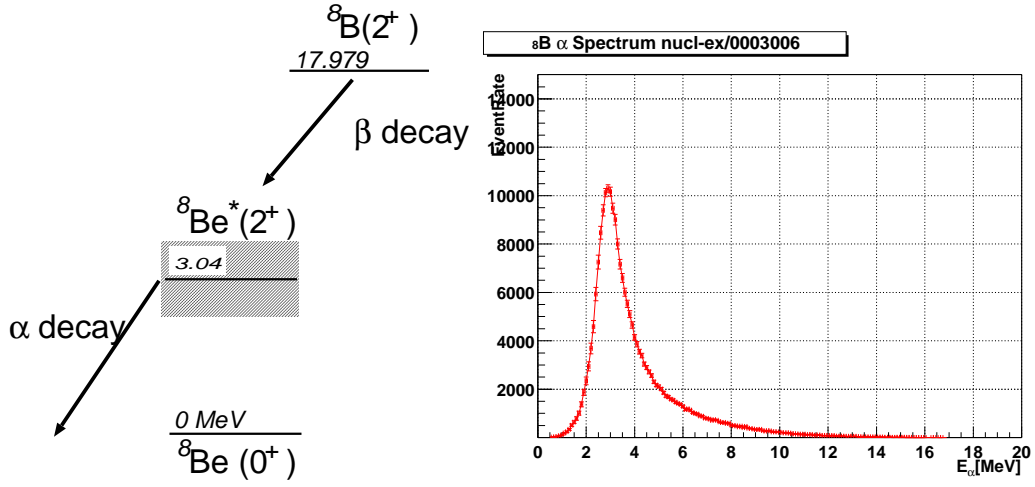


Figure 2.5: Energy levels of decay chains of $^8\text{B}(\beta^+)^8\text{Be}(2\alpha)$ and the energy spectrum of 2α

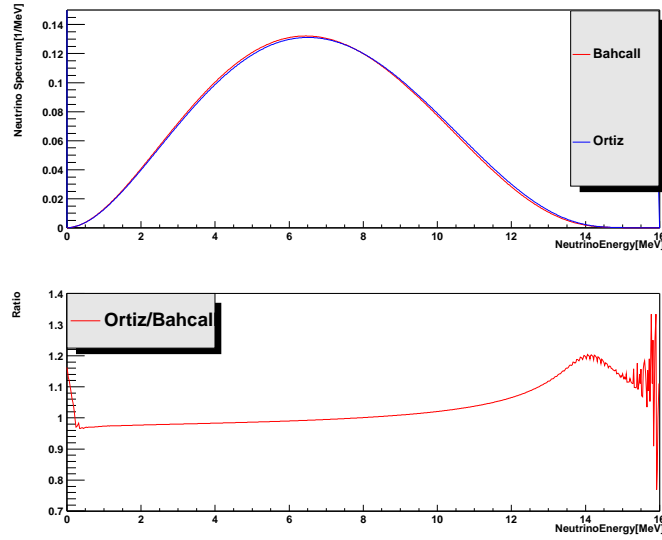


Figure 2.6: Neutrino spectrum of Ortiz et.al. and Bahcall's work (top) and ratio of the two spectra (bottom)

detection of all the major solar neutrino sources (^8B , ^7Be and pep) except for the pp neutrino. The largest contribution is ^8B neutrino. The expected event rate of solar neutrino interaction is predicted to be $7.6^{+1.3}_{-1.1}$ SNU in the BP2000. The measured count rate is [12]:

$$2.56 \pm 0.16(stat.) \pm 0.16(syst.) SNU \quad (2.11)$$

and ratio to the theoretical prediction is :

$$\frac{Data(Cl)}{SSM} = 0.34 \pm 0.03 \quad (2.12)$$

The measured flux of solar neutrinos is significantly smaller than the prediction of the SSM. This is the first solar neutrino problem.

Next solar neutrino experiment is Kamiokande detector. Kamiokande used a water Cherenkov counter with 3000 ton pure water. Location is 1000 m below the top of the Mt.Ikenoyama, in Kamioka town, Gifu prefecture. Kamiokande solar neutrino detection was started in 1986. The solar neutrinos are detected using the reaction :

$$\nu_e + e^- \rightarrow \nu_e + e^- \quad (2.13)$$

The recoil electron emits the Cherenkov photons in the water, which are detected by the PMTs. Cherenkov photon roughly keeps the neutrino direction that is correlated to the sun. The energy threshold for the recoil electron in Kamiokande was ~ 7.5 MeV. So detected neutrino is only ^8B neutrinos. The flux of solar neutrinos measured over 2079 days is [13]:

$$2.80 \pm 0.19(stat.) \pm 0.33(syst.) \times 10^6 cm^{-2} s^{-1} \quad (2.14)$$

while BP2000 predicts $5.05(1 \times \frac{+0.20}{-0.16}) \times 10^6 cm^{-2} s^{-1}$. This result confirmed the deficit of the solar neutrinos with Homestake and lead the new problem, disappearance of ^7Be neutrino with Homestake result.

For detection of pp neutrinos, radiochemical techniques were used in two other experiments - SAGE and GALLEX using ^{71}Ga targets. The reaction is :

$$\nu_e + ^{71}\text{Ga} \rightarrow ^{71}\text{Ge} + e^- \quad (2.15)$$

The energy threshold of this reaction is 0.234 MeV which is below the endpoint of the pp neutrinos (0.420 MeV). Since the flux of pp neutrinos is very large, they are expected to give the main contribution to the observed events in the experiments. The observed flux by SAGE [14] and GALLEX [15] is as follows :

$$67.2^{+7.2}_{-7.0}(stat.)^{+3.5}_{-3.0}(syst.) SNU \quad \text{for SAGE} \quad (2.16)$$

$$77.5 \pm 6.2(stat.)^{+4.3}_{-4.7}(syst.) SNU \quad \text{for GALLEX} \quad (2.17)$$

The expected rate is 128^{+9}_{-7} SNU for the BP2000, this results means that SAGE and GALLEX observed significantly smaller solar neutrino flux than predicted and confirmed the deficit of solar neutrinos.

2.2.4 Observation of solar neutrinos - II SuperKamiokande and SNO

In this subsection, recent solar neutrino observations by SuperKamiokande and SNO experiments are described.

The SuperKamiokande detector is like Kamiokande, a water Cherenkov detector. But detector performance is improved. Detector size is 22.5 ktons for fiducial volume (33 times the Kamiokande). Also radioactive isotopes (mainly Rn) are removed significantly from the water and the energy threshold is lowered to 5 MeV. The ratio of the detected neutrino flux (^8B only) to the SSM prediction is [16]:

$$\frac{Data}{SSM} = 0.465 \pm 0.005(stat.)_{-0.012}^{+0.014}(syst.) \quad (2.18)$$

In 1999, a new realtime solar neutrino experiment, SNO started operation. This experiment uses 1000 tons of ultra-pure heavy water (D_2O). The reactions of the ^8B neutrino detection are :

$$\nu_e + d \rightarrow p + p + e^-(CC) \quad (2.19)$$

$$\nu_x + d \rightarrow p + n + \nu_x(NC) \quad (2.20)$$

$$\nu_x + e^- \rightarrow \nu_x + e^-(ES) \quad (2.21)$$

Normalized by the integrated rates above the kinetic energy threshold of $T_{eff} \geq 5$ MeV, the flux of ^8B neutrinos measured with each reaction in SNO is extracted [1]:

$$\phi_{CC}^{SNO} = 1.76_{-0.05}^{+0.06}(stat.)_{-0.09}^{+0.09}(syst.) \times 10^6 \text{cm}^{-2} \text{s}^{-1} \quad (2.22)$$

$$\phi_{ES}^{SNO} = 2.39_{-0.23}^{+0.24}(stat.)_{-0.12}^{+0.12}(syst.) \times 10^6 \text{cm}^{-2} \text{s}^{-1} \quad (2.23)$$

$$\phi_{NC}^{SNO} = 5.09_{-0.43}^{+0.44}(stat.)_{-0.43}^{+0.46}(syst.) \times 10^6 \text{cm}^{-2} \text{s}^{-1} \quad (2.24)$$

A simple change of variables resolves the data directly into electron (ϕ_e) and non-electron ($\phi_{\mu\tau}$) components :

$$\phi_e = 1.76_{-0.05}^{+0.05}(stat.)_{-0.09}^{+0.09}(syst.) \quad (2.25)$$

$$\phi_{\mu\tau} = 3.41_{-0.45}^{+0.45}(stat.)_{-0.45}^{+0.48}(syst.) \quad (2.26)$$

$$(2.27)$$

Figure 2.7 gives flux of ^8B solar neutrinos, ϕ_e and $\phi_{\mu\tau}$, deduced from SNO's CC, ES and NC results. Now $\phi_{\mu\tau}$ is 5.3σ above 0. Adding the SuperKamiokande ES measurement of the ^8B flux $\phi_{ES}^{SK} = 2.32 \pm 0.03(stat.)_{-0.07}^{+0.08}(syst.)$ as an additional constraint, $\phi_{\mu\tau} = 3.45_{-0.62}^{+0.65}$ is 5.5σ above 0. Sum of the ϕ_e and $\phi_{\mu\tau}$ is in excellent agreement with the SSM prediction.

This result gives strong evidence for the neutrino flavor conversion.

2.3 Neutrino oscillation

There are many possible solutions proposed to the solar neutrino problem, the most natural one being the neutrino oscillations. This would imply that the neutrino has mass and different generations mix. In this section, neutrino oscillation are explained in detail. Here, the discussion is restricted to the two-flavor neutrinos.

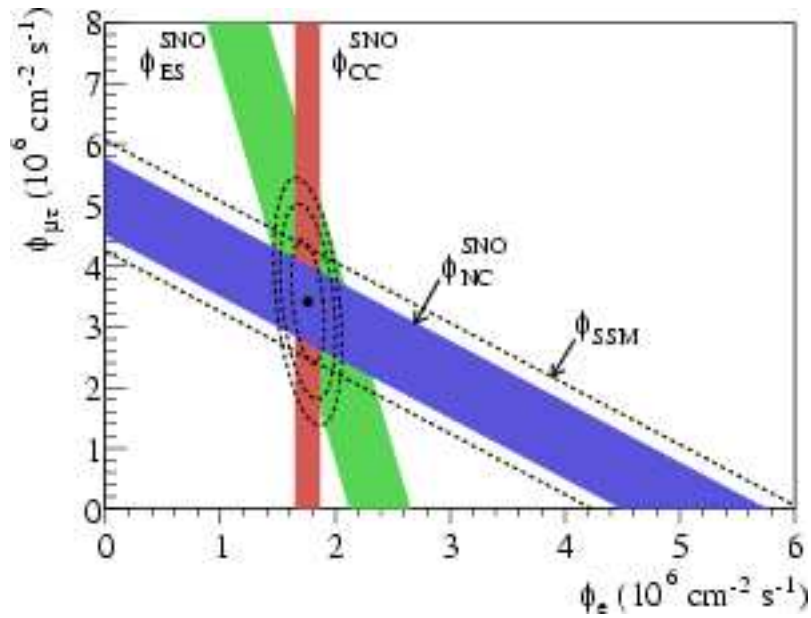


Figure 2.7: Flux of ^8B neutrinos which are μ or τ flavor vs flux of electron neutrino for SNO [1].

2.3.1 Neutrino oscillation in vacuum

Let us now consider the two neutrino case and the neutrino oscillation in vacuum case. The mixing matrix U can be written as :

$$U = \begin{pmatrix} \cos \theta & \sin \theta \\ -\sin \theta & \cos \theta \end{pmatrix} \quad (2.28)$$

where θ is the mixing angle. The neutrino mass and flavor eigenstates are therefore related through :

$$\begin{pmatrix} |\nu_e\rangle \\ |\nu_\mu\rangle \end{pmatrix} = \begin{pmatrix} \cos \theta & \sin \theta \\ -\sin \theta & \cos \theta \end{pmatrix} \begin{pmatrix} |\nu_1\rangle \\ |\nu_2\rangle \end{pmatrix} \equiv U \begin{pmatrix} |\nu_1\rangle \\ |\nu_2\rangle \end{pmatrix} \quad (2.29)$$

where $|\nu_1\rangle$ and $|\nu_2\rangle$ are the mass eigenstates. The propagation of mass eigenstates is expressed as :

$$|\nu_i(t)\rangle = e^{-iE_i t} |\nu_i(0)\rangle \quad (2.30)$$

where t is the time in laboratory frame and E_i is the energy of a neutrino of the mass eigenstate i . E_i is approximated as follows,

$$E_i = \sqrt{p^2 + m_i^2} \simeq p + \frac{m_i^2}{2p} \simeq p + \frac{m_i^2}{2E} \quad (2.31)$$

where m_i is the mass of eigenstate i . eq(2.29) is rewritten as:

$$|\nu_a(t)\rangle = \sum_i U_{ai} |\nu_i(t)\rangle \quad (2.32)$$

substitution of (2.30) in (2.30) yields :

$$\begin{aligned} |\nu_a(t)\rangle &= \sum_i U_{ai} e^{-iE_i t} |\nu_i(0)\rangle \\ &= \sum_i \sum_b U_{ai} U_{ib}^{-1} e^{-iE_i t} |\nu_b(0)\rangle \end{aligned} \quad (2.33)$$

Therefore, the amplitude that the same flavor is maintained is:

$$\begin{aligned} \langle \nu_a | \nu_a(t) \rangle &= \sum_i \sum_b U_{ai} U_{ib}^{-1} e^{-iE_i t} \langle \nu_a | \nu_b(0) \rangle \\ &= \sum_i U_{ai} U_{ia}^{-1} e^{-iE_i t} \end{aligned} \quad (2.34)$$

The survival probability that the same flavor $P(a \rightarrow a, t)$ is :

$$\begin{aligned} P(a \rightarrow a, t) &= |\langle \nu_a | \nu_a(t) \rangle|^2 \\ &= 1 - \sin^2 2\theta \sin^2 \frac{\Delta m^2}{4E} t \end{aligned} \quad (2.35)$$

Here $\Delta m^2 = m_2^2 - m_1^2$. The transition probability is $P(\nu_e \rightarrow \nu_\mu) = 1 - P(\nu_e \rightarrow \nu_e)$. It is convenient to rewrite the transition probability in terms of the distance L travelled by neutrinos. For relativistic neutrinos $L \simeq t$, and one has :

$$P(\nu_e \rightarrow \nu_e, L) = 1 - \sin^2 2\theta \sin^2 \frac{\pi L}{l_{osc}} \quad (2.36)$$

where l_{osc} is the oscillation length defined as

$$l_{osc} = \frac{4\pi E}{\Delta m^2} \simeq 2.48m \frac{E(MeV)}{\Delta m^2(eV^2)} = 2.48km \frac{E(GeV)}{\Delta m^2(eV^2)} \quad (2.37)$$

It is equal to the distance between any two closest minimum or maximum of the survival probability. l_{osc} is inversely proportional to energy difference of neutrino mass eigenstates : $l_{osc} = 2\pi/(E_2 - E_1)$. Another convenient form of expression for the survival probability is

$$P(\nu_e \rightarrow \nu_e, L) = 1 - \sin^2 2\theta \sin^2 \left(1.27 \Delta m^2 \frac{L}{E} \right) \quad (2.38)$$

where L is in m and E in MeV or L is in km and E in GeV.

2.3.2 Neutrino oscillation in matter

When neutrinos propagate through matter ν_e and other flavors ν_μ (and ν_τ) feel different potentials, because ν_e scatters off electrons via the charged current & neutral current but ν_μ scatters only through the neutral current. This mechanism is called as the Mikheyev-Smirnov-Wolfenstein (MSW) effect [17]. This induces a coherent effect in which maximal conversion of ν_e into ν_μ take place even for a rather small mixing angle in the vacuum, when the phase arising from the potential difference between the two neutrinos cancels the phase caused by the mass

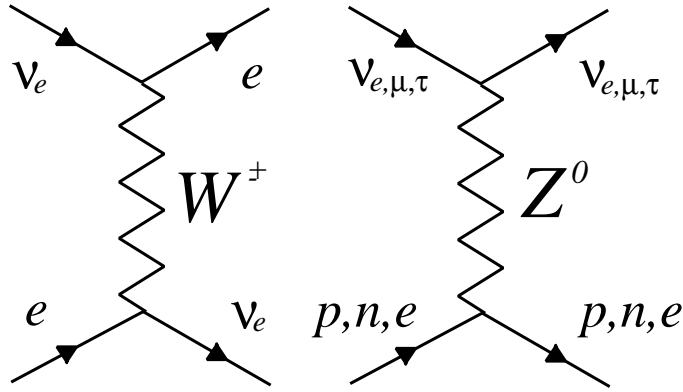


Figure 2.8: Feynman diagrams for neutrino scattering for electron and neutron

difference in vacuum. Figure 2.8 gives the neutrino scattering diagrams for charged current (CC) and neutral current (NC). CC interaction is mediated by W^\pm exchange. NC interaction is mediated by Z^0 exchange. At low neutrino energies, CC interactions are described by the effective Hamiltonian :

$$H_{cc} = \frac{G_F}{\sqrt{2}} [\bar{e} \gamma_\mu (1 - \gamma_5) \nu_e] [\bar{\nu}_e \gamma^\mu (1 - \gamma_5) e] = \frac{G_F}{\sqrt{2}} [\bar{e} \gamma_\mu (1 - \gamma_5) e] [\bar{\nu}_e \gamma^\mu (1 - \gamma_5) \nu_e] \quad (2.39)$$

And we obtain :

$$(V_e)_{CC} \equiv V_{CC} = \sqrt{2} G_F N_e \quad (2.40)$$

where N_e is electron number density. Samely, one can find the NC contribution V_{NC} to the matter-induced neutrino potentials. Since NC interaction are flavor independent, these contributions are the same for neutrinos of all three flavors. The direct calculation of the contribution due to the NC scattering of neutrinos off neutrons gives :

$$(V_n)_{NC} = \frac{-G_F N_n}{\sqrt{2}} \quad (2.41)$$

where N_n is the neutron number density. Together with eq.(2.40) this gives:

$$V_e = \sqrt{2} G_F \left(N_e - \frac{N_n}{2} \right), \quad V_{\mu,\tau} = \sqrt{2} G_F \left(-\frac{N_n}{2} \right) \quad (2.42)$$

So we can obtain time development Schrödinger equation:

$$i \frac{d}{dt} \begin{pmatrix} |\nu_e(t)\rangle \\ |\nu_\mu(t)\rangle \end{pmatrix} = \left\{ U \begin{pmatrix} E_1 & 0 \\ 0 & E_2 \end{pmatrix} U^{-1} + \begin{pmatrix} V_C + V_N & 0 \\ 0 & V_N \end{pmatrix} \right\} \begin{pmatrix} |\nu_e(t)\rangle \\ |\nu_\mu(t)\rangle \end{pmatrix} \quad (2.43)$$

V_e and V_μ contain a common term due to NC interaction. Such common term in the diagonal elements are of no consequence for neutrino oscillations. We can therefore omit them. eq.(2.43) is rewritten :

$$i \frac{d}{dt} \begin{pmatrix} |\nu_e(t)\rangle \\ |\nu_\mu(t)\rangle \end{pmatrix} = \begin{pmatrix} -\frac{\Delta m^2}{4E} \cos 2\theta + \sqrt{2} G_F N_e & \frac{\Delta m^2}{4E} \sin 2\theta \\ \frac{\Delta m^2}{4E} \sin 2\theta & \frac{\Delta m^2}{4E} \cos 2\theta \end{pmatrix} \begin{pmatrix} |\nu_e(t)\rangle \\ |\nu_\mu(t)\rangle \end{pmatrix} \quad (2.44)$$

In general, the electron number density N_e depends on the coordinate along the neutrino trajectory or, on t . The simple case of constant matter density $N_e = \text{const}$ is considered. Diagonalization of the effective Hamiltonian in eq.(2.44) gives the following neutrino eigenstates in matter:

$$\begin{pmatrix} |\nu_{1m}\rangle \\ |\nu_{2m}\rangle \end{pmatrix} = \begin{pmatrix} \cos \theta_m & -\sin \theta_m \\ \sin \theta_m & \cos \theta_m \end{pmatrix} \begin{pmatrix} |\nu_e\rangle \\ |\nu_\mu\rangle \end{pmatrix} \quad (2.45)$$

where the mixing angle θ_m is given by :

$$\tan 2\theta_m = \frac{\frac{\Delta m^2}{2E} \sin 2\theta}{\frac{\Delta m^2}{2E} \cos 2\theta - \sqrt{2}G_F N_e} \quad (2.46)$$

The difference of neutrino eigenenergies in matter is :

$$E_{1m} - E_{2m} = \sqrt{\left(\frac{\Delta m^2}{2E} \cos 2\theta - \sqrt{2}G_F N_e\right)^2 + \left(\frac{\Delta m^2}{2E}\right)^2 \sin^2 2\theta} \quad (2.47)$$

It is easy to find the probability of $\nu_e \leftrightarrow \nu_\mu$ oscillations in matter :

$$P(\nu_e \rightarrow \nu_\mu, L) = \sin^2 \theta_m \sin^2 \left(\pi \frac{L}{l_m} \right) \quad (2.48)$$

where :

$$l_m = \frac{2\pi}{E_{1m} - E_{2m}} = \frac{2\pi}{\sqrt{\left(\frac{\Delta m^2}{2E} \cos 2\theta - \sqrt{2}G_F N_e\right)^2 + \left(\frac{\Delta m^2}{2E}\right)^2 \sin^2 2\theta}} \quad (2.49)$$

It has exactly the form as probability of oscillation in vacuum, except that the vacuum mixing angle θ and oscillation length l_{osc} are replaced by those in matter, θ_m and l_m . In the limit of zero matter density $\theta_m = \theta$, $l_m = l_{osc}$, the vacuum oscillation probability is recovered. The oscillation amplitude :

$$\sin^2 \theta_m = \frac{\left(\frac{\Delta m^2}{2E}\right)^2 \sin^2 2\theta}{\left(\frac{\Delta m^2}{2E} \cos 2\theta - \sqrt{2}G_F N_e\right)^2 + \left(\frac{\Delta m^2}{2E}\right)^2 \sin^2 2\theta} \quad (2.50)$$

has a typical resonance form, with a maximum value $\sin^2 2\theta = 1$ when the condition :

$$\sqrt{2}G_F N_e = \frac{\Delta m^2}{2E} \cos 2\theta \quad (2.51)$$

is satisfied. It is called the MSW resonance condition. The electron density at which the resonance condition is :

$$N_{e,res} \equiv \frac{\Delta m^2 \cos 2\theta}{2\sqrt{2}G_F E} \quad (2.52)$$

Next, the condition of solar neutrino is considered.

In the sun, the density of electrons is non-uniform. Figure 2.9 shows the radial dependence of electron and neutron density in the sun. The evolution equation .. does not allow an analytic

solution and has to be solved numerically. But the approximation of probability, jump transition $|\nu_{2m}\rangle \rightarrow |\nu_{1m}\rangle$ is given. The probability of this jump, P_{jump} is calculated by Landau-Zener function [18]

$$P_{jump} = \exp \left(-\frac{\pi}{4} \frac{\sin^2 2\theta}{E \cos 2\theta} \frac{\Delta m^2}{\left| \frac{1}{N_e} \frac{dN_e}{dr} \right|} \right) \quad (2.53)$$

Therefore, the condition :

$$\sin^2 2\theta \Delta m^2 \geq E \cos 2\theta \left| \frac{1}{N_e} \frac{dN_e}{dr} \right| \quad (2.54)$$

is required to not change from ν_{2m} to ν_{1m} .

Figure 2.10 shows the ν_e survival probability at six solutions.

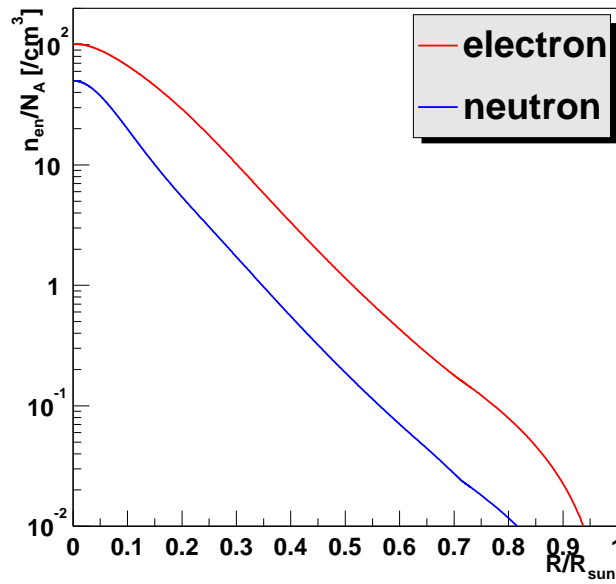


Figure 2.9: the radial dependence of electron and neutron density in the sun normalized by Avogadro constant N_A . n_{en} is the electron or neutron density ($/\text{cm}^3$).

2.4 Neutrino oscillation analysis for solar neutrino problem

The SNO neutral current results have shown that the lack of the solar neutrino has been caused by the neutrino flavor transition and suggested the neutrino oscillation strongly. The oscillation parameters given by the solar neutrino experiments have different regions. They are called 'Large Mixing Angle solution' (LMA), 'Small Mixing Angle solution' (SMA), 'Low Δm^2 solution' (LOW) and 'Vacuum Oscillation solution' (VAC) in Figure 2.11.

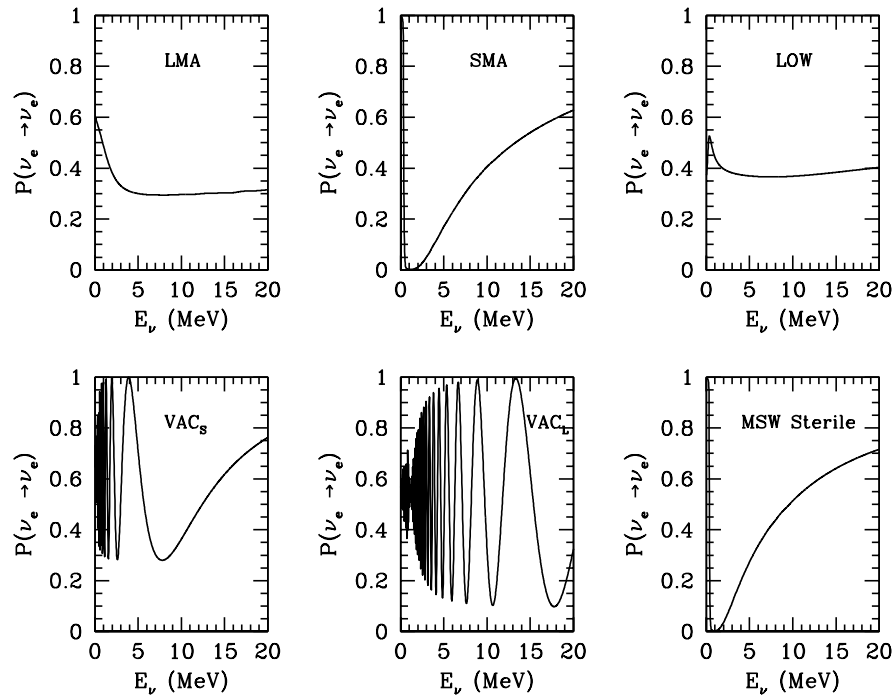


Figure 2.10: Solar neutrino survival probability in six solutions

In these four solution, Super Kamiokande new result [16] based on the zenith angle spectrum data has excluded the two solutions VAC and SMA. The remaining allowed solution are LMA and LOW by SK+SNO combined fit and only LMA by SK+all rates.

In 2002, KamLAND reactor experiment [2] has suggested that all oscillation solutions are excluded except LMA solution using disappearance of reactor $\bar{\nu}_e$ flux (see Figure 2.12). Now the best-fit parameters in LMA is

$$\begin{aligned} \Delta m^2 &= 5.5 \times 10^{-5} & \sin^2 2\theta &= 0.833 & \text{(Solar best) [19]} \\ \Delta m^2 &= 6.9 \times 10^{-5} & \sin^2 2\theta &= 1.0 & \text{(KamLAND best)} \end{aligned}$$

There are two overlap solutions between solar LMA solution and the KamLAND allowed solutions. The 'LMA(1)' solution covers the LMA best fit solution $\Delta m^2 = 5.5 \times 10^{-5}$. The other one 'LMA(2)' covers the upper part of the LMA solution $\Delta m^2 \sim 1 \times 10^{-4}$. The future KamLAND result will determine either of the two solutions by increasing the data.

Accepting the LMA-MSW solution to the solar neutrino anomaly, as indicated by the first KamLAND results, one can still probe the admixture of alternative mechanisms of the solar neutrino conversion, **Spin Flavor Precession** and **Neutrino Decay**. In the next chapter, the potentiality and the indicator of these two processes, the production of solar anti-neutrino are discussed.

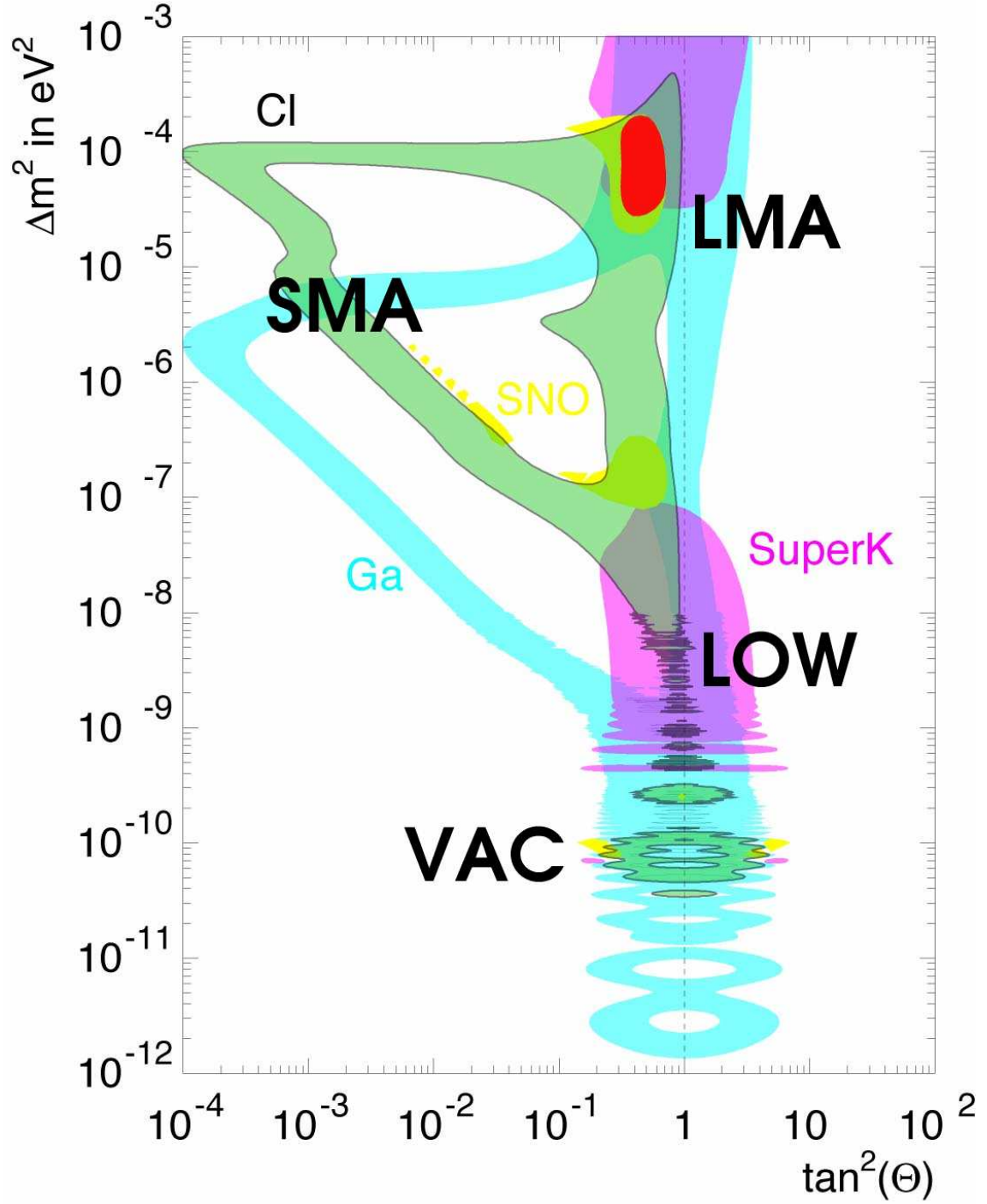


Figure 2.11: Oscillation parameter plot for solar neutrino analysis [20]. The LMA solution is the most promising one for all solar neutrino experiments

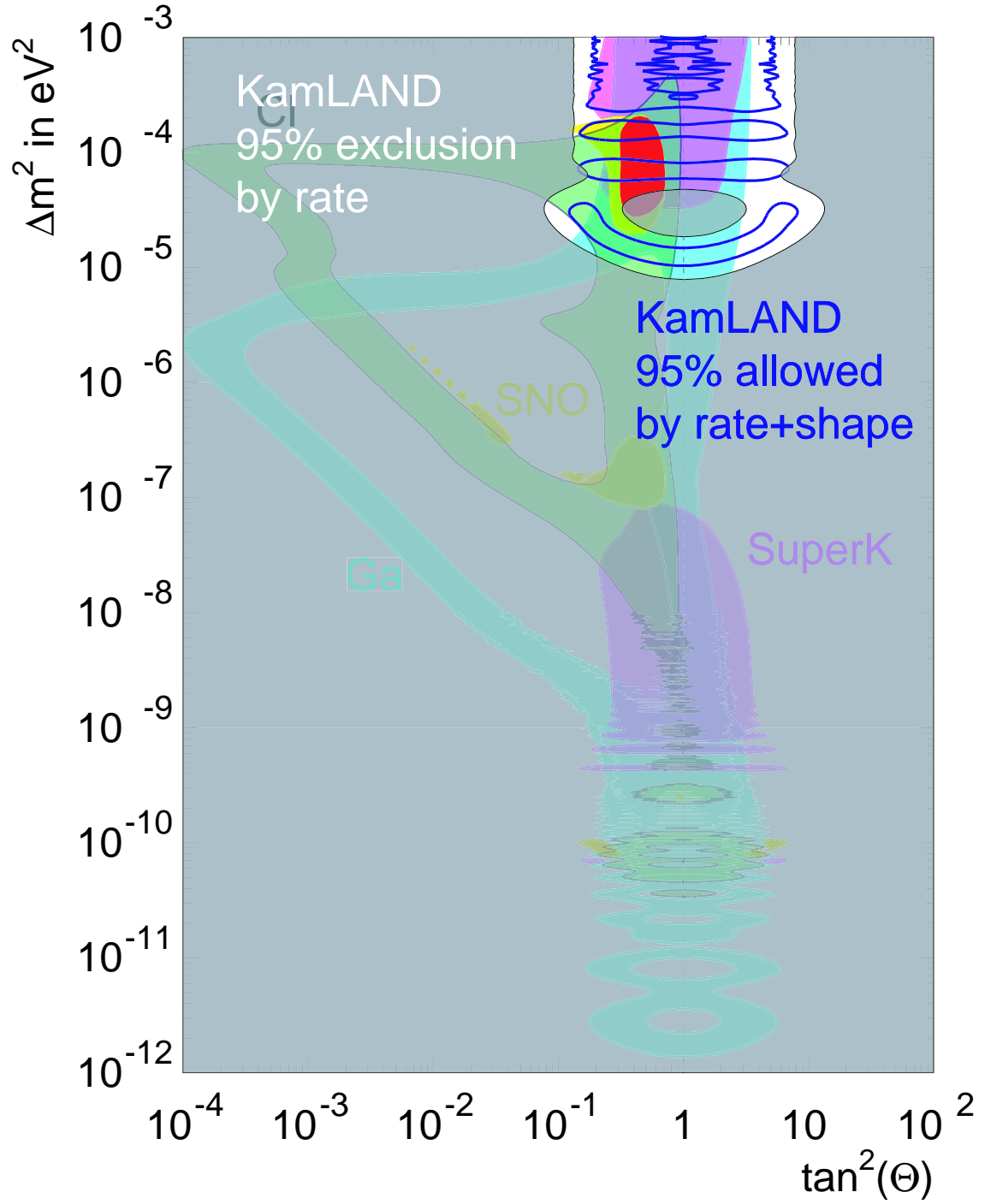


Figure 2.12: Oscillation parameter plot for solar + KamLAND result [20]. The KamLAND analysis uses the total rate and the spectrum shape distribution.

Chapter 3

Neutrino magnetic moment and neutrino decay

In this chapter, other interpretations the neutrino magnetic moment and the neutrino decay for solving solar neutrino problem are discussed. And the method of the search by KamLAND detector are discussed.

3.1 Neutrino magnetic moment

In the framework of the standard Weinberg-Salam theory, neutrino magnetic dipole moment for Dirac neutrinos is induced by radiative corrections and is calculated to be [21]:

$$\mu_\nu \equiv \frac{3eG_F}{8\sqrt{2}\pi^2}m_\nu = 3 \times 10^{-19} \mu_B \left(\frac{m_\nu}{1\text{eV}} \right) \quad (3.1)$$

The order of the neutrino magnetic dipole moment is not enough to be detected directly. The experimentally obtained upper limit is $< \sim 10^{-10} \mu_B$ (see the next section). Majorana neutrinos cannot have the magnetic dipole moment because of CPT invariant. However, the transition moment, which is relevant to $\nu_i \rightarrow \nu_j$, may exist for both Dirac and Majorana neutrinos. If the magnetic moment would be found to have a value beyond (3.1), this would indicate the presence of interactions which violate chirality conservation beyond the standard model.

3.1.1 Experimental limit for neutrino magnetic moment

One direct method for measuring the neutrino magnetic moment is to detect an electro-magnetic (EM) effect against neutrino-electron scattering. If there is a neutrino magnetic moment μ_ν , cross section is increased :

$$\frac{d\sigma}{dE_\nu} = \frac{\pi\alpha^2\mu_\nu^2}{m_e^2} \left(\frac{1}{E_e - m_e} - \frac{1}{E_\nu} \right) \quad (3.2)$$

where E_ν is the neutrino energy, E_e is the scattered electron energy. The recent MUNU experiment [22] used $\bar{\nu}_e$ flux from power reactor and obtained the upper limit,

$$\mu_{\bar{\nu}_e} < 1.0 \times 10^{-10} \mu_B \quad (90\%C.L.) \quad (3.3)$$

As for the magnetic moment ν_e, ν_μ, ν_τ , accelerator-based experiment provided the following limits [23] [24] [25]:

$$\begin{aligned}\mu_{\nu_e} &< 10.8 \times 10^{-10} \mu_B \\ \mu_{\nu_\mu} &< 6.8 \times 10^{-10} \mu_B \\ \mu_{\nu_\tau} &< 3.9 \times 10^{-7} \mu_B \quad (90\% C.L.)\end{aligned}\tag{3.4}$$

3.1.2 Phenomenological limit for neutrino magnetic moment

Phenomenological upper limit for neutrino magnetic moment from astrophysics is induced lower than the one by the ground experiments.

If neutrinos have a large magnetic moment, the right-handed neutrinos can be produced through the magnetic interaction and they contribute to the energy density of neutrinos which increase the expansion rate in the early universe. This leads to a larger ${}^4\text{He}$ abundance than observed. Hence, the upper limit:

$$\mu_\nu < (0.1 - 0.2) \times 10^{-10} \mu_B \tag{3.5}$$

is obtained [26].

Other method for deriving the limit is the plasmon decay process $\gamma \rightarrow \nu\bar{\nu}$ in the star. If there are finite dipole magnetic moment, the coupling of neutrino and photon exit. If the energy loss rate of the Sun due to the $\gamma \rightarrow \nu\bar{\nu}$ process exceeded the solar luminosity, the Sun would have burnt out before reaching its observed age. Today, helioseismology allows for tighter constraints which have given [27]:

$$\mu_\nu < 4 \times 10^{-10} \mu_B \tag{3.6}$$

A more significant improvement is provided by globular-cluster stars [27]. Nonstandard neutrino losses would delay the ignition of helium in the cores of low mass red giants. Several observables in the color magnitude diagram of globular clusters allow one to derive a restrictive limit on the core mass at helium ignition, corresponding to the requirement that the new energy loss rate must not exceed the standard losses by more than a factor of a few. Thus one finds the limit :

$$\mu_\nu < 3 \times 10^{-12} \mu_B \tag{3.7}$$

Supernova 1987A provides another energy loss limit. The structure of electromagnetic dipole interaction couples neutrino states of opposite helicity. Therefore, neutrinos which are trapped in a SN core flip their helicity in electromagnetic interactions, taking them into nearly sterile right-handed states which escape directly from the inner SN core. This anomalous energy loss channel short-circuits the standard diffusive energy transfer and thus shortens the measurable signal of left-handed $\bar{\nu}_e$'s, in conflict with the observed duration of SN 1987A signal. The limit:

$$\mu_\nu < 10^{-12} \mu_B \tag{3.8}$$

is obtained [28].

We must mention that these limits have theoretical model dependence.

3.1.3 Progress of neutrino event rate and RSFP

The interpretation of solar neutrino problem by inducing the large neutrino magnetic moment was pointed out. Figure 3.1 shows the yearly progress of neutrino event rate at ^{37}Cl experiment and Kamiokande. In the left picture, the neutrino capture rate at ^{37}Cl experiment seems to be changed with a change of the sunspot number in 22 years' period of the change of the magnetic field [29]. Several authors [30, 31] found that a magnetic moment of neutrino can cause the resonant transition of neutrino helicity like the MSW effect in the sun. This effect is called Resonant Spin Flavor Precession (RSFP).

This RSFP model can explain the time variation of ^{37}Cl experiment with a very large magnetic moment such as $10^{-10}\mu_B$. Such large magnetic moment seems to be excluded by the limit mentioned previous subsection. In addition, the result of kamiokande [32] (right picture of Figure 3.1) seems not to support the time variation. So simple RSFP model is eliminated.

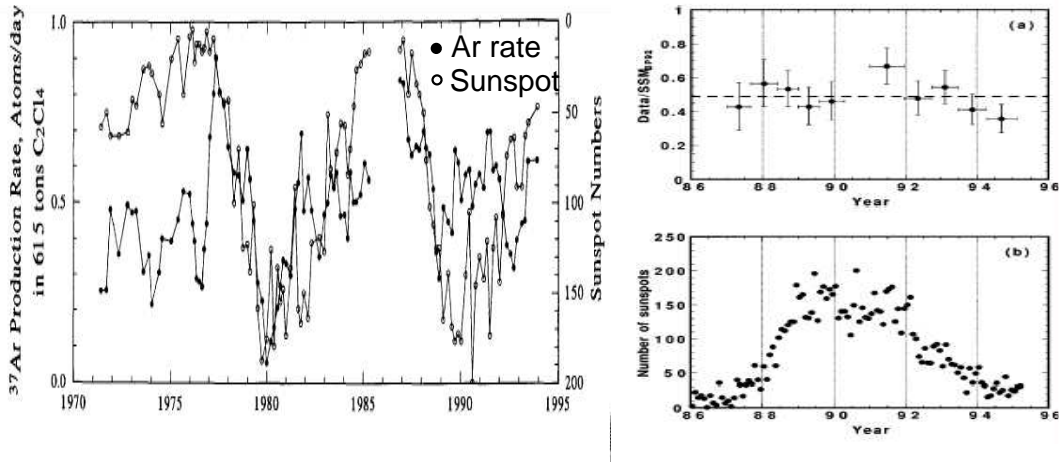


Figure 3.1: The progress of neutrino event rate and sunspot number. In left figure (Homestake), the sunspot are plotted on an inverted scale.

3.1.4 Hybrid model (RSFP+MSW) and anti-electron neutrino production

The defect of the simple RSFP model is compensated by inducing the hybrid model which is including the MSW effect in the sun simultaneously with RSFP. The propagation equation of Dirac neutrino under the hybrid model is :

$$i \frac{d}{dt} \begin{pmatrix} \nu_{eL} \\ \nu_{\mu L} \\ \nu_{eR} \\ \nu_{\mu R} \end{pmatrix} = \begin{pmatrix} \frac{G}{\sqrt{2}}(2N_e - N_n) & \frac{\Delta m^2}{4E} \sin 2\theta & \mu_{ee}B & \mu_{e\mu}B \\ \frac{\Delta m^2}{4E} \sin 2\theta & -\frac{G}{\sqrt{2}}N_n + \frac{\Delta m^2}{2E} \cos 2\theta & \mu_{\mu e}B & \mu_{\mu\mu}B \\ \mu_{ee}B & \mu_{e\mu}B & 0 & 0 \\ \mu_{\mu e}B & \mu_{\mu\mu}B & 0 & \frac{\Delta m^2}{2E} \cos 2\theta \end{pmatrix} \begin{pmatrix} \nu_{eL} \\ \nu_{\mu L} \\ \nu_{eR} \\ \nu_{\mu R} \end{pmatrix} \quad (3.9)$$

In a Dirac neutrino case, there are no weak interactions by ν_{eR} and $\nu_{\mu R}$ because they are sterile. Neutrino flavor mixing is considered only for left-handed neutrino.

In a Majorana neutrino case, the transition is $\nu_{iL} \rightarrow \nu_{jL}^c$ ($\bar{\nu}_j$) which are not sterile. The propagation equation of the Majorana neutrinos is :

$$i \frac{d}{dt} \begin{pmatrix} \nu_e \\ \nu_\mu \\ \bar{\nu}_e \\ \bar{\nu}_\mu \end{pmatrix} = \begin{pmatrix} \frac{G}{\sqrt{2}}(2N_e - N_n) & \frac{\Delta m^2}{4E} \sin 2\theta & 0 & \mu B \\ \frac{\Delta m^2}{4E} \sin 2\theta & -\frac{G}{\sqrt{2}}N_n + \frac{\Delta m^2}{2E} \cos 2\theta & -\mu B & 0 \\ 0 & -\mu B & -\frac{G}{\sqrt{2}}(2N_e - N_n) & \frac{\Delta m^2}{4E} \sin 2\theta \\ \mu B & 0 & \frac{\Delta m^2}{4E} \sin 2\theta & \frac{G}{\sqrt{2}}N_n + \frac{\Delta m^2}{2E} \cos 2\theta \end{pmatrix} \begin{pmatrix} \nu_e \\ \nu_\mu \\ \bar{\nu}_e \\ \bar{\nu}_\mu \end{pmatrix} \quad (3.10)$$

Neutrino flavor mixing is also considered for anti-neutrino and we can expect solar $\bar{\nu}_e$ production [31, 33]. There are essentially two ways in which $\bar{\nu}_e$'s can be produced : One is that the originally produced solar ν_e first oscillate into ν_μ and then converted into $\bar{\nu}_e$ by RSFP.

$$\nu_e \xrightarrow{osc.} \nu_\mu \xrightarrow{RSFP} \bar{\nu}_e \quad (3.11)$$

The other is that solar ν_e are first converted to $\bar{\nu}_\mu$ and then oscillate into $\bar{\nu}_e$.

$$\nu_e \xrightarrow{RSFP} \bar{\nu}_\mu \xrightarrow{osc.} \bar{\nu}_e \quad (3.12)$$

3.2 Neutrino decay

The neutrino decay scenario for solar neutrino is possible to make the solar $\bar{\nu}_e$ by specific decay mode [34, 35, 36]. In this section, the detail of the neutrino decay scenario is discussed.

3.2.1 The limit for neutrino lifetime

Now the weak interaction in terms of the Weinberg-Salam model is considered and it is assumed that all left (right)-handed components are transformed as doublets (singlets) under the weak SU(2) transformation. This weak interaction eigenstate ν_e can be written as a superposition $\nu_e = \sum_i U_{ei} \nu_i$ of mass eigenstates ν_j . This matrix U induces the decay of a massive neutrino ν_i into a lighter neutrino ν_j and a photon :

$$\nu_i \rightarrow \nu_j + \gamma \quad (3.13)$$

as well as the decay into ν_L and an electron positron pair, if $m_j - m_i > 2m_e$:

$$\nu_i \rightarrow \nu_j + e^+ + e^- \quad (3.14)$$

But this decay mode is excluded by the neutrino mass limit. Thus possible decay mode is only $\nu_i \rightarrow \nu_j + \gamma$. The decay rate is given by [38]:

$$\Gamma(\nu_i \rightarrow \nu_j + \gamma) = \frac{9}{16} \frac{\alpha}{\pi} \frac{G_F^2}{128\pi^3} \frac{(\Delta m_{ij}^2)^3}{m_i} \left(\sum_{\alpha} U_{i\alpha}^* U_{\alpha j} \left(\frac{m_{\alpha}^2}{m_W^2} \right) \right)^2 \quad (3.15)$$

where $\Delta m_{ij}^2 = m_i^2 - m_j^2$, α is the fine structure constant and m_W represents the mass of the weak W-boson.

In this decay mode, there are several lifetime limits estimated by non-observation of the final state γ ray. The most stringent bounds from reactor and accelerator based experiments are [39, 40]:

$$\begin{aligned}\tau(\nu_e)/m_\nu &> 300 \text{sec}/eV \\ \tau(\nu_\mu)/m_\nu &> 15.4 \text{sec}/eV\end{aligned}\quad (3.16)$$

From the non-observation of γ 's in coincidence with the neutrinos from the SN1987A [41] :

$$\tau/m_\nu > 6.3 \times 10^{15} \text{sec}/eV \quad (3.17)$$

From solar x-ray and γ -ray fluxes [42] :

$$\tau/m_\nu > 7 \times 10^9 \text{sec}/eV \quad (3.18)$$

All these bounds depend on assuming that $m_i \gg m_j$ in the mode $\nu_i \rightarrow \nu_j + \gamma$. But this decay mode doesn't induce the neutrino \rightarrow anti-neutrino transition. Thus the non-radiative decay mode, majoron decay is proposed in the next section.

3.2.2 Anti-neutrino production by neutrino decay

Now two flavor mixing between ν_e and $\nu_{\mu,\tau}$ with the mass eigenstates ν_1 and ν_2 are considered. Also it is considered that the heavier mass state ν_2 is unstable while the lighter neutrino mass state ν_1 has lifetime much larger than the sun-earth flight time and hence can be taken as stable. If neutrinos are Majorana particles, the decay mode of the form $g_{12}\nu_{L1}^T C^{-1}\nu_{L2}J$ is :

$$\nu_2 \rightarrow \bar{\nu}_1 + J \quad (3.19)$$

where J is a Majoron, produced as a result of spontaneous breaking of a global $U(1)_{L_e-L_\mu}$ symmetry [35]. In this model the $\bar{\nu}_1$ can be observed as a $\bar{\nu}_e$ with a probability $|U_{e1}|^2$.

The rest frame lifetime of ν_2 is given by [36] :

$$\tau_0 = \frac{16\pi}{g^2} \frac{m_2(1 + m_1/m_2)^{-2}}{\Delta m^2} \quad (3.20)$$

where g is the coupling constant which is obtained to $g^2 < 4.5 \times 10^{-5}$ from K decay modes [37]. m_i is the ν_i mass and $\Delta m^2 = m_2^2 - m_1^2$. The neutrino decay will deplete the flux of neutrinos of energy E_2 and mass m_2 over the flight time t ;

$$\exp\left(-\frac{t}{\tau_{lab}}\right) = \exp\left(-\frac{t}{E_2} \times \frac{m_2}{\tau_0}\right) \quad (3.21)$$

Thus the lifetime in the laboratory frame is expected to be $\tau_{lab} = E_2/m_2 \times \tau_0$.

The basic scheme for solar $\bar{\nu}_e$ production is that ν_e are resonantly converted to the heavier mass eigenstate, ν_2 , which can then decay rapidly, i.e.:

$$\nu_e \rightarrow \nu_2 \xrightarrow{\text{decay}} \bar{\nu}_1 \rightarrow \bar{\nu}_e \quad (3.22)$$

3.3 Search for the solar anti-neutrino in KamLAND

The detection of $\bar{\nu}_e$ from the sun suggests that the neutrino transition following the RSFP or neutrino decay is happened. The detection method is to use an interaction $\bar{\nu}_e + p \rightarrow e^+ + n$ with positron energy $E_{e^+} \sim E_{\bar{\nu}_e} - 1.3\text{MeV}$. The latest result of the Super-Kamiokande (SK) has provided an upper limit of the $\bar{\nu}_e$ flux from the sun :

$$\Phi_{\bar{\nu}_e} \leq 0.8\% \times \Phi_{SSM\nu_e} \quad (90\%C.L.) \quad (3.23)$$

for $8 \leq E \leq 20\text{MeV}$ [43].

KamLAND solar $\bar{\nu}_e$ measurement is quite excellent both in identification of the $\bar{\nu}_e$ and background rejection by using $\bar{\nu}_e + p \rightarrow e^+ + n$ reaction with the $e^+ - n$ delayed coincidence. So KamLAND solar $\bar{\nu}_e$ measurement is expected to provide a significantly improved search for the $\bar{\nu}_e$ even if the total volume of the detector is much smaller and total livetime is shorter than SK. The main background sources for the solar $\bar{\nu}_e$ search at KamLAND are $\bar{\nu}_e$ from the power reactors. Figure 3.2 shows the observed positron energy spectrum for the reactor neutrino and the expected solar anti-neutrino that is converted solar ^8B neutrino flux about 1 % of SSM. The energy resolution is fixed to $\Delta E/E = 7.5\% / \sqrt{E(\text{MeV})}$. The peak of energy distribution is about 3 MeV and the upper endpoint is about 8 MeV for reactor neutrino. The ^8B neutrino is mentioned at subsection 2.2.2 for detail. The peak is about 8.5 MeV and the upper endpoint is about 14 MeV.

It is necessary for the solar anti-neutrino analysis to avoid the reactor neutrino energy range and fully cover the ^8B neutrino energy range. Figure 3.3 shows the detector sensitivity for solar anti-neutrino detection. The left figure shows the threshold energy dependence of the ratio of the reactor + solar $\bar{\nu}_e$ event rate to the ^8B neutrinos for the SSM when the solar neutrino conversion probability are 1% and 0.1%. In the reactor neutrino dominant region, $0 \leq E_{th} \leq 6$ MeV, the reactor neutrinos contaminate the solar $\bar{\nu}_e$ and the conversion probability becomes worse. In $E \geq 7.5\text{MeV}$, there are no serious contamination of the reactor $\bar{\nu}_e$. Thus the lower energy threshold is determined to be 7.5 MeV.

Also the higher energy threshold is determined as follows. The right of Figure 3.3 shows the total number of event rate from the solar $\bar{\nu}_e$ in which the ^8B neutrino conversion probability is 1% of the SSM. The lower energy threshold is fixed to 7.5MeV. The increase of the event rate is saturated in $E_{th}=14\text{MeV}$. Thus the higher energy threshold is determined to 14 MeV.

The energy region of the prompt positron for the solar anti-neutrino analysis is determined to be $7.5 \leq E \leq 14\text{MeV}$.

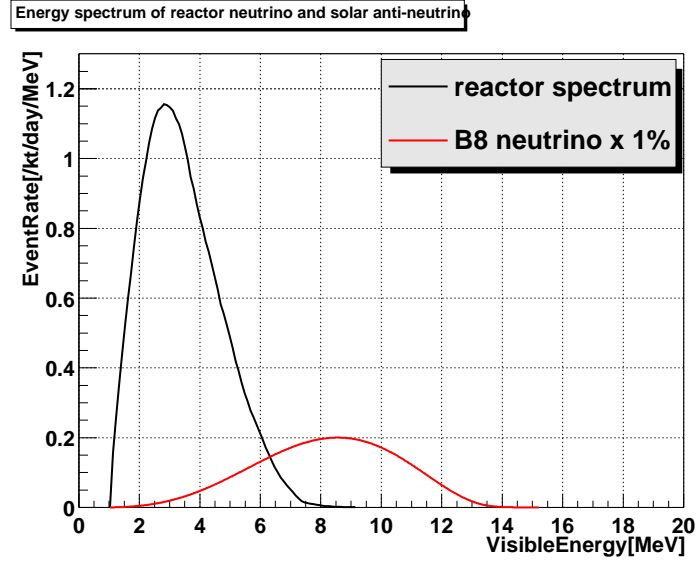


Figure 3.2: The energy spectrum of reactor anti-neutrino and anti-neutrino from solar ^8B neutrino [10]

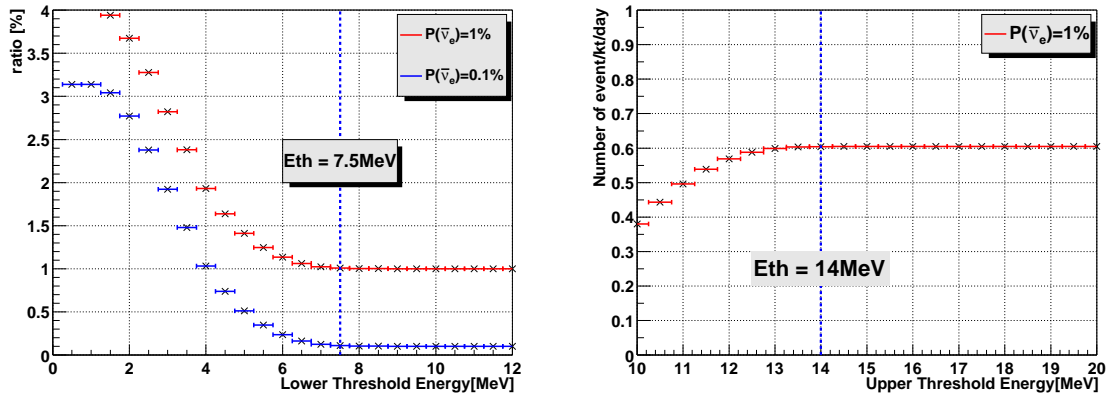


Figure 3.3: The detector sensitivity for the solar anti-neutrino. The left figure shows the lower energy dependence of the ratio of the reactor + solar $\bar{\nu}_e$ event rate to the ^8B neutrinos for the SSM. The solar neutrino conversion probability are supposed to 1% and 0.1%. The right figure shows the total number of event rate from solar $\bar{\nu}_e$ in which the ^8B neutrino conversion probability is 1% of the SSM. The lower energy threshold is fixed to 7.5 MeV.

Chapter 4

KamLAND Detector

4.1 The Site

The KamLAND detector locatess in a cavity which was used for the Kamiokande detector under the summit of Mt. Ikenoyama in Kamioka town, Gifu prefecture. The latitude and longitude are 36.42°N and 137.31°E respectively. Figure 4.1 gives the location of KamLAND in Japan. Figure 4.2 gives a view of the KamLAND experimental area which have a detector and some systems. The rock overburden is more than 1,000 m in any directions with an average rock density of 2.7 g/cm^3 . The minimum energy required for a cosmic ray muon to reach the detector is about 1.3 TeV. The cosmic ray muons are significantly reduced by 10^5 with respect to the earth surface and the rate of the muons penetrating the detector is around 0.34Hz.

4.2 The detecotor Design

4.2.1 Overview

The view of the KamLAND main detector is shown in Figure 4.3. The central part of the detector is a 1000ton liquid scintillator contained in a transparent plastic balloon with 13m in diameter. The balloon is surrounded by two layers of buffer oil of 2.5m thick. The liquid scintillator and the buffer oil are contained in a stainless steel spherical vessel of 18m in diameter. The liquid scintillator is viewed by 1879 photomultipliers which are mounted in the inner surface of the spherical vessel and dipped in the buffer oil. Between the two layers of the buffer oil, an acrylic plate is installed to stop the radon from photomultipliers.

The balloon is made of $135\text{ }\mu\text{m}$ thick transparent nylon/EVOH (Ethylene vinyl alcohol copolymer) composite film. The balloon film intercepts the radons in the buffer oil to enter the liquid scintillator. The transparency of the balloon film is more than 90% in the 370 nm to 500 nm wavelength.

It is supported by a network of kevlar ropes. The every tension of the 44 kevlar ropes is monitored by 44 load cells installed at the top of the detector.

The stainless steel sphere is mounted in the cylindrical rock cavity of 20m in diameter and 20m deep. The space between the sphere and the rock wall is filled with 3.2kton water to form a



Figure 4.1: The location of KamLAND in Japan

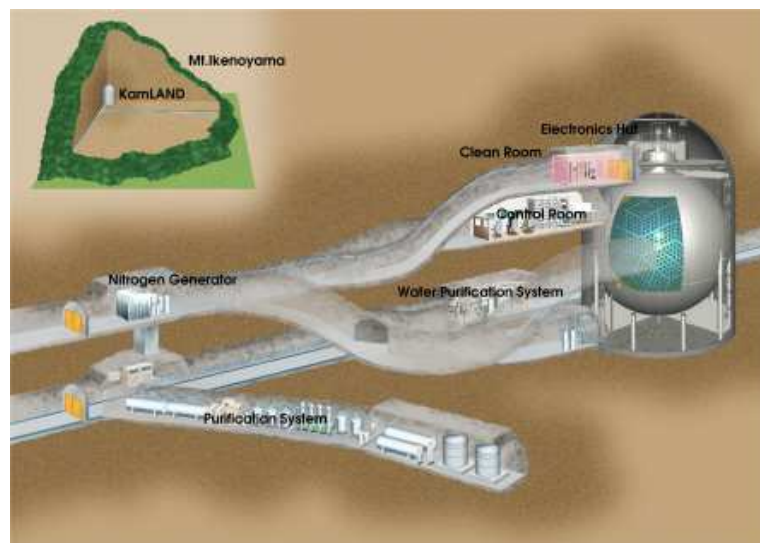


Figure 4.2: The whole view of KamLAND detector and the laboratory area

shield against the environmental radioactivity from the surrounding rocks and a water Cerenkov counter to discriminate cosmic ray muons penetrating the detector. 225 20" PMTs are used for the system and are distributed on the top, the bottom and the side of the walls of the water vessel. All the surface of the rock wall and the outer surface of the spherical tank is covered with a white reflective sheet (TYVEK). The Cerenkov light emitted by the incoming muons in the water will be detected after they bounce back to the PMTs. The 20" PMTs are the reused ones from the former Kamiokande experiment.

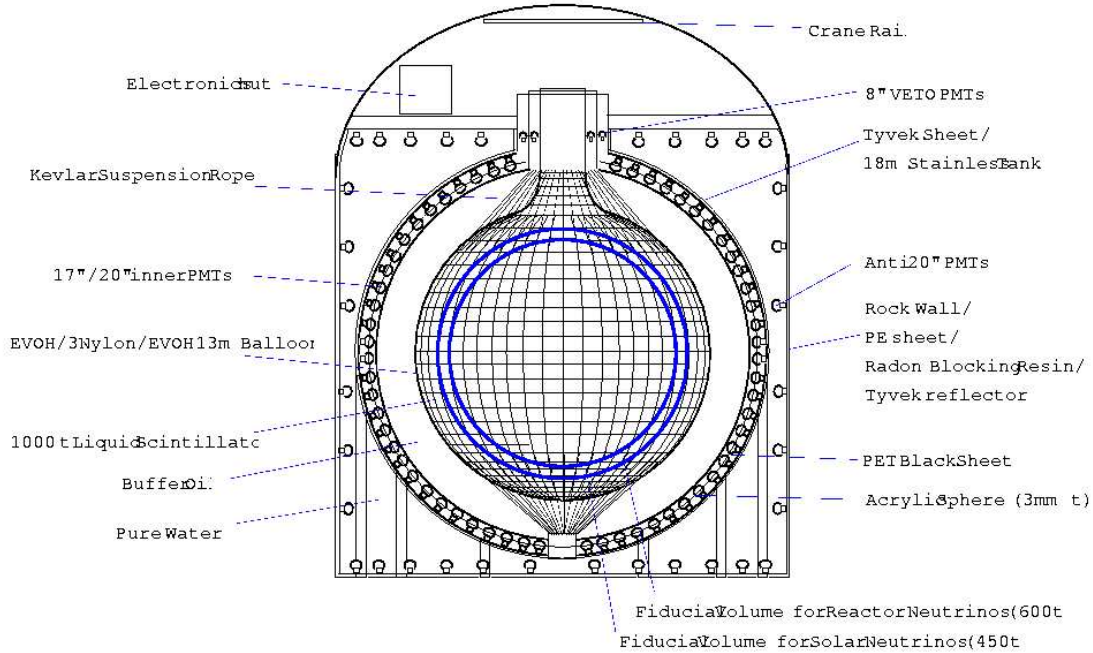


Figure 4.3: The picture of KamLAND main detector. The rock wall is covered by a polyurethane resin (called 'mine guard') to stop the Rn diffusion from the rock.

4.2.2 The Liquid Scintillator and buffer oil

The liquid scintillator filled in the balloon is the main component of the KamLAND detector. The liquid scintillator (LS) is a mixture of 80% dodecane, 20% pseudocumene (1,2,4-

trimethylbenzene) and 1.52 g/liter of PPO (2,5-Diphenyloxazole) as a fluor.

The buffer oil (BO) is filled between the ballon and the stainless steel sphere. It is a mixture of 52% dodecane and 48% isoparaffin oil and the density of the BO is 0.04% less than the LS density of 0.7775 g/cm^3 .

4.2.3 The Scintillator Purification System

LS and BO are required to have a sufficient level of purity. Main contaminants are radioactive isotopes like uranium, thorium and potassium etc. that cause the backgrounds to the neutrino signal. The other contaminants are dusts, oxygen and water components in the LS and BO that cause the deterioration of the optical characteristics of especially the light attenuation and the light emission of the LS. So purification system is developed for removing these contaminants and the two systems are constructed for the LS and BO. The main parts of the system are :

- Water extraction system

- The radioactive isotopes are removed from the LS and the BO by mixing them with ultra-pure water. Figure 4.4 shows the water extraction method. The LS or the BO enter from the bottom of the extraction tower. The ultra-pure water is supplied by a water purification system and flowing through the tower. When the oil is kept contact with water, radioactive metal elements in the oil are electrically attracted by polarized molecules of the water while the molecules of the oil don't have such polarization.

The characteristics of the LS is confirmed to be unchanged if the water is dissolved and saturated in the LS after the water extraction. The left picture of Figure 4.5 shows the LS light outputs by varying the water concentration in the LS. The light output is stable from 20 ppm to 70 ppm which is the saturation of the water in the LS. The light transparency of the LS before and after the water extraction is shown in the right of the Figure 4.5. There is no serious difference of the transparency before and after the water extraction.

- Nitrogen purge system

- Because radons are easy to dissolve into the oil, the LS and the BO can easily be contaminated by the radons in the mine air, which leads to backgrounds. Although our system is made radon-tightness, a small amount of radons may sneak into the system and they should be removed. Also the water extraction process makes the LS and BO almost saturated with water which should be removed in the view point of the long-term stability of the LS and BO. In addition the oxygen is dissolved in the oil and has to be removed. These radon, water and oxygen is removed by nitrogen purge process.

Figure 4.6 shows the nitrogen purge system. The nitrogen flow rate is $\sim 40 \text{ Nm}^3/\text{h}$ with the LS and BO flow at $\sim 2 \text{ m}^3/\text{h}$. The nitrogen is circulated between the nitrogen buffer tank and the purge tower. The water component purged out with the nitrogen is taken out by a compressor and a cooling unit. The nitrogen is periodically replaced with a fresh one supplied by a nitrogen gas generator system.

Water Extraction Devices

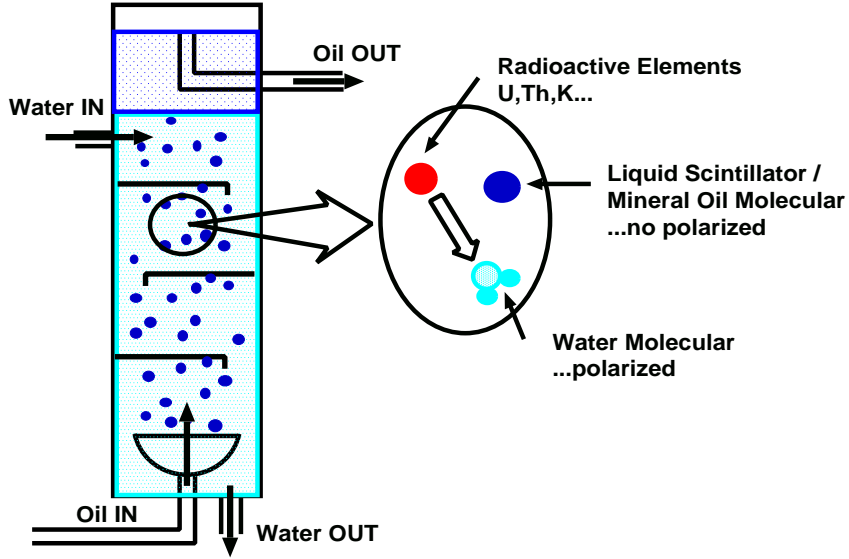


Figure 4.4: The view of the water extraction tower and the mechanism of the transfer of the radioactive elements from the oil (LS or BO) to the ultra-pure water.

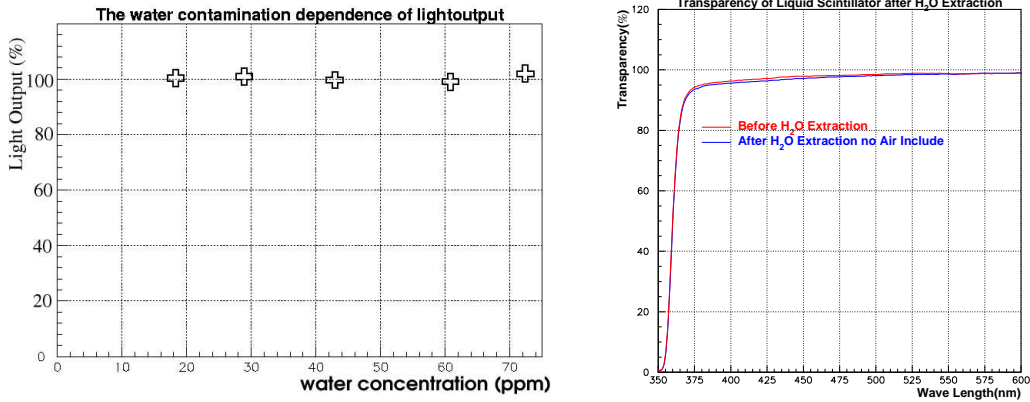


Figure 4.5: The left picture shows a small bottle test of the LS light output at various contaminations of the water in the LS. The ^{60}Co compton edge is used to determine the light output. The light output is normalized to 100% at 18ppm water contamination. The right picture is the transparencies measured as a function of the wave length before and after the water extraction.

The water in the oil is removed to 30 ppm by the one pass through the nitrogen purge tower. A laboratory test of removing the oxygen in the oil is shown in Figure 4.7. The light output of the LS depends on the oxygen concentration. If the LS is saturated with oxygen, the light output decreases to 70% of the oxygen free case. Thus the oxygen in the LS is reduced to 25% of the oxygen level fully exposed to the air to keep the light output more than 95%. The nitrogen purge system was designed to satisfy the required performance based on the test.

The Rn rejection by nitrogen purge have been confirmed by the small beaker test in Figure 4.8. The Rn in the LS is reduced to $(0.16 \pm 0.03)\mu\text{Bq}/\text{m}^3$ in the actual KamLAND experiment.

Nitrogen Purge devices

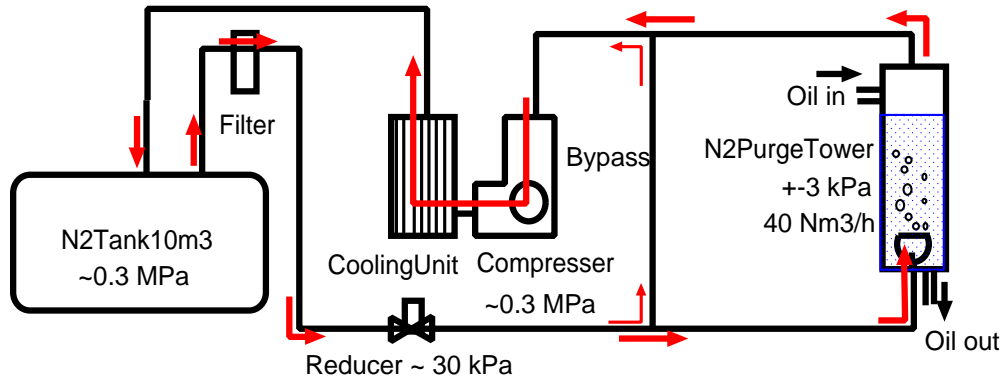


Figure 4.6: The circulation of the nitrogen purge system. The nitrogen pressure in the tank is about 0.3 MPa and the whole circulation system have a slightly positive pressure to make the Rn sneaking into the system as small as possible from the external air.

It is worried about small amount of radons to be emanated from the inner surface of the stainless steel tanks and circulation pipes of the purification system which are found to contain $\sim 1\text{ppb}$ level of uranium. Thus a material with small permeability for radon is used to line the inner surface of the LS buffer tanks, the nitrogen buffer tank and the LS circulation pipes as possible. The lining material is the nylon. The Rn diffusion from the nylon surface is $\sim 1 \times 10^{-6}\text{Bq}/\text{m}^2$ while the stainless steel is $\sim 1 \times 10^{-3}\text{Bq}/\text{m}^2$. The estimated Rn emanation is reduced to 1/10 by these partial coating for all inner surface. Figure 4.9 shows the works for the nylon/EVOH film coating in the tanks and preparing the nylon pipes to be installed in the circulation pipes. These works were done after the careful cleaning of the whole system to remove the dusts and rusts stucked on the inner surface.

After the constructions, the acid cleaning had been done for all the circulation pipes in the system and then the system had been flown by the buffer oil. Figure 4.10 shows the LS and BO circulation system including the detector. The direction of the liquid flow can be changed from 'bottom in - top out' to 'top in - bottom out'. Four sets of filter units ($1\mu\text{m}$, $0.1\mu\text{m} \times 2$ and $0.05\mu\text{m}$) are installed in the each system of the LS and BO to remove particles remaining in the

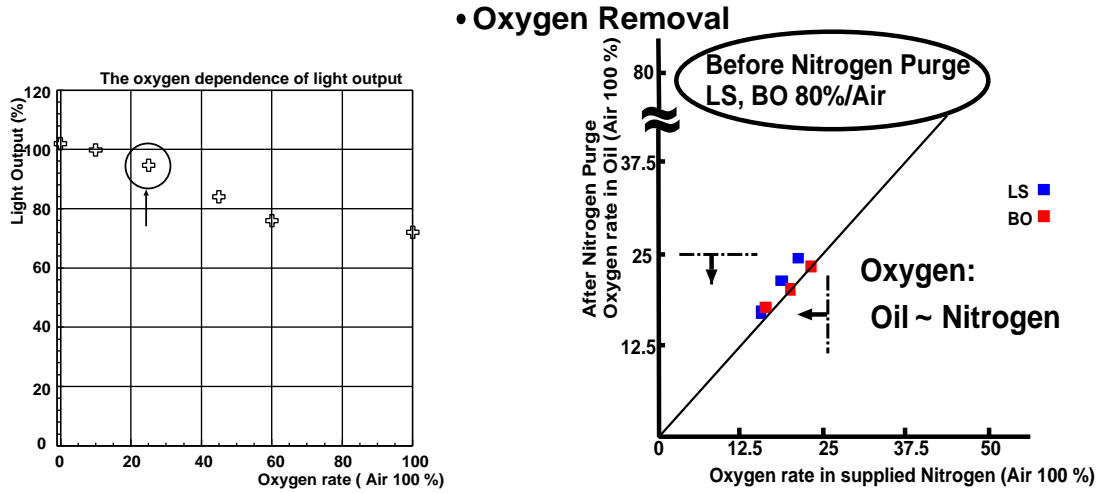


Figure 4.7: The left figure is the dependence of the LS's light output on the oxygen contamination. 'Air 100%' in the oil means the oxygen contamination in the LS in the exequilibrium with the normal air. The right figure is the nitrogen purge performance which depends on the oxygen contamination in the nitrogen. If the oxygen contamination in the nitrogen gas exceeds 25% of the one in the normal are, the nitrogen is exchanged.

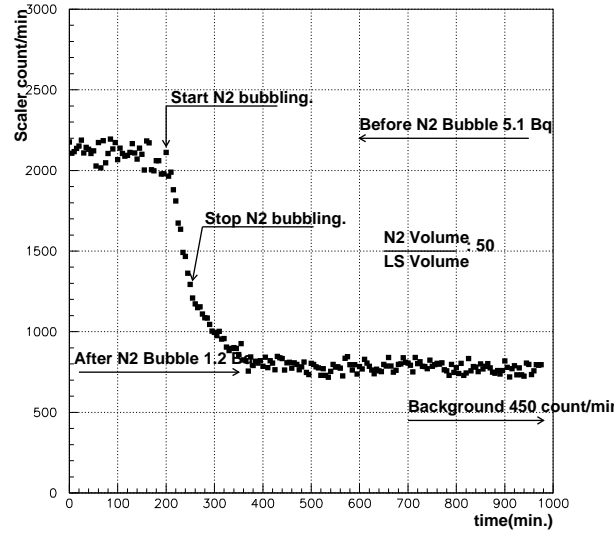


Figure 4.8: The result of small beaker experiment to check the Rn rejection. The ^{222}Rn gas is dissolved in the LS and the α particle from ^{214}Po are counted by a 2-inch PMT. The amount of nitrogen gas is ~ 50 times the LS volume. During the nitrogen purge, Rn counting are reduced rapidly.



Figure 4.9: The left figure shows the work of the nylon/EVOH film coating with bond in the stainless steel tank. The right figure shows the preparation of the nylon pipes to be installed in the circulation pipes.

system and in the oil.

The observed radioactive impurities in the LS in the balloon are found to be :

$$\begin{aligned} {}^{238}\text{U} &\sim (3.5 \pm 0.5) \times 10^{-18} \text{ g/g} \\ {}^{232}\text{Th} &\sim (5.2 \pm 0.8) \times 10^{-18} \text{ g/g} \\ {}^{40}\text{K} &< 2.7 \times 10^{-16} \text{ g/g} \end{aligned}$$

The ${}^{238}\text{U}$ and ${}^{232}\text{Th}$ concentrations are obtained from studies of Bi-Po sequential decays, and ${}^{40}\text{K}$ concentration limit is induced from the observed energy spectrum of the single events.

4.2.4 The Photomultiplier

The photons from the LS are detected by the 1325 17" and 554 20" photomultiplier tubes (PMT) distributed in the inner surface of the stainless steel tank. Figure 4.11 shows a structure of the 17" diameter PMT which is newly developed for the KamLAND experiment and made by HAMAMATSU Photonics Company.

The 17" PMT has a line-focus type dinode and used with a light shield to mask the outer fringe of the photo-cathode plane to obtain better timing resolution and larger P/V ratio for 1 photo-electron signals than 20" PMT which has a venetian blind type dinode and being used in Super-Kamiokande experiment. Figure 4.12 shows the performance difference between 17" and 20" PMT. The transit time spread (TTS) is significantly improved from $\sim 5.5\text{nsec}$ (FWHM) to $\sim 3\text{nsec}$ (FWHM). And the peak-to-valley ratio is increased from ~ 1.5 to ~ 3 .

Figure 4.13 shows the quantum efficiency for 17" PMT as a function of the wavelength. The mean value for 400ns is about 20%. The Gain G of a PMT is given by:

$$G = aV^b \quad (4.1)$$

where a and b are characteristic constants, and V is the high voltage applied. The gain is measured and fixed by adjusting a high voltage value at $\sim 0.5 \times 10^7$ for KamLAND experiment.

Purification system-detector flow line

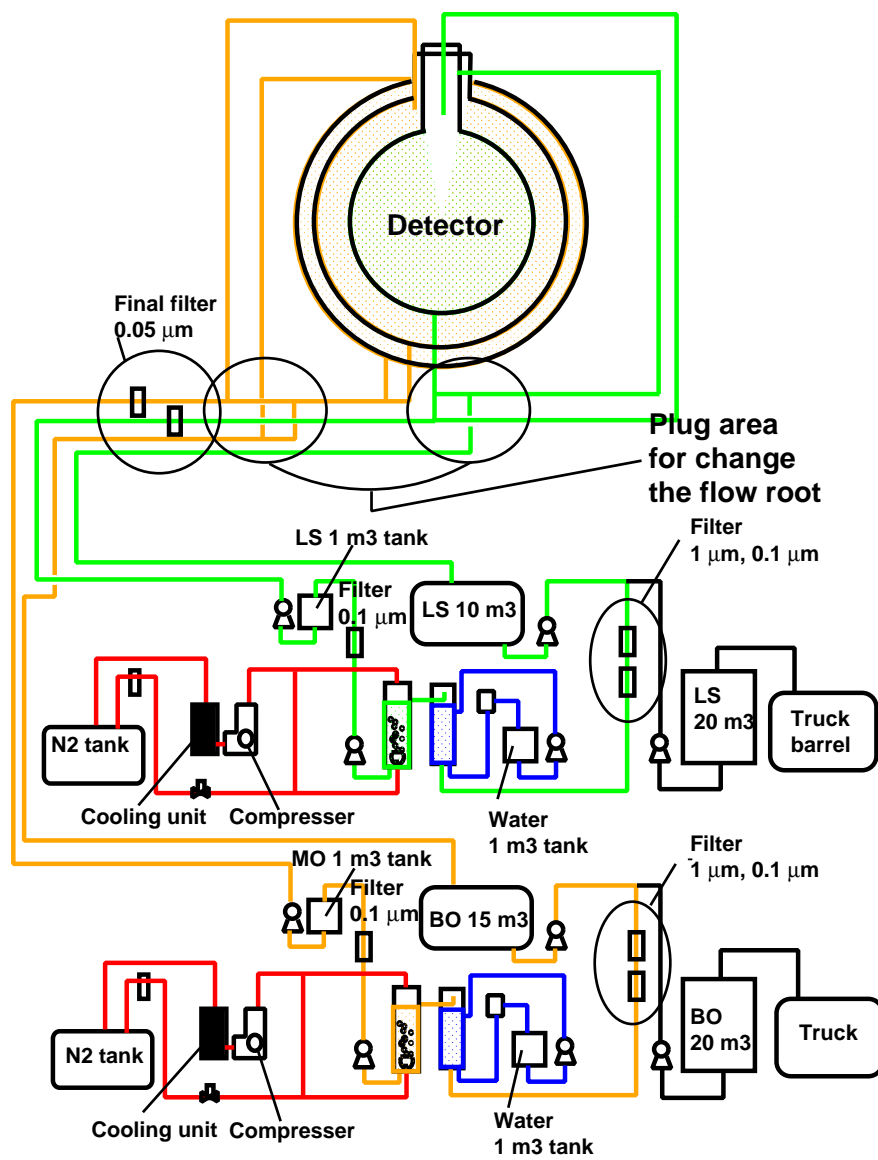


Figure 4.10: The purification and circulation system

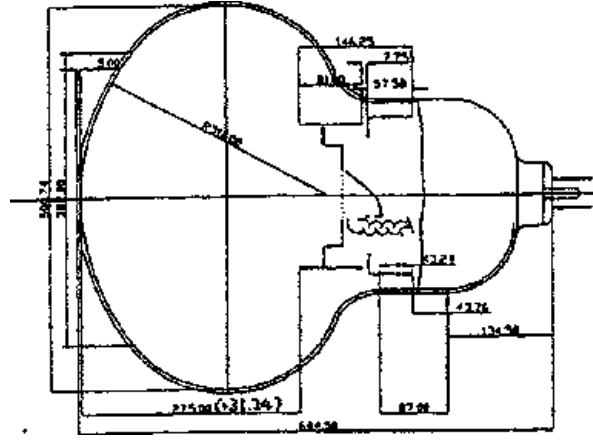


Figure 4.11: The view of 17" PMT

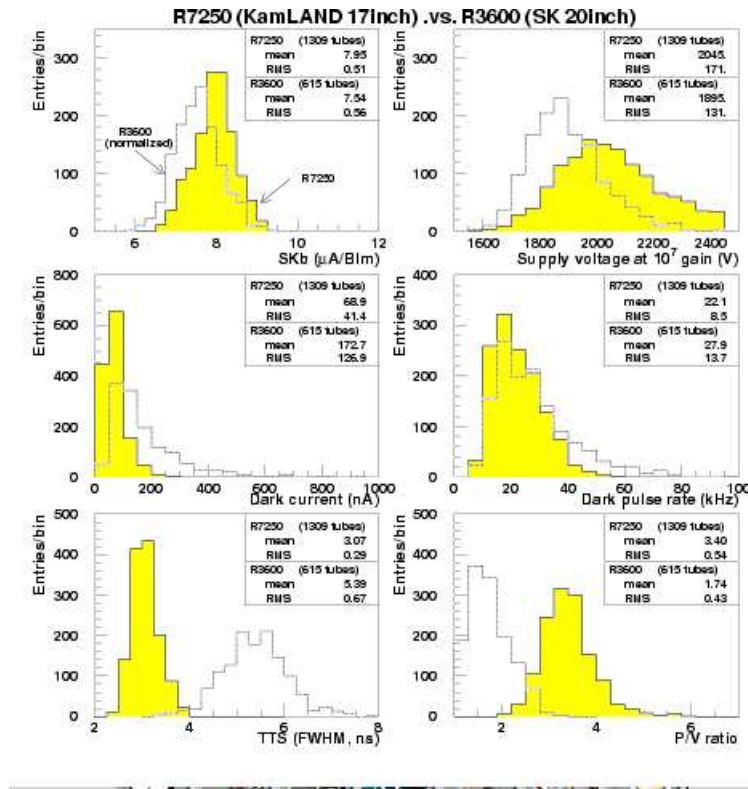


Figure 4.12: The comparisons of the performance between 17" and 20" PMT. The filled histogram is 17" PMT and the blank one is 20" PMT.

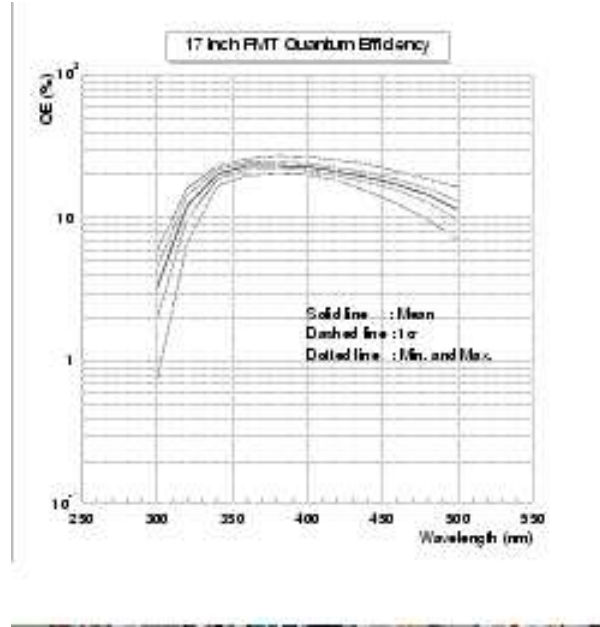


Figure 4.13: Quantum efficiency of 17" PMT

4.2.5 The Front-end Electronics (FEE)

The KamLAND electronics are based on a chip called the ATWD (Analog Transient Waveform Digitizer). Figure 4.14 shows a picture of the original ATWD board. The ATWD is a custom ASIC (application-specific integrated circuit) developed for KamLAND experiment. The ATWD allows the fast sampling of the PMT pulse as a function of time with 128 samples in 1.5ns steps. The ATWD output is a "waveform" such as shown in Figure 4.15. The electronics allow timing resolution at the nanosecond scale, which is critical for reconstructing the position of events in the detector. The noise level is very low and we can set the discriminator threshold at $1/3$ of the 1p.e. peak. As a result, the efficiency to detect single photoelectrons is 95% or better. Figure 4.16 shows the block diagram of the ATWD board. The electronics have a large dynamic range, covering the PMT pulse amplitudes from single photoelectrons up to thousands. This allows us to detect high-energy muon events with deposit energies larger than 2GeV as well as low-energy neutrino events with sub-MeV energy region. Finally, the electronics have two ATWD's for each PMT channel. This minimizes the "dead" time of each channel, since the second ATWD is ready to take data if the first one is busy.

4.2.6 Trigger

The primary ID (inner detector) trigger threshold is set at 200PMT hits which corresponds to about 0.7MeV. This threshold is lowered to 120PMT hits for 1msec window after the primary trigger to observe the lower energy delayed events. Thus the primary ID trigger is called the prompt (global) trigger and the later is called the delayed trigger.



Figure 4.14: The FEE board with ATWD circuits

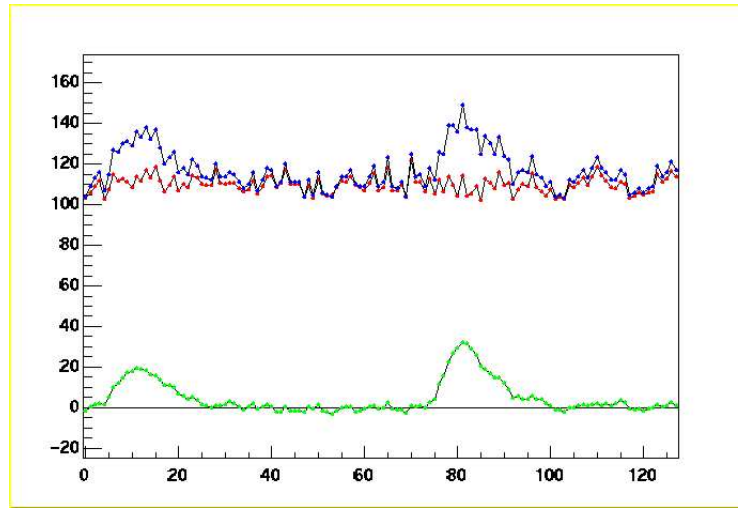


Figure 4.15: A sample KamLAND waveform showing two PMT pulses. The horizontal axis is samples taken 1.5 ns apart. The vertical axis is ADC counts; each count is approximately 120 microvolts at the FEE input. The blue points are the raw data. The red points are the pedestal, the ADC values that would be read out with no input signal. The green points are the pedestal-subtracted waveform, the measurement of voltage vs. time. The peaks in the waveform are the PMT pulses.

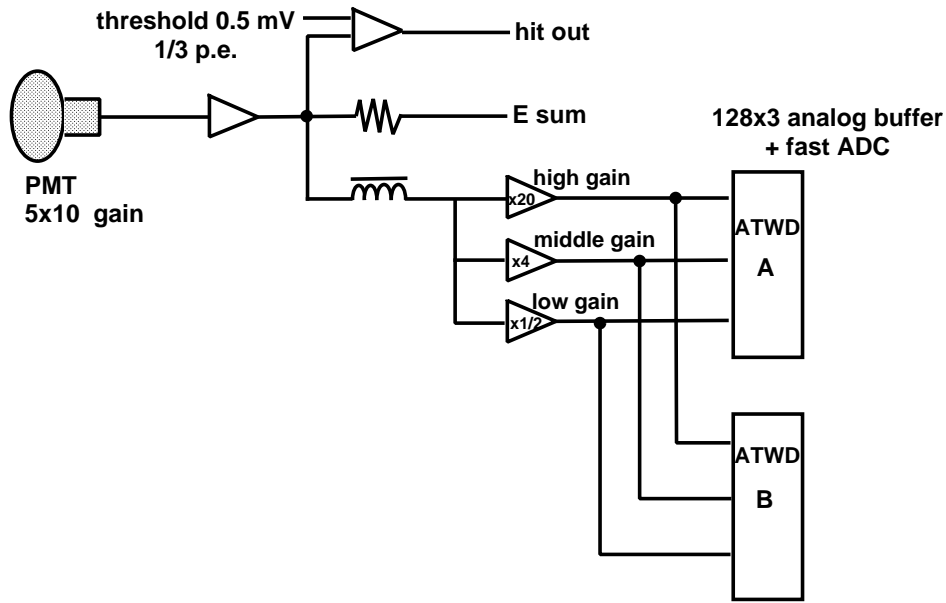


Figure 4.16: The block diagram of the ATWD board

The OD is separated into four regions, the top, the upper and lower barrels and the bottom. The trigger thresholds of these regions are 6, 5, 6, 7 PMT hits, respectively. The history trigger is issued every 25nsec while PMT hits exceed the lower threshold up to a maximum of 200nsec. The maximum value of Nsum in this history information for an event is called 'NsumMax'.

4.2.7 Data acquisition system

The main task of the data acquisition system (DAQ) is to read data from electronics devices to save the data into files on storage devices. Also the system controls the electronics devices and monitors the acquired data in realtime. Sometimes some online data analysis are made for the realtime data monitoring, and/or to reduce loads of offline analysis, and/or to reduce size of data recorded.

In the KamLAND experiment, a total of 15 VME crates are used; 10 for the 17" PMT's electronics (FBE), 4 for 20" PMTs (ID and OD) electronics and 1 for the trigger electronics. To keep the front-end part simple, and to read data as fast as possible, one PC is exclusively connected to each VME crate.

Figure 4.17 shows the structure of the KamLAND DAQ system. At present, 15 PCs (called `hoots01` - `hoots15`) are used for the data readout and for some online analysis, 1 PC (`hoots16` or `hoots17`) is used for data stream manipulation, realtime data monitoring, system control, and so on. Collected data is written to a disk connected to another PC (`zoe1`) via NFS (Network File System) as KDF file (KamLAND Data Format).

The stocked KDF data on `zoe1` is formatted to SF file (Serial Format) made by event builder.

SF file have 6 banks :

- Header Bank - information mainly from the trigger modules.
- Histry Bank - information for frequent using parameters like: nsum, trigger type ..
- HitHeader Bank - information for hit cable of inner (ID) .
- ATWD Bank - information for waveform gain channel, ATWD channel, and TimeOffset for ID.
- AntiHitHeader Bank - same with HitHeader Bank for outer (OD).
- AntiHitATWD Bank - same with HitATWD Bank for outer (OD).

The data capacity is reduced from > 160 GB/day for KDF to 120 GB/day for SF. SF files are copied to tapes and sent to the RC ν S in Tohoku university in Sendai.

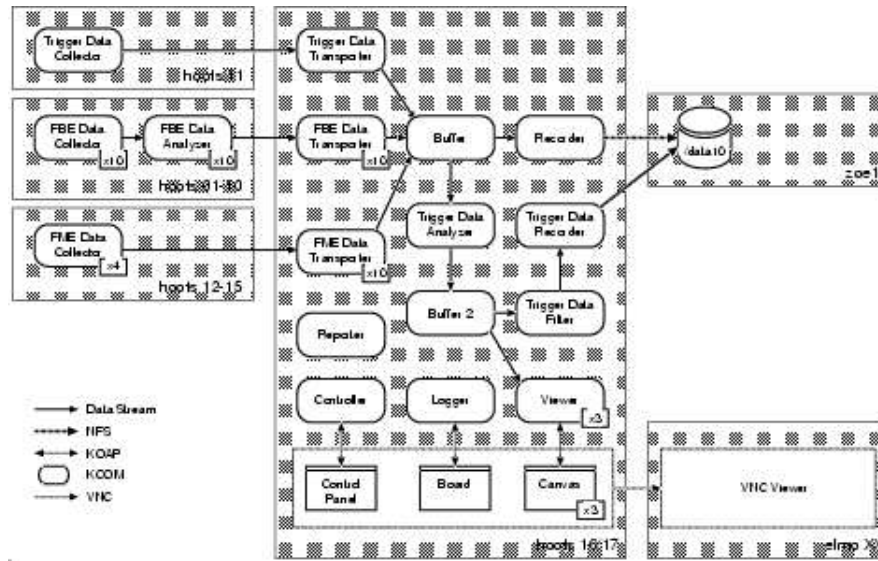


Figure 4.17: KamLAND DAQ system structure

4.3 Detection principle for electron anti-neutrino

The inverse β -decay reaction in the liquid scintillator in the KamLAND detector,

$$\bar{\nu}_e + p \rightarrow e^+ + n \quad (4.2)$$

is utilized to detect $\bar{\nu}_e$'s with energies above the threshold energy of 1.8MeV. The neutron emitted by the reaction is thermalized in the liquid scintillator by elastic scatterings and about $210\mu s$ later, is captured by a proton in a hydrogen. Then a 2.2MeV γ -ray is emitted to produce

a deuteron. The prompt energy deposit of e^+ and two annihilation γ 's, followed by the 2.2MeV γ make a delayed coincidence event which drastically reduces background events.

In the limit where the kinetic energy of the recoil neutron is neglected compared to the nucleon mass M , the positron energy is expressed as the zero-th order of the expansion in $1/M$ [44] :

$$E_e^0 = E_\nu - \Delta \quad (4.3)$$

where $\Delta = M_n - M_p$. In the each order in $1/M$, the positron momentum $p_e = \sqrt{E_e^2 - m_e^2}$ and the velocity $v_e = p_e/E_e$ are defined. The zeroth order differential cross section is ;

$$\left(\frac{d\sigma}{d\cos\theta} \right)^{(0)} = \frac{\sigma_0}{2} [(f^2 + 3g^2) + (f^2 - g^2)\nu_e^{(0)} \cos\theta] E_e^{(0)} p_e^{(0)} \quad (4.4)$$

where $f = 1.0$ is the vector coupling constant and $g = 1.267$ is the axial-vector coupling constant. The global constant σ_0 , including the energy independent inner radiative corrections, is

$$\sigma_0 = \frac{G_F^2 \cos^2\theta_C}{\pi} (1 + \Delta_{inner}^R) \quad (4.5)$$

where $\Delta_{inner}^R \sim 0.024$ and θ_C is the Cabibbo. This gives the standard result for the total cross section,

$$\begin{aligned} \sigma_{tot}^{(0)} &= \sigma_0 (f^2 + 3g^2) E_e^{(0)} p_e^{(0)} \\ &= 0.0952 \left(\frac{E_e^{(0)} p_e^{(0)}}{1 \text{ MeV}^2} \right) \times 10^{-42} \text{ cm}^2 \end{aligned} \quad (4.6)$$

The energy-dependent inner radiative corrections affect the neutron beta decay rate in the same way, and hence the total cross section can be written :

$$\sigma_{tot}^{(0)} = \frac{2\pi^2/m_e^5}{f_{p.s.}^R \tau_n} E_e^{(0)} p_e^{(0)} \quad (4.7)$$

where τ_n is the measured neutron lifetime and $f_{p.s.}^R = 1.7152$ is the phase space factor, including Coulomb weak magnetism, recoil and outer radiative corrections, but not inner radiative correction.

At first order in $1/M$, the positron energy depends on the scattering angle :

$$E_e^1 = E_e^{(0)} \left[1 - \frac{E_\nu}{M} (1 - \nu_e^{(0)} \cos\theta) \right] - \frac{y^2}{M} \quad (4.8)$$

where $y^2 = (\Delta^2 - m_e^2)/2$. the differential cross section is :

$$\begin{aligned} \left(\frac{d\sigma}{d\cos\theta} \right)^{(1)} &= \frac{\sigma_0}{2} [(f^2 + 3g^2) + (f^2 - g^2)\nu_e^{(1)} \cos\theta] E_e^{(1)} p_e^{(1)} \\ &\quad - \frac{\sigma_0}{2} \left[\frac{\Gamma}{M} \right] E_e^{(0)} p_e^{(0)} \end{aligned} \quad (4.9)$$

where :

$$\begin{aligned}
 \Gamma = & 2(f + f_2)g \left[(2E_e^{(0)} + \Delta)(1 - \nu_e^{(0)} \cos \theta) - \frac{m_e^2}{E_e^{(0)}} \right] \\
 & + (f^2 + g^2) \left[\Delta(1 + \nu_e^{(0)} \cos \theta) + \frac{m_e^2}{E_e^{(0)}} \right] \\
 & + (f^2 + 3g^2) \left[(E_e^{(0)} + \Delta)(1 - \frac{1}{\nu_e^{(0)}} \cos \theta) - \Delta \right] \\
 & + (f^2 - g^2) \left[(E_e^{(0)} + \Delta)(1 - \frac{1}{\nu_e^{(0)}} \cos \theta) - \Delta \right] \nu_e^{(0)} \cos \theta
 \end{aligned} \tag{4.10}$$

θ is angle between the $\bar{\nu}_e$ and positron direction in the laboratory frame. The energy threshold of the $\bar{\nu}_e$ in this reaction is calculated in the laboratory frame :

$$E_\nu^{thr.} = \frac{(M_n + m_e)^2 - M_p^2}{2M_p} = 1.806 \text{ MeV} \tag{4.11}$$

Figure 4.18 shows the total cross section to 20 MeV.

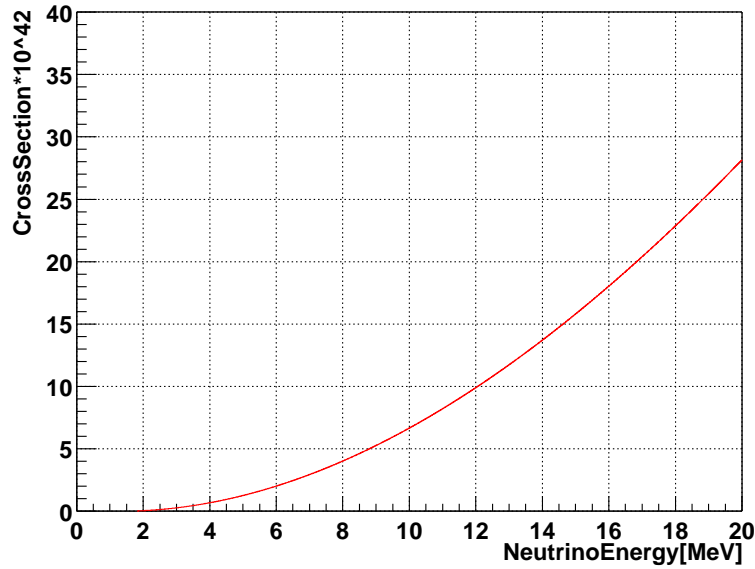


Figure 4.18: Total cross section for $\bar{\nu}_e + p \rightarrow e^+ + n$ energy dependence

Chapter 5

Event Reconstruction

In this chapter, the analysis procedure to obtain the event vertex position, event energy and the muon tracks which are reconstructed by timing, charge information of each PMT are shown. Also the correction in the reconstruction is discussed.

5.1 Vertex Reconstruction

The origin of the coordinate axis is taken at the center of the spherical tank of the KamLAND detector with a z-axis as the vertical line pointing upward direction and the x and y-axis taken in the horizontal plane to form a right-handed system. The ranges of x , y and z axis in the inner detector (ID) which is the main part of the detector inside the spherical vessel, are -651.4cm to +651.4cm with a constraint of $\sqrt{x^2 + y^2 + z^2} \leq 651.4\text{cm}$.

The reconstruction of the vertex is based upon the timing information and position of the hit PMTs. For determining the vertex position, the relative timing of the hit PMTs is important. Let us denote the recorded time of the i -th hit PMT as $T_i(r_i)$ and the PMT position as $r_i = (x_i, y_i, z_i)$. When an event happened at the position r , the time of the flight of the scintillation photon corresponds directly to the distance between the vertex and the PMT, and $T'_i(r, r_i)$ which is the time of the emission of the scintillation photons at the vertex measured by the i -th PMT is expressed as :

$$T'_i(r, r_i) = T_i(r_i) - \frac{R(r, r_i)}{c} - T_{offset}(r_i) \quad (5.1)$$

where $R(r, r_i)$ is a distance between r and r_i , and c is the light velocity in the scintillator. $T_{offset}(r_i)$ is the timing offset of the PMT. The effective speed of lights is given as the function of the distance from the center. Figure 5.1 shows the speed of light measured in the source calibration run. The points are source position as z-axis coordinate and the line is the speed of light function.

Figure 5.2 shows the timing offset (T_{offset}) distribution of one cable. T_{offset} have difference on each cables and trigger types. Figure 5.3 shows the all cable's T_{offset} . T_{offset} is changed run by run.

After the T_{offset} subtraction, the vertex position x,y,z are determinated. When an event happens, the time structure of the waveform of the light output is almostly alike. This waveform is

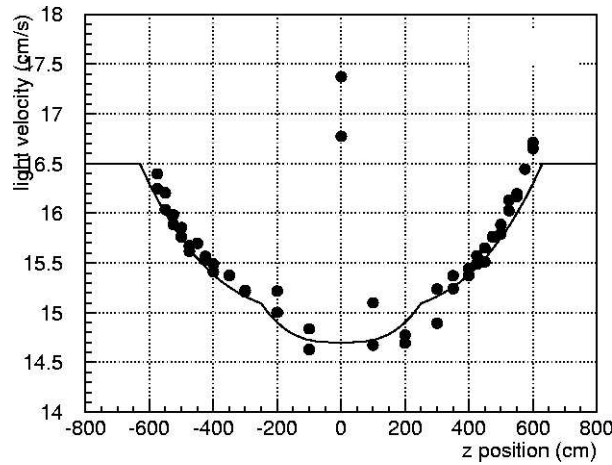


Figure 5.1: The effective speed of light as a function of z position

characteristic of the scintillator component and is estimated from calibration results. Thus the vertex is fitted little by little until the timing spectrum becomes the typical waveform. Figure 5.4 shows the $T'_i(r, r_i)$ distribution of the hit PMTs in one event in the vertex reconstruction procedure. The vertex position is assumed first as the center of the detector, $(0, 0, 0)$ and searched by iteration to obtain the relevant position ($z = -450$ cm for source position).

5.2 Energy Reconstruction

The relevant energy region are $0.9 \leq E \leq 8 \text{ MeV}$ for reactor anti-neutrino detection and $7.5 \leq E \leq 14 \text{ MeV}$ for solar anti-neutrino detection. The light output of the KamLAND liquid scintillation are ~ 330 p.e./MeV. The energies expressed by the hit PMT numbers have better energy resolution than the one expressed by the charge distribution because the charge distribution of 1 p.e. signals is so broad. But there are much multi hit PMTs depending on the energy and the vertex position. Sometimes it is difficult to distinguish the waveform (photon) number exactly. So the KamLAND energy estimator is based on the charge measured by PMT, not by the number of hit PMTs.

The energy reconstruction process are described in the following subsections.

5.2.1 Gain correction

PMT gains are adjusted at around 0.5×10^7 by the LED calibration. But to get the more precise energy information, the relative gain correction of each PMTs and the correction of the gain drift are needed. The reason of the gain variation is for the change of HV condition, the change of the detector temperature, other hardware updates on modifications.

The gain correction is done by 1p.e. signals in low energy events in a normal run. Figure 5.5 shows the criteria of the events selected for the gain correction. Low energy events with $120 < \text{Nsum} < 160$ are analyzed to obtain the vertex (X, Y, Z) . PMTs are selected by $|(X, Y, Z) -$

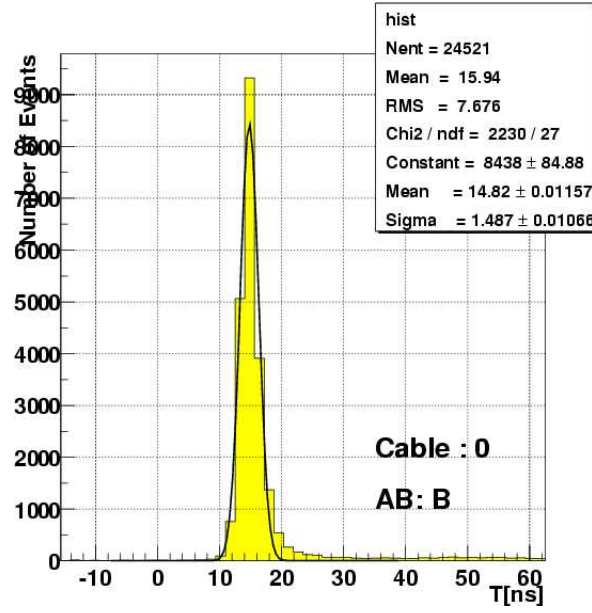
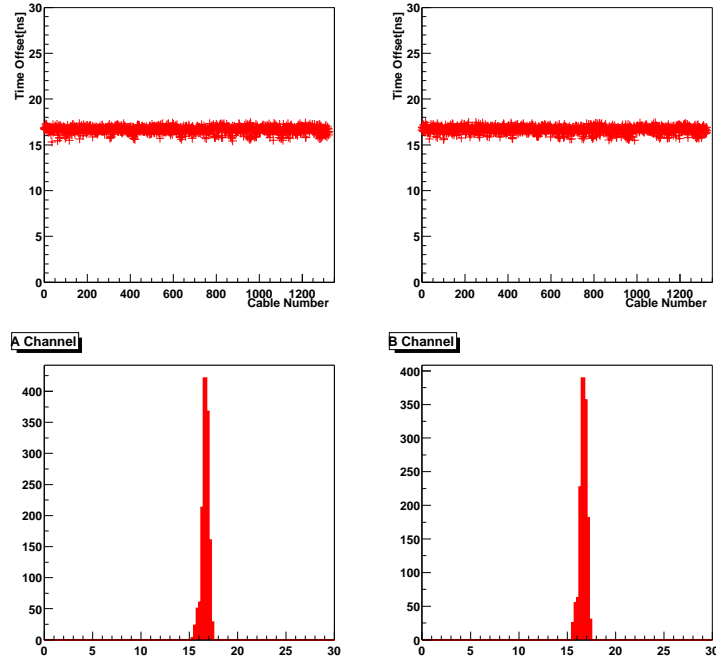


Figure 5.2: The time offset of cable 0-B

Figure 5.3: The all cable's T_{offset} for one run

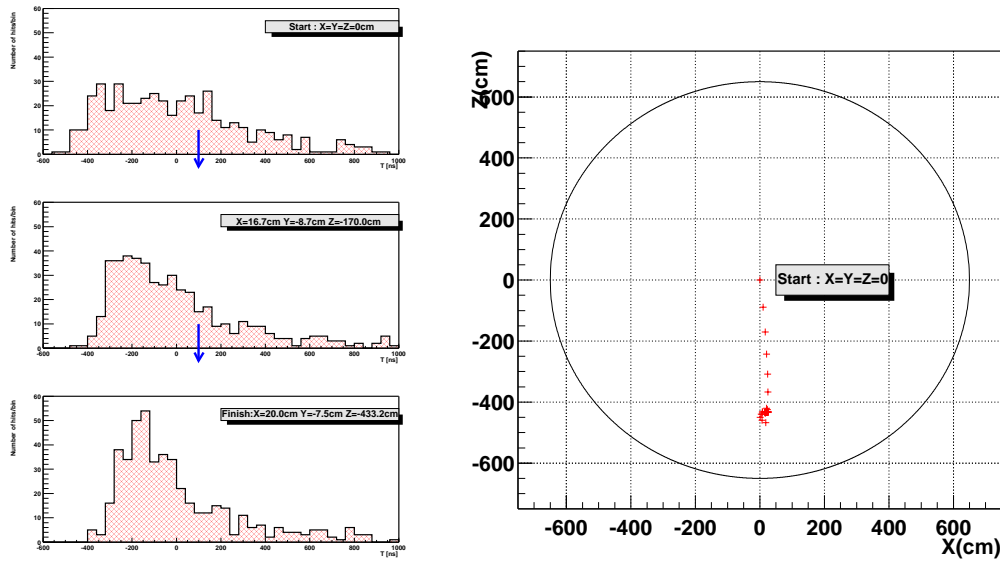


Figure 5.4: The $T'_i(r, r_i)$ distribution in the vertex reconstruction process. The events are from Zn source calibration data with the source positioned at $z=-450$ cm.

$(X_{PMT}, Y_{PMT}, Z_{PMT})| > 600$ cm to obtain 1 p.e. signals. Figure 5.6 shows the typical charge distribution for one PMT. The events are collected in about 8000/1PMT/day for each A/B channel of the ATWD. It can be said that multi-photon signals are excluded. The charge distribution is fitted by an asymmetric gauss function. The peak channel of the gaussian peak is taken as the 1p.e. peak position.

Figure 5.7 shows the 1 p.e. mean charge distribution for all channels. The difference of 1 p.e. is about 0.15σ for each channels. Figure 5.8 shows the time variation of the average 1 p.e. for all PMTs. From March to November in 2002, gains increased by about 5%. The gain table is updated for each PMTs run by run. The corrected ADC value is;

$$Q_{ADC_{corrected}} = Q_{ADC}/Q_{table} \times N_{ADC} \quad (5.2)$$

where $N_{ADC}=210$ is standard ADC counts of ATWD estimated by LED calibration. For run by run correction, about 8 hours runtime are required to make 1 p.e. peak statistically. The gain value in a short run are given by the ones in the neighboring long run's gain table.

5.2.2 Bad channel cut

The bad channels are defined as follows and they are not regarded as having a good quality to be included in the analysis. Therefore, they are masked with bad channel table which is made by normal run. There are 3(high, middle, low gain) \times 2(A/B channel) entries per 1 PMT. Bad channel selection criteria are:

- Hit rate in low energy events is less than 1% of the total low energy events (for high gain).

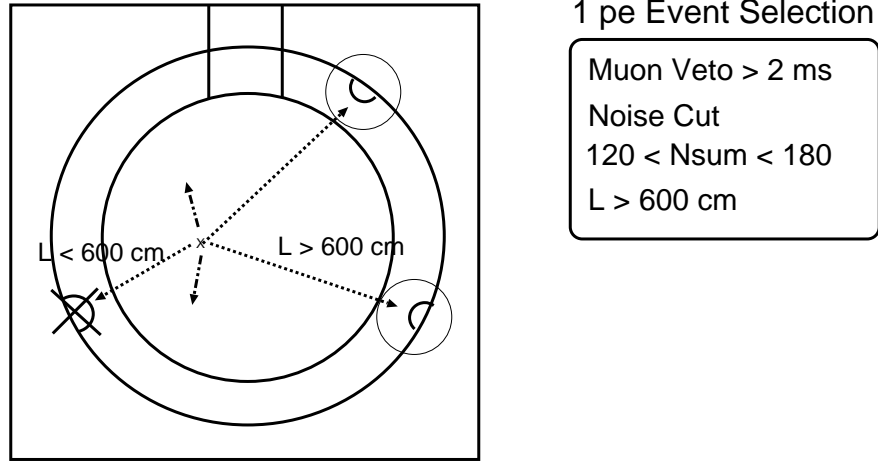


Figure 5.5: The criteria of event selection for gain correction.

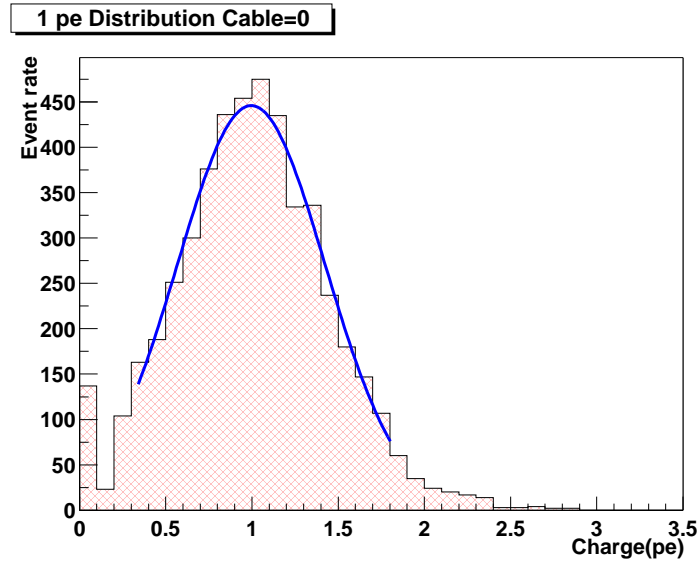


Figure 5.6: The typical 1 p.e. charge distribution of one PMT in a low energy event sample.

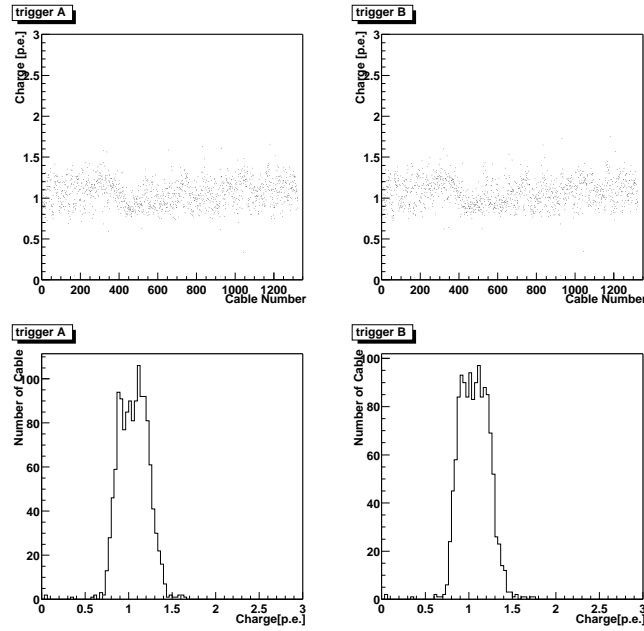


Figure 5.7: The 1 p.e. mean charge distribution for all channel. The left figure is for trigger A and the right figure is for trigger B. The very low gain (≤ 0.3 p.e.) is almostly identified as 'bad channel'.

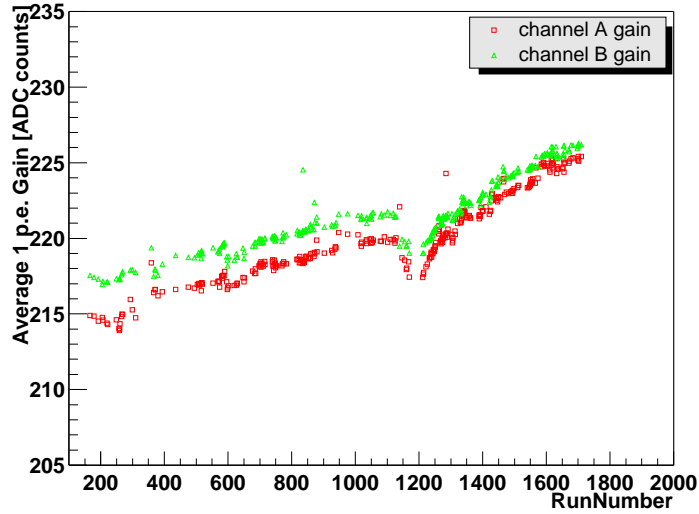


Figure 5.8: The time variation of average 1 p.e. for all PMTs. The dip at \sim run1200 has been caused by a check on the hardwares and is recovered soon.

- Hit rate in muon events is less than 80% of the total muon events (for middle and low gain).
- Noise rate is larger than 10% of the total events.
- Large difference ($>20\%$) in the hit rates between A channel and B channel.
- The accepted charge is quite large compared with the adjacent PMTs.

These selection is made run by run. Figure 5.9 shows the time variation of the number of the bad channels. At \sim run200 (March,2002), there had been 15 \sim 20 bad channels. By the fixing troubles in the HV cabling and electronics system, the number of bad channels are reduced to \sim 5.

The bad channels are masked off and regarded as the imaginary channel at the energy reconstruction.

Occasionally it happens that sudden increase occurs in bad channels by 30 \sim 100. This is because of the electronics board trouble which has the \sim 20 PMT channels per 1 board. These runs are regarded as a 'bad run' and the data during the trouble are removed from physics analysis.

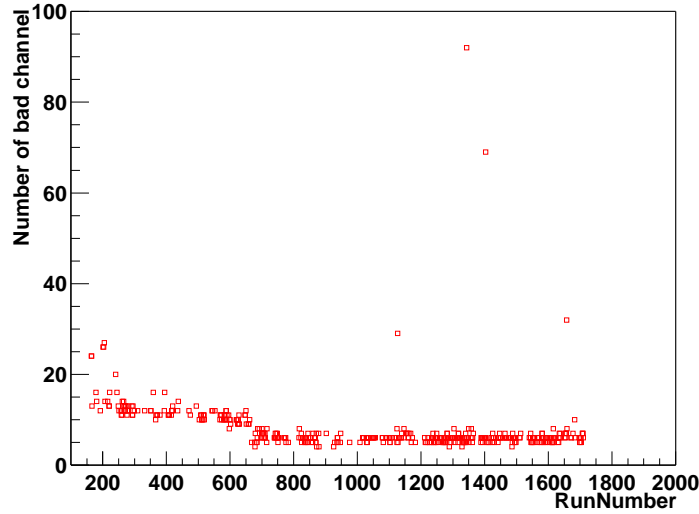


Figure 5.9: The time variation of the number of bad channels

5.2.3 Energy fitter tuning

In this subsection, the energy fitter tuning is discussed.

The PMT hits within 150 nsec time window with a charge larger than 0.3 p.e. are used for energy estimation to reduce the accidental dark hit noise. Figure 5.10 shows the relative time distribution of the hit PMTs to the trigger signal in ^{65}Zn source calibration runs. The T_{offset}

is subtracted.

At the bottom and the chimney part of the detector, part of the scintillation photons are shad-

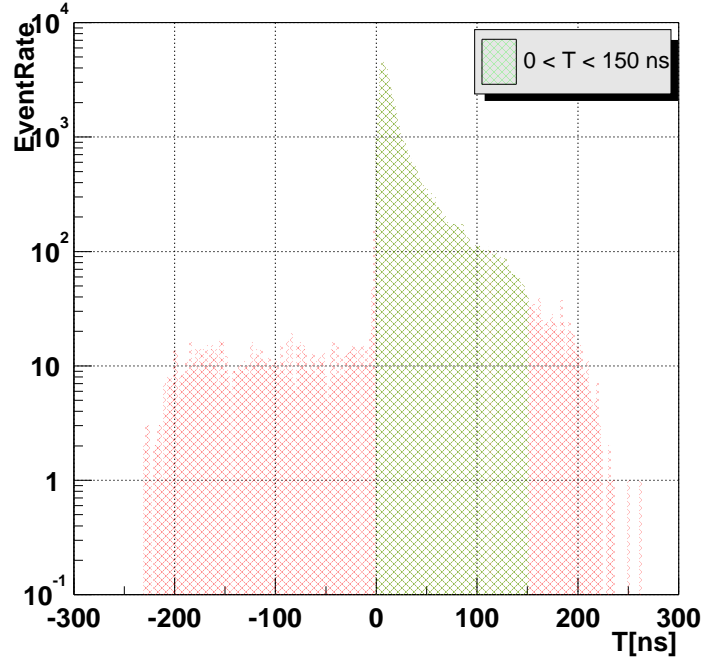


Figure 5.10: The relative time distribution of the hit PMTs to the trigger signal in ^{65}Zn source calibration runs. The green zone is used to energy estimation and the red zone is regarded as accidental dark noise hit.

owed by the balloon straps. The shadow effect is calculated by Geant4 simulation. Figure 5.11 shows the normalized total charges obtained by the ^{65}Zn γ -ray source positioned along the z-axis to the one at the center.

After the shadow correction, the position dependence and the asymmetry of the energy scale along the z-axis still remains, and a further correction in the radial direction is applied by using the radial dependence of the charge of the spallation neutron events.

After this correction, the position dependence and the asymmetry of the total charge along the z-axis is still large. On the other hand, r-dependent position dependence is much smaller than z-axis one. the asymmetry along the z-axis is forced to be caused by missing PMT around the chimney and the bottom region of the detector. Number of the missing channels are ~ 20 PMTs around the chimney and ~ 5 PMTs around the bottom. Therefore, the charge of the missing channels are corrected(added) by using a solid angle dependent function. Figure 5.12 shows the z-dependence of the total charge ratio after the correction.

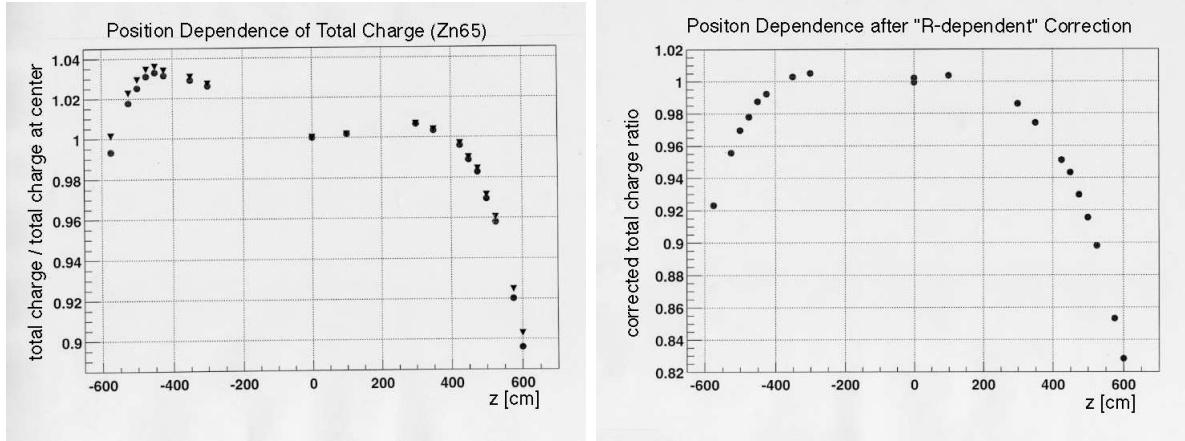


Figure 5.11: Normalized total charges obtained by the γ -rays from the ^{65}Zn positioned at the center of the detector. Horizontal axis shows the source position along the z-axis. The left figure is 'before correction' and the right figure is 'after correction'. The large difference of the charge ratio between $Z > 0$ and $Z < 0$ is caused by the density difference of the balloon straps.

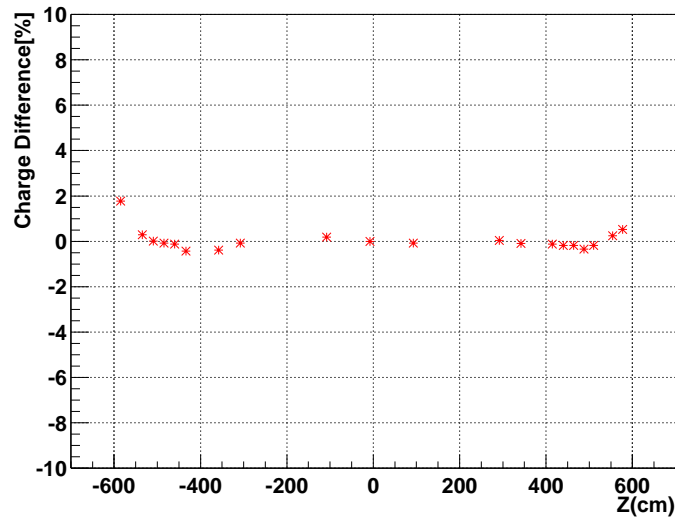


Figure 5.12: Normalized total charges in ^{65}Zn γ -rays (1.116 MeV) data by total charge at the center after the correction of the missing PMTs at the top and the bottom part of the detector.

5.3 Muon Reconstruction

Cosmic ray muons are generated in the following interaction of the primary cosmic ray particles in the atmosphere:

$$p(H, He..) + Air \rightarrow \pi^\pm + X$$

$$\pi^\pm \rightarrow \underline{\mu^\pm} + \nu_\mu(\bar{\nu}_\mu) \quad (5.3)$$

A part of the energetic muons can penetrate 1000 m rock above the detector and reach the ID. They often break ^{12}C nuclei in the scintillator and produce radioactive elements which decay by emitting electrons, positrons, neutrons or γ -rays with energies ranging up to about 20 MeV. The energy of the events after the muons overlaps the region of the positron events of the reactor neutrinos and the solar anti-neutrinos. Also some spallation decay process is similar to the correlated events in these neutrino events detected with $e^+ + n$ delayed coincidence. Thus spallation events would become a serious background. In order to reject spallation events, precise reconstruction of the muon tracks is crucial, because the vertex position of spallation events is strongly correlated in space and time with the track of the parent muon.

Figure 5.13 is the event display of the muon event by charge information. The right upper corner displays the OD PMTs. The almost muon event strike the all ID PMTs except bad channel. The muon event is defined as the one which satisfies either of the following conditions :

- Total charge of the photo-electron is greater than 10^4 p.e.
- Total charge of the photo-electron is greater than 500 p.e. and number of the hit PMTs in the OD is greater than 5.

The left of Figure 5.14 shows charge distribution of the muon event defined above. The charge distribution have two peaks. The higher one energy is the muon passed through the liquid scintillator and the lower one corresponds to the muon passed only the buffer oil. The right of Figure 5.14 shows the time distribution between the muon events. The straight line shows the fit by an exponential line and the average muon rate is found as ~ 0.3 Hz.

The positions of the muon entering and exiting the balloon is reconstructed by timing information. The entrance point is defined as the position of the PMT with the earliest hit and more than 2 neighboring hit PMTs within 10 nsec. The exit point is defined as the center of the gravity of the high charge PMTs. Figure 5.15 shows time and charge distribution of PMTs in a muon event shown by Figure 5.13. The entrance and exit point have high charge. As PMT go away from the entrance and exit point, the charge is decreased.

The track of the muon is defined as the line connecting the entrance and exit points. The left of Figure 5.16 shows charge distribution vs. the track length (buffer oil + scintillator). In the scintillator region, ID charge increase in proportion to the track length. The right of Figure 5.16 shows the charge distribution with a distance from the detector center. There is a sharp structure at $R \sim 650\text{cm}$ corresponding to the balloon edge. The normal muon events penetrating the balloon and the clipping muon events can be separated easily.

The average charge per unit track length are estimated for the buffer oil (the left of Figure 5.17) and the scintillator (the right of Figure 5.17). In the buffer oil region, the main source of the light is by Cherenkov radiation. The track length in the buffer oil is selected greater than 700 cm

to be a good quality. The estimated charge unit is ~ 30 p.e./cm. In the scintillator region, the main source of light is by scintillation. The contribution of Cherenkov radiation is subtracted. The estimated charge unit is ~ 600 p.e./cm.

The muon total charge is sometimes higher than the one being proportional to the track length due to the occurrence of shower. The excess of the charge by the shower is calculated by :

$$\Delta Q = Q_{total} - q_{buffer} \times L_{buffer} - q_{scint} \times L_{scint} \quad (5.4)$$

where q_{buffer} , q_{scint} are the average charge per unit track length. This ΔQ charge is used to select the neutrons and spallation events generated by the muons.

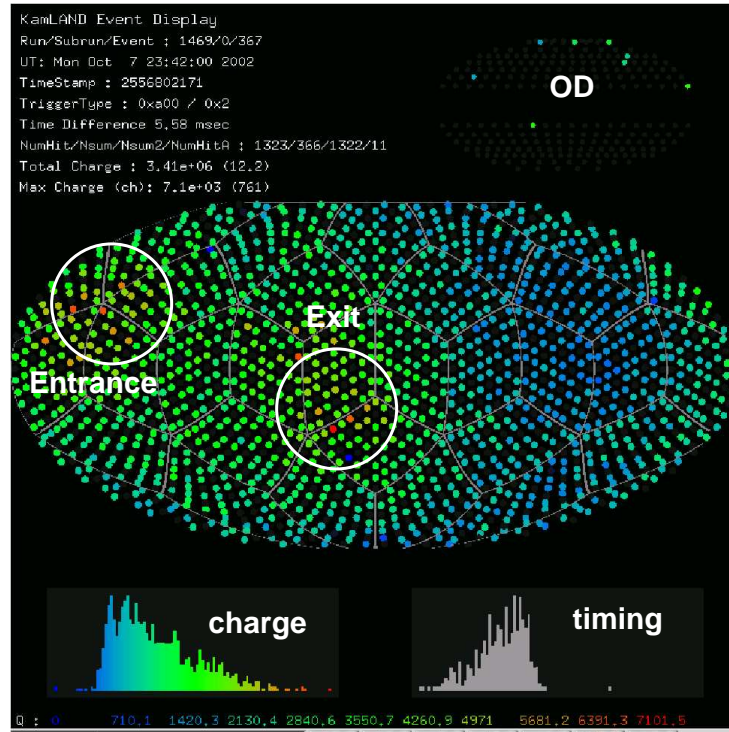


Figure 5.13: KamLAND event display for the muon event. Dots show the charge quantity of the hit PMTs.

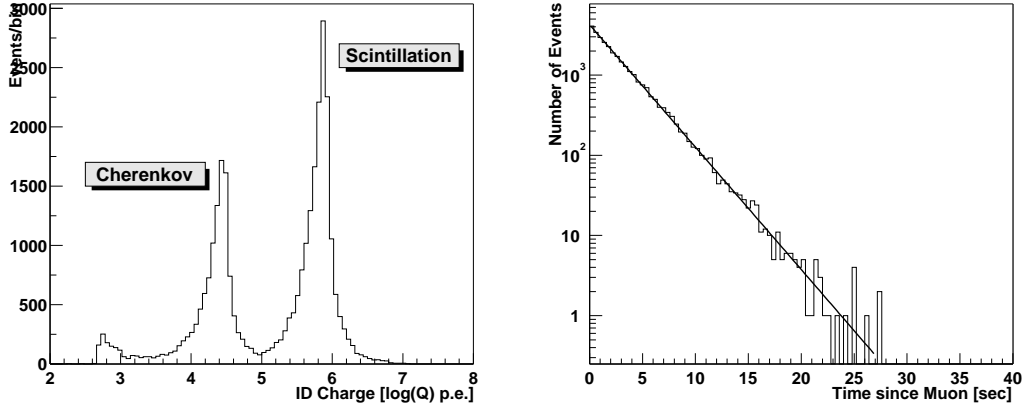


Figure 5.14: Inner charge distribution and time distribution for muon events

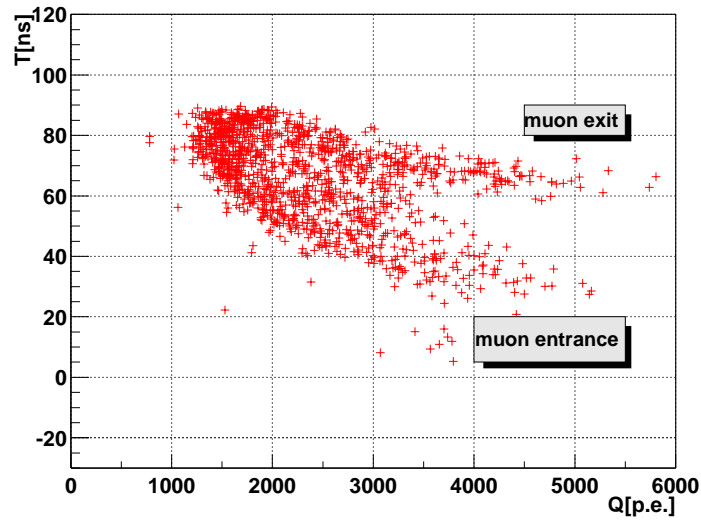


Figure 5.15: Muon event time and charge distribution

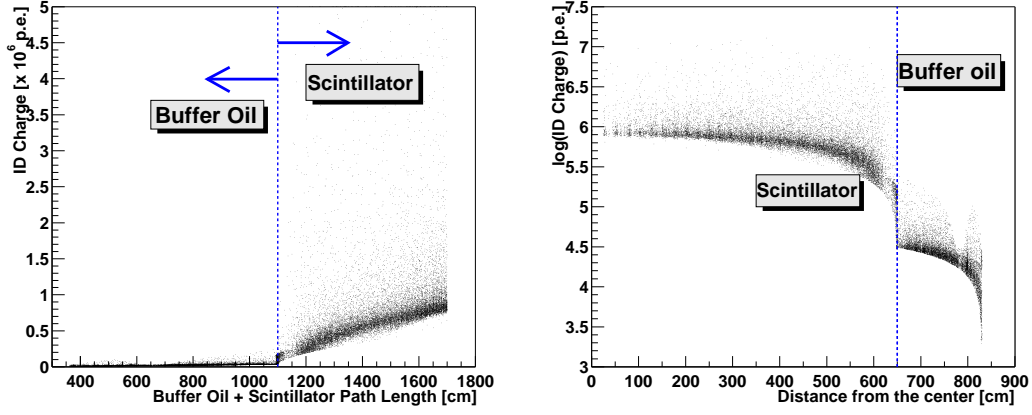


Figure 5.16: Track length vs. charge distribution. The structure corresponding to the BO and the LS region is shown.

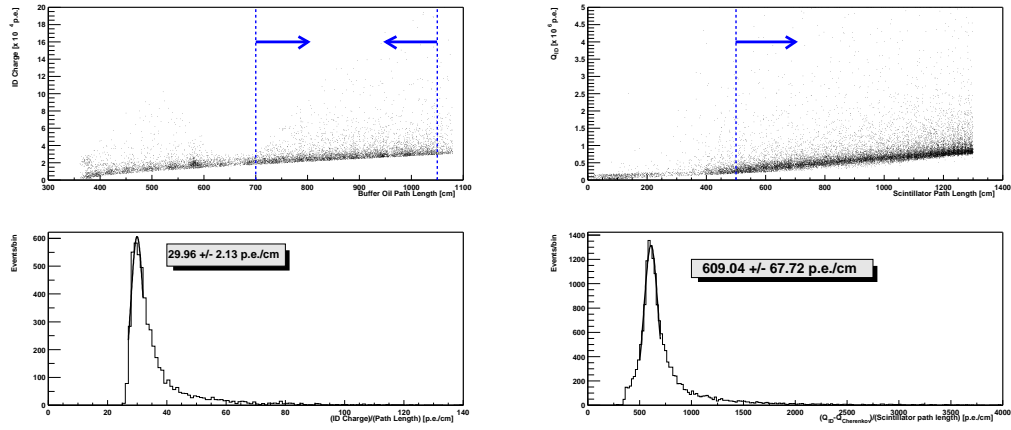


Figure 5.17: Track length vs. charge and the charge per unit track length in the BO and the LS. Left figure shows the BO region and the right figure shows the LS.

5.4 Trigger efficiency

When the number of the hit PMTs exceeds 200, a global trigger is issued. It is important to know the energy threshold of the trigger to detect $\bar{\nu}_e$. In order to investigate the trigger efficiency, the low energy delayed events are used.

The trigger is issued when the number of hit PMTs exceeds 200 as a prompt trigger and then the threshold is lowered to 120 in 2.5 ms after the prompt signal. Thus the delayed part covers the energy region to study the trigger efficiency following :

$$\epsilon_{\text{prompt trigger}} = \frac{N_{\text{PMThits} \geq 200}}{N_{\text{PMThits} \geq 120}} \quad (5.5)$$

The left histogram of Figure 5.18 shows the energy spectrum obtained by the delayed signal in the data taken in about 10 days. Blank histogram is for events with the delayed trigger and filled histogram is the events with the number of the hit PMTs exceeding 200 in delayed trigger. The energy bin is 0.05 MeV. The events are selected with the vertex in $R \leq 550\text{cm}$. The right graph of Figure 5.18 shows the $\epsilon_{\text{prompt trigger}}$, the trigger efficiency derived by the ratio of the filled histogram to the blank histogram in each energy bin in the left histogram of Figure 5.18. As shown by the results, the trigger efficiency increases steeply from 0.6MeV reaching to 100% at 0.8MeV, showing no event loss at the trigger level for the reactor $\bar{\nu}_e$ detection above 0.9MeV.

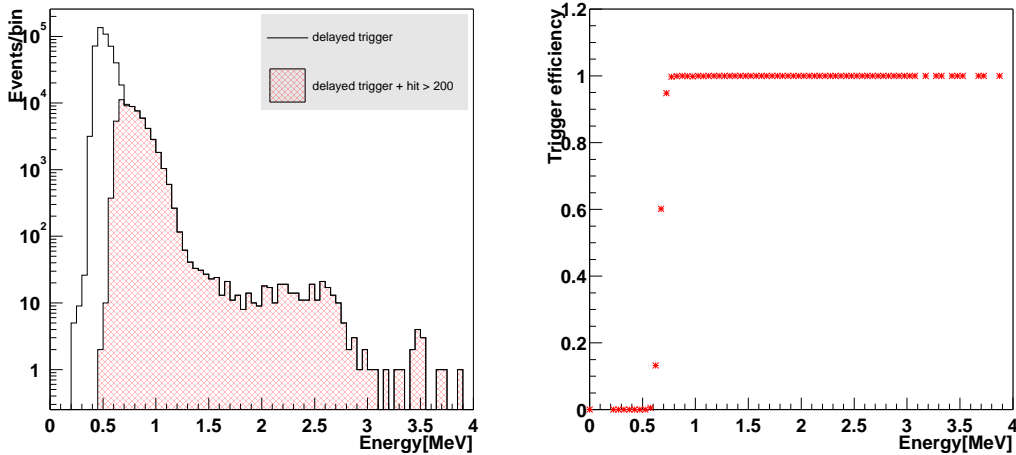


Figure 5.18: Trigger efficiency

5.5 Charge efficiency

The events with $Q_{ID} \geq 10^4 \text{p.e.}$ are defined as the muon events regardless of the OD hits. There may be a finite possibility that events which are not the muon events but are associated with

$Q_{ID} \geq 10^4$ p.e. are misidentified as the muon events. (for example, the high energy fast neutron events induced by the muons through the rock, atmospheric neutrino and relic neutrino etc.) Thus the energy dependence of the charge and charge efficiency which is defined as below :

$$\epsilon_{\text{charge eff.}} = \frac{N(E, Q < 10^4)}{N(E, Q < 10^4) + N(E, Q \geq 10^4)} \quad (5.6)$$

are given at Figure 5.19.

The left picture is the energy dependence of the charge. The events are collected from all volume. Now the particle ID (muon or not) is disregarded. The reconstructed energy has a clear linearity with the charge. The right picture shows the energy dependent efficiency of the charge that are defined as the low energy events with OD hits being less than 5. The efficiency is decreased above 25 MeV. But at the energy region for the solar anti-neutrino analysis ($7.5 \leq E \leq 14$ MeV), the efficiency is 100 %.

This result is including the all volume events. The charge efficiency in the fiducial volume ($R \leq 550$ cm) is expected to be improved to the high energy (~ 30 MeV) because the reconstructed energy have dependence of radius and reduce the mean energy.

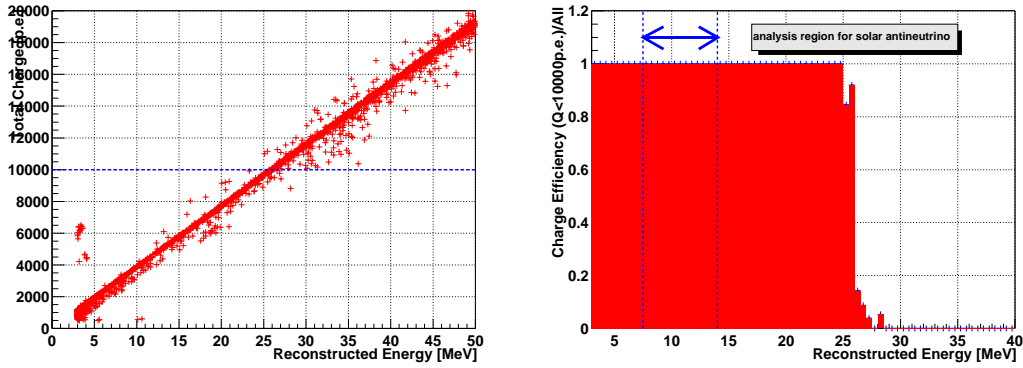


Figure 5.19: Charge efficiency

Chapter 6

Calibration

In this chapter, the KamLAND detector calibration system and the result of the studies are given. At first, the baseline calibration (gain, timing) to improve the detector performance are described. And the calibration using radioactive sources for the detection of the low energy electron anti-neutrinos are described.

6.1 Calibration support system structure

The calibration device is brought into the detector from a chimney hole at the top of the detector. The top area above the detector (dome area) is flushed by clean air which is made of mine air passed through the activated carbon filter. The supplying system keeps the radon concentration in the top of detector is much lower than 50Bq/m^3 . But the highly concentrated radon is diffused from the the dome area surrounding. Thus very careful treatment is needed for the calibration source installation not to let the radon diffuse into the detector.

Figure 6.1 shows sideview of calibration source delivery system - called 'glove box'. The glove box is separated from the detector by gate valves. The calibration source is first put into a left corner of the box. Then the glove box is purged by radon free nitrogen to remove radons in the glove box before opening the gate valve.

A Z-axis deployment system in the glove box is currently being used in KamLAND for detector calibration. It allows the deployment of various calibration sources along the z-axis of the detector by attaching a source which is then lowered into the detector via a remotely controlled motor.

6.2 Gain calibration

In this section, PMTs gain calibration is explained. The adjusted gain was $4.7 \times 10^6 \pm 6\%$ by providing the high voltage. For the gain measurement, 30 LEDs scattered in the spherical tank is used. The wavelength of the light is about 470 nm, which is in a region of the response of the PMTs but not absorbed by the liquid scintillator. So LED light hits the PMTs directly. Figure 6.2 shows the setup of the LED calibration. The LED light goes through the scintillator and

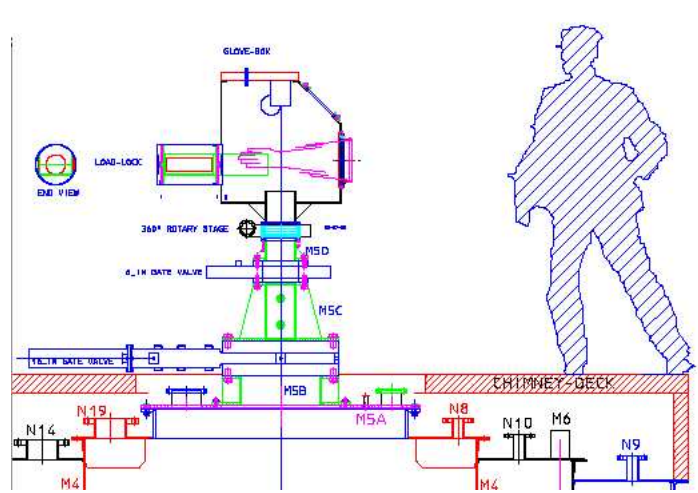


Figure 6.1: The view of the glove box at the top of KamLAND detector. The worker puts the calibration device into this box and uses the glove to handle the calibration device. There are two gates valve to separate the detector from the glove box. The gate valves are opened only after the preparation in the glove box over.

illuminate the opposite side of the PMTs. The light intensity is adjusted to 1 p.e. at the PMTs. The trigger signal of the LED radiation is sent to ATWD.

The 1 p.e. charge distribution of the typical PMT is shown in Figure 6.3. There is a clear peak of 1 p.e. in this figure. The steep rise at the lowest charge is due to the dark noise hit. Using the position of the 1 p.e. peak, the gain is adjusted by tuning the HV values.

Figure 6.4 shows the 1 p.e. peak positions before and after the gain adjustments by using the LED data. The width of the 1 p.e. peak position is reduced from 16% to 6%.

6.3 Timing calibration

In order to get the vertex position, relative timing and timing resolution of all PMTs have to be known. If the relative timing is different, it has to be adjusted. The relative timing is determined by the transit time in PMT, the length of the signal cable, and the signal charge. So we need to check the charge dependence of the relative timing, so-called TQ-map, for PMT by PMT.

Figure 6.5 shows the setup of the timing calibration system. The light source is a DYE laser with a wavelength adjusted to 500 nm. The light intensity is adjusted by the attenuation filters. The light is separated at the diffusion ball. One light is sent to a diffuser ball in the center of the detector through an optical fiber, the other is used for monitoring and triggering by 2 inch PMTs. The data taking rate is from 8 to 10 Hz.

Figure 6.6 shows the relation between timing response and charge in the typical PMT called as 'TQ-map'. The high, middle and low gain have different timing response. The fitting function

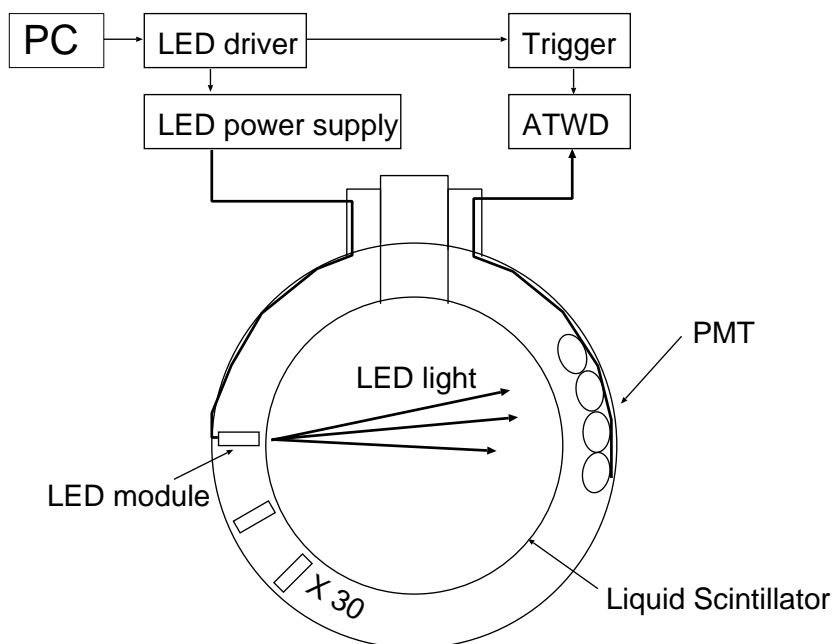


Figure 6.2: LED calibration setup

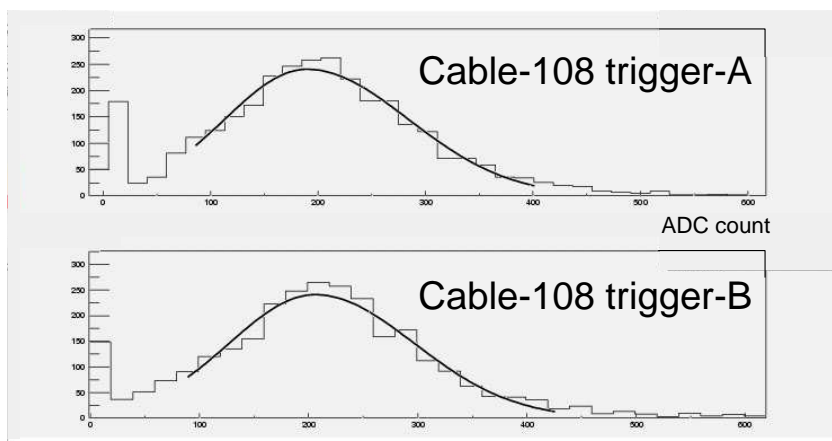


Figure 6.3: The 1 p.e. distribution of a typical 17 inch PMT. The upper picture is at the cable-0 ATWD A channel and the lower picture is at ATWD B channel.

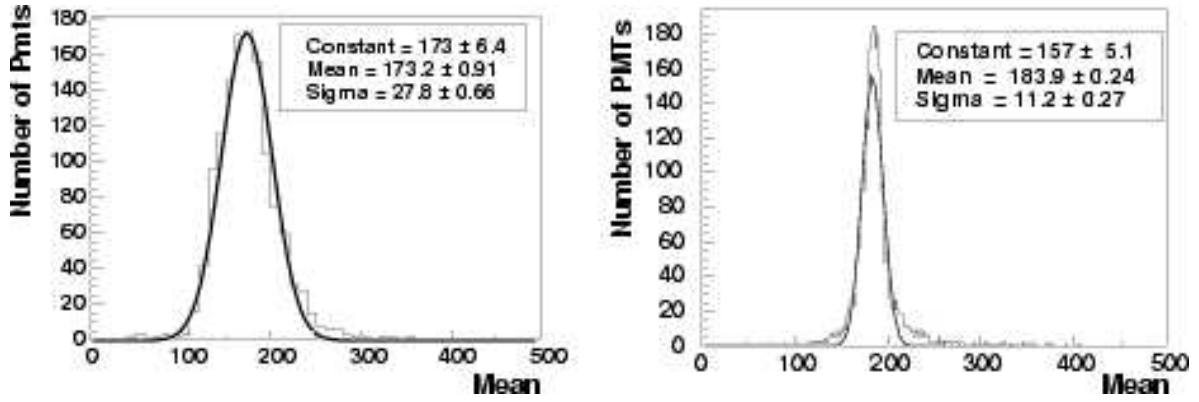


Figure 6.4: The 1 p.e. peak position before and after the HV adjustment for all 17" PMTs with both trigger A and B. The left figure is the results on 4th of March, 2002 before the adjustment and right figure is the ones on 9th March, 2002 after the adjustment.

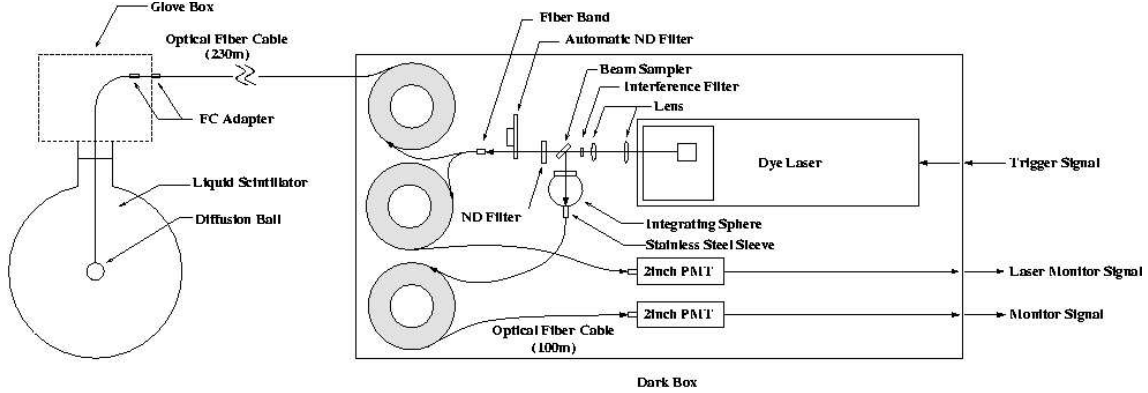


Figure 6.5: The laser calibration system setup

for the TQ-map is introduced as :

$$t(q) = P_0 + P_1 \log_{10} q + P_2 (\log_{10} q)^2 \quad (6.1)$$

where $t(q)$ is a charge dependent timing peak, q is a charge by ATWD count, P_0 , P_1 and P_2 are free parameters to be obtained for each PMT by the fit. Typical values by fitting are $P_0=16.19$, $P_1=-4.15$ and $P_2=0.60$.

The all PMT is fitted for each A/B channel and the resultant parameters in the TQ-map are used as the correction constants at the event reconstruction. The fitting of Eq. 6.1 are used for high gain and the average constants are used for middle and low gain. Figure 6.7 shows the timing calibration result. The upper figure indicates the leading edge of the 1 p.e. for the all PMTs in the laser calibration run before the correction, and right figure indicates the one after the correction. The global time resolution is improved from 6.7 ns to 2.0 ns.

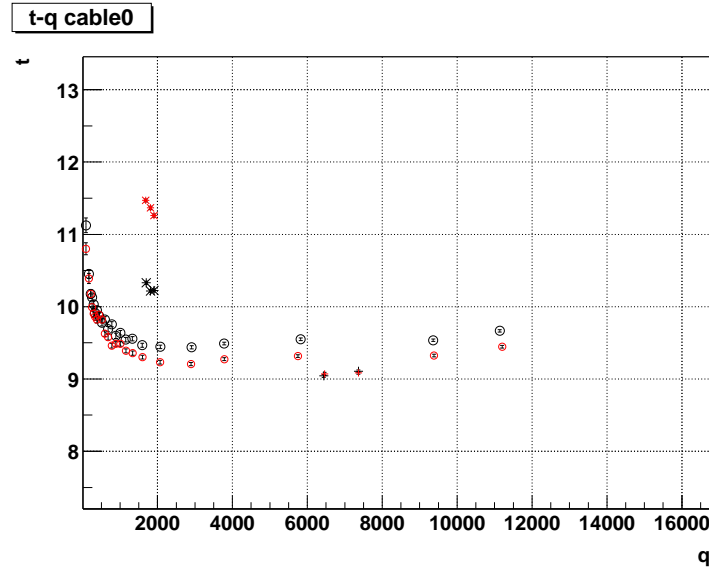


Figure 6.6: The TQ-map for a typical PMT. Circle marks indicate the high gain, plus marks indicate the middle gain and star marks indicate the low gain.

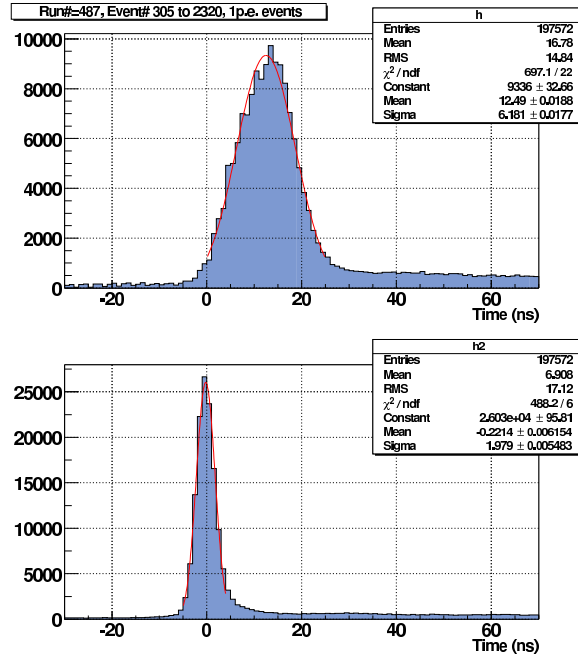


Figure 6.7: The result of the timing calibration. The upper figure is the 1 p.e. timing distribution of all PMTs before the correction and the lower figure is after the correction.

Nuclei	Half life	Energy
^{68}Ge	270.82 d	$E_\gamma=0.511 \text{ MeV} \times 2$
^{65}Zn	244.26 d	$E_\gamma=1.116_{(50.6\%)} \text{ MeV}$
^{60}Co	5.27 yr	$E_\gamma=1.173_{(100\%)} \text{ MeV}, 1.333_{(100\%)} \text{ MeV}$
$^{241}\text{Am/Be}$	432.2 yr	$E_n=2.225 \text{ MeV}, E_\gamma=4.436, 7.653, 9 \text{ MeV}$

Table 6.1: The list of radioactive calibration source

6.4 Energy & vertex calibration by radioactive sources

The four radioactive γ -ray sources are prepared to cover energy range between 1MeV to 8MeV. They are ^{68}Ge , ^{65}Zn , ^{60}Co , and Am/Be. From the Am/Be source a γ -ray of 2.224 MeV is emitted from a neutron capture taking place in the source material. So we can study the detector response to the neutron capture event in the neutrino delayed signal.

Energy resolution are required $< 10 \%$ to avoid the contamination of the accidental background and reduce the systematic error. The uniformity in the vertex resolution are required too. It reflects the systematic error of the expected event rate in the neutrino event analysis.

6.4.1 Radioactive isotopes

Table 6.1 shows the γ -ray sources for the calibration.

^{68}Ge becomes ^{68}Ga after the electron capture. ^{68}Ga emits the positron with a maximum energy of 1.9 MeV and captured in the source material to emit two 0.511 MeV γ -ray.

^{65}Zn emits a 1.116 MeV γ -ray. ^{60}Co emits 1.1732 and 1.3325 MeV γ -rays. At KamLAND, these two γ -rays are detected as the summed energy of 2.5057 MeV.

In the Am/Be, an α particle emitted from Am interacts with ^9Be to form $^{12}\text{C}^*$ and various energies of γ -ray and a neutron are emitted. The emitted γ -ray energies are 4.436, 7.653 MeV γ -rays and multi γ s with a total energy of 9MeV. The emitted neutron is captured in the surrounding material to produce a 2.225 MeV γ -ray.

^{68}Ge , ^{65}Zn and ^{60}Co sources are contained in a stainless steel capsule of $20 \text{ mm} \times 5 \text{ mm}\phi$ and jointed to a 230 mm length rod. Am/Be is contained in a box which is $130 \text{ mm} \times 130 \text{ mm}\phi$ packed in several layers, from inner to outer, Pb (1 mm), plastic sheet, parafine, plastic sheet, acrylic vessel. These sources are shown in Figure 6.8. They are cleaned by diluted nitric acid and checked for the radioactive contamination.

6.4.2 Energy spectrum

The energy spectrum of the source calibration data includes the γ -ray signals from the source and the accidental background. Figure 6.9 shows the data for ^{65}Zn deployed at the detector center ($Z=0 \text{ cm}$). The accidental background is distributed at low energy, mainly from the balloon edge. The source position is changed in a region $-600 \leq Z \leq 600 \text{ cm}$ along the vertical line (z -axis). After the vertex reconstruction, the events at $Z \geq 700\text{cm}$ or $\sqrt{X^2 + Y^2} \geq 100\text{cm}$ are discarded.

Figure 6.10 shows the energy spectrum for ^{68}Ge , ^{65}Zn and ^{60}Co at $Z=0 \text{ cm}$ (center of the



Figure 6.8: The devices of calibration source box. The left picture is devices of Ge, Zn and the right is for Am/Be.

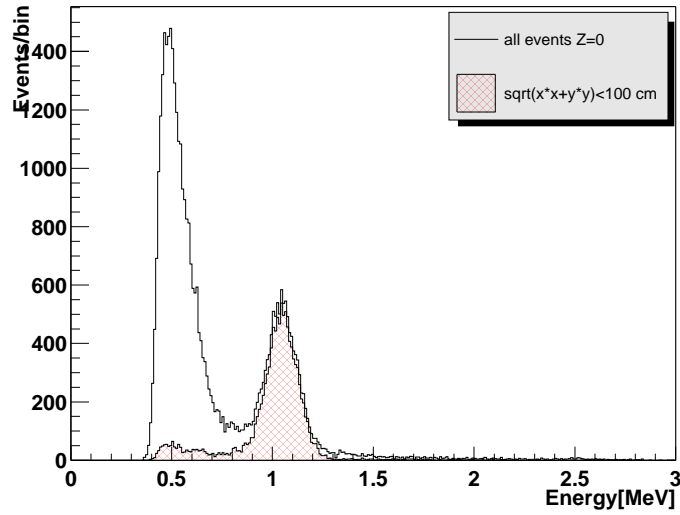


Figure 6.9: Energy spectrum for ^{65}Zn source with a vertex positions in all the volume and only a cylindrical region around z-axis ($\sqrt{x^2 + y^2} < 100\text{cm}$). The low energy accidental background events are induced from the near of balloon edge.

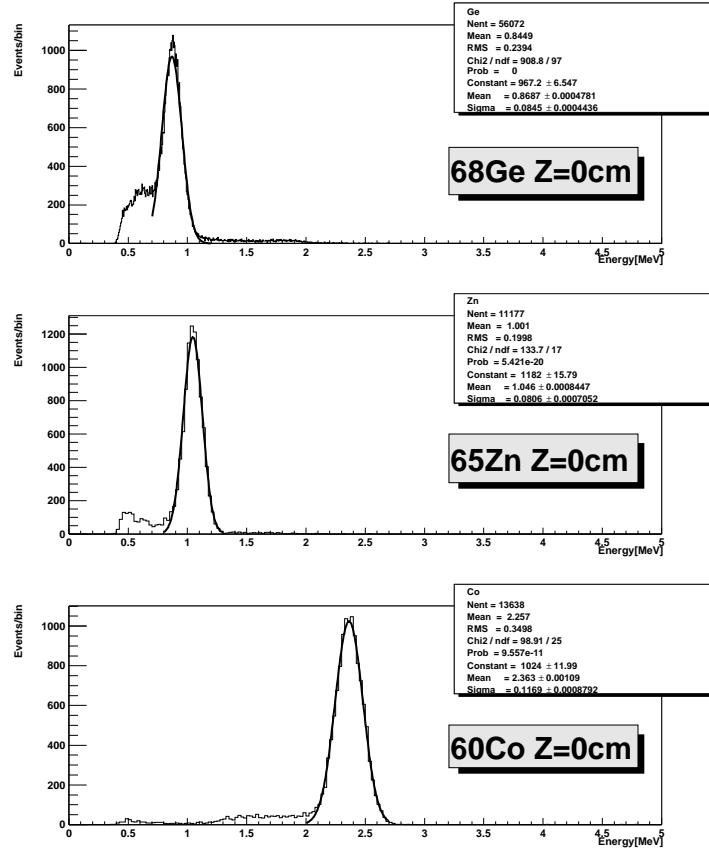


Figure 6.10: The energy spectrum for ^{68}Ge , ^{65}Zn and ^{60}Co source at Z=0 cm after the vertex cut.

detector) after background rejection. The energy is shown as 'visible energy' and different from the actual energies of the γ -rays. This is explained by the reduction of the light yield due to the recombination and quenching effects of the excited molecules in the liquid scintillator. These effect are discussed in the next subsection 6.4.3.

For examples, total energy of ^{60}Co γ should be 2.506 MeV as 'real energy' (1.1173 + 1.333 MeV) but calibration result of ^{60}Co γ peak is 2.363 MeV. The ratio of the energies due to the quenching is $E_{vis}/E_{real} = 0.943$. Besides in a ^{65}Zn , the visible energy and real energy of the peak are 1.046 MeV and 1.116 MeV, respectively and the quenching effect is appeared as $E_{vis}/E_{real} = 0.937$. Thus the quenching effect is mostly the same between ^{65}Zn and ^{60}Co at the energy $\sim 1.1\text{MeV}$, the energy calibration results are consistent with each other.

The position dependence of the mean energy and the energy resolution are examined. Figure 6.11 shows the energy distribution and energy resolution for ^{65}Zn source at $-600 \leq Z \leq 600$ cm. The visible energies difference between $-500 \leq Z \leq 500$ cm are the same as the one at Z=0 within $\pm 1\%$. The energy resolution is $\Delta E/\sqrt{E(\text{MeV})} \sim 7.7\%$ between $-500 \leq Z \leq 500$ cm.

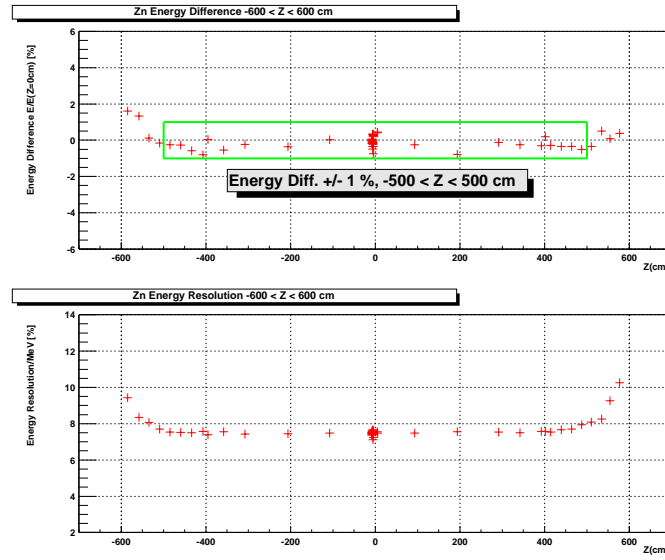


Figure 6.11: The energy distribution and energy resolution by the ^{65}Zn source position at $-600 \leq Z \leq 600$ cm.

6.4.3 Energy scale

The energy calibration results indicate that there are non-linearity in the energy scale and decrease of observed energy against the true energy described in the previous subsection 6.4.2. In this subsection, the mechanism of these phenomenon is discussed.

- Quenching effect

Organic scintillator do not respond linearly to the ionization density. Dense ionization columns along the track emit less light than expected from the dE/dX for minimum-ionizing particles. A widely used semi-empirical model by Birks points that recombination and quenching effects between the excited molecules reduce the light yield [45]. These effects are more pronounced when the density of the excited molecules is greater. Birks formula is described by :

$$\frac{dL}{dx} = L_0 \frac{dE/dx}{1 + k_B dE/dx} \quad (6.2)$$

where L is the luminescence, L_0 is the ideal luminescence at sufficiently low specific ionization density, and k_B is the Birks constant, which must be experimentally determined for the scintillator.

- Dark hit

The number of accidental dark hits is reduced by imposing the 150 ns time window in the energy reconstruction process but not zero. From the 1 pps trigger information, 10 PMTs are hitting for 125 ns window, while the energy estimator have 150 ns window. So

$10 \times 150 / 125 = 12.0$ PMTs are expected to make dark hit. The scintillation photon yield is 300 p.e./MeV. Thus this dark hit corresponds to $12/300 = 0.04$ MeV, if mean charge of the dark hit of the PMT is 1 p.e.. If the mean charge is $1/3$ p.e., which is trigger threshold, then the minimum case, the dark energy will 0.013 MeV. Thus the dark energy is assumed to be $E_{dark} = 0.013 \sim 0.04$ MeV.

- Single photo-electron efficiency

Single photo-electron inefficiency can also cause the energy non-linearity. Probability of 1 p.e. detection if there is no threshold effect, is :

$$p(1) = u \exp(-u) \quad (6.3)$$

where u is the mean number of photons in the deposit energy of E [MeV], $u = 1/1325 \times E \times (300 \text{ p.e./MeV})$. The detection efficiency (ϵ) of 1 p.e. is a concern, and probability of 0 p.e., 1 p.e. and N p.e. ($N \geq 2$) detection efficiency are :

$$\begin{aligned} p(0) &= \exp(-u) + (1 - \epsilon)u \exp(-u) \\ p(1) &= \epsilon \times u \exp(-u) \\ p(N) &= u^N \frac{\exp(-u)}{N!} \end{aligned} \quad (6.4)$$

The visible energy is calculated by adding up charges, so :

$$E_{vis} = Q(1) \times p(1) + \sum_{N \geq 2} (Q(N) \times p(N)) \quad (6.5)$$

If no threshold effect :

$$\sum_{N \geq 1} (Q(N) \times p(N)) = uQ_1 \equiv E_{vis-no-thr} \quad (6.6)$$

where Q_1 is the mean charge of the 1 p.e. events with no threshold effect. Then, considering that only 1 p.e. events are affected by the threshold effect, eq(6.5) is converted to :

$$\begin{aligned} E_{vis} &= uQ_1 - u \exp(-u)Q_1 + Q_1 \epsilon u \exp(-u) \\ &= E_{vis-no-thr} \left(1 - \exp(-u) \left(1 - \frac{Q(1)}{Q_1} \epsilon \right) \right) \end{aligned} \quad (6.7)$$

Here, $Q(1)$ is determined from the following relation.

$$Q_1 = Q(1)\epsilon + Q_{loss}(1 - \epsilon) \quad (6.8)$$

where Q_{loss} is the mean charge of the events under threshold, then, it should be less than $1/3$ p.e.. From eq(6.7) and (6.8),

$$E_{vis} = E_{vis-no-thr} (1 - \exp(-u)\delta) \quad (6.9)$$

$$\delta = \frac{Q_{loss}}{Q_1} (1 - \epsilon) \quad (6.10)$$

This contribution is also only in one direction and maximum contribution is limited by the relation of visible energy between ^{65}Zn and ^{60}Co calibration to be 0.6%. This corresponds to $\delta=0.05$.

All these effects are included into the Monte Carlo simulation and 6 sets of calibration data are fitted by the three parameters (Birks constant, Cherenkov intensity and global normalization factor). Calibration data of γ -ray energies from ^{60}Co , ^{65}Zn , ^{68}Ge , Am/Be sources and neutron capture γ s after the muon. The result are shown in Figure 6.12. The uncertainty from the energy non-linearity is estimated to be 1.1%. Figure 6.13 shows the fractional difference of the reconstructed γ energy including the systematic error of the energy scale estimation. Total systematic error is about 2% from 1 to 8 MeV.

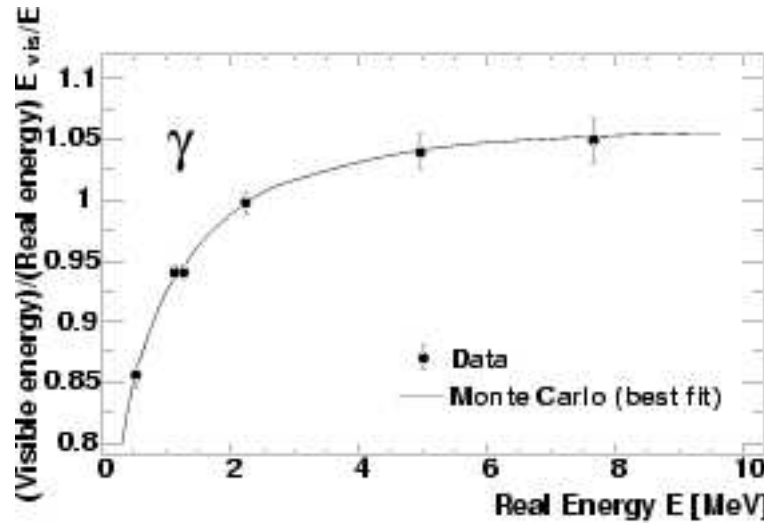


Figure 6.12: The calibration data points from ^{60}Co , ^{65}Zn , ^{68}Ge , Am/Be and neutron capture γ s after muon with a fit obtained result by a Monte Carlo simulation. The neutron capture γ result is discussed in section 6.6

6.4.4 Vertex distribution

Vertex distribution and the resolution at KamLAND detector are also studied by the source calibration run. Figure 6.14 shows the ^{65}Zn vertex distribution for x-axis and z-axis. The selected energy is $E_{vis} \geq 0.7$ MeV to reduce the accidental background events. The installed source position is $Z=0$ cm. The distribution is uniform around the center of detector.

The reconstructed vertex position distribution along the X, Y and Z axes for the source placed at (0,0,0) is given in Figure 6.15 and Figure 6.16. The accidental background is almost rejected by the energy cut. Thus the reconstructed position and the resolution is studied.

The deviations of the reconstructed vertex from the actual source position for Ge, Zn, Co and Am/Be source are estimated for the region $-600 \leq Z \leq 600$ cm at Figure 6.17. The vertex

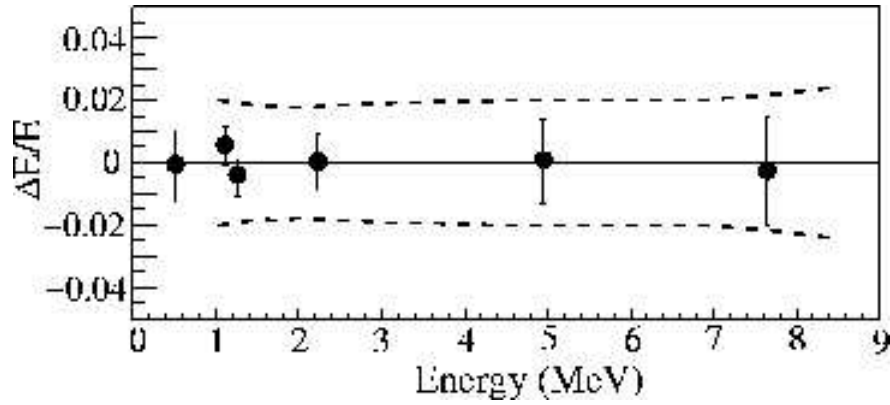


Figure 6.13: The point and bar show the fractional difference of the reconstructed γ energy. The dashed lines show the systematic error.

deviations in the case of Am/Be source are ± 5 cm at $-550 \leq Z \leq 550$ cm source position. This corresponds to the volume variation of $\sim 3\%$ as the systematic error. At Ge, Zn and Co results, the vertex deviation at $Z \geq 500$ cm exceeds -5 cm. These excess are caused by missing PMTs at chimney region.

The vertex resolution of the three dimensional space is estimated as $\Delta R = \sqrt{\Delta X^2 + \Delta Y^2 + \Delta Z^2}$ cm in which the resolution along the three axes are ΔX^2 , ΔY^2 and ΔZ^2 and they are estimated from the fit to the vertex distribution by a gauss function. Figure 6.18 shows the vertex resolution for Zn and Co. The resolution ΔR is 55 cm for Zn and 40 cm for Co. The one axis resolution is ~ 35 cm for Zn and ~ 25 cm for Co.

6.4.5 Detector stability

As mentioned in the section 5.2.1, the PMT gains have been changing since the beginning of the data taking in KamLAND. The gain change is corrected for the energy reconstruction process. To check the correction, time variation of the energy scale is checked. Figure 6.19 shows the energy variation for Zn and Co calibration from March 2002 (run number ~ 200) to November 2002 (run number ~ 1500). The energy variation is within $\pm 1\%$ besides the gain variation is $\sim +4\%$ (see Figure 5.8). Thus the energy stability is kept by the gain correction.

6.5 Calibration for delayed coincidence

The electron anti-neutrino is detected by inverse beta decay process and this reaction is detected as delayed coincidence event at KamLAND. The reaction of Am/Be source calibration have *delayed coincidence* event for γ and neutron. Thus the efficiency of the time and space correlation for neutron capture are calibrated with Am/Be.

The reaction of Am/Be source is ;



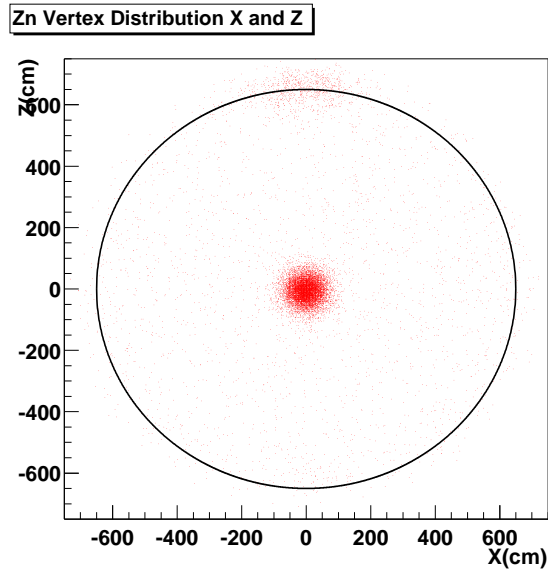


Figure 6.14: ^{65}Zn vertex distribution plot for xz-axis. The source position is $Z=0\text{cm}$. The event concentration at $Z\sim 600\text{cm}$ is induced by the missing muon event and the accidental background from the SUS frame at the chimney.

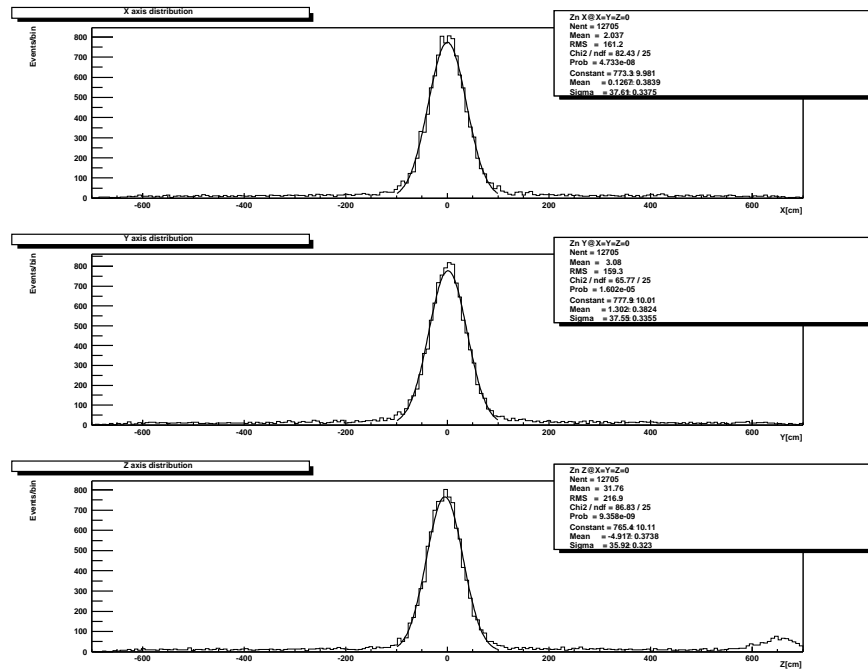
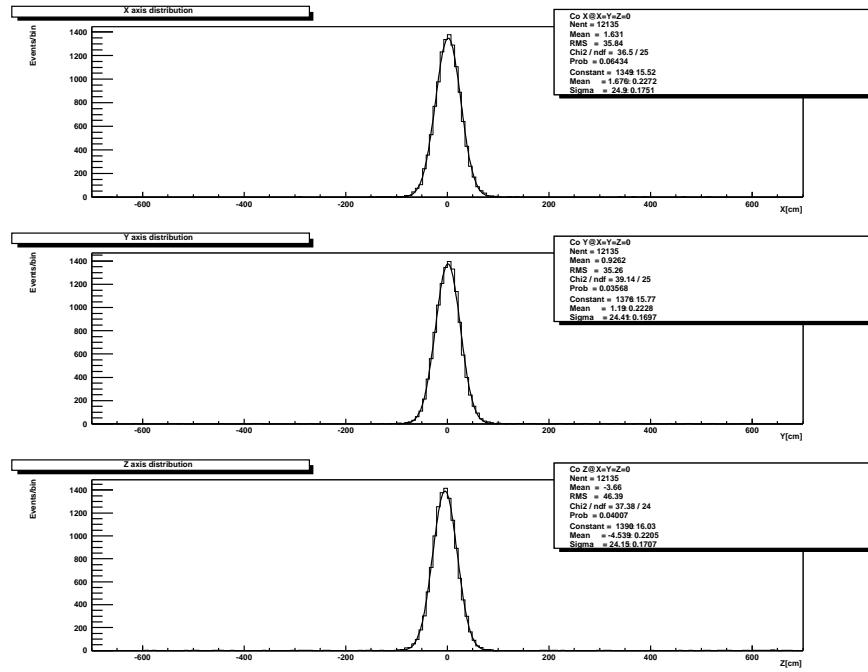


Figure 6.15: The vertex distribution at $(0,0,0)$ for ^{65}Zn

Figure 6.16: The vertex distribution at (0,0,0) for ^{60}Co

The α particle is emitted from Am and interact with Be. The excited state $^{12}\text{C}^*$ emits γ -rays with three energies (4.438, 7.653, 9 MeV). The neutron is captured by a proton in a hydrogen atom in the liquid scintillator and emit a 2.224 MeV γ -ray. The kinetic energy of the neutron are 3 ~ 7MeV for the 4.438MeV state and 1 ~ 3MeV for the 7.653MeV state, and recoil proton by the neutron is observed as same event of γ -rays. Figure 6.20 shows the single spectrum of Am/Be source positioned at Z=0 cm. The spectrum of 4.438 MeV γ is broad by the recoil proton contribution. The value of the neutron-capture peak is 2.16 MeV. This difference is happened by the shadow of the source box and the loss of energy in the source box. The 2.224 MeV γ is reduced about 2.6 %.

These energy effects are studied by MC simulation. The MC simulation predicts the energy decrease about 2.6, 1.4 and 0.8 % for the neutron capture, 4.438 MeV and 7.653 MeV respectively. Thus, the peaks in Figure 6.20 correspond to 2.16, 4.376 and 7.592 MeV for each process. Though the measured peaks is 2.16, 4.60 and 7.97 MeV. Thus the energy scale factor defined as the ratio of the reconstructed energy to the MC simulation is ~ 1 for the neutron capture and 1.05 for the 7.653 MeV γ -ray.

6.5.1 Neutron capture time and neutron capture length by Am/Be source

In the inverse beta decay process, emitted neutron is captured by a proton in a hydrogen in the liquid scintillator. The neutron capture time and length is measured by Am/Be source calibration. Figure 6.21 shows the energy spectrum of Am/Be delayed coincidence. The prompt

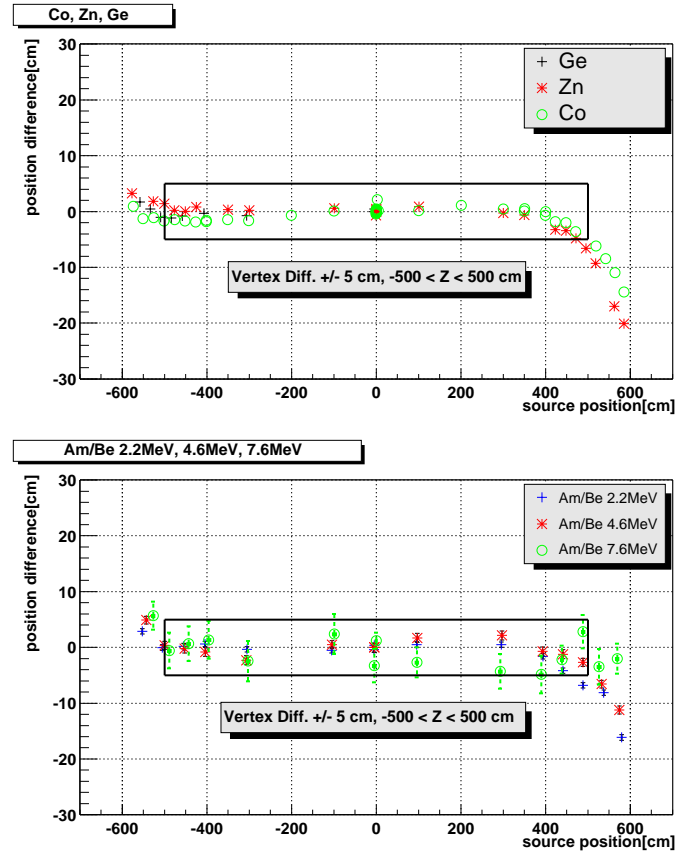


Figure 6.17: The vertex deviation for ^{68}Ge , ^{65}Zn , ^{60}Co and Am/Be. The upper figure is for ^{68}Ge , ^{65}Zn and ^{60}Co . The lower figure is for Am/Be.

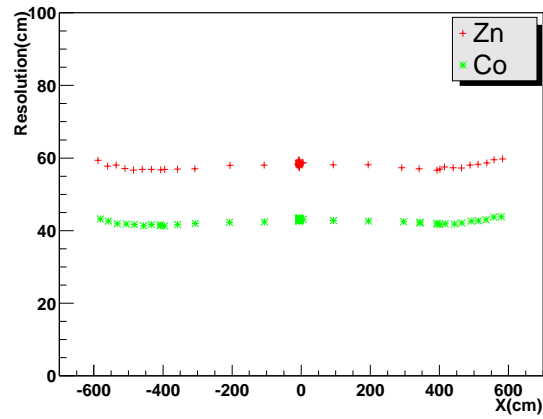


Figure 6.18: The vertex resolution for ^{65}Zn and ^{60}Co at z-axis

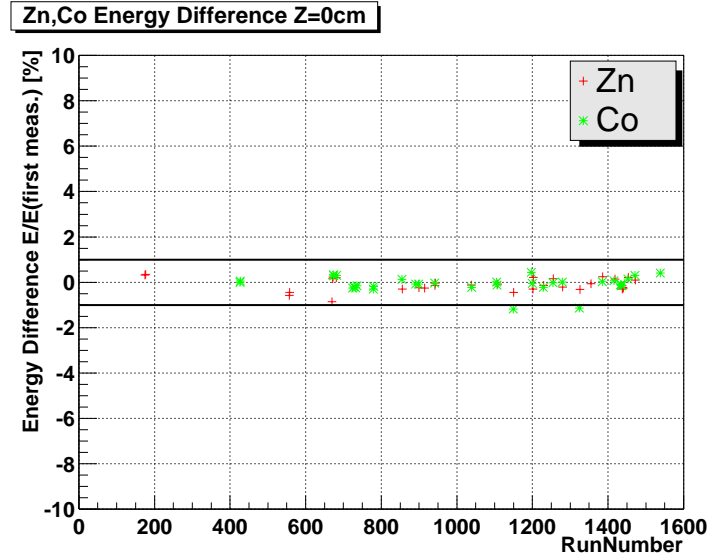


Figure 6.19: The time variation for Zn and Co mean energy distribution.

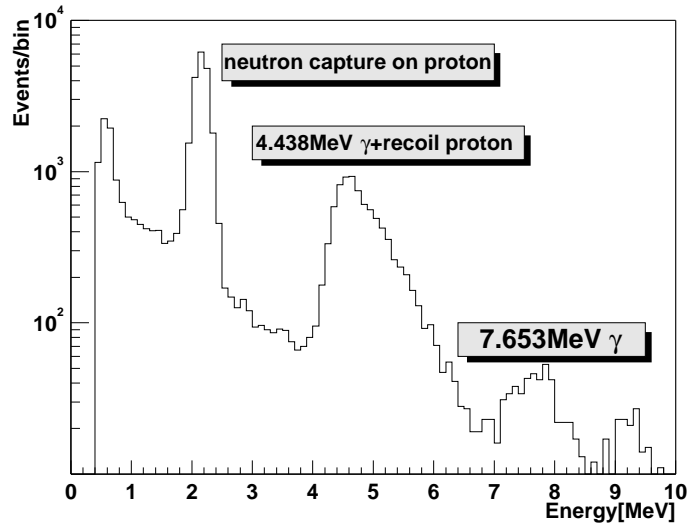


Figure 6.20: The energy spectrum for Am/Be source. The broadness of the higher energy side of the 4.438 MeV peak is caused by the recoil proton contribution. The ~ 9 MeV γ is rejected from the energy scale fitting at Figure 6.12 and 6.13 due to the small statistics.

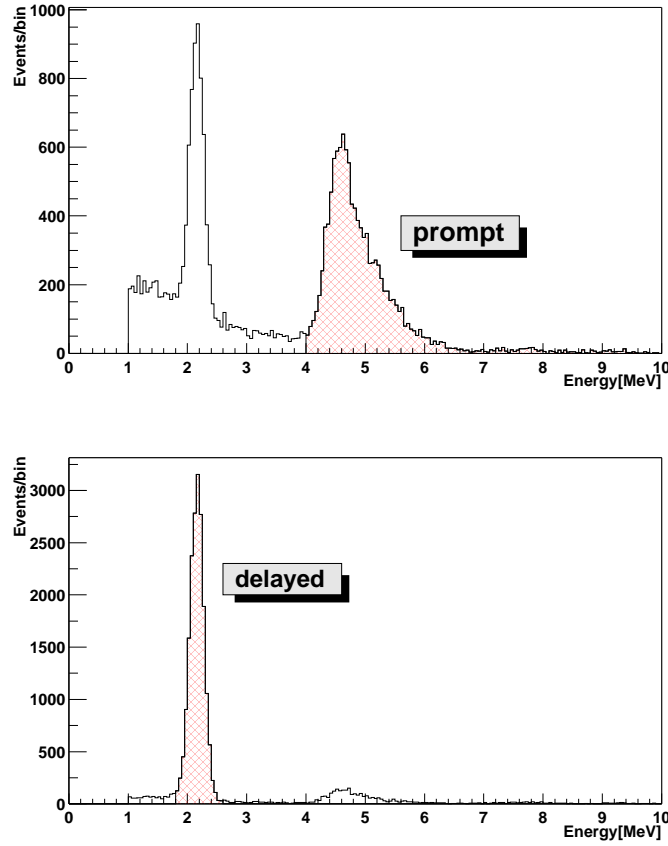


Figure 6.21: The energy spectrum of Am/Be delayed coincidence. The events larger than 4 MeV are selected as prompt events. The delayed events in the lower figure are selected by the prompt energy ≥ 4 MeV only. The events $1.8 \leq E \leq 2.6$ MeV are selected as delayed events.

events include accidental neutron events at 2.224 MeV. The events larger than 4 MeV are selected as prompt events. The delayed events are almostly 2.224 MeV neutron and some events are 4.4 MeV accidental events. The events $1.8 \leq E \leq 2.6$ MeV are selected as delayed events.

Figure 6.22 shows the time difference between prompt events and delayed events selected below. The neutron capture time is estimated about $207 \mu\text{s}$. Figure 6.23 shows the neutron capture length. The mean capture length is about 50 cm. The efficiency of the selection by the capture length are 99.2 % for $L \leq 160$ cm and 99.9 % for $L \leq 200$ cm.

6.6 Neutron events after muon

The radioactive source calibration is made only along the z-axis. The z-axis top and bottom have the problem of shadow effect by balloon rope and PMTs mask effect. it needs for whole

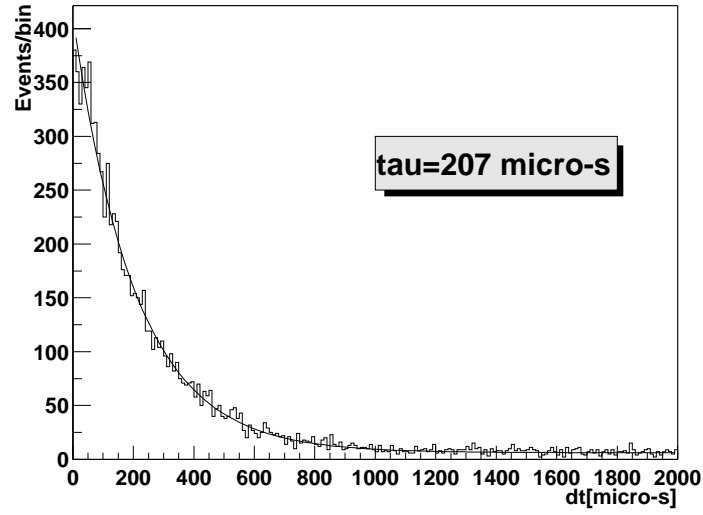


Figure 6.22: The time difference between Am/Be prompt events and delayed events and the decay time fitting result.

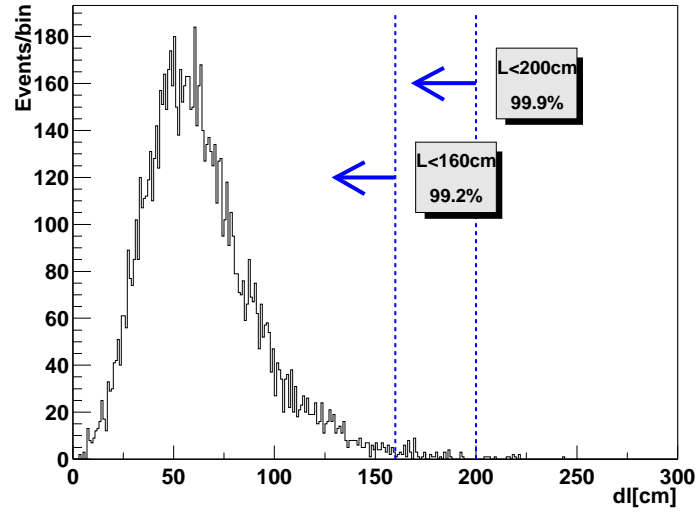


Figure 6.23: The neutron capture length from Am/Be.

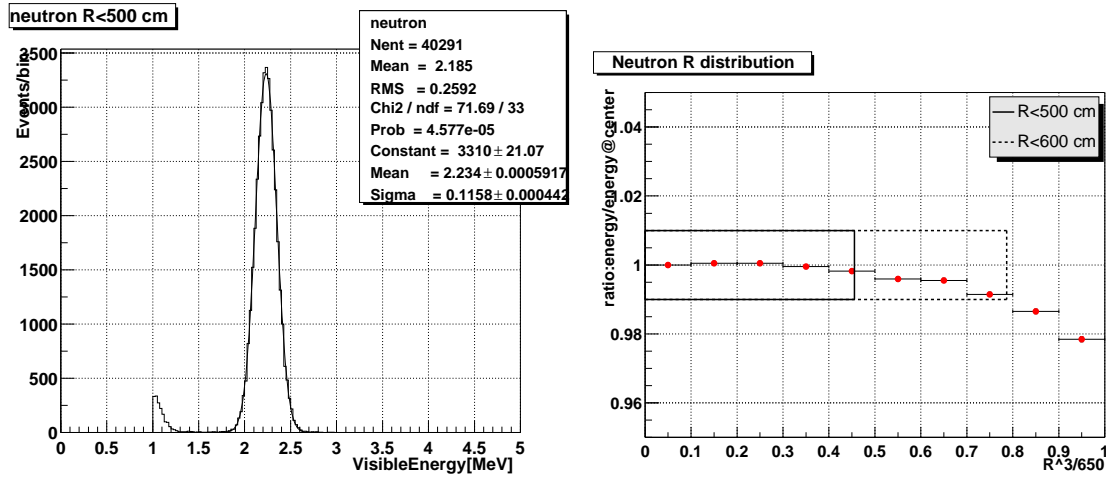


Figure 6.24: The left figure shows the energy distribution of neutron events after the muon. The right figure shows the radial dependence of the energy normalized to the one at the center.

detector to adopt the z-axis calibration results.

The neutrons event after the muon be used as good calibration sources to examine the performance in reconstruction both energy and vertex because (1) energy distribution have the peak about 2.2 MeV, (2) events are uniformly distributed throughout the detector with the large statistics.

The neutron events extracted by a method is given in Appendix A.1 in detail. In this section, both energy distribution and vertex distribution of neutron events after the muon are discussed.

6.6.1 Energy distribution

The left Figure 6.24 shows the energy distribution of the events in $R \leq 500$ cm after the muon. The mean energy is 2.234 MeV and energy resolution is $\Delta E / \sqrt{E(\text{MeV})} = 7.7\%$. The peak corresponds to the neutron capture γ -rays. This result agrees well with the source calibration results.

The right Figure 6.24 shows the ratio of energy to the one at the center as a function of the cube of the normalized distance. It is mentioned in the section 5.2 that the R dependence is corrected by neutrons after the muon for energy reconstruction process. The energy difference is within $\pm 1\%$ for $R \leq 600$ cm by energy reconstruction.

6.6.2 Vertex distribution

It is mentioned in Appendix A.1 that the lack of the PMT data just after the muon due to the finite recovery time of the front-end electronics affect the vertex distribution. Thus neutrons are selected in the events with $0.8 \leq dT \leq 2$ ms for the vertex distribution check.

The R^3 distribution is shown in Figure 6.25. Accidental backgrounds are subtracted here. Thus,

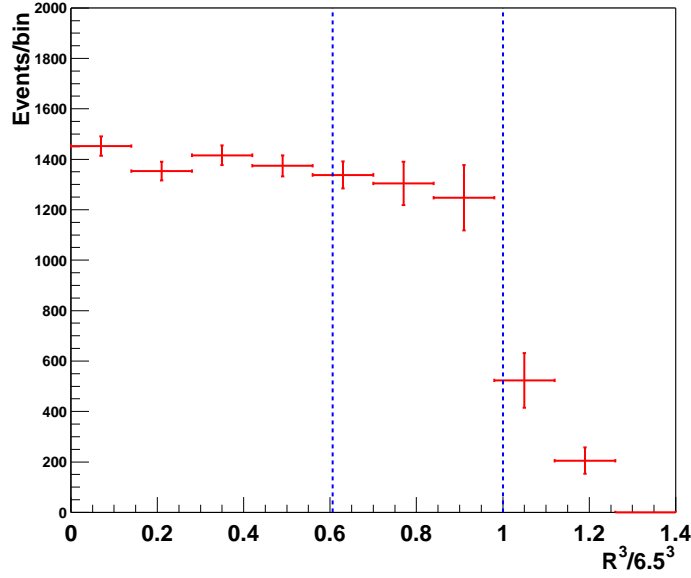


Figure 6.25: R^3 distribution of neutrons after the muon. The dashed line the $R^3/6.5^3=1$ is at balloon edge. The events beyond the balloon edge ($R^3/6.5^3 \geq 1$) reflect the vertex resolution. The dashed line at $R^3/6.5^3=0.6058$ is at the fiducial radius $R=550\text{cm}$ in the present analysis.

the ratio with the same definition as before is given by ;

$$\frac{N(R < 550)}{N(All)} = \frac{6059}{10219} = 0.5933 \pm 0.0096 \quad (6.12)$$

which is compared to the detector volume ratio given by $V(R < 550)/V(All) = 0.6058$. The difference of the double ratio from unity is ;

$$\frac{N(R < 550)/N(All)}{V(R < 550)/V(All)} - 1 = (-2.06 \pm 1.59)\% \quad (6.13)$$

The error is estimated from the statistical errors in neutron events and subtracted background events. Thus the error of total events in the fiducial volume is estimated as 3.65% by taking the linear sum of the two numbers.

6.6.3 Neutron capture time

The neutron capture time is also estimated by using the neutrons after the muon. The time distribution of the neutrons is fitted to an exponential + a constant function in the time from $100 \mu\text{s}$ to 4 ms after the muons. The early time range less than $100 \mu\text{s}$ is avoided in the fit to reject other interactions than neutron capture events. The estimated neutron capture time is about $213 \mu\text{s}$. This result is consistent with the one obtained in the Am/Be source run.

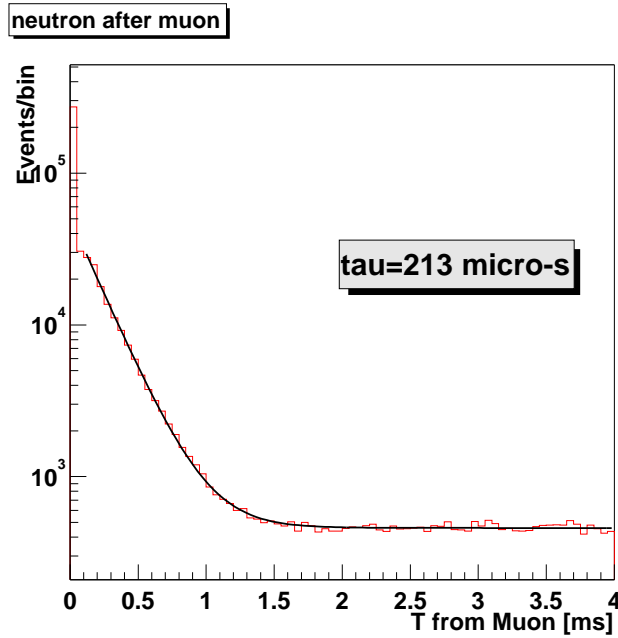


Figure 6.26: Time distribution of the neutrons after the muon. The fitting function (exponential + constant) region is from $100\mu\text{s}$ to 4 ms.

6.7 Neutrons captured by carbon

The neutron after the muon are mostly captured by a proton in a hydrogen with a probability of about 99.5 %. But of 0.5 % neutrons are captured by ^{12}C and 4.947 MeV γ -ray ($n + ^{12}\text{C} \rightarrow ^{13}\text{C} + 4.947\text{MeV}\gamma$) is emitted. This can be used as a good calibration source. Figure 6.27 shows the energy spectrum of the emitted γ from neutrons captured by ^{12}C . The peak position is reconstructed to be 5.133 MeV as visible energy. The ratio of the visible energy to the actual energy is then 1.04 and there is 4 % energy deviation at 5 MeV. This energy non-linearity is discussed in the section 6.4.3.

6.8 Spallation events

The spallation events after the muon is discussed in Appendix A.2.2. The dominated isotope is ^{12}B with a short decay time ($T_{1/2}=20.2\text{ms}$) after the muon. Thus the events of ^{12}B are used as calibration events for the energy scale and the vertex distribution.

6.8.1 Energy distribution

Figure 6.28 shows the energy distribution for the spallation events. The decay time range is from 2 ms to 60 ms and the background is subtracted. The solid curves are expected energy spectrum in β decays of ^{12}B and ^{12}N . The ratio of ^{12}N is fixed to 2 % in this figure. Although

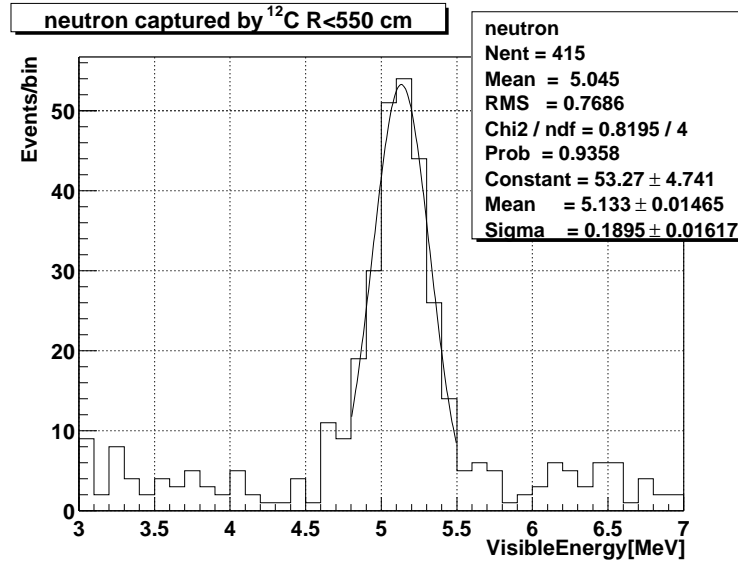


Figure 6.27: 4.947MeV γ energy spectrum which comes from the muon induced neutron captured by carbon.

the long lifetime isotopes may contaminate this time range, the effect is very small. Thus only two isotopes ^{12}B and ^{12}N are considered here.

The energy scale is estimated by 2 parameters which are mean energy scale and the production ratio of ^{12}N to ^{12}B . The χ^2 function is used :

$$\chi^2 = \sum_i \left[2(N_i^{th} - N_i^{obs}) + 2N_i^{obs} \log(N_i^{obs}/N_i^{th}) \right] \quad (6.14)$$

for 0.4MeV bin where N_i^{th} and N_i^{obs} are the expected and observed rates in the i th bin, respectively.

The energy scale calibration are divided two region. One is whole spallation energy region from 4 MeV to ~ 14 MeV (7.25 MeV mean) and the other is near the endpoint of the spectrum larger than 12 MeV. Figure 6.29 shows the χ^2 distribution for the energy scale difference and the ratio of ^{12}N . At the low energy region $E \geq 4$ MeV, the energy scale difference is $-1 \pm 1\%$. At the high energy region $E \geq 12$ MeV, the energy scale difference is $-0.8 \pm 1.2\%$. Thus the energy scale error for $4 \leq E \leq 14$ MeV is estimated to 2 %.

6.8.2 Vertex distribution

The R^3 distribution of the spallation events are shown in Figure 6.30. The spallation time window is $2 \leq dt \leq 60$ ms that is ^{12}B region. The accidental backgrounds are subtracted here.

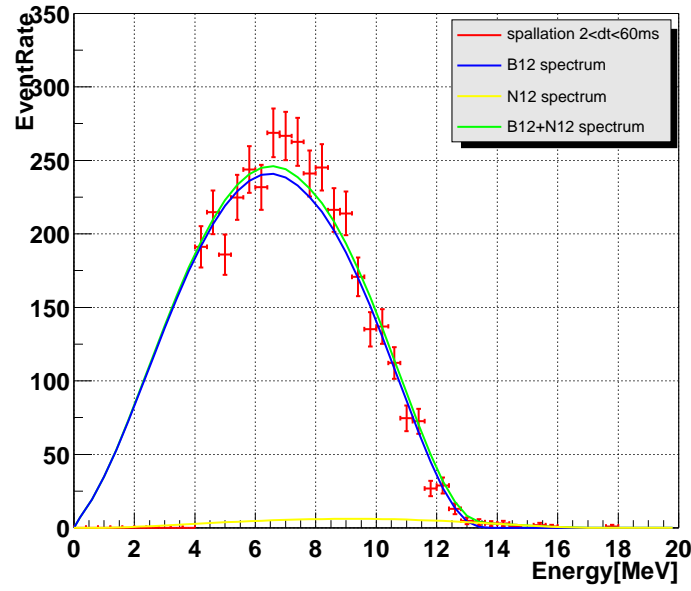


Figure 6.28: Spallation from ^{12}B and ^{12}N spectrum. The ratio of ^{12}N is fixed to 2 % in this figure.

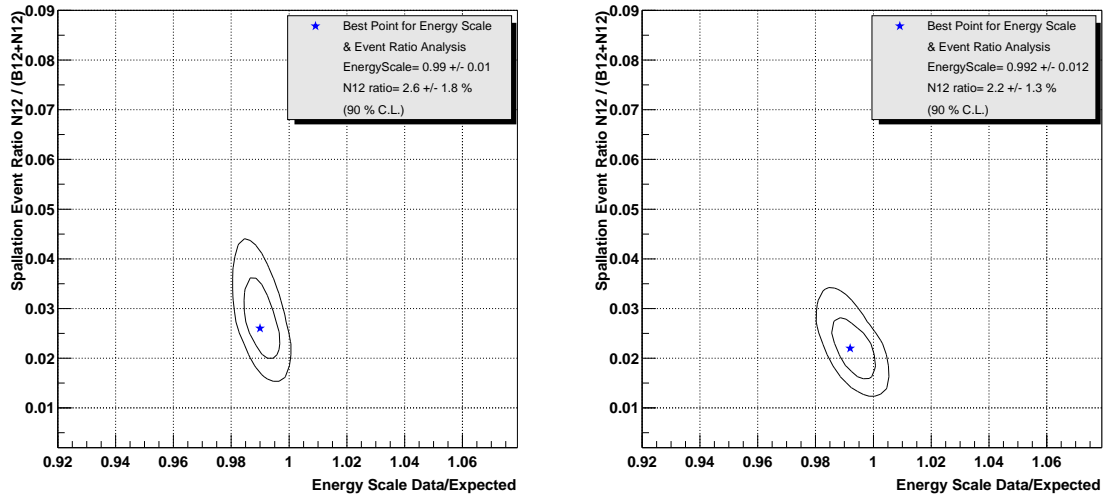
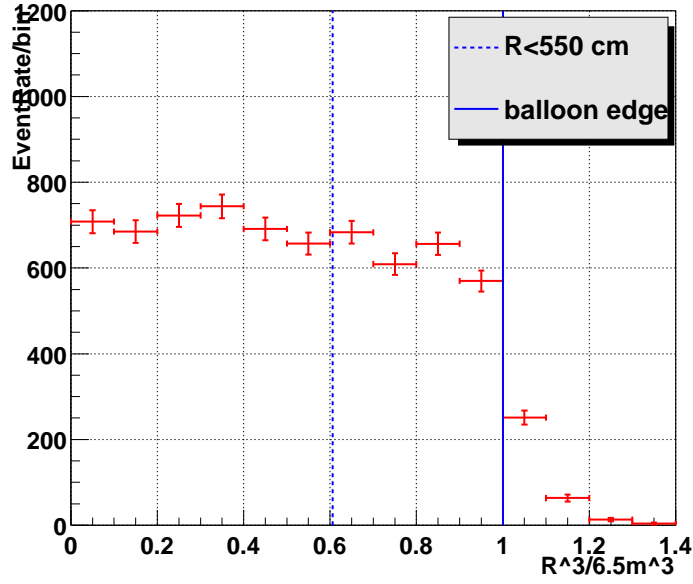


Figure 6.29: The χ^2 distribution about energy scale and ^{12}N ratio. The left figure is $E \geq 4\text{MeV}$ (7.25MeV mean) and the right figure is $E \geq 12\text{MeV}$ (nearly endpoint).

Figure 6.30: ${}^3\text{R}$ distribution spallation ${}^{12}\text{B}$ and ${}^{12}\text{N}$

The ratio of number of events in the fiducial ($R \leq 550\text{cm}$) to the whole volume is given by ;

$$\frac{N(R < 550)}{N(R(All))} = \frac{4246.49}{7058.22} = 0.6016 \quad (6.15)$$

The error are the statical error of event rate and the energy threshold error at 4 MeV energy cut. The statical error is smaller than neutron R^3 distribution's one (see section 6.6.2) because the accidental background rate is very small. The energy threshold error is estimated by calculated ${}^{12}\text{B}$ spectrum. At Figure 6.24, the detector radius dependence of energy scale error at 2.2 MeV are 0.25 % for $R < 550\text{ cm}$ and 2 % for $R < 650\text{ cm}$. Now these error are adopted to 4 MeV energy threshold of spallation events. The error of spallation event rate are estimated as $\pm 0.13\%$ for $R < 550\text{ cm}$ and $\pm 1\%$ for $R < 650\text{ cm}$. Thus the difference of the number of spallation events results in ;

$$\frac{N(R < 550)/N(All)}{V(R < 550)/V(All)} - 1 = -0.69 \pm 1.95\% \quad (6.16)$$

Thus the systematic error of the fiducial volume is estimated as 2.64 % by taking the linear sum of the two numbers.

Chapter 7

Data Reduction

This chapter describes the data reduction procedures to select $\bar{\nu}_e$ candidates. KamLAND experiment started on Jan.22, 2002. Data sample corresponding to the ~ 9 month runs from March 2002 to November 2002 is analysed. The bad runs selection is explained in section 7.1. The selection of the low energy events and fiducial volume cut are explained in section 7.2 and 7.3. Also the delayed coincidence in section 7.4, the spallation cut in section 7.5 are described.

7.1 Bad runs selection

First step of the reduction is to examine the 'bad run'. The data taking of KamLAND experiment is basically done from AM 9:00 to AM 9:00 of the next day for the normal run. When there are some operation of the check or calibration, the normal data taking is stopped.

If there are problems for some data quality in the analysis step, the run is judged as the bad run and rejected from the physics analysis.

The bad run is defined if the data has at least one of the following criteria ;

- number of badchannel are too much (> 20) or exceeds board unit in ID or OD
- gain stability of the PMTs are too bad compared with the adjacent runs.
- abnormal muon rate ($\sim 0.3\text{Hz}$ normaly) or charge
- abnormal trigger rate
- too many noise event
- electronics deadtime is too high
- abnormal T_{offset}
- OD inefficiency is too high
- too short runtime
- mentioned as abnormal runs specifcly by the shift member

If the bad run criteria happened during the run, the data in the period of the bad status is rejected. Figure 7.1 shows the integrated time of the good-run data and the bad-run data. The bad-run gathered in March '02 because of electronics problems remained in the starting stage of the experiment. The data taking has been running well since April. Finally, the total good run time used for the analysis is 209.7 days.

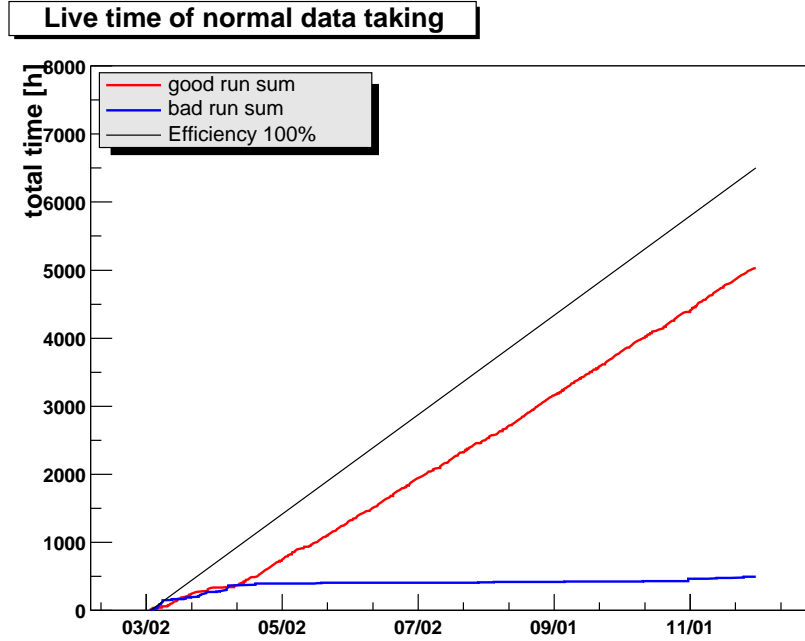


Figure 7.1: Running time of the normal data taking. The black line corresponds to the ideal running time with 100% efficiency. The red line shows the good-run time which is used to physics analysis. The blue line shows the bad-run time which is excluded from the physics analysis. The ratio of the bad run time is about 5% for all the running time. The calibration runs and the test runs are not included in the calculation of the good-run and the bad-run.

7.2 Selection of low energy events

This step of reduction is to select low energy events from the normal good runs. The rejected events are the cosmic ray muon events, flasher tube events, noise events, and so on.

7.2.1 Rejection of muon events

Figure 7.2 shows the total charge distribution of the inner detector in a logarithmic scale. The two clear peaks in $Q \geq 10^4 \text{p.e.}$ in Figure 7.2 are the events where muons pass through the liquid scintillator and the buffer oil layer, mentioned in section 5.3. Muon events is identified with either of the following conditions;

- total charge in the ID $Q_{ID} \geq 10^4$ p.e.
or
- $Q_{ID} \geq 500$ p.e. and $OD \geq 5$

These criteria cover the muon events sufficiently, and the inefficiency to drop the electron anti-neutrino events is negligible.

Some low energy events (not muon events) exceed to $Q_{ID} \geq 10^4$. These are noise events. These events are rejected at noise event cut process and muon 2 ms cut process.

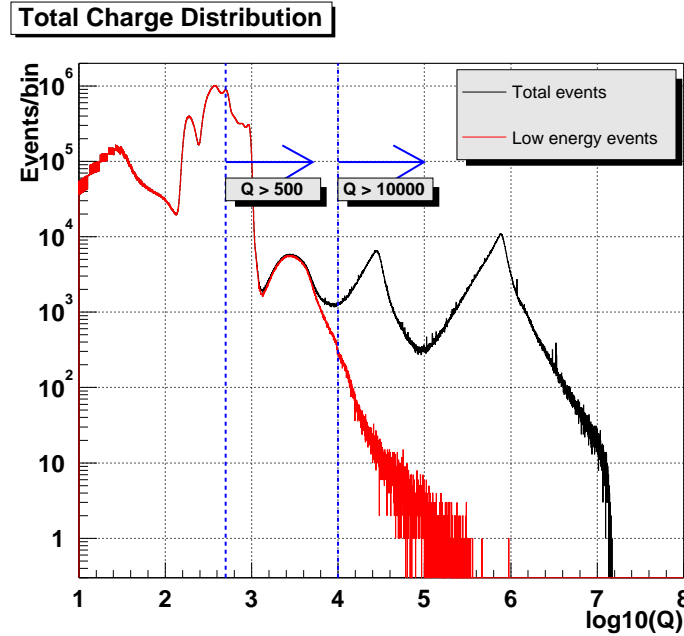


Figure 7.2: The total charge distribution of the inner detector. The black line is charge distribution of all events and the red line is only low energy events (not muon events). The exceed of the total charge ≥ 10000 as low energy is the noise events which are not selected as muon. These events are rejected in the next reduction step.

7.2.2 Rejection of noise events

In the electronics system used in KamLAND, electronics noise sometimes happens. Source of the noise are the PMT flashing, electronics noise from fluorescent light in the electronics hut, the finite recovery time of the electronics after the energetic events such as muon and so on. Figure 7.3 shows an example of the event display of the noise event. Also the time distribution of the noise event and normal good event is shown in Figure 7.4. The definition of noise events is ;

$$N_{100ns} \leq \frac{N_{hit} + 50}{2} \quad (7.1)$$

where N_{hit} is the number of hit PMTs in the events and N_{100ns} is the maximum number of the hit PMTs within 100 ns. Eq 7.1 means that the generated timing doesn't have clear distribution. Figure 7.5 shows the N_{100ns} vs. N_{hit} . The line shows the Eq. 7.1. The noise events are clearly seen as the separated clusters.

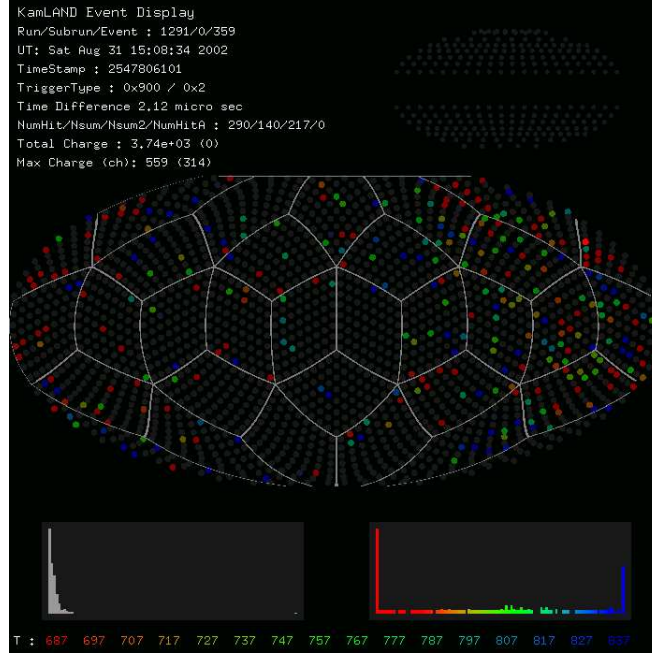


Figure 7.3: The event display of the typical noise event. There are no clear waveform at the timing distribution display (the lower right side).

7.2.3 Flasher event cut

The flasher events are caused by the light emission from a PMT due to electrical discharge. Figure 7.6 shows the example of the flasher event. The flasher event occurs about 0.1 % and the problematic PMTs are almost the same one and the number of the PMTs is about 20. When a PMT starts flashing, it often generates a big pulse and the neighbouring PMTs also have signals. The flasher event criterion is ;

- total charge in the ID $Q_{ID} \geq 2500$ p.e. and $Q_{max}/Q_{ID} \geq 0.6$

where Q_{max} is the maximum charge of one PMT. Figure 7.7 shows the total charge and maximum charge distribution for one run. The flasher events are rejected by the criteria.

7.2.4 Muon 2ms cut

The events after the muon have many neutrons, as described in Appendix A.1. Also, sometimes decay of muons happen in the detector. So the all events within 2 ms which cover the neutron

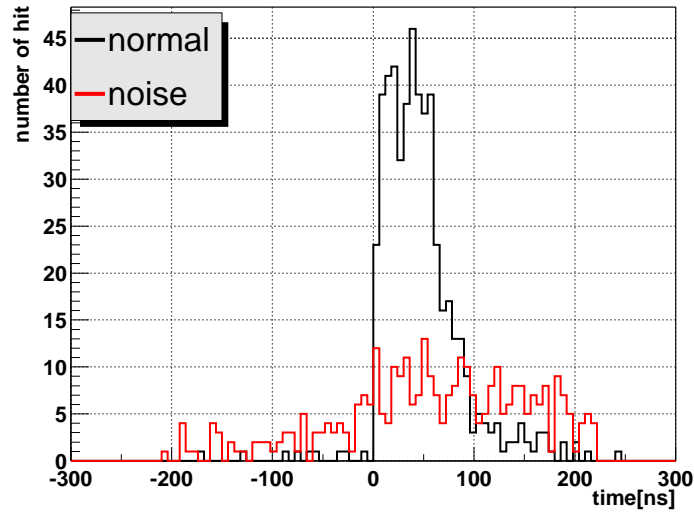


Figure 7.4: The time distribution of the typical low energy event and the noise event.

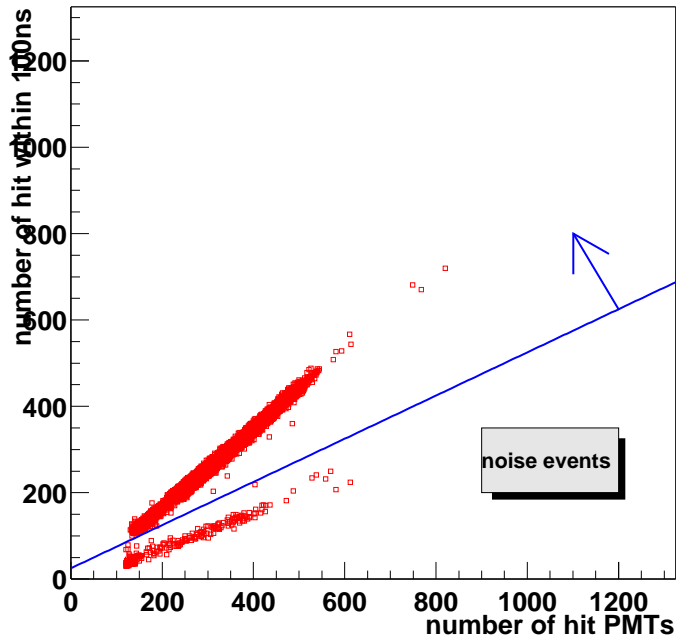


Figure 7.5: The N_{100ns} vs. N_{hit} . The noise criteria given by Eq. 7.1 is shown by the blue line.

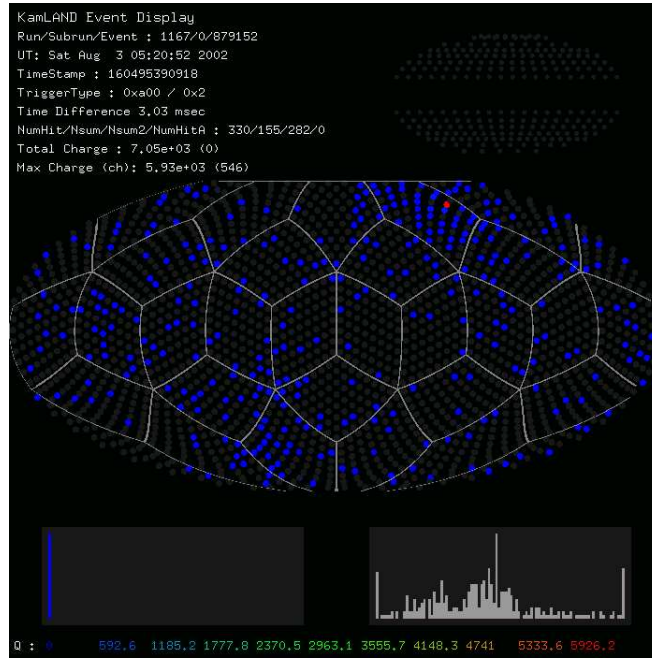


Figure 7.6: The event display of the typical flasher event

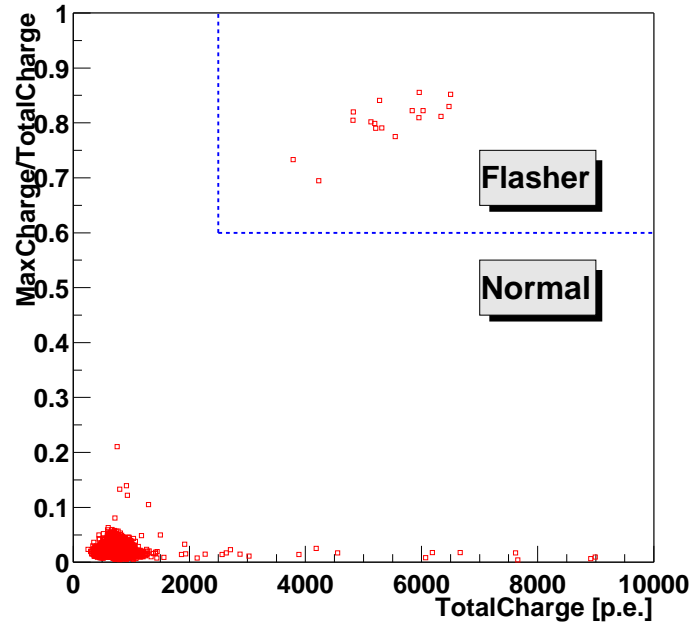


Figure 7.7: The flasher event charge distribution for one run.

capture time and muon lifetime sufficiently after the muon is rejected.

7.2.5 summary

Figure 7.8 shows the energy distribution of the low energy data in the reduction process. The number of events before the low energy event selection (all events) is 551323331. After the reduction process (noise cut and muon 2ms cut), it is reduced to 401073660, about 73% of the initial data sample before the reduction.

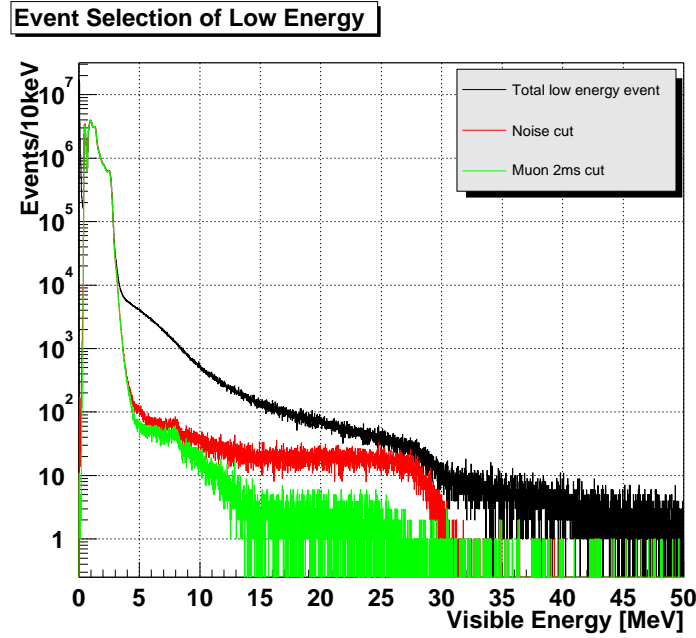


Figure 7.8: The energy spectrum of low energy events in each reduction process

7.3 Fiducial cut

This step is to select events within the fiducial volume. Figure 7.9 shows the energy spectrum for various fiducial cuts. The events are successively reduced by the factor of around 10 between 1 and 3 MeV per fiducial cut process. A peak of around 1.5 MeV is potassium (^{40}K) and 2.5 MeV peak is due to the γ from thallium (^{208}Tl) at the balloon ropes. The broad energy spectrum at larger than 5 MeV are dominantly caused by spallation events after the muon.

Figure 7.10 shows the R distribution divided by the factor R^2 . The events around the balloon edge can be removed by a cut at $R = 550\text{cm}$ sufficiently. The excess peak at $R \sim 0\text{cm}$ is the accidental background events from a thermometer, the suspending wire along the vertical axis of the detector and the missing muon.

Figure 7.11 shows the vertex distribution of low energy events in several energy region. The events with $E \leq 1\text{MeV}$ are dominated by ^{210}Pb and ^{85}Kr which distributes uniformly. The events

with $E \geq 1\text{MeV}$ are mainly from the potassium and thallium decays from suspending ropes at the balloon surface which still remains in $R \leq 550\text{cm}$ region.

In the energy region of $2 \leq E \leq 3\text{MeV}$ shown in Figure 7.12, there is a cluster of the events due to the thallium decay in the thermometer at the detector center. But the effect of these events are neglected in the solar anti-neutrino analysis. And for the high energy region $E \geq 4\text{MeV}$ in the Figure 7.13, the missing muon events are distributed. One cluster exists at chimney region and other events generate outside of the balloon at $Z \sim 0\text{cm}$. The events in these two regions are can not be detected by OD. But missing muon events are distributed in $R \geq 550\text{cm}$ region.

Thus the fiducial volume is determined on $R \leq 550\text{cm}$.

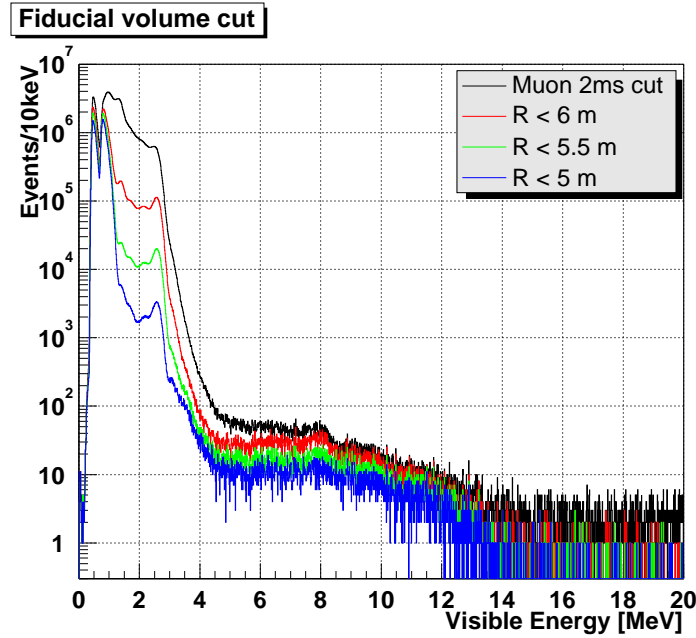


Figure 7.9: The energy spectrum in the various fiducial cuts. The four lines show the spectra without the cut and with cut at $R=6, 5.5$ and 5m .

7.4 Selection of the delayed coincidence events

In this section, the reduction process to get the delayed coincidence events is described. In a first step, the loose selection is made with the following criteria :

- $E_{\text{delayed}} \geq 1\text{ MeV}$
- $0.5\mu\text{s} \leq dt \leq 2.5\text{ms}$
- $dL \leq 200\text{ cm}$

where dt is the time difference between the prompt and the delayed events, dL is the distance between the prompt and the delayed events. The tighter cut is described below.

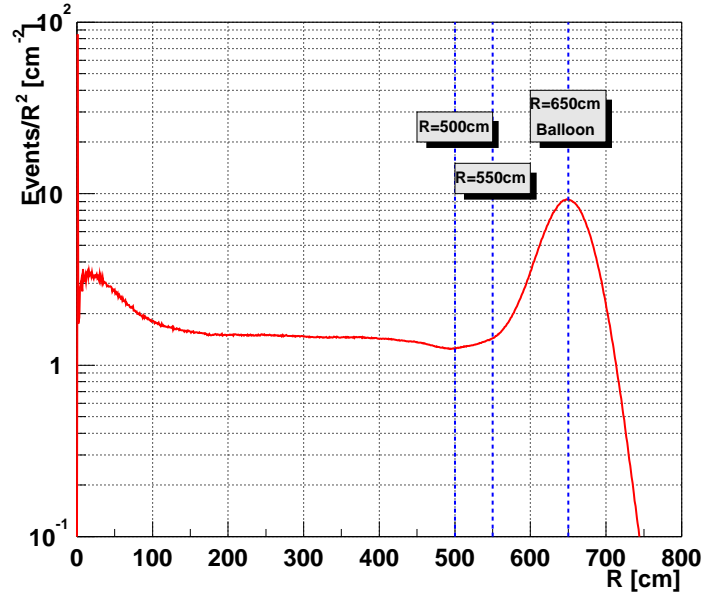


Figure 7.10: The R distribution of low energy events divided by a factor R^2 .

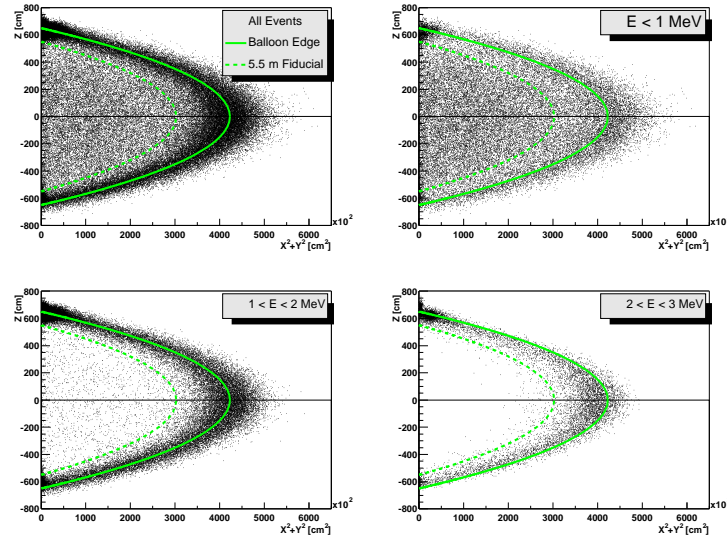


Figure 7.11: The vertex distribution of the low energy events (1). The energy region is all, $E \leq 1 \text{ MeV}$, $1 \leq E \leq 2 \text{ MeV}$ and $2 \leq E \leq 3 \text{ MeV}$. The line is at balloon edge and the dash line is at $R=550 \text{ cm}$.

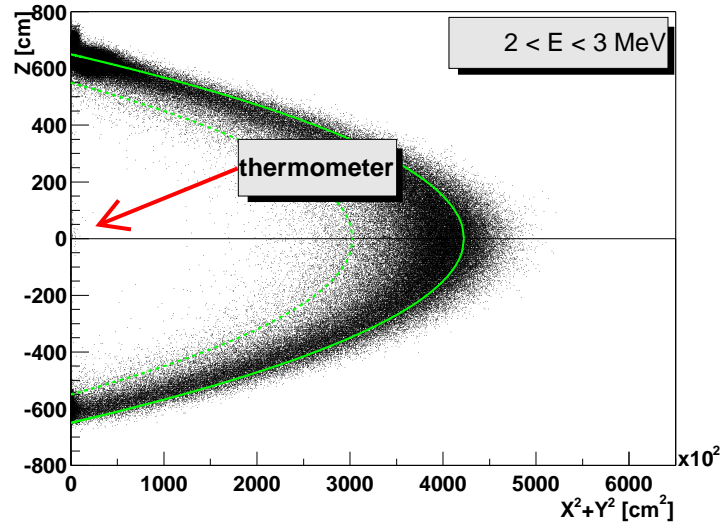


Figure 7.12: The vertex distribution of the low energy events (2). The energy region is $2 \leq E \leq 3 \text{ MeV}$. The events are accumulated more than the event sample in Figure 7.12.

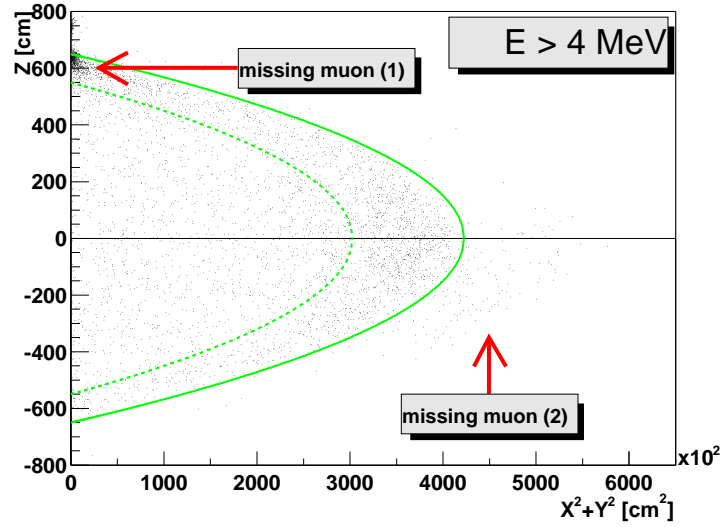


Figure 7.13: The vertex distribution of the low energy events (3). The energy region is $E \geq 4 \text{ MeV}$.

7.4.1 dt and dL cut

The capture time of the neutron is estimated to be $207 \mu s$ by Am/Be calibration and $212 \mu s$ by neutrons after the muon events described at section 6.5 and 6.6.3. These results are consistent with each other.

The reduction criterion for dt is set as :

- $0.5 \leq dt \leq 660 \mu s$

The efficiency of the neutron is about 95%.

dL distribution is estimated by Geant4 simulation as shown in Figure 7.14. The detection efficiency is estimated as 98.8% for $dL \leq 160 cm$ and 99.7% for $dL \leq 200 cm$. The selection criterion for dL is :

- $dL \leq 160 cm$

Figure 7.15 shows the 2-dimensional plot of dt and the energy of the delayed events. Figure 7.16 shows the plot of dL and the energy of the delayed events. Events around 2.2 MeV neutron capture are clearly seen. Figure 7.17 and Figure 7.18 show the energy spectrum of prompt events and delayed events before and after the selection. The rejected events are mostly accidental backgrounds around 1 MeV.

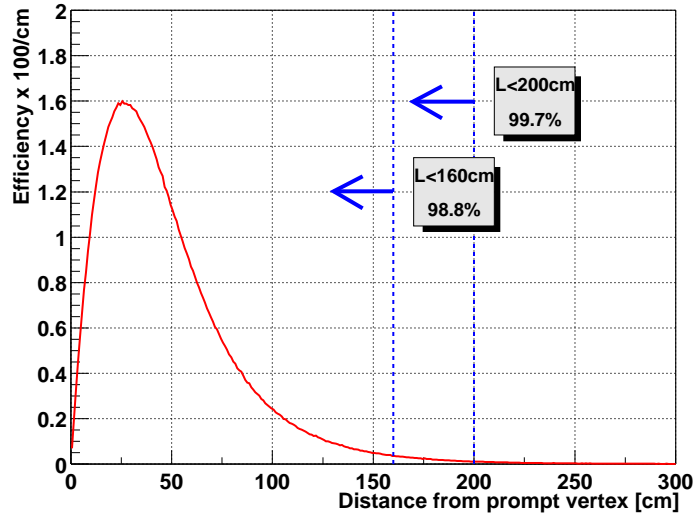
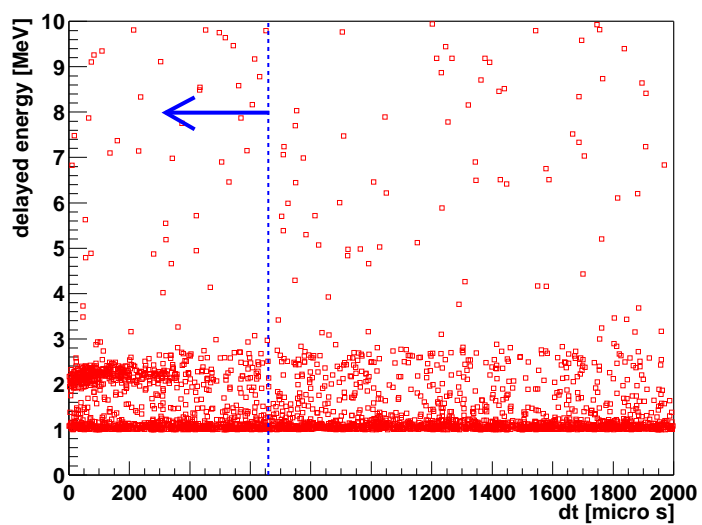
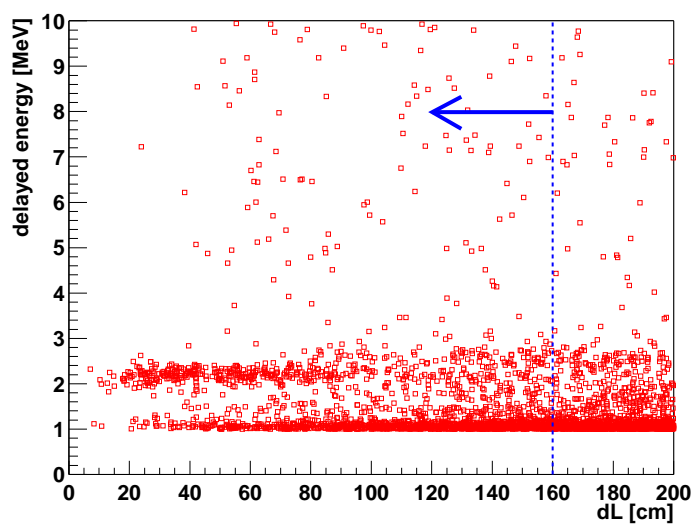


Figure 7.14: The neutron dL distribution by Geant4 simulation. The mean diffusion length is about 25cm.

7.4.2 Energy cut

At the energy distribution of prompt vs. delayed events (Figure 7.19), the accidental background mostly gathers at low energy. So further criteria for prompt and delayed energies are applied :

Figure 7.15: The dt vs. delayed energy distribution.Figure 7.16: The dL vs. delayed energy distribution

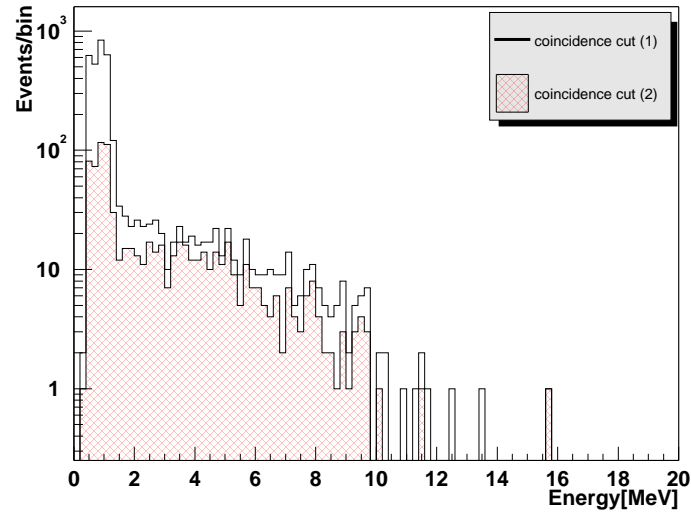


Figure 7.17: The prompt energy distribution before and after the cut on dt and dL. 'coincidence(1)' means loose coincidence and 'coincidence(2)' is after the cuts.

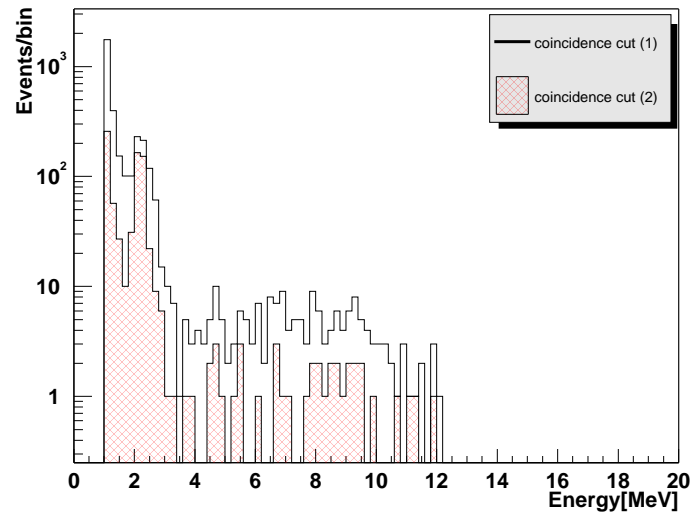


Figure 7.18: The delayed energy distribution before and after the cut on dt and dL. 'coincidence(1)' means loose coincidence and 'coincidence(2)' is after the cuts on dt and dL. The peak around 2.2MeV is delayed events of neutron capture.

- $E_{prompt} \geq 0.9\text{MeV}$
- $1.8 \leq E_{delayed} \leq 2.6\text{MeV}$

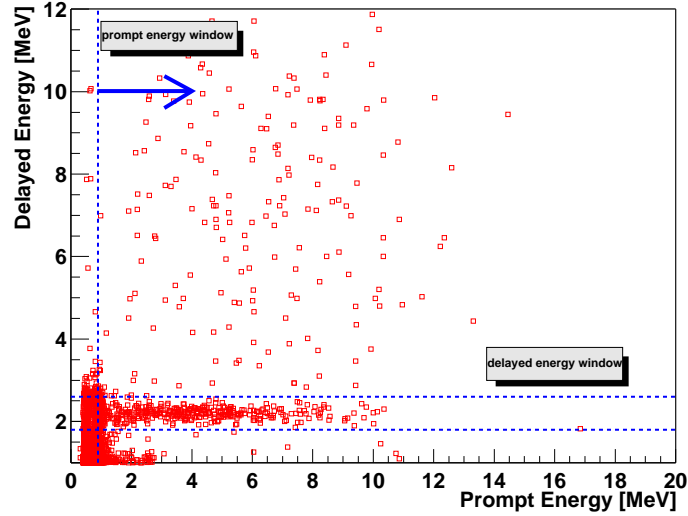


Figure 7.19: The energy distribution for prompt and delayed energies(1). The blue dash lines are energy cut criteria. The events distributed at $E_{prompt} > 0.9\text{MeV}$ and $E_{delayed} > 2.6\text{MeV}$ are the accidental backgrounds after the muon events which are rejected in the next reduction process.

7.5 Spallation event cut

The major part of the remaining events after the delayed coincidence cut are the spallation events. The explanation of the spallation events is given in Appendix A.2.2. Especially serious events are ^9Li and ^8He events whose decay generate β -n delayed coincidence to mimic the signal of electron anti-neutrinos.

Fortunately, the spallation events are correlated with muons. The life time of ^9Li and ^8He are 256.8 ms and 173 ms. If a veto of 2 sec is applied after the muon, they are expected to be rejected to less than 0.1%.

The spallation events are correlated with $dQ (=Q_{ID} - Q_{track})$, as described in Appendix A.2.2. The criteria to eliminate the spallation events are as follows :

- if $dQ \geq 10^6$ p.e., veto all the volume in 2sec after the muon.
- if $dQ < 10^6$ p.e., veto the region within 3m from the muon track in 2sec after muon.

The events after electronics dead time could be the spallation events if the muon events are lost in the period of the dead time. Also some muon events are difficult to evaluate the muon track length (so-called 'mis-reconstructed muon'). So the additional veto is applied :

- veto all the volume in 2sec after the electronics dead time.
- veto all the volume in 2sec after mis-reconstructed muon event.

Figure 7.20 shows the energy spectrum of the prompt events before and after removing the spallation events.

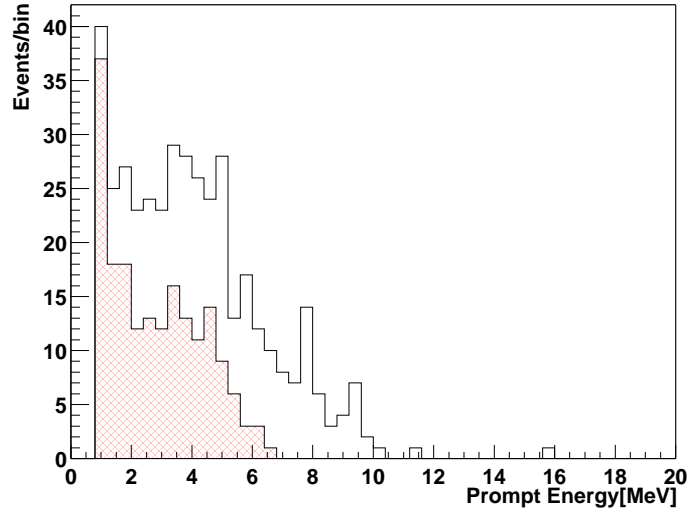


Figure 7.20: The prompt energy spectrum before and after the spallation cut process. The event around 16MeV is found to be a fast neutron and the event around 11MeV is ${}^9\text{Li}/{}^8\text{He}$ delayed coincidence. they are rejected both by 2 sec cut after the muon.

7.6 Final samples

In the previous section, the delayed coincidence events are selected with a cut on the spallation events. Figure 7.21 shows the vertex distribution for prompt and delayed events remained in the fiducial volume. The vertex distribution looks like uniform. Also Figure 7.22 shows the scatter plots of energy vs. dt and dL of prompt and delayed events which have good correlation.

The final reduction step is to make a prompt energy cut. Figure 7.23 shows distribution of prompt energy vs. delayed energy. There is a cluster of events with delayed energies around 2.2 MeV. One event, $(E_{prompt}, E_{delayed}) = (3.1\text{MeV}, 4.7\text{MeV})$ is considered to be a neutron captured by carbon. The remained events at $0.9 \leq E_{prompt} \leq 7$ MeV are mainly reactor anti-neutrino spectrum. The criterion for solar anti-neutrino events is set as :

- $7.5 \leq E_{prompt} \leq 14$ MeV

as the final condition. No events are remained after the cut. The limit of the solar anti-neutrino flux is estimated in the next chapter.

Table 7.1 shows a summary of the number of selected events in each step of the criteria.

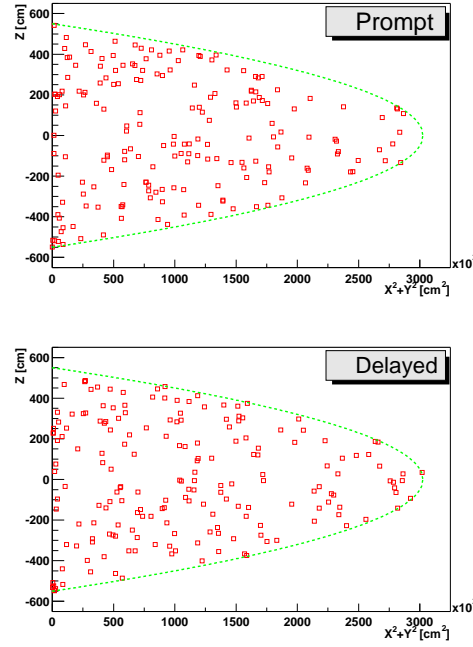


Figure 7.21: The vertex distribution for prompt and delayed events with $E_{prompt} \geq 0.9 \text{ MeV}$ and $1.8 \leq E_{delayed} \leq 2.6 \text{ MeV}$.

	Reduction step	Real Data
low energy events selection	all events	551323331
	muon cut	545103776
	noise cut	403365557
	muon 2ms cut	401073660
fiducial cut	$R \leq 6\text{m}$	111433077
	$R \leq 5.5\text{m}$	76148638
delayed coincidence(1)	$1 \leq E_{delayed}$, $0.5\mu\text{s} \leq dt \leq 2.5 \text{ ms}$, $dL \leq 200 \text{ cm}$	3420
delayed coincidence(2)	$0.5\mu\text{s} \leq dt \leq 660 \mu\text{s}$, $dL \leq 160 \text{ cm}$	791
energy cut	$E_{prompt} \geq 0.9 \text{ MeV}$ $1.8 \leq E_{delayed} \leq 2.6 \text{ MeV}$	357
spallation cut	dead time cut	329
	mis-reconstructed muon cut	295
	spallation event cut	178
final reduction	$7.5 \leq E_{prompt} \leq 14 \text{ MeV}$	0

Table 7.1: The summary of event reduction in each step of the selection.

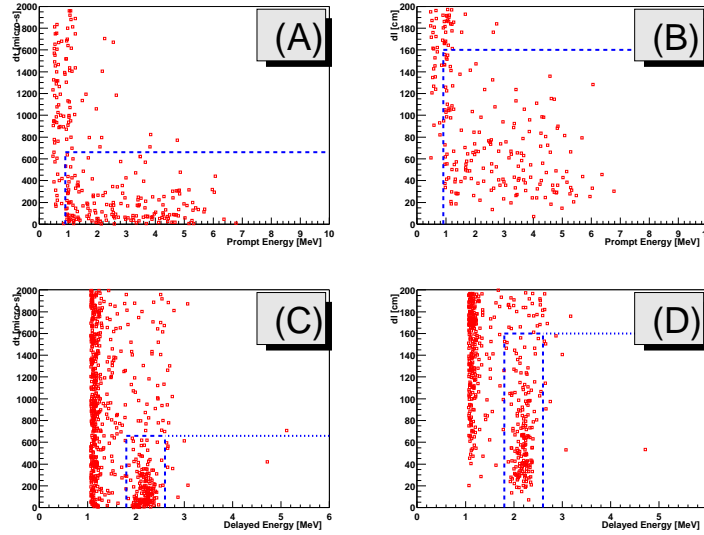


Figure 7.22: The correlation of the prompt and delayed events. (A):prompt energy vs. dt (B):prompt energy vs. dL (C):delayed energy vs. dt (D):delayed energy vs. dL . The event selection criteria are all included except for the variables shown in the plot.

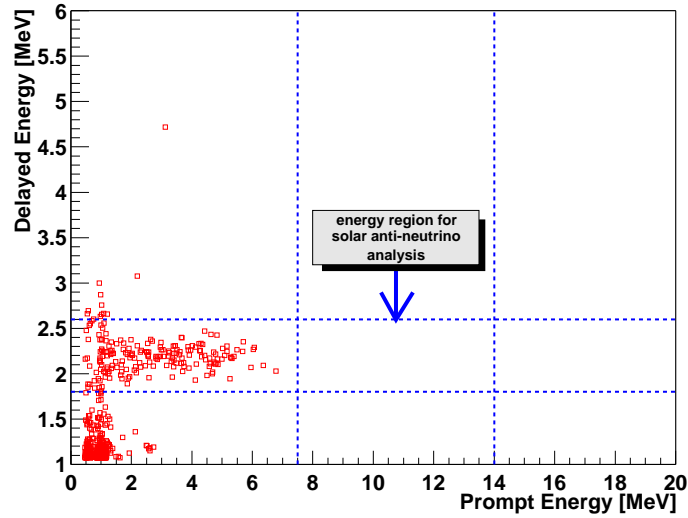


Figure 7.23: The scatter plot of E_{prompt} vs. $E_{delayed}$ before the final selection by imposing the energy cuts. There is no event in the energy region $7.5 \leq E_{prompt} \leq 14$ MeV and $1.8 \leq E_{delayed} \leq 2.6$ MeV made by the final cuts.

Chapter 8

Analysis

In this chapter, the limit of the solar anti-neutrino flux is obtained by using the Poisson distribution.

For the limit calculation, the livetime and the detection efficiency are needed. The livetime means the effective volume and time of the detector by considering the dead volume and dead time introduced by the veto in the analysis. The items to be considered in the detection efficiency are space correlation, time difference correlation in the delayed coincidence, trigger efficiency, charge efficiency, delayed energy efficiency and the neutron capture efficiency.

Also the systematic errors and background are obtained. Finally, the limit of the solar $\bar{\nu}_e$ flux is estimated. These items are mentioned in detail in this chapter.

8.1 Livetime calculation

The total running time of the physics run is estimated as 209.67 days as described in the section 7. The dead time estimation criteria are overlapped with the spallation cut and the 2 ms after the muon.

- all the volume of the detector is vetoed in either of the following conditions :
 - 2 ms after all the muon
 - 2 sec after the electronics dead time
 - 2 sec after the mis-reconstructed muon event
 - 2 sec after the energetic muon with $dQ \geq 10^6$ p.e.
- partial volume (within a cylindrical region of 3m in radius along the muon track) is vetoed in :
 - 2 sec after the muon with $dQ < 10^6$ p.e.

Figure 8.1 shows the cylindrical dead volume along the muon track as a function of the distance between the track and the detector center. The dead volume is maximum of about 275 m^3 when the muon passes the detector center. The dead time criteria sometimes have the timing overlap

with each other. The dead time of all volume veto criteria are preceded in the partial one. The dead time is estimated in all the muons and electronics dead time. The deadtime and livetime (runtime-deadtime) is calculated for the 5.5m radius fiducial volume. The total fraction of the livetime in the runtime is 0.885. The estimated livetime is 16030548 second, that is, 185.54 days for the fiducial volume.

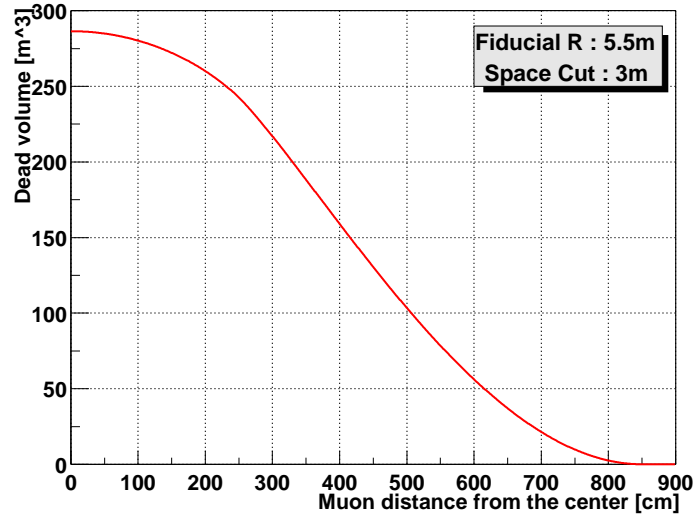


Figure 8.1: The dead volume along the muon track as a function of the distance of the muon track from the detector center.

8.2 Detection efficiency

Space correlation

The anti-neutrino events are correlated events in space and time. Spatially correlated events are selected by requiring that both of the prompt and delayed events are within the fiducial volume ($R \leq 5.5\text{m}$) and the distance (dL) between them is 160cm.

The efficiency of the event selection by the neutron capture length is discussed in section 7, with is about 98.7%.

The detection efficiency due to the finite vertex resolution and the capture length is estimated by a Monte Carlo simulation. Figure 8.2 shows the distribution of the MC generated prompt and delayed events. The vertex resolution is given as 25 cm per axis and the neutron capture length is generated by Geant4. The prompt events are generated in a region $R \leq 550$ cm. As a result, the selection efficiency of the spacial condition is estimated to be 89.77 %.

The systematic error of the efficiency is estimated by the using the result of the neutron capture length obtained by Am/Be source, as described in section 6.5. The above simulation is done by using the Am/Be neutron capture length instead of the Geant4. The total efficiency of the space correlation is estimated to 88.36 %. The systematic error is estimated by the difference of the

two results. Thus the combined efficiency is estimated to be $89.77\% \pm 1.41\%$.

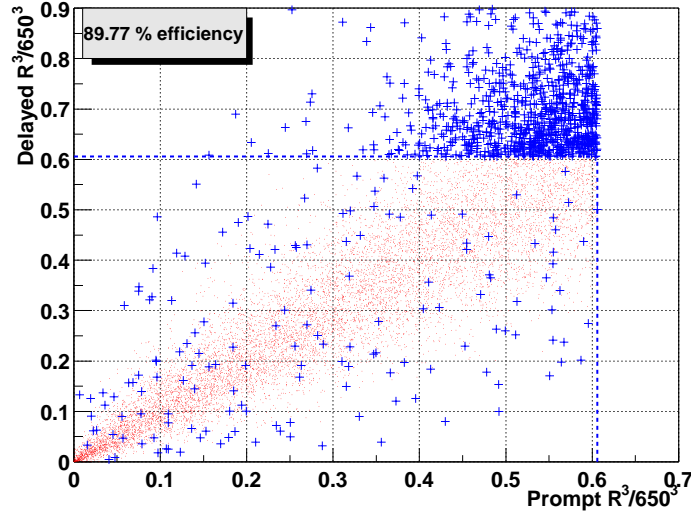


Figure 8.2: Result of the simulation for the distribution of the prompt and delayed events. The red marks are the generated events which pass the neutrino selection criteria $R_{delayed} \leq 550\text{cm}$ and $dL \leq 160\text{cm}$. The blue marks are excluded from the neutrino criteria. The selection efficiency by the spacial cut is estimated to be 89.77%.

Time correlation

Time correlation means the selection efficiency with a cut on the time difference dt between the prompt and delayed events, which is $0.5 \leq dt \leq 660 \mu\text{s}$ as described in subsection 7.4.1. The dt efficiency is defined as :

$$\text{Eff}_{dt} = \frac{1}{\tau} \int_{0.5}^{660} e^{-t/\tau} dt \quad (8.1)$$

where τ is the neutron mean life in the liquid scintillator that is estimated as $207\mu\text{s}$ by Am/Be source data and $212\mu\text{s}$ by spallation neutron data. The efficiency are 95.63% for $207 \mu\text{s}$ lifetime and 95.29% for $212 \mu\text{s}$ lifetime. Now the spallation neutron data is used as the time correlation efficiency because the spallation neutrons are distributed in the whole detector. The systematic error is estimated by the difference of the two efficiency results. Thus the total dt efficiency is $95.29\% \pm 0.34\%$.

Trigger efficiency and charge efficiency

The trigger efficiency is discussed in section 5.4. The efficiency for the prompt events with an energy larger than 1 MeV is almost 100%. The threshold energy for the prompt events is decided to 7.5 MeV for solar anti-neutrino analysis and the trigger efficiency is estimated to be 100 %. The detail of the charge efficiency is discussed in section 5.5 and the estimated efficiency for the events in the region $7.5 \leq E \leq 14 \text{ MeV}$ is 100 %.

isotope	natural abundance[%]	$\sigma_{capture}$ [barn]	number [/kton]	fraction [%]	energy [MeV]
^1H	99.985	0.332	8.469×10^{31}	99.45	<u>2.22457</u>
^2H	0.015	0.0105	1.271×10^{28}	2×10^{-7}	6.2547
^{12}C	98.893	0.0034	4.225×10^{31}	0.55	4.9463
^{13}C	1.107	0.0009	4.732×10^{29}	2×10^{-5}	8.1762
^{14}N	99.634	0.0750	2.593×10^{28}	9×10^{-5}	10.8348
^{16}O	99.759	0.000178	6.047×10^{25}	5×10^{-9}	4.1425

Table 8.1: The neutron capture fraction and emitted energy

Efficiency	dR \leq 160cm, R _p \leq 550cm, R _d \leq 550cm with Spallation Cut
Space Correlation	89.77 \pm 1.41 %
Time Correlation	95.29 \pm 0.34 %
Trigger Efficiency	100%
Charge Efficiency	100%
Delayed Energy	98.85 \pm 0.10%
Nuetron capture on proton	99.45%
Total	84.09 \pm 1.36 %

Table 8.2: The summary of detection efficiency

Delayed energy efficiency

The delayed energy efficiency is the fraction of the γ -ray from the neutron capture within the criterion $1.8 \leq E_{delayed} \leq 2.6$ MeV. The efficiency is estimated by including the energy resolution $\Delta E / \sqrt{E} (\text{MeV}) = 7.7\%$, discussed in section 6.4.2 and the energy scale error 2%. The estimated efficiency is 98.85 \pm 0.10%.

Neutron capture on proton

The neutron produced in the liquid scintillator is mostly captured by a free proton. But a small fraction of neutrons are captured by other nuclei and emit the γ -rays of specific energies. The fraction of these capture processes and the emitted γ -ray energies in the liquid scintillator is listed in Table 8.1. In the present analysis, the capture on proton (^1H) is selected. The selection efficiency is thus 99.45%.

Table 8.2 summarizes the detection efficiencies discribed in this section.

8.3 Systematic errors

Systematic errors in the flux estimation are described in this section and summarized in Table 8.3.

Total mass of the liquid scintillator and the fiducial mass ratio

The total quantity of the liquid scintillator in the balloon is $1154.22 \pm 25 \text{ m}^3$. The sum comes from the uncertainty of the flow meter used for measuring the liquid scintillator in the filling stage, and is 2.17%.

The error of the fiducial volume is estimated by a uniform distribution of the neutron captures and ^{12}B decays in the spallation events as described in subsections 6.6.2 and 6.8.2. The ratio of these events in the fiducial volume to the total volume agrees with the geometrically determined fraction of the fiducial volume within 3.65% for the neutron capture events and 2.64% for spallation ^{12}B decays.

Thus the systematic error is taken as 3.65 %. The total systematic uncertainty of the fiducial volume is obtained as the square root of the quadratic sum of the two errors (2.17% and 3.65%) and set as 4.25%.

Uncertainty of the cuts

The uncertainty of the cuts in data reduction process are from space correlation, time correlation and delayed energy efficiency. These three efficiencies and the error are estimated at section 8.2. The total systematic error of the cuts is $1.36\%/0.8409=1.62\%$.

Energy threshold

The error of the energy scale leads to the uncertainty of the energy threshold and estimation of the ^{12}B solar neutrino flux in the analysis region. The energy threshold is set at 7.5 MeV which is close to the peak of the ^8B spectrum.

The error of the energy scale is estimated from the calibration by the radioactive sources and ^{12}B decay spectrum as described in subsections 6.4.3 and 6.8.1. It is estimated to be 2 % in the analysis region, which leads to the uncertainty of the estimation of the ^8B solar neutrino flux to be 4.02%.

Live time

The trigger is sending a special flag periodically per sec, and it is called '1PPS trigger'. To check the calculation of the livetime, the number of 1PPS trigger without deadtime is examined. It is checked by comparing the count of the 1PPS trigger with the estimated livetime. Percentage of the unknown deadtime in all the physics runs is:

$$1 - \frac{N_{pps-trigger}}{t_{runtime} - t_{deadtime}} = 0.0069\% \quad (8.2)$$

This number is counted as the systematic error.

Table 8.3 shows the summary of the systematic error.

systematic Error	dR≤160cm, R _p ≤550cm, R _d ≤550cm with Spallation Cut
mass uncertainly	4.25%
efficiency of cut	1.62%
energy threshold	4.02%
livetime	0.07%
cross section	0.2%
total	6.07%

Table 8.3: Summary of the systematic errors

8.4 Background

Two kinds of backgrounds are considered in the analysis. One is the electron anti-neutrinos from existing neutrino sources and the other is the reaction mimicking the electron anti-neutrino signal. Because the energy threshold is set high (7.5 MeV), the backgrounds from radioactive isotopes with lower energies are rejected. In this section, the remaining background events are summarized.

8.4.1 Reactor anti-neutrino

The essential background events are electron anti-neutrinos from existing power reactors. There are many power reactors scattered around KamLAND and the reactor neutrinos are used for studying the neutrino oscillation in KamLAND. However, these are backgrounds for the solar anti-neutrino analysis and this is the main reason to set the energy threshold in the analysis at 7.5 MeV.

Figure 8.3 shows the energy spectra of the reactor neutrinos and the expected solar anti-neutrinos. The reactor neutrino spectra are shown in the figure for the two case ; one is the LMA neutrino oscillation with best fit parameters to the KamLAND data, and the other one is the non-oscillation case. The solar anti-neutrino spectrum is assumed just for presentation as the 1% of the ^8B neutrinos predicted from the SSM. Note that recent upper limit on the solar $\bar{\nu}_e$ flux for $E_\nu=8\text{-}20\text{MeV}$ region.

The event rate of the reactor anti-neutrinos with energies larger than 7.5MeV threshold is estimated to be 0.21 ± 0.20 events/datasets for the LMA neutrino oscillation case. The error is estimated from the energy scale error of 2%.

8.4.2 Atmospheric neutrino

The atmospheric neutrinos are generated by the following processes:

$$\begin{aligned}
 p(H, He..) + Air &\rightarrow \pi^\pm + X \\
 &\hookrightarrow \mu^\pm + \nu_\mu(\bar{\nu}_\mu) \\
 &\hookrightarrow e^\pm + \nu_e(\bar{\nu}_e) + \bar{\nu}_\mu(\nu_\mu)
 \end{aligned} \tag{8.3}$$

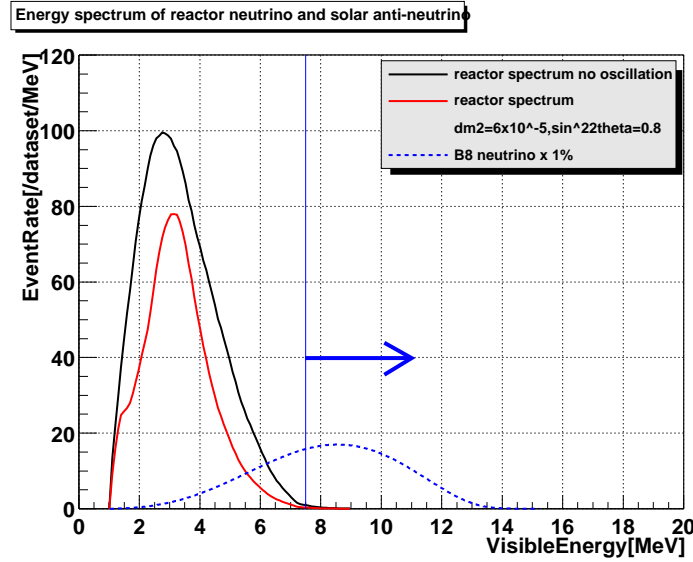


Figure 8.3: Visible energy spectra of reactor anti-neutrino and the solar anti-neutrino as the 1% of the ^8B solar neutrino predicted by the SSM

Thus when μ^- are generated and decay, the electron anti-neutrinos are generated. The atmospheric neutrino flux depends on primary cosmic ray flux, geomagnetism, hadronic interactions and generated particle decays. Some authors have calculated the atmospheric neutrino flux [46, 47, 48] as shown in Figure 8.4. All calculated fluxes are integrated for the whole direction of KamLAND.

BGS flux [46] and HKHM flux [47] are calculated by one-dimensional particle generation in the interaction and decay processes. The difference between BGS and HKHM comes from the simulation code for the hadronic interaction. FLUKA [48] includes the three-dimensional particle generation, but the energy region covered is too high (~ 100 MeV) to be used in the present analysis. We use the BGS flux because the energy threshold is lower than HKHM flux and covers the full energy region of the present analysis ($7.5 \leq E \leq 14$ MeV). The estimated background from the BGS flux is 7×10^{-4} events/dataset.

We must point out that the estimation for the low energy region has a large uncertainty. But it can be said that the estimated background is so small that the contribution by the atmospheric neutrino is negligible.

8.4.3 Spallation

The background events induced by spallation is mainly from $^9\text{Li}/^8\text{He}$ that make the correlation events. It is estimated in section A.2.1, to be 0.58 ± 0.21 events/dataset.

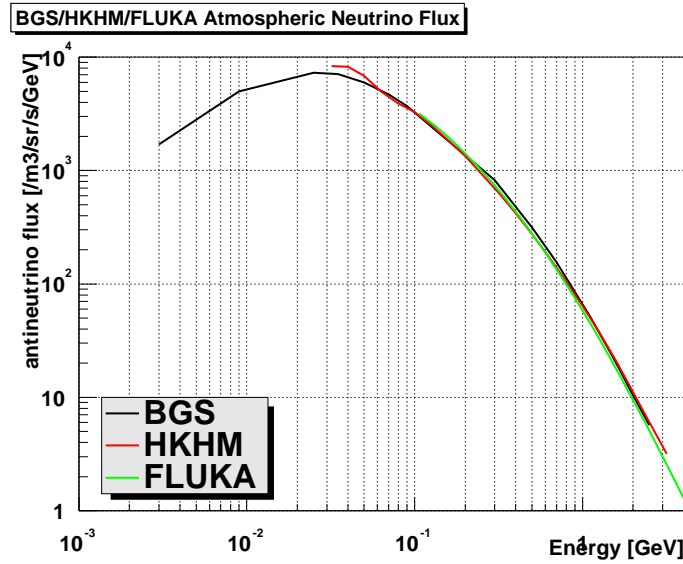


Figure 8.4: Energy distribution of atmospheric neutrino flux calculation for BGS, HKHM and FLUKA. The spectra show $\bar{\nu}_e$ only and the KamLAND location is assumed.

8.4.4 Fast neutron

The fast neutrons are from the muons which interact in the OD water and the rock surrounding the detector and generate neutrons some of which entering the detector (see Figure 8.5). These neutrons are so energetic to kick a proton to mimic the prompt signal and captured to emit a 2.2MeV γ -ray as a delayed signal.

They are rejected by the muon veto of about 2 ms if there is a muon signal in the OD. But there is a finite inefficiency of the muon detection by the OD which is about 8%. Also the muons which pass outside of the OD are not detected. Thus the background from these events are estimated.

The fast neutron events with a muon signal in the OD are collected. The selection criteria for the fast neutron are:

- The number of hit PMT in the OD ≥ 5
- Total charge Q of the ID is ≤ 10000 (about 0 to 30 MeV) for prompt events
- $10 \mu\text{s} \leq dt \leq 660 \mu\text{s}$ and $dL \leq 160 \text{ cm}$ for delayed events
- $7.5 \leq E_{\text{prompt}} \leq 14 \text{ MeV}$ and $1.8 \leq E_{\text{delayed}} \leq 2.6 \text{ MeV}$

The space and time cut is the same as the neutrino event selection. The time cut of $10 \mu\text{s}$ is to remove the decay electron event from the muon with a lifetime of $2.197 \mu\text{s}$.

Figure 8.6 shows the time distribution of the neutron capture events for fast neutron samples. The neutron capture time obtained by a fit is $206 \pm 26 \mu\text{s}$. Figure 8.7 shows the energy spectrum

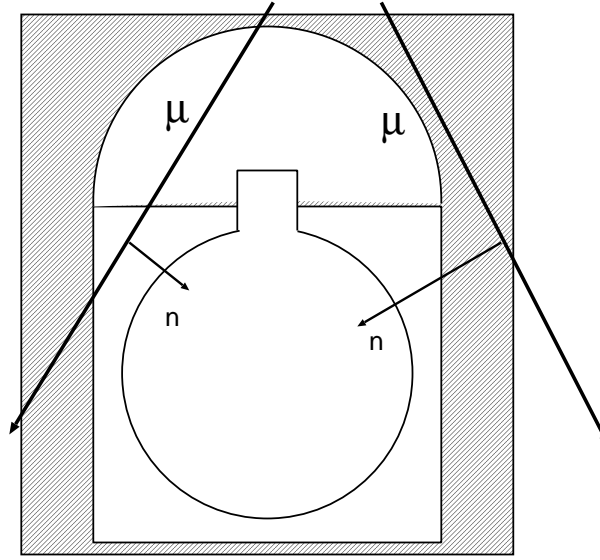


Figure 8.5: An illustration of the fast neutron events

of delayed and prompt events for fast neutron samples. The left picture is delayed events. The peak at 2.14 MeV corresponds to the γ -rays from the neutron capture events. A peak value is a bit lower than the actual capture energy of 2.2 MeV, because these events occur mostly outside the fiducial volume and the energy are decreased. The right picture is for the prompt events. The energy distribution is almost flat and has no clear energy structure.

Figure 8.8 shows the radial distribution of the vertex of the prompt events measured from the detector center. There are four events in the fiducial volume. They are rejected in the neutrino event selection because they are recognized as muon events by the OD counters and occur in the veto of 2ms. This radial distribution is fitted by an exponential function. From the fitted function, total number of events is estimated to be 25 ± 5 events/dataset and decay length is 41 ± 11 cm. Thus the number of events entering the fiducial volume is estimated to be 1.22 ± 1.45 events/dataset.

As mentioned above, these events are associated with the OD hits. The OD efficiency is 92%. Thus fast neutron events without the OD hits that mimic the neutrino delayed coincidence signal are expected to be about 0.10 ± 0.12 events/dataset (0.22 events/dataset as upper limit).

The fast neutron events from the rock outside of the OD detector are calculated by a simple simulation, and total ratio of the neutrons from the muon passing outside the OD to the neutrons from the muon passing through the OD is 0.11, so the contribution from the rock is 0.15 ± 0.18 events/dataset (0.33 events/dataset as upper limit). In total number of the background from the fast neutron is expected to be 0.25 ± 0.22 events/dataset (0.47 events/dataset as upper limits)

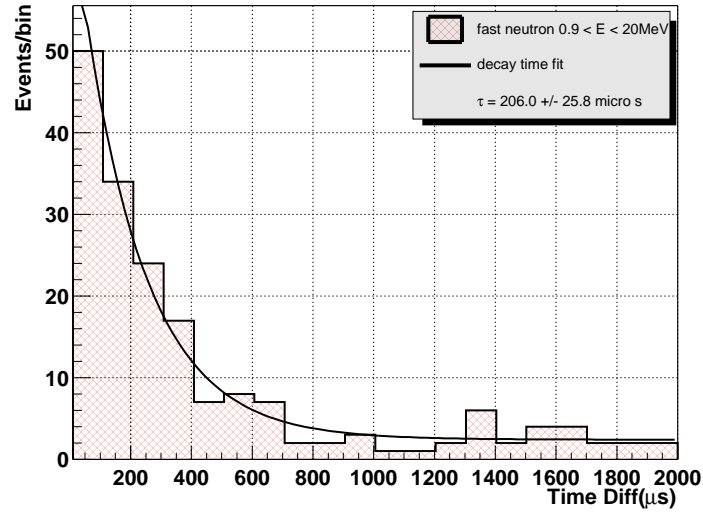


Figure 8.6: The time distribution between the muon and the neutron capture events for fast neutron samples.

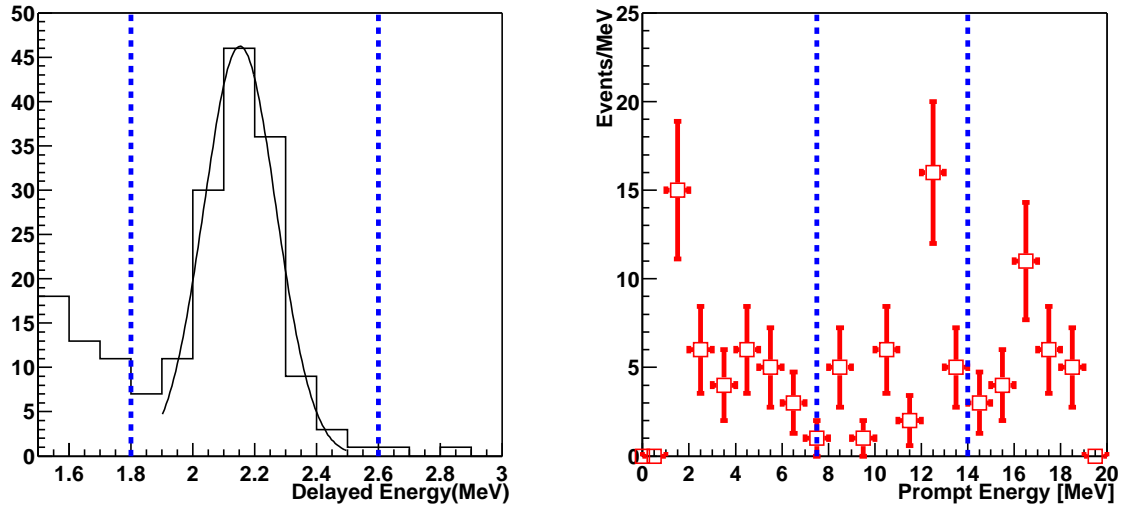


Figure 8.7: The energy distribution of delayed and prompt events for fast neutron samples

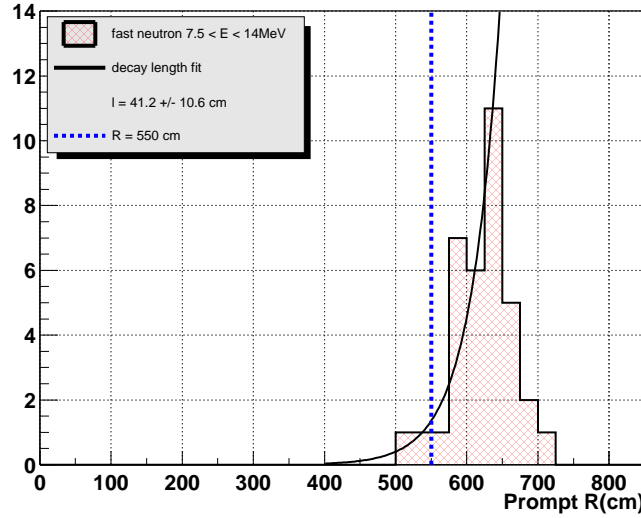


Figure 8.8: The radial distribution for fast neutron samples

8.4.5 Accidental background

The event selection by the delayed coincidence technique significantly reduces the uncorrelated background events. But some events can remain as accidental background events. They are estimated by applying the same criteria as the neutrino event selection except for a time window being set from 1 to 10 seconds. This window is about 13600 times wider than the window for the neutrino selection ($0.5 \leq dt \leq 660 \mu s$).

Figure 8.9 shows the time and the vertex distribution of the accidental background events taken in about 24 hours running time. The prompt energy is larger than 0.9 MeV. For all the volume, time distribution is almost flat. The vertex points are concentrated at the top, bottom and the balloon edge. They are reduced by the fiducial cut of $R > 550$ cm. Thus the accidental background events are generated in the fiducial volume are collected from the whole data sample.

Figure 8.10 shows the time distribution of the accidental events. The energy region of the solar anti-neutrino analysis includes accidental event about 217 events, and corresponds to 0.02 ± 0.0014 events/dataset for the time window of the neutrino selection. Thus the number of the accidental background is estimated to be 0.02 events/dataset in the energy region of the solar anti-neutrino analysis.

8.4.6 background summary

The expected background events from reactor neutrino, atmospheric neutrino, spallation events and fast neutron events are estimated. Table 8.4 shows the summary of the estimation.

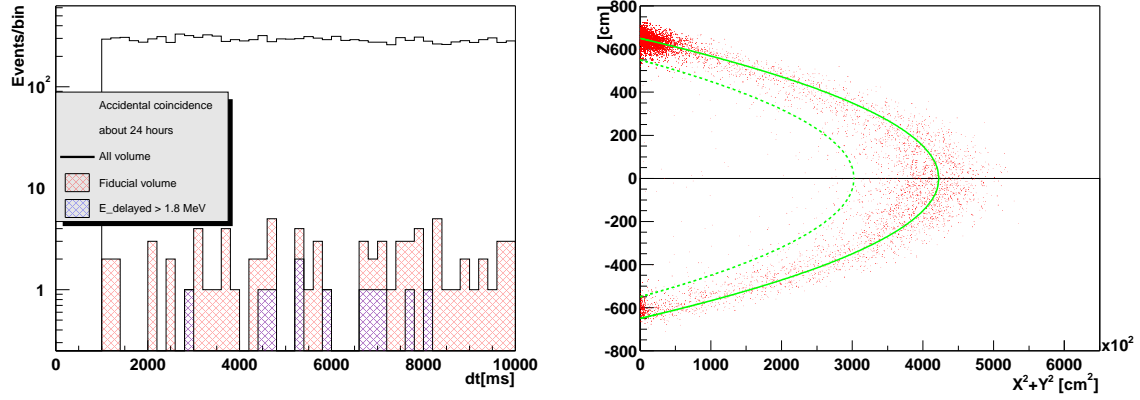


Figure 8.9: The time and the vertex distribution for the accidental background events in a data sample of 24 hours running time. The accidental backgrounds are dramatically reduced in the processes from the event sample ($E_{prompt} \geq 0.9\text{MeV}$) by the fiducial cut and then the energy cut of $E_{delayed} \geq 1.8\text{MeV}$.

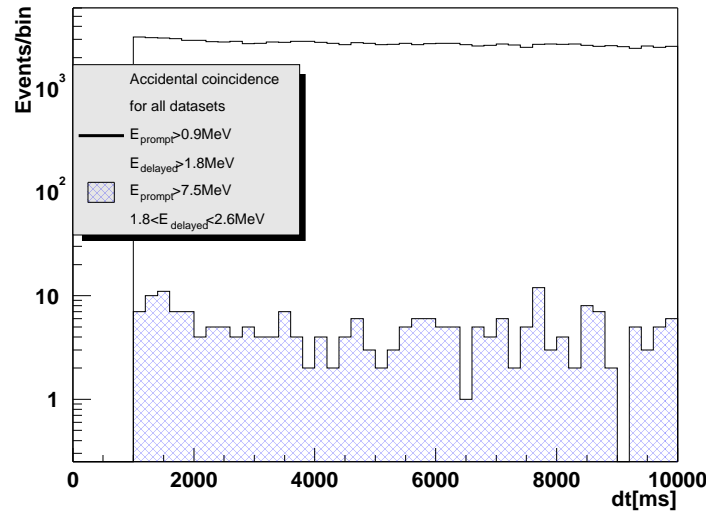


Figure 8.10: The time distribution of the accidental events collected from the whole data. All the events are distributed into the fiducial volume. The cross-hatched histogram shows the one in the energy region of the solar neutrino analysis.

background source	events/dataset
reactor neutrino	0.21 ± 0.20
atmospheric neutrino	7×10^{-4}
spallation ${}^9\text{Li}/{}^8\text{He}$	0.58 ± 0.21
fast neutron	0.25 ± 0.22
accidental	0.02
total	1.06 ± 0.36

Table 8.4: The summary of background events estimation

8.5 Limit calculation

The result of the data reduction is that there is no evidence of the solar anti-neutrino. Thus the upper limit of the solar anti-neutrino flux is calculated.

The quantities including in the calculation are the detection efficiency of 84.09%, 0 events in $E \geq 7.5$ MeV, livetime 16030548 sec and the number of the free protons 4.60×10^{31} in the fiducial volume. The upper limit at a confidence level CL on the number of signal N given by a Poisson distribution as a probability function :

$$CL = 1 - e^{-N} \sum_{n=0}^{n_0} \frac{N^n}{n!} \quad (8.4)$$

where n_0 is the number of observed candidates. Since $n_0 = 0$, the upper limit on N is 2.30 at 90 % coincidence level. The energy region $7.5 \leq E_{prompt} \leq 14$ MeV corresponds to $8.3 \leq E_{\bar{\nu}_e} \leq 14.8$ MeV in the approximation of neglecting the recoil neutron energy. The expected neutrino flux is :

$$\Phi_{\bar{\nu}_e}(8.3 \leq E_{\bar{\nu}_e} \leq 14.8 \text{ MeV}) = \frac{N}{\bar{\sigma} \times \bar{S} \times T \times \epsilon \times N_p \times f_v} \quad (8.5)$$

where ϵ is the detection efficiency, N_p is the number of free protons in the total volume, f_v is the fraction of the fiducial volume in the total volume and T is the livetime. $\bar{\sigma}$ and \bar{S} mean the average cross section and ${}^8\text{B}$ neutrino spectrum shape [11] given by $\bar{\sigma} \times \bar{S} = \int_{8.3}^{14.8 \text{ MeV}} \frac{d\sigma}{dE} \cdot S \cdot dE$. Applying eq.(8.5), this translates into a flux limit of $5.39 \times 10^2 \text{ cm}^{-2} \text{ s}^{-1}$. Using the SSM prediction for the ${}^8\text{B}$ neutrino flux of BP2000 [10], the upper limit on the probability of neutrino conversion $\nu_e \rightarrow \bar{\nu}_e$ is obtained as $P_{\nu_e \rightarrow \bar{\nu}_e} \leq 0.035\%$ (90 % C.L.).

We account for the systematic uncertainties 6.07% in eq.(8.5) by scaling this limit upward by 7.77% (1.28σ : 1-sided 90% C.L.). The estimated background rate is not included because of 0 candidate. The upper limit at the 90% C.L. which we finally obtain on the $\bar{\nu}_e$ flux in the energy range $8.3 \leq E_{\bar{\nu}_e} \leq 14.8$ MeV is **$5.81 \times 10^2 \text{ cm}^{-2} \text{ s}^{-1}$** . Normalizing to the total ${}^8\text{B}$ flux [10], this corresponds to an upper limit on the probability of the neutrino conversion $\nu_e \rightarrow \bar{\nu}_e$ is **0.038%** at 90% C.L. This limit improves on the previous limit [43] by about a factor 20.

Chapter 9

Interpretation and Discussions

This chapter shows the physics interpretation of the solar anti-neutrino limit obtained in the previous chapter.

9.1 Neutrino magnetic moment

9.1.1 Input parameter and solar magnetic field

In assuming the neutrino magnetic moment, the production of solar anti-neutrino is calculated by the Hybrid model (RSFP+MSW) discussed in section 3.1.4. The neutrino propagation in the Majorana neutrino case is calculated by eq.(3.10).

As seen in the propagation equation (3.10), the solar parameters, the electron number density N_e , the neutron number density N_n , and the profile of magnetic field B_{sun} in the sun are needed. The neutrino mass squared difference Δm^2 and the neutrino mixing angle $\sin^2 2\theta$ are varied in the allowed solution region. In these parameter region, the transition neutrino magnetic moment μ are explored.

The density N_e and N_n are shown in Figure 2.9 that are obtained from the standard solar model (BP2000) [10]. The transition probability is given by a function $\mu_{11}B_{\perp}$, μ_{11} being the magnetic moment a unit of 10^{-11} of the Bohr magneton and magnetic field B_{\perp} is the perpendicular component of the solar magnetic field that is changeable input in the following argument.

Unfortunately, little is known about the magnetic field inside the sun, and we have to use various models on the magnetic field profiles in the discussion of the RSFP mechanism. Although there is no direct information on the magnetic fields of the solar core, there are theoretical reasons that the magnetic field in the central part of the sun is very low. Otherwise the present magnetic field in the convective zone would be quite large, leading to a visible enhancement in the sunspot activity.

Here the three simple models on the magnetic field in the sun are presented from the previous works [49]. The first profile (profile 1) is ;

$$B = 0, \quad x < x_R \quad (9.1)$$

$$B = B_{max} \frac{x - x_R}{x_C - x_R}, \quad x_R \leq x < x_C \quad (9.2)$$

$$B = B_{max} \left[1 - \frac{x - x_C}{1 - x_C} \right], \quad x_C \leq x < 1 \quad (9.3)$$

where B_{max} is the maximum strength of the magnetic field in the sun. Here x is the normalized radial distance from the center, r/R_{sun} , with the R_{sun} being the solar radius, and the two parameters take the values like $x_R = 0.7$, $x_C = 0.85$.

The next profile (profile 2) is ;

$$B = 0, \quad x < x_R \quad (9.4)$$

$$B = B_{max} \frac{x - x_R}{x_C - x_R}, \quad x_R \leq x < x_C \quad (9.5)$$

$$B = B_{max} \left[1 - \left(\frac{x - 0.7}{0.3} \right)^2 \right], \quad x_C \leq x < 1 \quad (9.6)$$

$$(9.7)$$

where $x_R = 0.65$, $x_C = 0.75$ are taken.

The profile 3 is a modification of the previous one ;

$$B = 2.16 \times 10^3 G, \quad x < x_C \quad (9.8)$$

$$B = \frac{B_{max}}{0.998} \left[1 - \left(\frac{x - 0.75}{0.04} \right)^2 \right], \quad x_R \leq x < x_C \quad (9.9)$$

$$B = \frac{B_{max}}{\cosh 30(x - x_C)}, \quad x_C \leq x < 1 \quad (9.10)$$

$$(9.11)$$

where $x_R = 0.7105$, $x_C = 0.7483$ are taken.

Figure 9.1 shows the radial distribution of the solar magnetic field. The maximum magnetic field B_{max} is fixed to 300 kG in this figure. The maximum magnetic fields are given in the region from $x \sim 0.75$ to $x \sim 0.85$.

Another magnetic field model based on the general framework of self-consistent magneto-hydrodynamic (MHD) models of the Sun [50] is adopted also considered. The corresponding MHD magnetic field profiles are rather complicated. However, there are static solutions which are known analytically in terms of relatively simple functions given [51]:

$$\nabla p - \frac{1}{c} \vec{j} \times \vec{B} + \rho \nabla \Phi = 0 \quad (9.12)$$

where p is the pressure, j is the electric current, B is the static magnetic field, ρ is the matter density and Φ is the gravitational potential. The solution to the equation is given by the spherical Bessel function $f_{5/2} = \sqrt{z} J_{5/2}(z)$ which is expressed as follows :

$$\begin{aligned} B_r^k(r, \theta) &= 2\hat{B}^k \cos \theta \left[1 - \frac{3}{r^2 z_k \sin z_k} \left(\frac{\sin(z_k r)}{z_k r} - \cos(z_k r) \right) \right] \\ B_\theta^k(r, \theta) &= -\hat{B}^k \sin \theta \left[2 + \frac{3}{r^2 z_k \sin z_k} \left(\frac{\sin(z_k r)}{z_k r} - \cos(z_k r) - z_k r \sin(z_k r) \right) \right] \\ B_\phi^k(r, \theta) &= \hat{B}^k z_k \sin \theta \left[r - \frac{3}{r z_k \sin z_k} \left(\frac{\sin(z_k r)}{z_k r} - \cos(z_k r) \right) \right] \end{aligned} \quad (9.13)$$

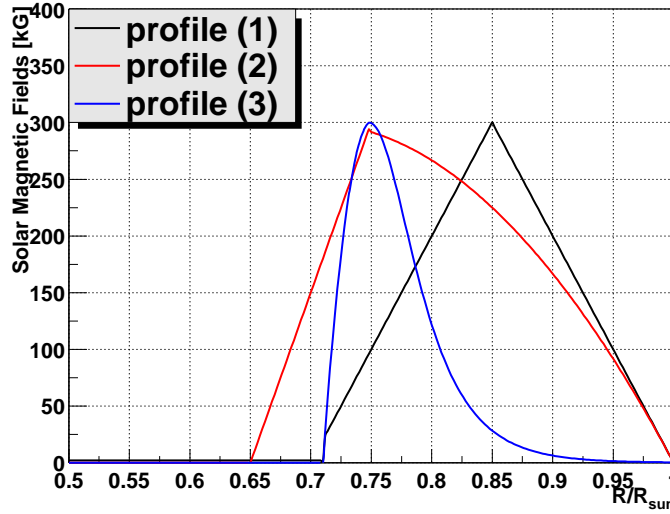


Figure 9.1: The radial dependence of the solar magnetic field profile (1), (2) and (3). The maximum magnetic field is fixed to 300kG.

where

$$\hat{B}^k = \frac{B_{core}}{2(1 - z_k / \sin z_k)} \quad (9.14)$$

r is an normalized distance by the solar radius R_{sun} and θ is the polar angle that must be averaged over for narrow range (about 83° - 97°). The modulus of the perpendicular component which is relevant to the neutrino spin-flavour transition is $B_\perp = \sqrt{B_\phi^2 + B_\theta^2}$.

The estimated B_\perp have k dependence and grow up in the solar interior. The general knowledge of the solar magnetic field models is that the magnetic field increases at the convective zone and decreases as going further into the solar interior, opposite to the one expressed in eq.(9.13). The basic equilibrium MHD equation in eq.(9.12) is a linear equation and any linear combination of solutions \hat{B}^k ($k=1,2,\dots,k_M$):

$$\vec{B} = \sum_{i=1}^{k_M} c_i \vec{B}^i \quad (9.15)$$

is allowed as a solution. c_i 's are free parameters and are determined by requirements that combined magnetic field is equal to zero in the solar center and the total energy must be minimum in the bottom of the convective zone [51]. The integer k is limited and does not exceed 10 by solar parameters. Now $k_M = 6$ is adopted for this study. Figure 9.2 shows the magnetic field configuration obtained by combining individual mode for $k_M = 6$.

There are many studies of the astrophysical restrictions on the magnetic field in the sun. The Fermi-Chandrasekhar limit [52] requires an upper bound on $B_{core} \leq 2$ MGauss. It has recently been argued [53] that fields up to 7 MGauss can be existing in the radiative zone for billions of years and are consistent with current observational bounds. On the other hand, other authors

explain that the magnetic field is 20 kGauss at radiative zone and 300 kGauss at the convective zone [54]. Therefore, the solar magnetic field is quite uncertain and B_{max} is changed over 20k, 50k, 100k, 300k, 1M, 3M and 10MG in this study.

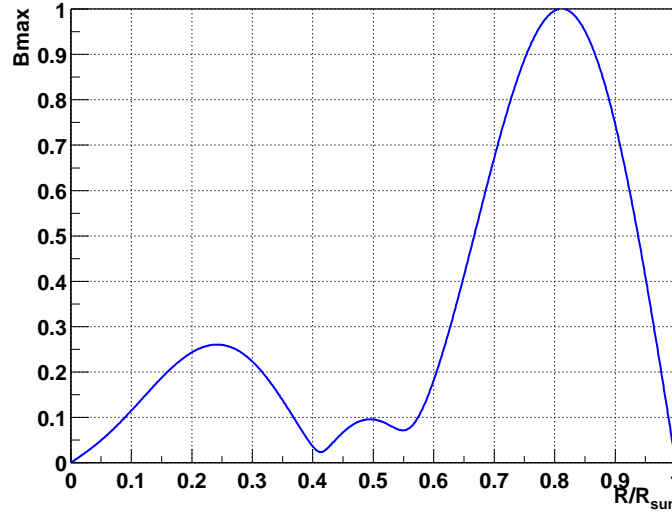


Figure 9.2: The radial dependence of the solar magnetic field given by MHD function. The maximum magnetic field is fixed to 300kG.

9.1.2 Neutrino propagation

To examine the propagation of the neutrinos in the sun, the evolution equation eq. 3.10 for ν_e , ν_μ , $\bar{\nu}_e$ and $\bar{\nu}_\mu$ is calculated numerically.

The wave function of neutrinos are defined at $t = 0$:

$$\phi_\nu = \begin{pmatrix} \nu_e \\ \nu_\mu \\ \bar{\nu}_e \\ \bar{\nu}_\mu \end{pmatrix} = \begin{pmatrix} 1 \\ 0 \\ 0 \\ 0 \end{pmatrix} \quad (9.16)$$

The neutrino propagates with the equation :

$$i \frac{d}{dt} \phi = H \phi \quad (9.17)$$

where H is the hamiltonian which is expressed in eq. 3.10. To solve the equation, the orthogonalized matrix is used at each step instead of the flavor basis matrix. Suppose that the Hamiltonian $H(t)$ can be regarded as constant in a very short time interval Δt ($H(t) \simeq H(t + \Delta t) = H_0$), then the propagation equation $i \frac{d}{dt} \phi(t) = H_0 \phi(t)$ can be solved, and the result is :

$$\phi'(t + \Delta t) = \phi'(t) e^{-i H_0' \Delta t} \quad (9.18)$$

where $H'_0 = VH_0V^{-1}$ is an orthogonal matrix, V is the rotation matrix, and $\phi'(t) = V\phi(t)$ is the eigen-vector. Then the wave function at $t = t + \Delta t$ can be obtained with $V(t + \Delta t) \simeq V(t)$:

$$\phi(t + \Delta t) = V^{-1}(V\phi(t)e^{-iH'_0\Delta t}) \quad (9.19)$$

where the rotation matrix V can be numerically calculated in each step of the time interval i (from 1 to N) to diagonalize the Hamiltonian :

$$\begin{aligned} H' &= \begin{pmatrix} H'_{11} & & 0 \\ & \ddots & \\ 0 & & H'_{44} \end{pmatrix} \\ &= V_N \dots \begin{pmatrix} \cos \theta_i & 0 & \sin \theta_i & 0 \\ 0 & 1 & 0 & 0 \\ -\sin \theta_i & 0 & \cos \theta_i & 0 \\ 0 & 0 & 0 & 1 \end{pmatrix} \dots V_1 H V_1^{-1} \dots \begin{pmatrix} \cos \theta_i & 0 & -\sin \theta_i & 0 \\ 0 & 1 & 0 & 0 \\ \sin \theta_i & 0 & \cos \theta_i & 0 \\ 0 & 0 & 0 & 1 \end{pmatrix} \dots V_N^{-1} \end{aligned} \quad (9.20)$$

then the rotation matrix :

$$V = \prod_{i=1}^N V_i \quad (9.21)$$

is obtained.

The step size for the calculation is chosen to $1/5000R_{sun}$. It is sufficiently small to trace the change of the propagation matrix. Figures 9.3 to 9.6 show the probabilities of a neutrino flavour to be observed at each point inside the sun for 4 magnetic field profiles (profile(1),(2),(3),MHD). All the plots show for $E_\nu=10\text{MeV}$. The maximum solar magnetic field and the neutrino magnetic moment are taken as $B_{max}=300\text{kG}$ and $\mu_\nu = 10^{-11}\mu_B$. The oscillation parameters are given by the nine combinations of $\Delta m^2=(2\times 10^{-5}, 7\times 10^{-5}, 2\times 10^{-4})$ and $\sin^2 2\theta=(0.3,0.6,0.9)$.

9.1.3 Average probability and expected flux

The distribution of the neutrino production point is predicted by the Standard Solar Model (see Figure 2.4). The ^8B neutrino production peaks at about 0.04 of the solar radius. The number of neutrino production points is taken as 21 for radial direction and 10 for polar angle direction. The transition probability to $\bar{\nu}_e$ is estimated by averaging the probabilities of these production points.

Figure 9.7 shows the energy dependence of the $\bar{\nu}_e$ transition probability. The magnetic field is taken as the 'profile (1)' and $B_0 = 300\text{kG}$. The mass difference is $2\times 10^{-5}\text{eV}^2$ in LMA region and $\sin^2 2\theta = 0.3, 0.6, 0.9$. The $\bar{\nu}_e$ probability is increased with neutrino energy and have the correlation with the mixing angle.

The energy region of $\bar{\nu}_e$ in the present analysis is from 8.3MeV to 14.8MeV. The total $\bar{\nu}_e$ probability is obtained by taking a product of the energy dependent probability and the ^8B neutrino spectrum shape. Figure 9.8 shows the total $\bar{\nu}_e$ probability as a function of the product $\mu_{11}B_{max}$, where μ_{11} is the magnetic moment in the unit of 10^{-11} Bohr magneton and B_{max} is the maximum magnetic field in the convective zone. The neutrino mass squared difference and

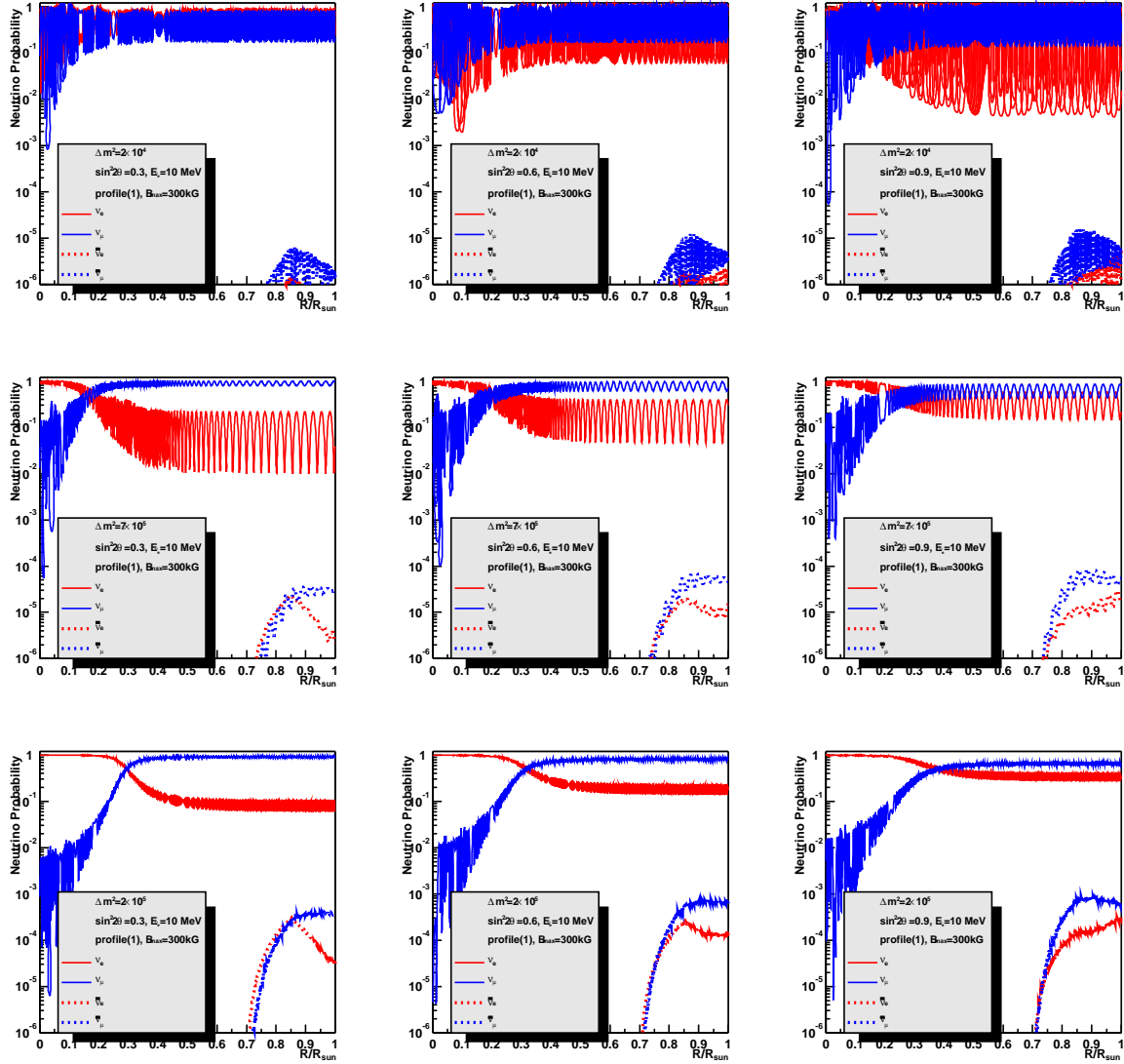


Figure 9.3: The radial dependence of neutrino flavour transition probability for the magnetic field profile (1) with $B_{max} = 300\text{kG}$ and $\mu_\nu = 10^{-11} \mu_B$. The oscillation parameters are given in the combination of $\Delta m^2 = (2 \times 10^{-5}, 7 \times 10^{-5}, 2 \times 10^{-4})$ and $\sin^2 2\theta = (0.3, 0.6, 0.9)$.

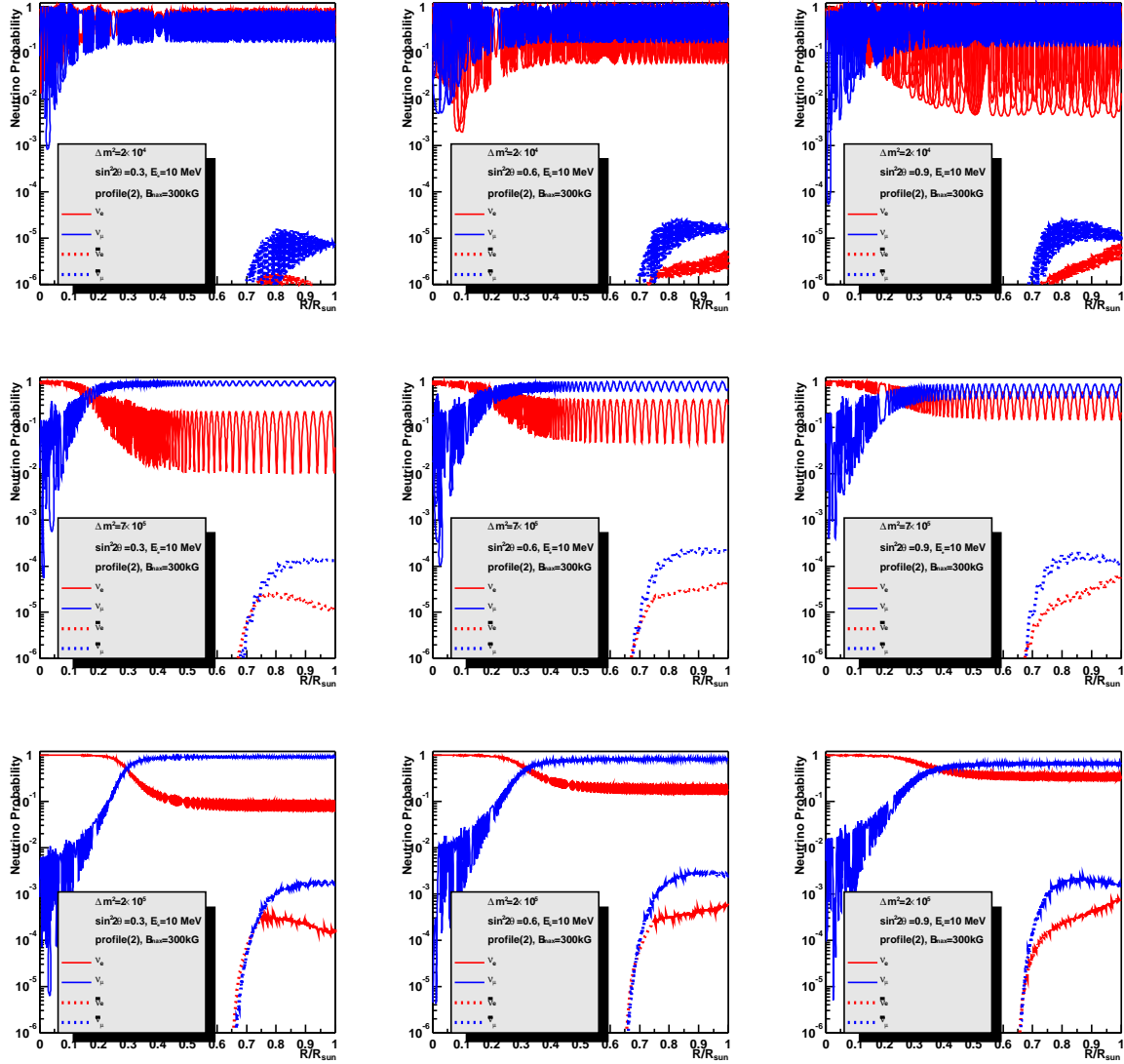


Figure 9.4: The radial dependence of neutrino flavour transition probability for the magnetic field profile (2) with $B_{max} = 300\text{kG}$ and $\mu_\nu = 10^{-11}\mu_B$. The oscillation parameters are given in the combination of $\Delta m^2 = (2 \times 10^{-5}, 7 \times 10^{-5}, 2 \times 10^{-4})$ and $\sin^2 2\theta = (0.3, 0.6, 0.9)$.

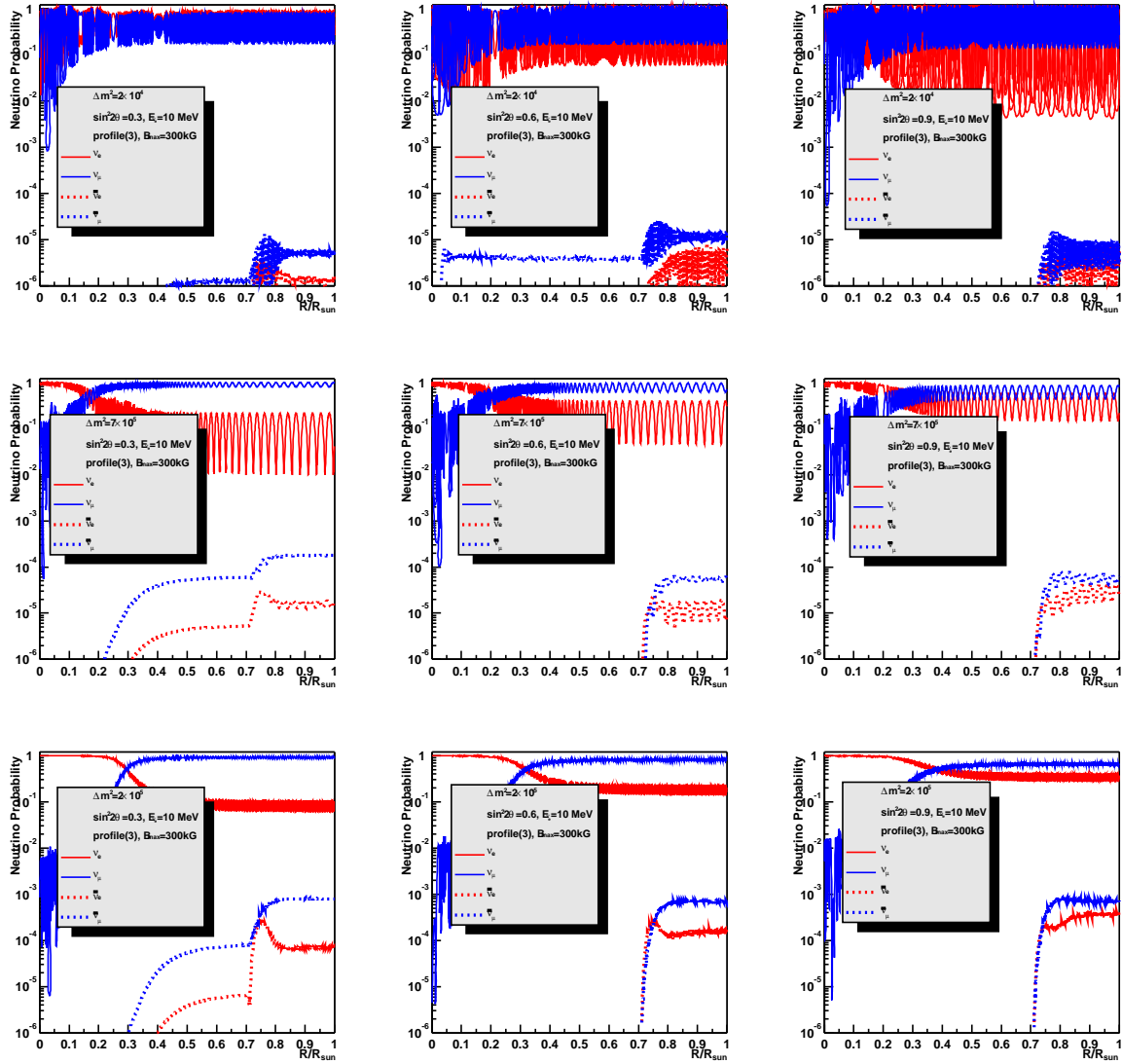


Figure 9.5: The radial dependence of neutrino flavour transition probability for the magnetic field profile (3) with $B_{max} = 300\text{kG}$ and $\mu_\nu = 10^{-11}\mu_B$. The oscillation parameters are given in the combination of $\Delta m^2 = (2 \times 10^{-5}, 7 \times 10^{-5}, 2 \times 10^{-4})$ and $\sin^2 2\theta = (0.3, 0.6, 0.9)$.

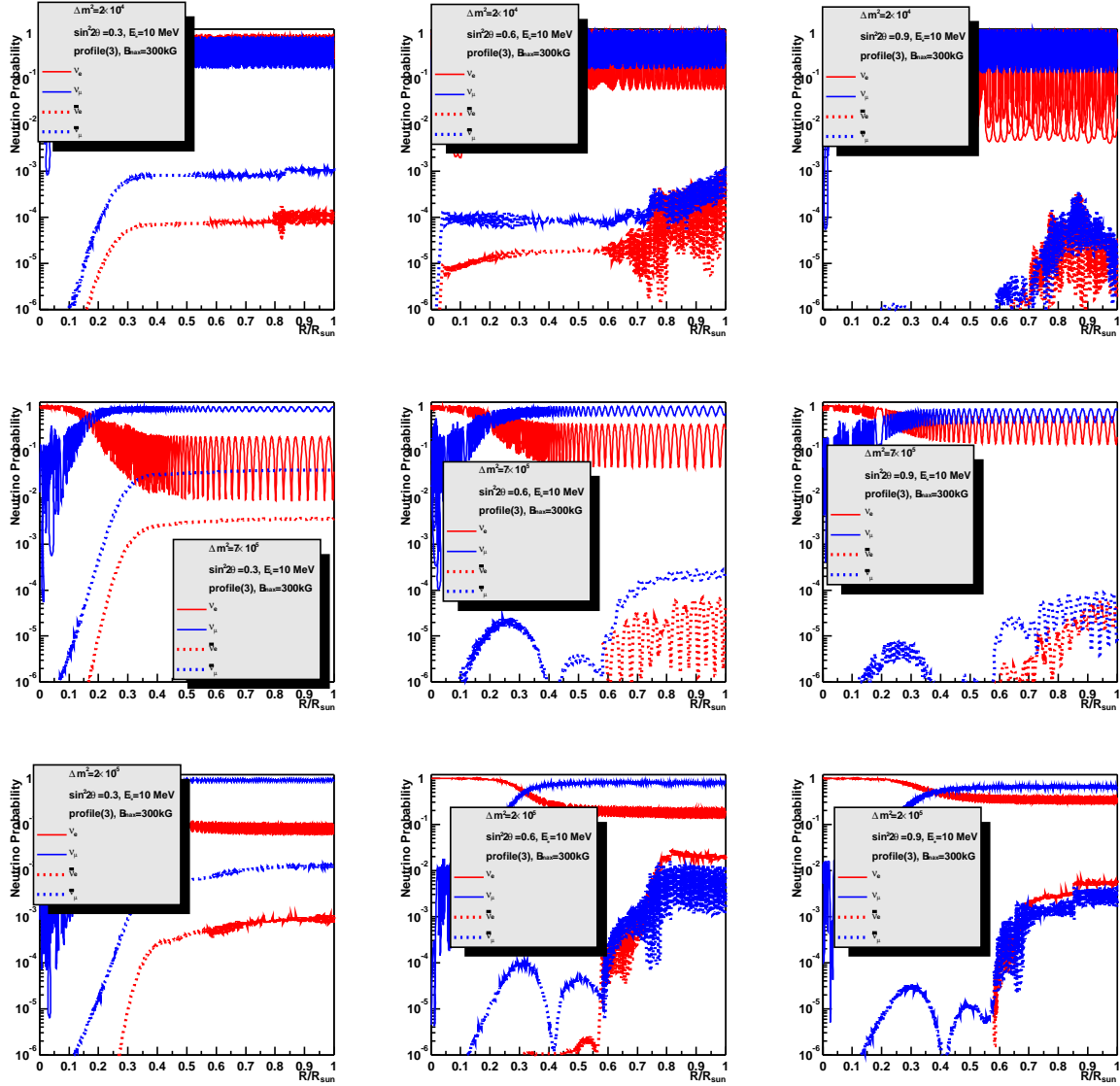


Figure 9.6: The radial dependence of neutrino flavour transition probability for the magnetic field profile MHD with $B_{max} = 300\text{kG}$ and $\mu_\nu = 10^{-11}\mu_B$. The oscillation parameters are given in the combination of $\Delta m^2 = (2 \times 10^{-5}, 7 \times 10^{-5}, 2 \times 10^{-4})$ and $\sin^2 2\theta = (0.3, 0.6, 0.9)$.

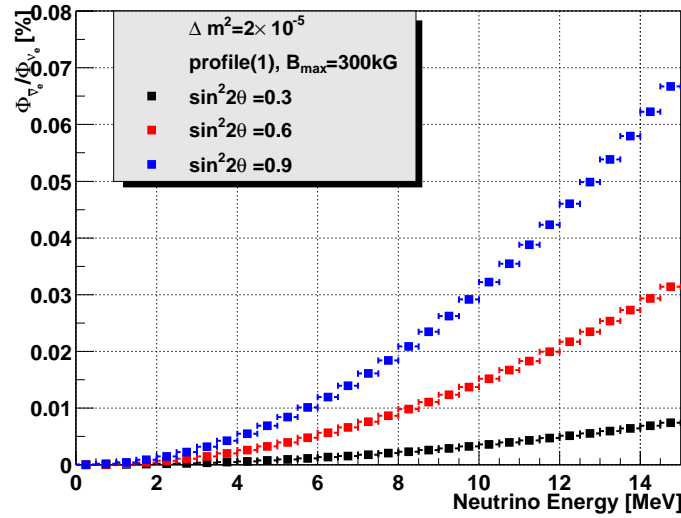


Figure 9.7: The typical energy distribution of average $\bar{\nu}_e$ probability. The magnetic field is 'profile (1)' and $B_0 = 300\text{kG}$. The mass difference is LMA region and $\sin^2 2\theta = 0.3, 0.6, 0.9$.

the mixing angle are taken as the LMA best-fit parameters. The three magnetic field profiles are shown in figure 9.1. The most stringent limit on $\mu_{11}B_{max}$ is obtained in the case of the 'profile (2)' to be limit is $\mu_{11}B_{max} \leq 5.7 \times 10^5\text{G}$ (90 % C.L.) which is imposed by the present analysis on the solar $\bar{\nu}_e$ limit 0.038% obtained in the presented analysis. This limit means that the neutrino transition magnetic moment is $\mu \leq 5.7 \times 10^{-12}\mu_B$ if B_{max} is $\sim 1\text{MG}$.

9.1.4 Analysis region for oscillation parameter

In this section the limit of the neutrino transition magnetic moment in the allowed region of the oscillation parameters is discussed. Here, we restrict the region of $\Delta m^2, \sin^2 2\theta$ to the LMA region which is only the allowed solution by the recent KamLAND reactor neutrino oscillation experiment [2]. Figure 9.9 shows the allowed and excluded region by KamLAND and the LMA region by solar neutrino experiments. There are two sub-regions of LMA obtained by combining the KamLAND results.

Thus studies on the limit on the neutrino magnetic moment are done in the following three regions ;

- region (A) \rightarrow full LMA region.
- region (B) \rightarrow A sub-region of LMA with higher Δm^2 obtained by KamLAND.
- region (C) \rightarrow A sub-region of LMA with lower Δm^2 obtained by KamLAND.

Also the best-fit parameters in the LMA ($\Delta m^2 = 5.5 \times 10^{-5}, \sin^2 2\theta = 0.833$) obtained by only solar neutrino experiments [19] are used in the study.

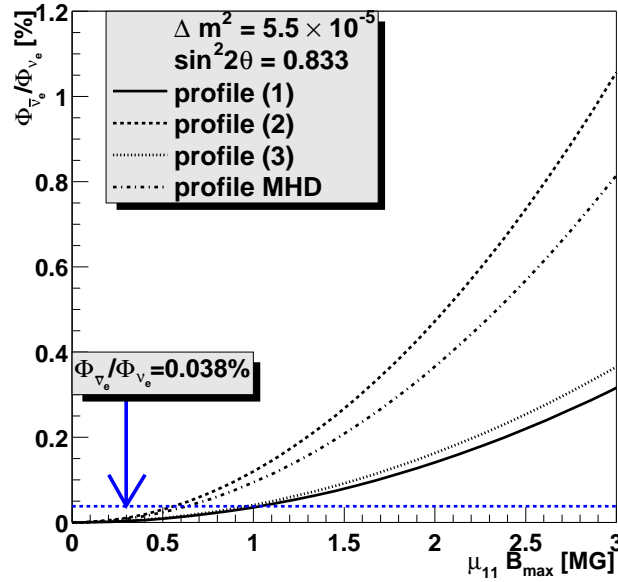


Figure 9.8: Total $\bar{\nu}_e$ probability depending to the neutrino transition magnetic moment function $\mu_{11} B_{max}$.

9.1.5 RSFP analysis

Figure 9.10 shows the calculated solar $\bar{\nu}_e$ probability as a function of the neutrino transition magnetic moment parameter $\mu_{11} B_{max}$ for the four magnetic field profiles. The $(\Delta m^2, \sin^2 2\theta)$ parameter region is the full LMA region ('region (A)'). The upper limits on $\mu_{11} B_{max}$ are 4.44MG, 2.77MG, 3.80MG 3.40MG for magnetic field profile (1), (2), (3) and MHD respectively. The oscillation parameters providing these limits are $(\Delta m^2 = 2.2 \times 10^{-4}, \sin^2 2\theta = 0.80_{(1)(2)(3)}, 0.89_{MHD})$. The best fit parameter of LMA solar neutrino global analysis ($\Delta m^2 = 5.5 \times 10^{-5}, \sin^2 2\theta = 0.833$) provides the upper limits of 1.04MG, 0.57MG, 0.97MG and 0.64MG for profile (1), (2), (3) and MHD respectively.

In the case of 'region (B)', Δm^2 is varied in the range $1 \times 10^{-4} \leq \Delta m^2 \leq 2 \times 10^{-4}$. Figure 9.11 shows the same figure for the parameter, 'region B'. The upper limits on $\mu_{11} B_{max}$ are 3.79MG, 2.44MG, 3.44MG and 2.95MG for the magnetic field profiles (1), (2), (3) and MHD respectively. The oscillation parameters providing these limits are $(\Delta m^2 = 2.0 \times 10^{-4}, \sin^2 2\theta = 0.76_{(1),(2),(3)}, 0.89_{MHD})$.

In the case of 'region (C)', Δm^2 is varied in a region $5 \times 10^{-5} \leq \Delta m^2 \leq 9 \times 10^{-5}$. This region also includes the LMA best-fit parameters. Figure 9.12 shows the fraction of the $\bar{\nu}_e$ flux for the four magnetic profiles. The upper limits on $\mu_{11} B_{max}$ are 1.65MG, 0.97MG, 1.53MG and 1.24MG for magnetic field profile (1), (2), (3) and MHD respectively. The oscillation parameters for these limits are $(\Delta m^2 = 8.0 \times 10^{-5}, \sin^2 2\theta = 0.71_{(1),(3)}, 0.97_{(2),(MHD)})$. Table 9.1 summarizes the $\mu_{11} B_{max}$ limits for the magnetic field profiles and LMA region.

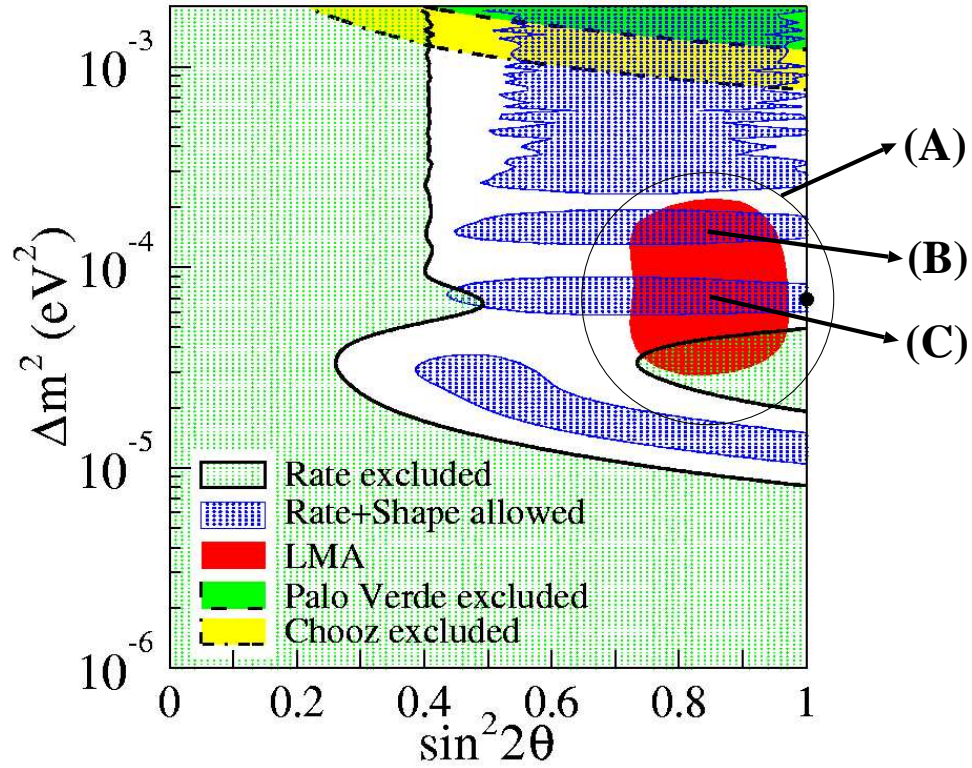


Figure 9.9: Exclude region of neutrino oscillation parameters for the 'Rate' analysis at 95%C.L. and 95%C.L. allowed region for the 'Rate+Shape' analysis above 2.6MeV energy threshold from KamLAND [2]. The dot indicates the best fit parameters in the physical region: $\sin^2 2\theta=1.0$ and $\Delta m^2=6.9 \times 10^{-5}$. At the top are 95% exclude region from CHOOZ [55] and Palo Verde [56] experiment. The 95%C.L. allowed region of LMA solution of solar neutrino experiments [19] is shown. The RSFP analysis region (A),(B) and (C) are also shown.

Now the rough limit of neutrino transition magnetic moment is estimated by the limit of strength of solar magnetic field. If the strength of solar magnetic field are adopted to 1MG, the limit of magnetic mament :

$$\begin{aligned}
\mu_\nu &< 2.8 - 4.4 \times 10^{-11} \mu_B && \text{(LMA whole)} \\
\mu_\nu &< 2.4 - 3.8 \times 10^{-11} \mu_B && \text{(region(B)) upper side of LMA} \\
\mu_\nu &< 1.0 - 1.7 \times 10^{-11} \mu_B && \text{(region(C)) lower side of LMA} \\
\mu_\nu &< 0.6 - 1.0 \times 10^{-11} \mu_B && \text{(LMA best)}
\end{aligned} \tag{9.22}$$

are estimated. These limit are better than MUNU experiment limit $\mu_\nu < 1 \times 10^{-10} \mu_B$ [22].

osillation parameter	(A)LMA whole	(B) LMA+Kam (1)	(C) LMA+Kam (2)	LMA Best
Δm^2	2.2×10^{-4}	2.0×10^{-4}	8.0×10^{-5}	5.5×10^{-5}
$\sin^2 2\theta$	$0.80_{(1)(2)(3)}$	$0.76_{(1)(2)(3)}$	$0.71_{(1)(3)}$	0.833
Limit param.	$0.89_{(MHD)}$	$0.89_{(MHD)}$	$0.97_{(2)(MHD)}$	
profile (1)	$4.44 \times 10^6 G$	$3.79 \times 10^6 G$	$1.65 \times 10^6 G$	$1.04 \times 10^6 G$
profile (2)	$2.77 \times 10^6 G$	$2.44 \times 10^6 G$	$0.97 \times 10^6 G$	$0.57 \times 10^6 G$
profile (3)	$3.80 \times 10^6 G$	$3.44 \times 10^6 G$	$1.53 \times 10^6 G$	$0.97 \times 10^6 G$
MHD	$3.40 \times 10^6 G$	$2.95 \times 10^6 G$	$1.26 \times 10^6 G$	$0.64 \times 10^6 G$

Table 9.1: The $\mu_{11} B_{max}$ limit obtained for the four magnetic field profiles and the oscillation parameters in allowed regions of LMA.

9.1.6 Compare the survival probability ν_e between RSFP+MSW and MSW only

It must be mentioned that the survival probability of ν_e in RSFP+MSW is different from the one at MSW only. For example, at the LMA best-fit parameters for the solar neutrino global analysis ($\Delta m^2 = 5.5 \times 10^{-5}$, $\sin^2 2\theta = 0.833$) [19] and $\mu_{11} B_{max} = 10 MG$, the survival probability of ν_e in RSFP+MSW at 10MeV is smaller by about 30% in the spectrum shape than the one of MSW (see Figure 9.13).

Actually, this estimation is an exaggerated one. At LMA best region, the $\bar{\nu}_e$ production probability is about 10% of the SSM for $\mu_{11} B_{max} = 10 MG$ and it is excluded by KamLAND solar $\bar{\nu}_e$ limit of 0.038%. Now the ν_e survival probability are checked at the $\mu_{11} B_{max}$ limit which is estimated from solar $\bar{\nu}_e$ limit 0.038% for each oscillation parameter. The $\mu_{11} B_{max}$ are scanned from ~ 0.3 to 3MG which conform to oscillation parameter and magnetic field profiles (see Figure 9.10). And the difference in the ν_e survival probability between MSW and RSFP+MSW are examined as a function of energy and Δm^2 .

Figure 9.14 shows the energy dependence between MSW and RSFP+MSW for each magnetic field profiles and each $\mu_{11} B_{max}$ limit obtained from the $\bar{\nu}_e$ limit of 0.038%. The maximum difference is about 0.2% at 15MeV. Figure 9.15 shows the Δm^2 dependence of the total ν_e survival

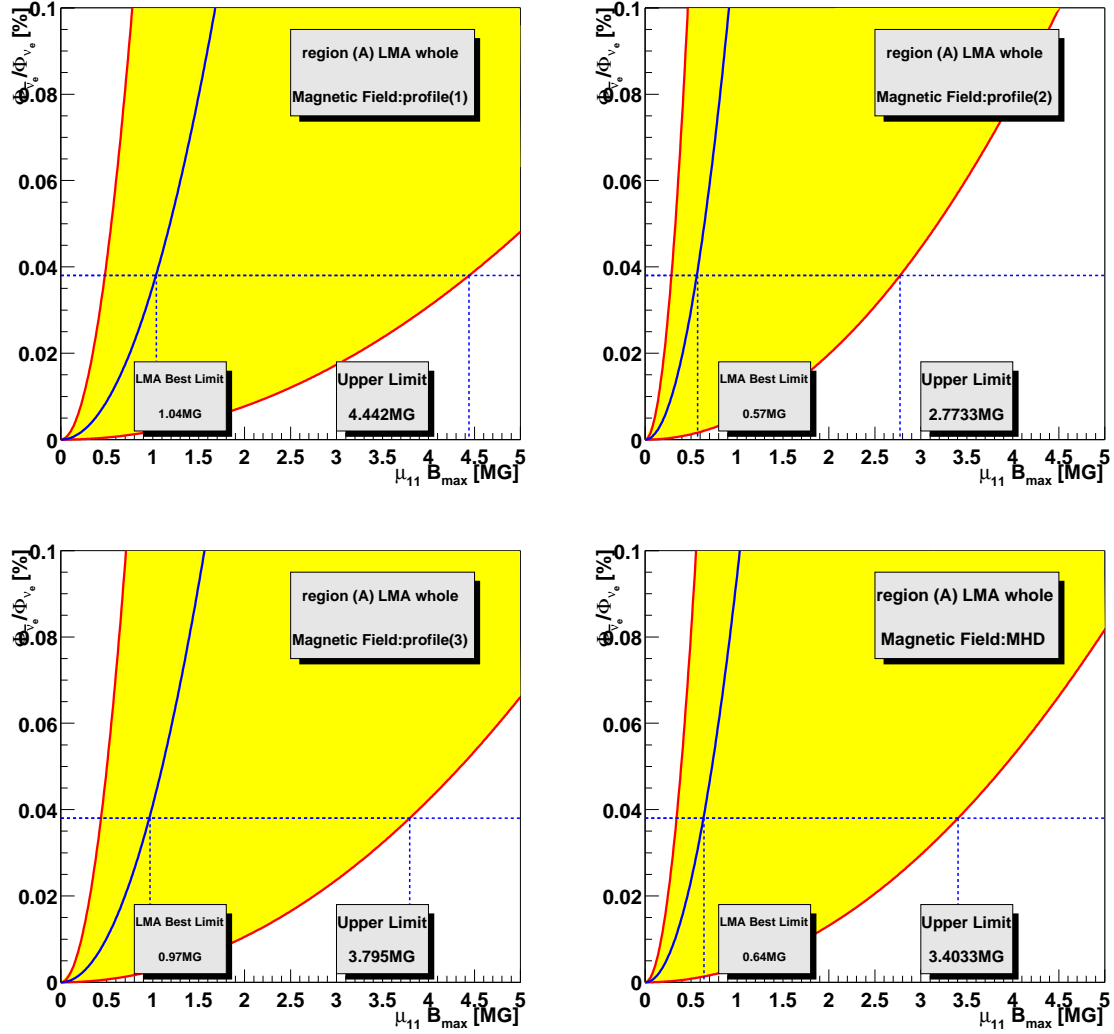


Figure 9.10: The calculated ratio of the $\bar{\nu}_e$ flux to the ^8B solar ν_e flux of the SSM prediction vs. the parameter $\mu_{11} B_{\max}$ for the four magnetic field profiles. The oscillation parameter region is region(A)-LMA all. The $\bar{\nu}_e$ probability limit is 0.038%(90% C.L.). Also the $\mu_{11} B_{\max}$ limit at the LMA best fit are estimated.

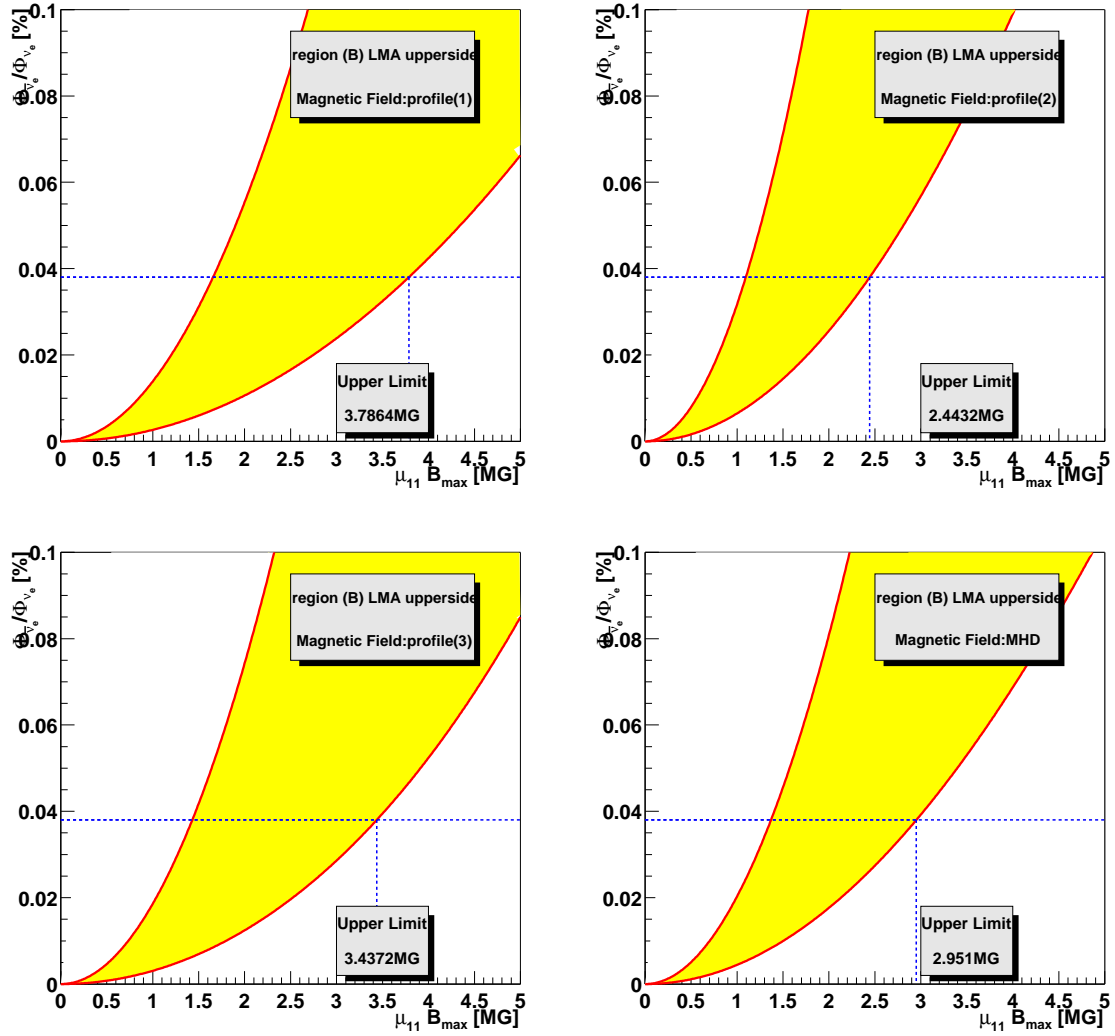


Figure 9.11: The calculated ratio of the $\bar{\nu}_e$ flux to be ^8B solar ν_e flux of the SSM prediction vs. the parameter $\mu_{11} B_{\max}$ for the four magnetic field profiles. The oscillation parameter region is region(B)

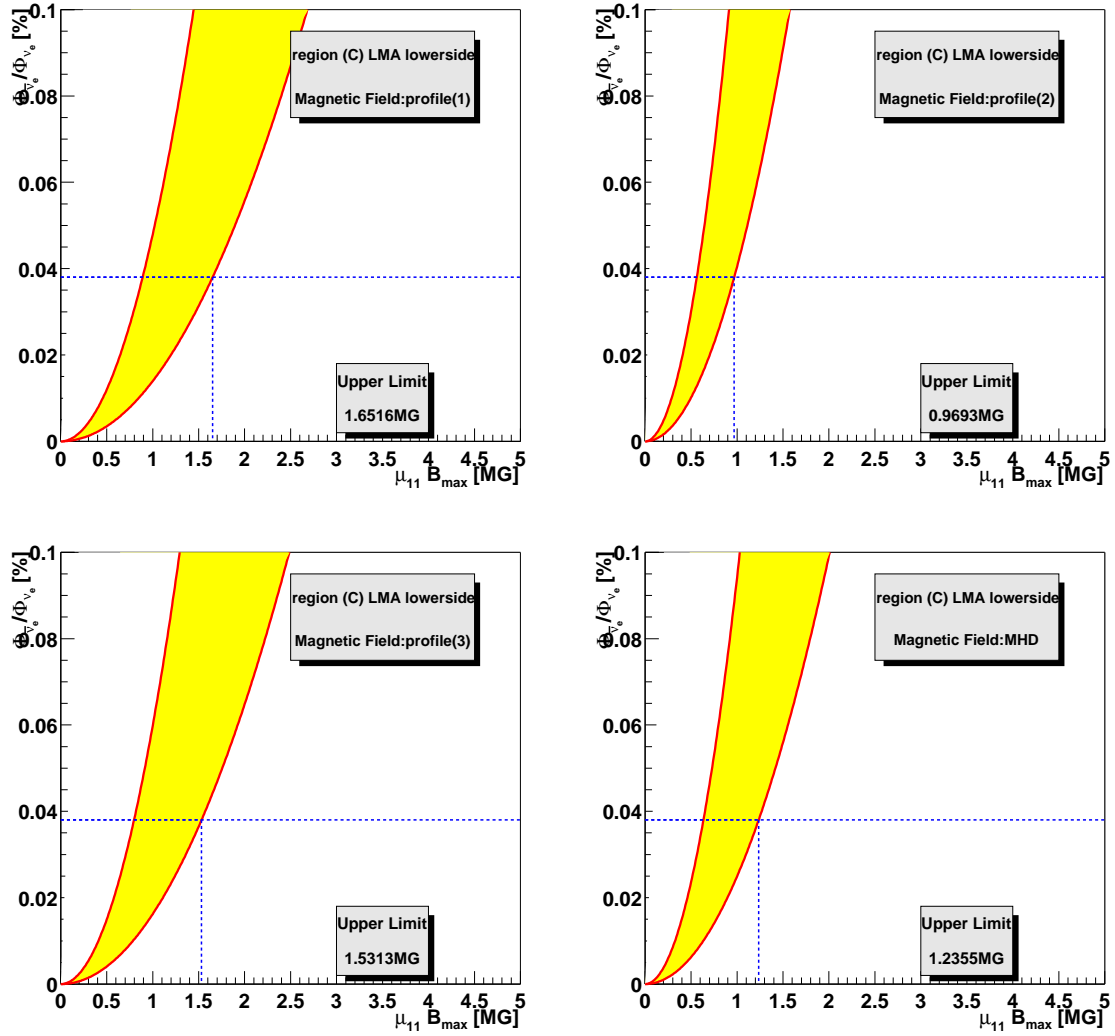


Figure 9.12: The calculated ratio of the $\bar{\nu}_e$ flux to the ^8B solar ν_e flux of the SSM prediction vs. the parameter $\mu_{11} B_{\max}$ for the four magnetic field profiles. The oscillation parameter region is region(C)

probability from 8MeV to 15MeV. The differences are less than 0.1% for whole LMA region. Thus the difference of ν_e survival probability can be neglected for the $\bar{\nu}_e$ limit of 0.038% at whole LMA region.

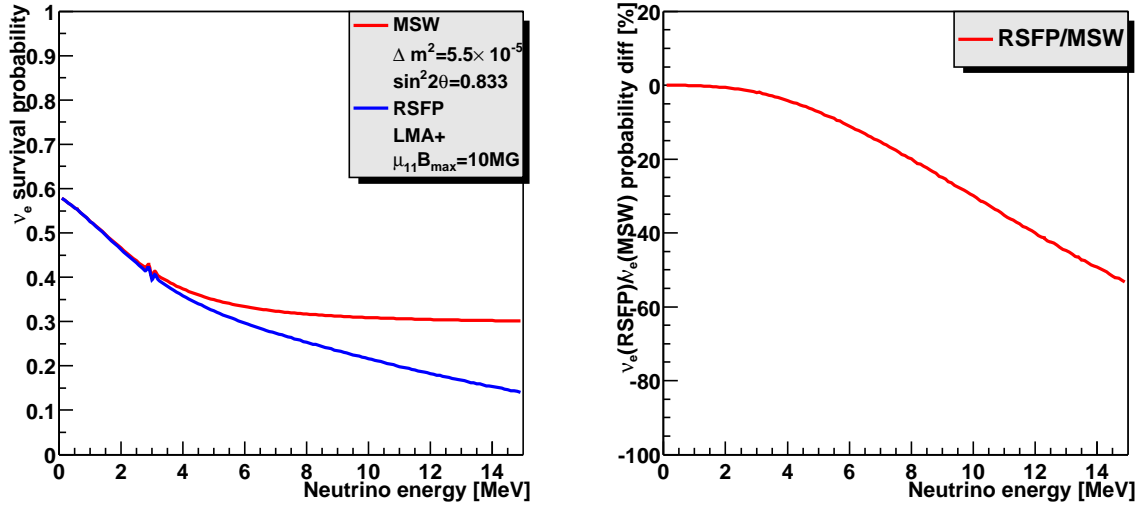


Figure 9.13: The example of difference between RSFP+MSW and MSW. The left figure shows the energy dependence of the ν_e survival probability for RSFP+MSW and MSW. The right figure shows the ratio of RSFP+MSW over MSW. The function $\mu_{11} B_{max}$ is fixed to 10MG. The oscillation parameter is LMA best fit ($\Delta m^2 = 5.5 \times 10^{-5}$, $\sin^2 2\theta = 0.833$).

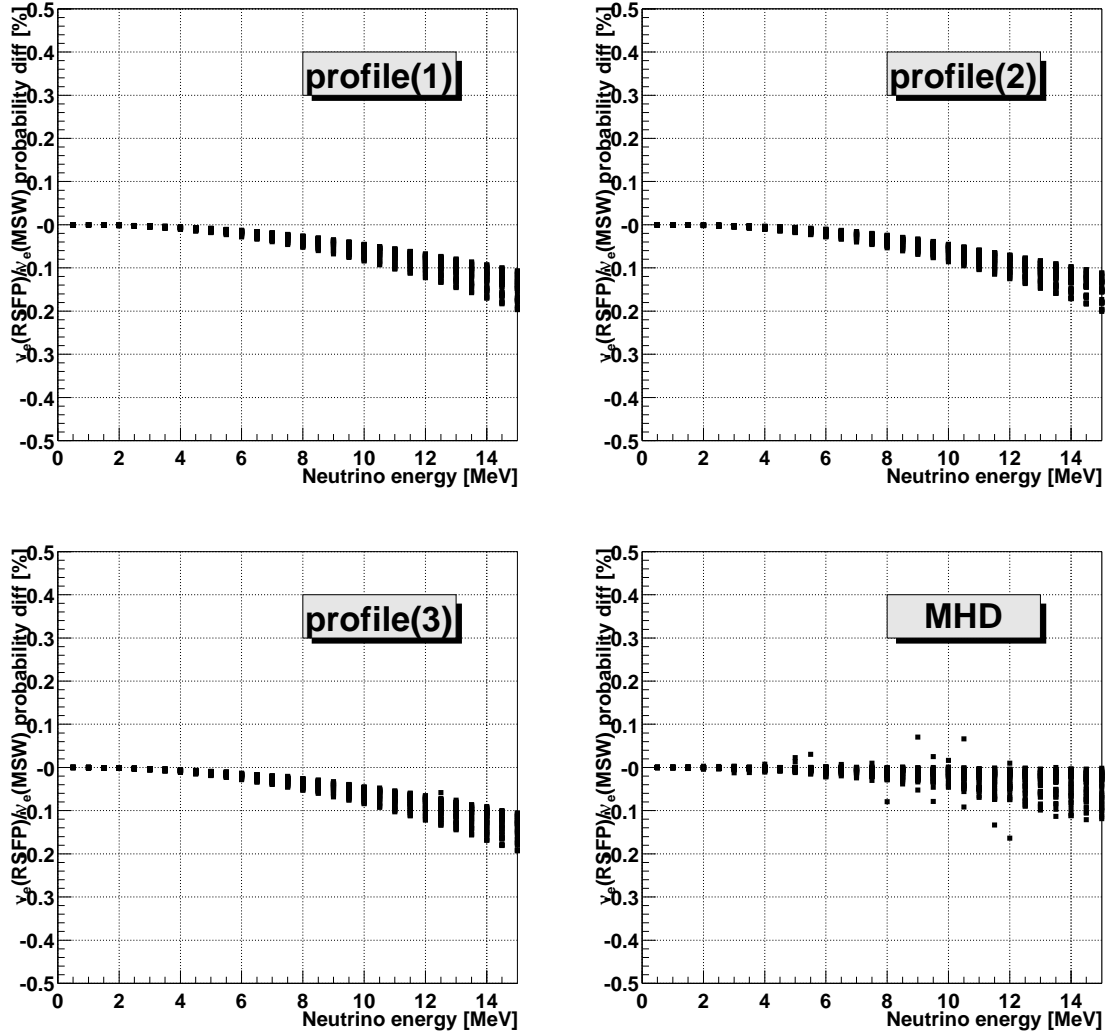


Figure 9.14: The energy dependence of the ratio of the ν_e fluxes in RSFP+MSW divided by MSW for each magnetic field profiles(1),(2),(3),MHD and the corresponding $\mu_{11}B_{max}$ limit obtained from the solar $\bar{\nu}_e$ limit of 0.038%.

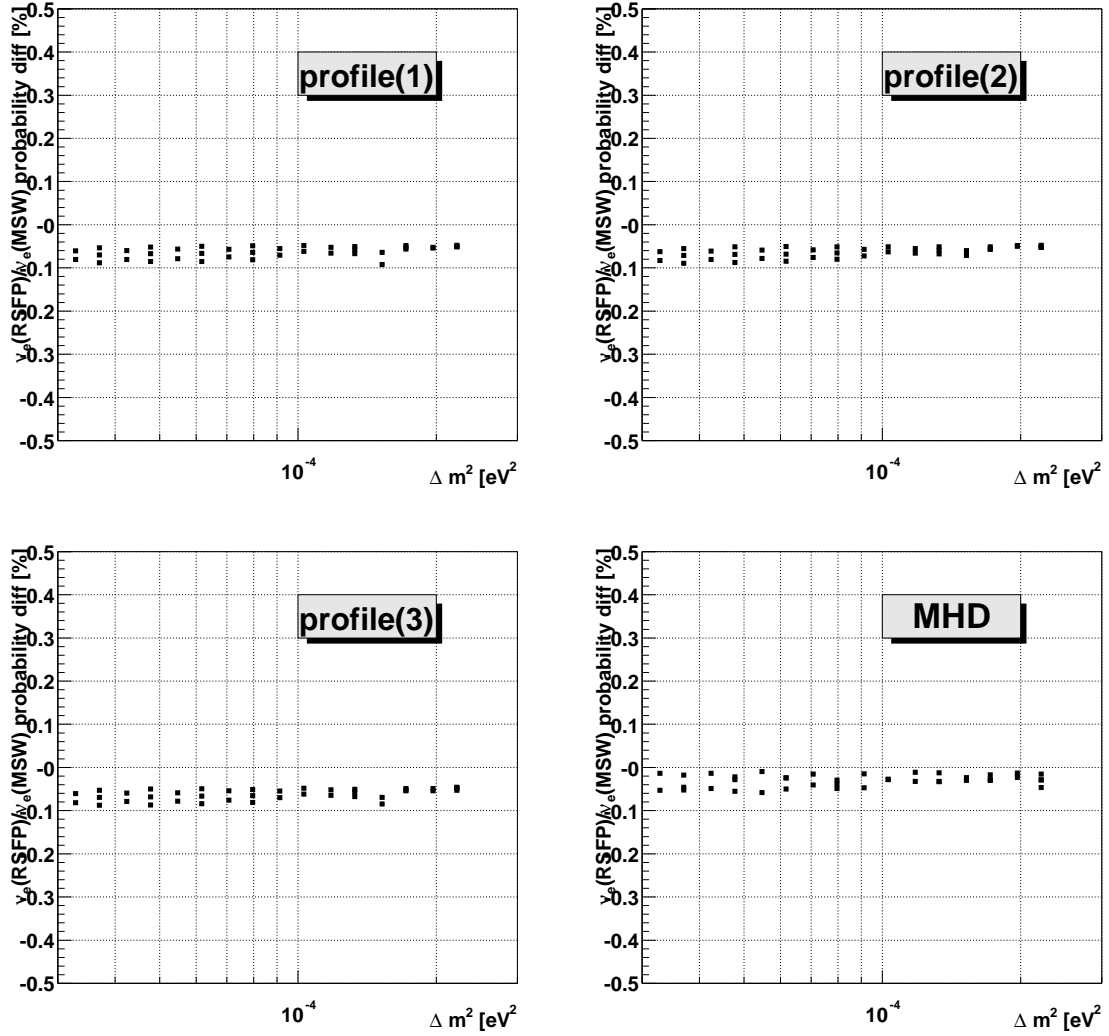


Figure 9.15: The ratio of the ν_e survival probabilities in RSFP+MSW divided by the one in MSW as a function of Δm^2 . The magnetic field are profiles(1),(2),(3),MHD. $\mu_{11} B_{max}$ limits obtained from the solar $\bar{\nu}_e$ limit of 0.038% are used in the calculation.

9.2 Neutrino Decay

9.2.1 Neutrino decay process

In neutrino decay, the heavier component of the mass eigenstate ν_2 decays into the lightest state ν_1 or $\bar{\nu}_1$ with the finite lifetime. In this thesis, limits on the neutrino lifetime are obtained for a case of the fast invisible two-body decay with an emission of Majoron :

$$\nu_2 \rightarrow \bar{\nu}_1 + J \quad (9.23)$$

where J is a Majoron. Now the $\bar{\nu}_e$ probability is determined by the ν_2 component $|U_{e2}|^2$ in $\bar{\nu}_e$ and the probability $|U_{e1}|^2$ of $\bar{\nu}_1$ to interact as $\bar{\nu}_e$.

The flux and the energy spectrum of $\bar{\nu}_e$'s produced by the decays is given by [35] :

$$\Phi(\bar{\nu}_e, E) = B|U_{e1}|^2|U_{e2}|^2 \times \int_E^\infty dE' \Phi(E') \frac{2(E' - E)}{E'^2} (1 - \exp[-T/\tau(E')]) \quad (9.24)$$

where E' is the parent neutrino energy and E is the $\bar{\nu}_e$ energy. Note that the energy of $\bar{\nu}_e$'s are degraded from the parent neutrino as the decay is backward peaked. T is the flight time from the sun (~ 500 s). $\tau(E)$ is the lifetime in the laboratory frame at energy E and $\tau(E) = (E/m_2)\tau_0$. $\Phi(E)$ is the flux of the ^8B solar neutrino predicted by the SSM. B is the decay branching ratio and is assumed as 0.5.

Figure 9.16 shows the energy spectrum of ^8B neutrino and the 'daughter' neutrino $\bar{\nu}_e$ from the decay in the case of $\tau_0 = 10^{-3}$ sec/eV and $m_{\nu_2} = 1\text{eV}$. The low energy neutrinos become dominant and the sensitivity to the $\bar{\nu}_e$ is reduced in the energy region ($8.3 \leq E_{\bar{\nu}_e} \leq 14.8$ MeV). This is the reason to obtain much less sensitivity to the lifetime in this analysis.

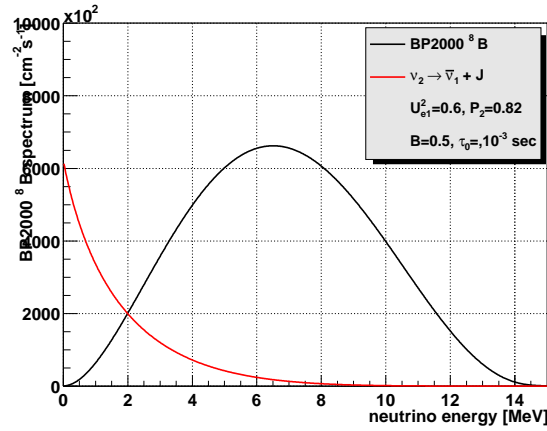


Figure 9.16: The energy spectrum for ^8B and the 'daughter' neutrino produced in the decay in the case of $\tau_0 = 10^{-3}$ sec/eV and $m_{\nu_2} = 1\text{eV}$.

9.2.2 Neutrino decay analysis

The analysis region $(\Delta m^2, \sin^2 2\theta)$ is the same as the one in the neutrino magnetic moment analysis (see section 9.1.4). Figure 9.17 shows the $\bar{\nu}_e$ conversion probability vs τ_0 for each analysis region. Now the conversion probability is less than the upper limit of 0.038% (90 %C.L.). The limit on neutrino lifetime are obtained as follows ;

$$\begin{aligned} \tau_0/m_{\nu_2} &> 7.8 \times 10^{-3} \text{sec/eV} && \text{(LMA all-region(A))} \\ \tau_0/m_{\nu_2} &> 8.2 \times 10^{-3} \text{sec/eV} && \text{(region (B))} \\ \tau_0/m_{\nu_2} &> 9.7 \times 10^{-3} \text{sec/eV} && \text{(region (C))} \\ \tau_0/m_{\nu_2} &> 1.3 \times 10^{-2} \text{sec/eV} && \text{(LMA best)} \end{aligned}$$

by assuming a ν_2 mass of 1 eV.

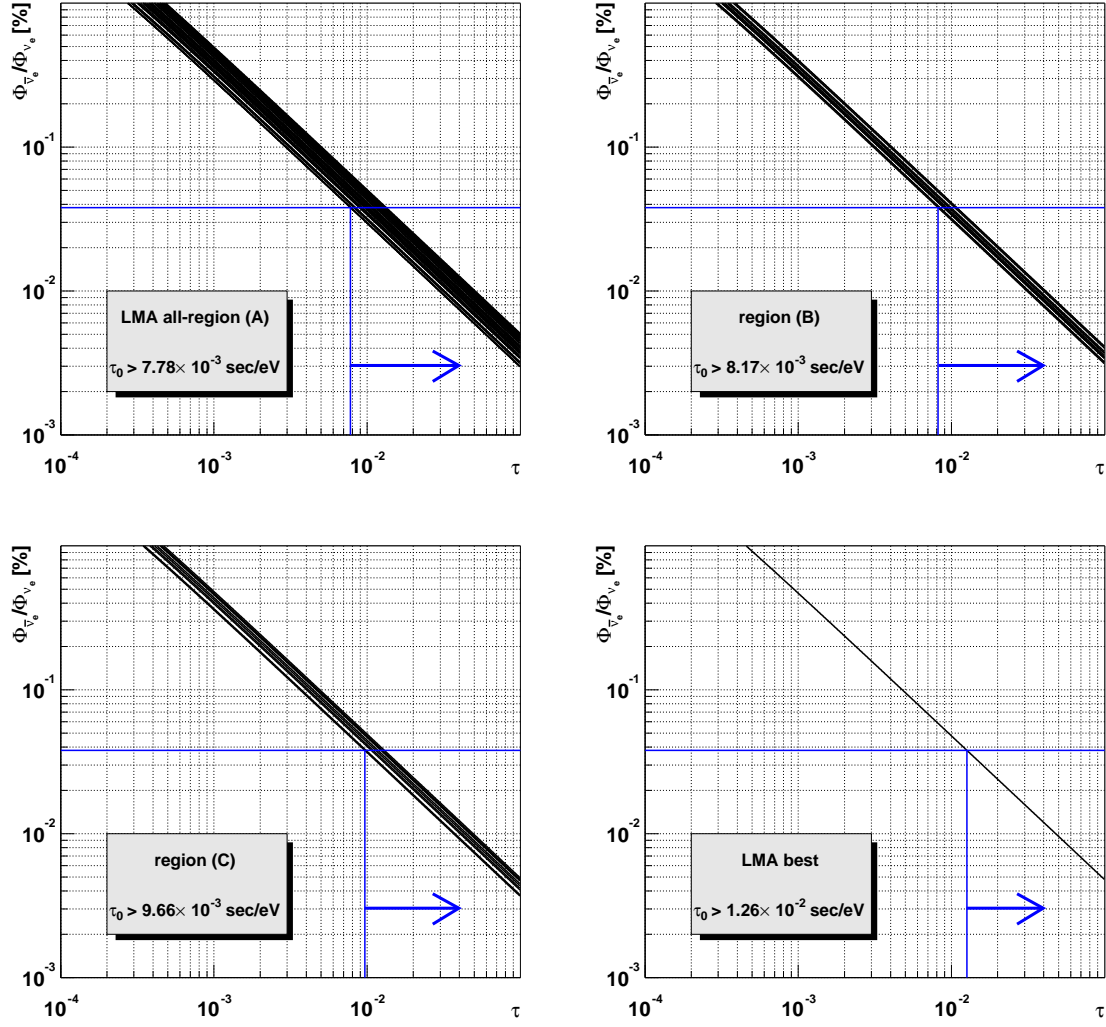


Figure 9.17: The $\bar{\nu}_e$ conversion probability vs τ_0 for region(A),(B),(C) and the LMA best-fit parameters.

Chapter 10

Conclusion

The search for $\bar{\nu}_e$'s in the energy range $8.3 \leq E_{\bar{\nu}_e} \leq 14.8 \text{ MeV}$ has been done for the 185.5 days data samples (0.28/yr/kton) of KamLAND from March 4 2002 to November 30 2002, and no candidates were found. The systematic error $\sigma = 6.07\%$ and the background $b = 1.06 \pm 0.32$ events are estimated. Assuming that $\bar{\nu}_e$'s have the same dependence on energy as the shape of the SSM ^8B flux, an upper limit of $5.81 \times 10^2 \text{ cm}^{-2} \text{ s}^{-1}$. This limit corresponds to 0.038% of the SSM ^8B ν_e flux.

The limit is interpreted in the framework of spin-flavor precession and neutrino decay models. If the strength of solar magnetic field are adopted to 1MG, the upper limit of the neutrino transition magnetic moment is $\mu_\nu < 0.6\text{--}1.0 \times 10^{-11} \mu_B$ (90% C.L.) at LMA best-fit parameters. Also the neutrino lifetime is obtained as $\tau_0 > 1.3 \times 10^{-2} \text{ sec/eV}$ (90% C.L.) at LMA best-fit parameters and $m_{\nu_2} = 1 \text{ eV}$.

Appendix A

Neutrons after the muon and the spallation events

KamLAND is shielded from the cosmic ray radiation by 2700 meter water equivalence of the rock. The total muon rate measured by KamLAND is 0.34Hz in the inner detector. There are 3 kinds of neutron events induced by cosmic ray muons. One is from neutrons emitted from the nuclei in the liquid scintillator after being hit by muons. The second one is from the decay of radioactive elements made by muon spallation where ^8He , ^9Li emit the neutron after the β decay which mimic the neutrino delayed coincidence events. The last one is the fast neutron events produced by cosmic ray muons going through the OD and the rock.

The background events from ^8He , ^9Li and fast neutrons are studied in appendix A.2.1 and subsection 8.4.4. The neutron capture and spallation events are utilized in the various calibrations of the neutron time, the vertex distribution and the energy scale.

A.1 Neutrons after the muon

The neutron capture selection criteria are as following :

- $200 \leq \text{Nsum} \leq 600$
- $dT \leq 2 \text{ ms}$

where Nsum means the number of hit PMTs from the trigger. Figure A.1 shows Nsum and the number of ATWD waveforms (Nhit) distribution at the time dT after the muon. $\text{Nsum} > \text{Nhit}$ means that some of the PMT information is lost in the finite recovery time of the electronics after the muon. It may cause the abnormal energy and the failure of the vertex reconstruction. Figure A.2 shows a time distribution of the events from the muon for all the neutron and the good neutron ($\text{Nhit} \geq \text{Nsum}$) events. The numbers of these events increases toward the $dT_{\text{muon}}=0$. Even if Nhit is larger than Nsum, it may not be a good neutron because some of the information may be lost but keeping $\text{Nhit} > \text{Nsum}$.

Thus tight time cut is applied as $0.8 \leq dT_{\text{muon}} \leq 2\text{ms}$. Figure A.3 shows the fraction of the neutron events with $\text{Nhit} \geq \text{Nsum}$ divided by all neutron. The $\text{Nhit} \geq \text{Nsum}$ ratio is more 90

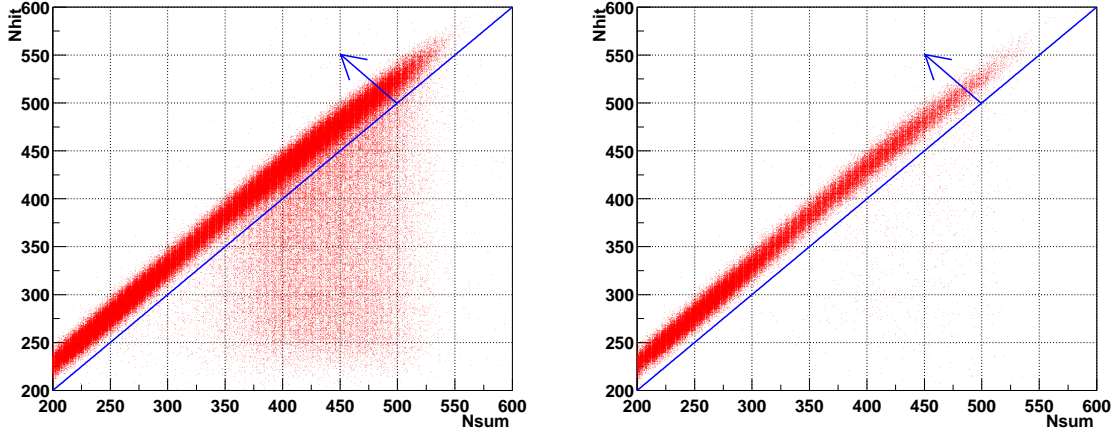


Figure A.1: Nsum and Nhit distribution at the time dT after the muon. The left figure's dT criteria is $0.2 \leq dT \leq 2$ ms from the muon. The right figure's dT criteria is $0.8 \leq dT \leq 2$ ms from the muon.

% at $dT_{muon} \geq 0.8$ ms. Thus it is expected that the number of events with a loss of information is small in this time region.

In addition, accidental background is subtracted by other time window $4 \leq dT_{muon} \leq 5.2$ ms when the time is far from the muon sufficiently. Figure A.4 shows histograms of energy spectrum and R^3 distribution selected by using the criteria with $4 \leq dT_{muon} \leq 5.2$ ms. The events in $4 \leq dT_{muon} \leq 5.2$ ms are the accidental background events which are mostly generated at the balloon edge.

The calibration by neutron at section 6.6 is done after the background subtraction. The $Nhit \geq Nsum$ cut are done at the energy calibration.

A.2 Spallation events

Spallation events in the ID are produced by energetic cosmic ray muons passing through the detector in the following interaction;

$$\mu + {}^{12}C \rightarrow \mu' + X \quad (A.1)$$

Spallation nuclei X after the muon are shown in Table A.1. In a short time (several 10 ms) after the muon, they are dominated by ${}^{12}B$ and ${}^{12}N$ nuclei. 9Li and 8He can produce correlated events which are detected by the delayed coincidence, and they are problematic in the anti-neutrino detection. 8B and 8Li are discriminated by the longer decay time than other reactions.

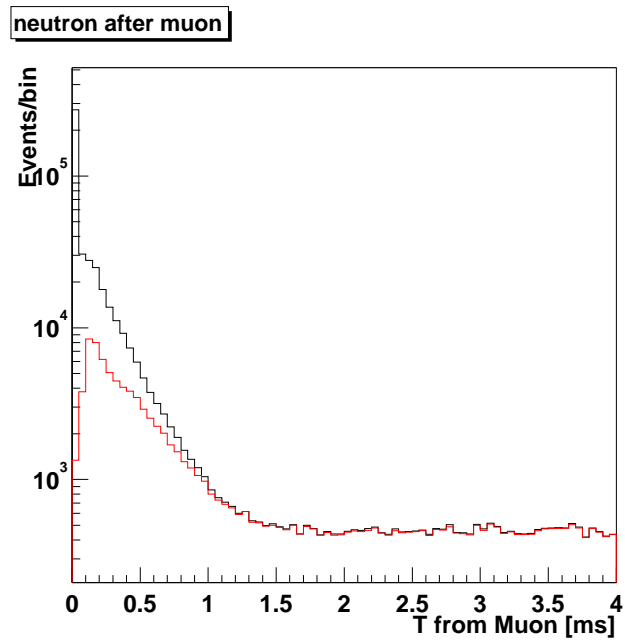


Figure A.2: Time distribution for neutron after muon. The black histogram shows all neutron events. The red histogram shows good neutron events.

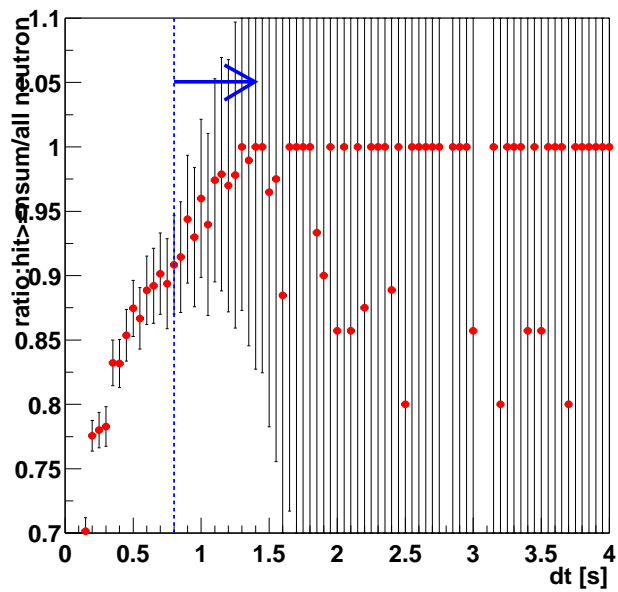


Figure A.3: Ratio of the good neutron events over all the neutron events

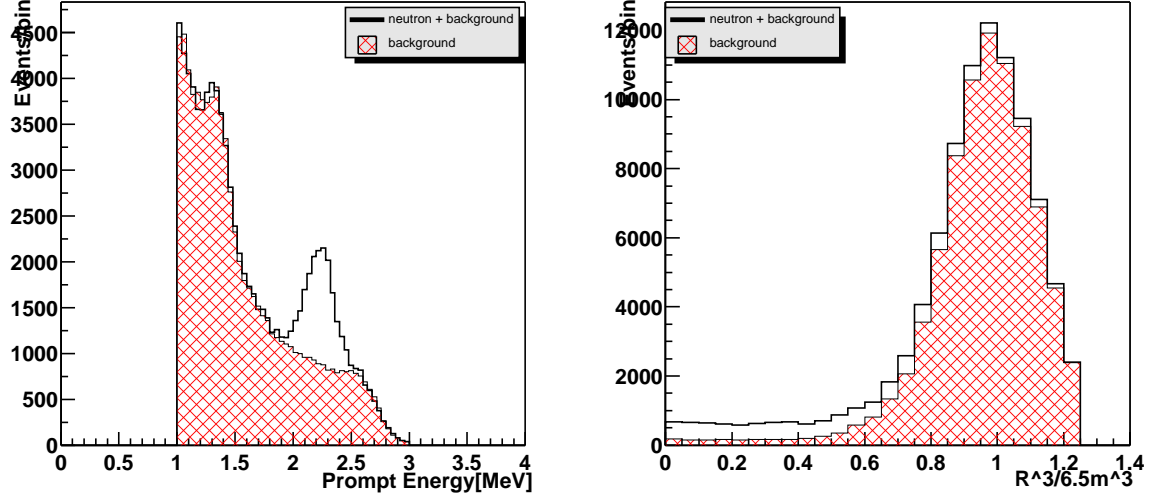


Figure A.4: Neutron background subtraction. The left figure shows the energy distribution and the right figure shows the R^3 distribution. The cross-hatched histogram is the events in $4 \leq dT_{muon} \leq 5.2\text{ms}$ which are regarded as the background distribution.

Isotopes	$T_{1/2}$	Emax(KeV)
^{12}B	20.2 ms	13369(β^-)
^{12}N	11.0 ms	17338(β^+)
^{11}Li	8.5 ms	20610(β^-)
^9Li	173.8 ms	13606(β^-)
^8He	119.0 ms	10653(β^-)
^9C	126.6 ms	16498(β^+)
^8Li	838.0 ms	16006(β^-)
^6He	806.7 ms	3508(β^-)
^8B	770.0 ms	17979(β^+)

Table A.1: The list of spallation nuclei produced after the cosmic ray muons

A.2.1 ${}^9\text{Li}$, ${}^8\text{He}$

${}^9\text{Li}$ and ${}^8\text{He}$ both decay through the β decay and the resultant nuclei (${}^9\text{Be}$ and ${}^8\text{Li}$) emit the neutrons with the branching ratio about 48%. They mimic the reaction of anti-neutrino. In this section, ${}^9\text{Li}$ and ${}^8\text{He}$ spallation event rate is estimated.

The selection criteria is the same as the anti-neutrino selection (see section 7) except the spallation cut process. The spallation events are induced from 2 ms to 2 second after the muon. The events from 2 second to 10 second after the muon are used to subtract the background events from the ones between 2 ms to 2 second. Figure A.5 shows the ${}^9\text{Li}+{}^8\text{He}$ prompt and delayed energy distribution. The energy distribution of the delayed events is fitted by gaussian function with a peak at 2.21 ± 0.02 MeV. The energy distribution of prompt events is superimposed with the theoretical β ray spectrum from ${}^9\text{Li}$ and ${}^8\text{He}$ β decays. The ${}^9\text{Li}$ dominates ${}^8\text{He}$ due to the much larger production cross section. Estimation of ${}^8\text{He}$ in the sample is done by χ^2 fitting as shown in Figure A.6. The ratio of ${}^8\text{He}$ at χ^2_{min} is zero % and the upper limit of 9.7% (68% C.L.) is obtained. This result shows that ${}^9\text{Li}$ events are the dominant source in the sample.

The spallation event rate is estimated by integration of the decay time distribution. The ${}^9\text{Li}$ and ${}^8\text{He}$ samples are divided into two subsamples. One is the energetic muon case defined by the residual charge in the detector being larger than 10^6 p.e. and the other is non-energetic muon case that the residual charge is less than 10^6 p.e. The event selection criterion for the spallation events by the non-energetic muon is that the distance of events is less than 300 cm from the muon track.

Figure A.7 shows the time distribution from the muon of the ${}^9\text{Li}$ and ${}^8\text{He}$ samples for (1) $dQ \geq 10^6$ and (2) $dQ < 10^6$, $dL \leq 300$ cm. The smooth line is the decay curve by the fit. The decay time is fixed to ${}^9\text{Li}$'s one. The observed ${}^9\text{Li}$ and ${}^8\text{He}$ candidates are ;

$$\begin{aligned} 87.81 \pm 9.92 & \quad \text{events/dataset for (1)} \\ 29.18 \pm 10.70 & \quad \text{events/dataset for (2)} \end{aligned} \tag{A.2}$$

Now the number of ${}^9\text{Li}$ and ${}^8\text{He}$ samples for KamLAND detector is estimated.

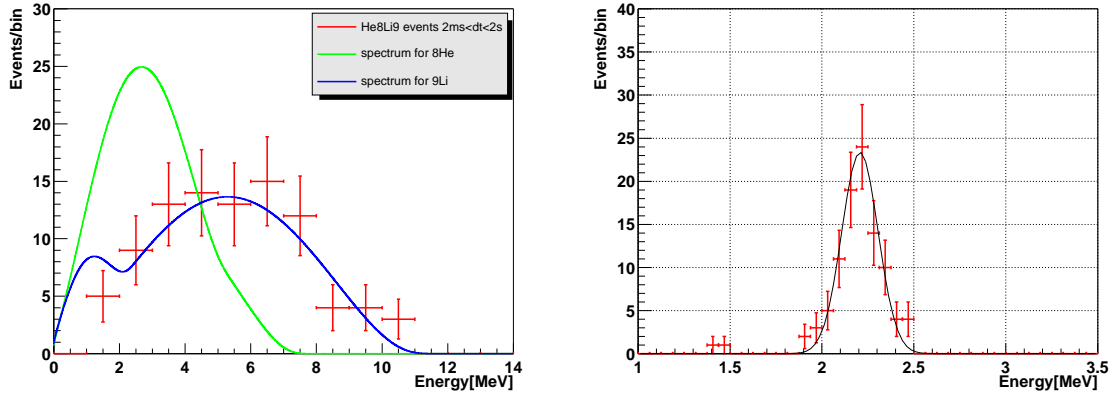
The efficiency for the selection of ${}^9\text{Li}$ and ${}^8\text{He}$ samples is shown in Table A.2. The criteria is almost the same as the neutrino selection criteria. Two criteria are added. One is the energy cut $E_{prompt} \geq 0.9$ MeV. The efficiency is estimated by theoretical calculation of ${}^9\text{Li}$ β decay. The other one is the efficiency of the distance $dL \leq 300$ cm from the muon track in the case of $dQ < 10^6$ p.e. Figure A.8 shows the distance of the neutrons from the non-energetic muons. The estimated efficiency of the condition $L \leq 300$ cm is 93.6% Thus the efficiency is 84.09% for (1) and 78.70% for (2) as shown in Table A.2.

The number of ${}^9\text{Li}$ and ${}^8\text{He}$ samples containing neutron is estimated to 141.50 ± 18.01 events/dataset. Considering the fiducial volume (542 ton), branching ratio (neutron attending reaction is 48% for ${}^9\text{Li}$) and the running time (209.67 day), the event rate of ${}^9\text{Li}$ for KamLAND detector is estimated to be 2.60 ± 0.33 /day/kton.

This result is consistent with the event rate estimated by an accelerator-based experiment [57] of about 2.4 ± 0.5 (${}^9\text{Li}+{}^8\text{He}$)events/day/kton.

Now the background in the neutrino event selection is examined. The neutrino selection criteria have spallation cut process. The criteria is set by dQ :

- veto in 2 sec for all the volume ($dQ \geq 10^6$) - (1)

Figure A.5: ${}^9\text{Li}/{}^8\text{He}$ prompt and delayed energy distribution

- veto in 2 sec for 3 m from the muon track ($dQ < 10^6$) - (2)

So the background event rate are estimated by (1) ${}^9\text{Li}$ decay time over the 2 sec veto and (2) the distance from the muon track longer than 3m (actual sample are shown in Figure A.9). The reduction factor is 4.1×10^{-4} for 2 sec veto and $0.064/0.936$ for muon track cut. The event rate for these situation is estimated in eq.(A.2) :

$$\begin{aligned} &0.04 \quad \text{events/dataset for (1)} \\ &2.00 \pm 0.73 \quad \text{events/dataset for (2)} \end{aligned} \tag{A.3}$$

with a 0.9 MeV energy threshold. This energy threshold is converted to 7.5 MeV for solar anti-neutrino analysis. The 26.9% of the total events, which is calculated from the theoretical β decay spectrum of ${}^9\text{Li}$ enter the energy region $E \geq 7.5$ MeV. Thus the total background events from ${}^9\text{Li}/{}^8\text{He}$ is :

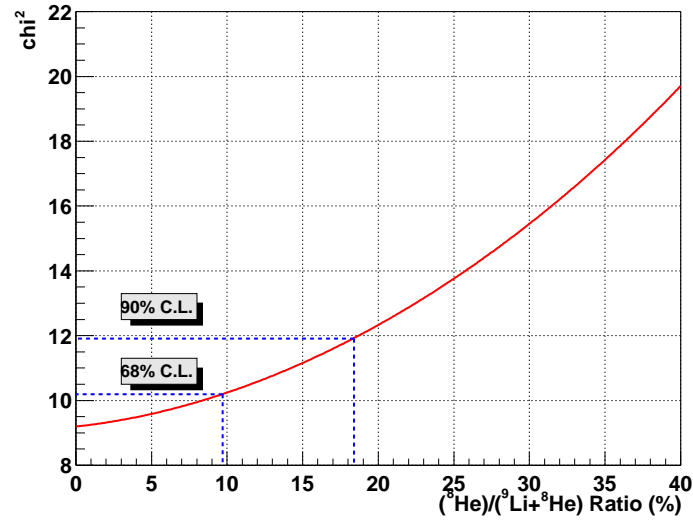
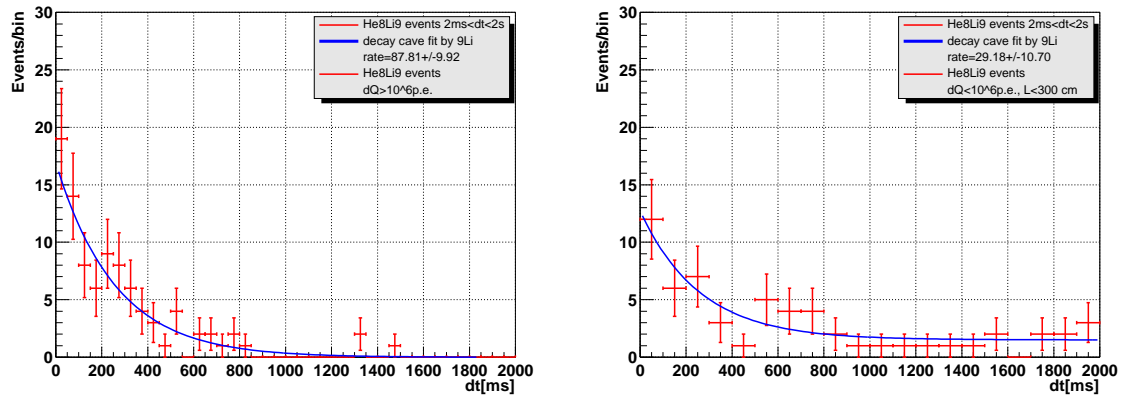
$$\frac{0.269}{0.942} \times (0.04 + 2.00 \pm 0.73) = 0.58 \pm 0.21 \quad \text{events/dataset} \tag{A.4}$$

A.2.2 Event selection criteria for other spallation events

The other spallation events are used in the calibrations of the vertex distribution and the energy scale.

For the event selection the following criteria are used:

- Originating from the muon selection
 - Muon $Q > 10^5$ p.e.
- Low energy event selection

Figure A.6: χ^2 distribution for ${}^8\text{He}/({}^9\text{Li}+{}^8\text{He})$ Figure A.7: ${}^9\text{Li}$ dt distribution

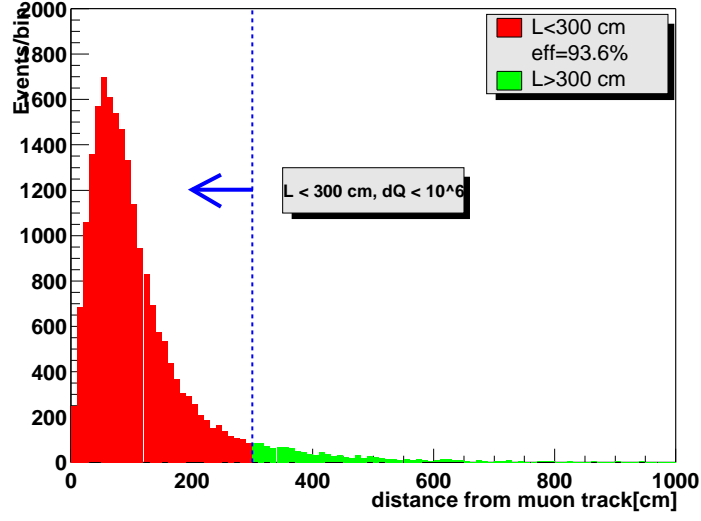


Figure A.8: The distance of the neutrons from the muons in the spallation neutron samples for non-energetic muons.

selection criteria	efficiency	remark
$0.5 \leq dt \leq 660 \mu s$	95.32%	for ${}^9\text{Li}$ ($dQ \leq 10^6$ only)
$1.8 \leq E_{\text{delayed}} \leq 2.6 \text{ MeV}$	98.85%	
$E_{\text{prompt}} \geq 0.9 \text{ MeV}$	94.2%	
fiducial cut effect $R \leq 550 \text{ cm}$	89.77%	
($dL \leq 300 \text{ cm}$)	(93.6%)	
total	84.09%(78.70%)	

Table A.2: The efficiency for the selection of ${}^9\text{Li}$ and ${}^8\text{He}$ samples.

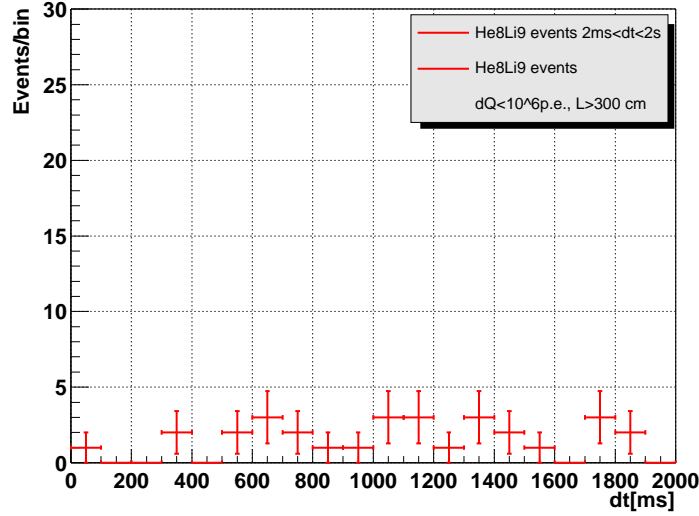


Figure A.9: The decay time distribution of the events whose distance from the non-energetic muon track is larger than 300cm.

- Bad run cut
- Noise cut
- NhitID > 50
- $2 \text{ ms} < dt \text{ (from the muon)} < 10 \text{ sec}$
- $dL > 400 \text{ cm}$ cut at mis-reconstructed muon & $dQ < 10^5 \text{ p.e.}$ (clean muon)
- Tight selection
 - $\text{Energy} \geq 4 \text{ MeV}$ for low energy event
 - $dQ > 10^6 \text{ p.e.}$ for muon or $dL < 400 \text{ cm}$ for low energy event

The energy cut is to reduce the accidental background events. The method of separation between the spallation events and the background events are defined as the time distribution from the muon. Figure A.10 shows the time distribution of the spallation events. The left picture shows the short time range $2 \text{ ms} \leq dt \leq 300 \text{ ms}$ after the muon. Most events are distributed within 100 ms. This shows that the most events are from the isotopes with a short lifetime like ^{12}B and ^{12}N . The right picture shows for the long time range of $2 \text{ ms} \leq dt \leq 10 \text{ sec}$. The time distribution is flat from 6 sec to 10 sec. The number of background events is estimated from this time range.

Figure A.11 shows the energy spectrum for spallation events which shows the events for $2 \text{ ms} \leq dt \leq 2 \text{ sec}$ and $6 \text{ sec} \leq dt \leq 10 \text{ sec}$ that is normalized by the time scale. The main background sources are in a low energy region about 3 MeV. Thus the spallation events are selected only

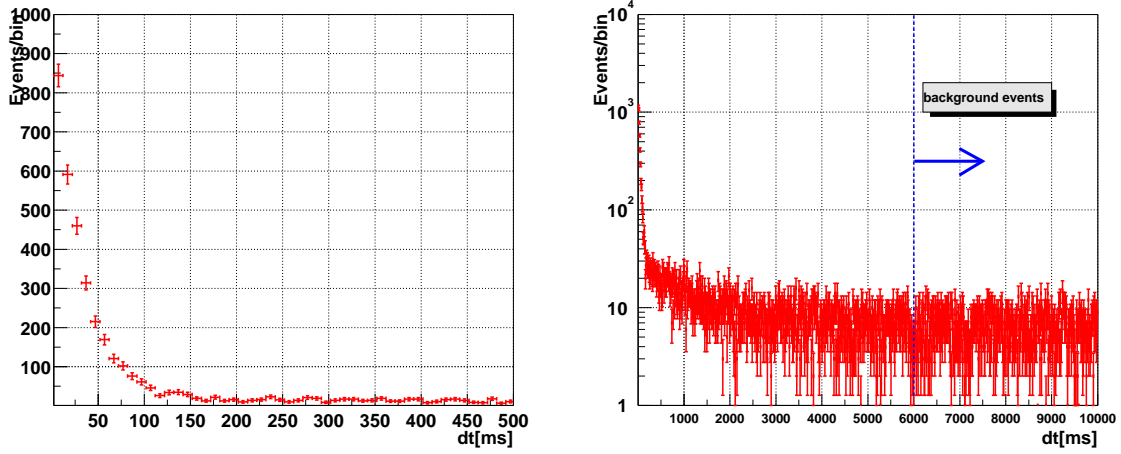


Figure A.10: The time distribution of the spallation events for the short range and the long range after the muon

by an energy cut of $E \geq 4$ MeV. The endpoint of energy spectrum is about 14MeV. In the next section, each of the spallation isotopes are described.

A.2.3 ${}^8\text{Li}+{}^8\text{B}$, ${}^9\text{C}$ and ${}^{12}\text{B}+{}^{12}\text{N}$

The production rate of the spallation nuclei is necessary to study the energy scale by comparing the data with the theoretical energy spectrum of the β rays.

The number of two spallation nuclei ${}^8\text{He} + {}^9\text{Li}$ is estimated in the section A.2.1 by delayed coincidence. The number of events detected as single events is 220.27 ± 28.03 events/dataset in the fiducial volume and energy threshold at 4 MeV. Thus the number of events for ${}^8\text{Li}+{}^8\text{B}$, ${}^9\text{C}$ and ${}^{12}\text{B}+{}^{12}\text{N}$ are estimated by the time distribution between 2 ms and 6 sec from the muon.

Figure A.12 shows the time distribution with a fit by the decay time of the spallation components. The number of events of ${}^8\text{Li}+{}^8\text{B}$ is 2102.5 ± 133.3 events/dataset for 4 MeV energy threshold which is estimated as 2712.3 ± 172.0 events/dataset for all energy region. The normalized event rate is 23.9 ± 1.17 events/day/kton. It is difficult to separate the rate between ${}^8\text{Li}$ and ${}^8\text{B}$ because the decay times are close with each other (1111 ms and 1211 ms) and the energy distribution are similar (see the left of Figure A.13). At [57], the production ratio between ${}^8\text{Li}$ and ${}^8\text{B}$ is 7 : 11. Thus the time distribution and the energy spectrum are adopted by this ratio. The number of ${}^9\text{C}$ is estimated but the error is very large. The estimated events from the time distribution is 96.4 ± 80.6 events/dataset for 4 MeV threshold based on the estimation of 142.7 ± 119.3 events/dataset for all the energy region. The normalized event rate is 1.3 ± 1.0 events/day/kton.

These results are different from the event rate obtained by an experiment by T.Hagner et al. [57]. Their estimates are 12.86 ± 1.86 event/day/kton for ${}^8\text{Li}+{}^8\text{B}$ and 5.50 ± 1.79 event/day/kton for ${}^9\text{C}$. The estimates are about twice for ${}^8\text{Li}+{}^8\text{B}$ and about one fourth for ${}^9\text{C}$.

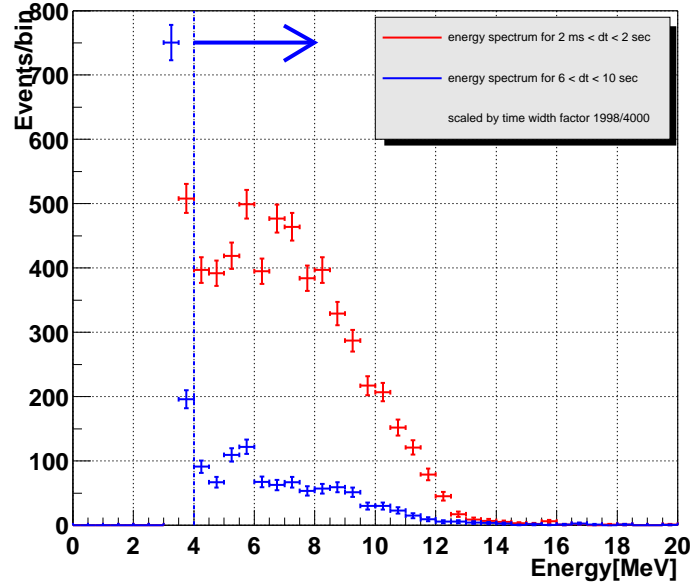


Figure A.11: The energy spectrum for the spallation events

The spallation events are dominated by $^{12}\text{B}+^{12}\text{N}$. The estimated number of events is 4974.6 ± 305.4 for energy threshold 4 MeV which is estimated as 6143.6 ± 377.2 events/dataset for all energy region. The normalized event rate is 54.1 ± 3.3 events/day/kton. The right of Figure A.13 shows the energy spectrum for $2 \text{ ms} \leq dt \leq 60 \text{ ms}$. The beta decay endpoint for ^{12}N is about 17.3 MeV. But the number of events with an energy greater than 13 MeV is very small. It suggests that $^{12}\text{B}+^{12}\text{N}$ spallation events are almost ^{12}B . The fraction of ^{12}N is about 3 % of all $^{12}\text{B}+^{12}\text{N}$ events. $^{12}\text{B}+^{12}\text{N}$ spallation events are used in the energy scale calibration in the section 6.8.

Table A.3 shows the summary of the estimation on the spallation events with the result from the experiment by Hagner et al. [57].

Isotopes	this works (events/day/kton)	Hagner et al. (events/day/kton)
$^{12}\text{B} + ^{12}\text{N}$	54.1 ± 3.3	-
^9C	1.3 ± 1.0	5.5 ± 1.8
$^9\text{Li} + ^8\text{He}$	2.6 ± 0.3	2.4 ± 0.5
$^8\text{B} + ^8\text{Li}$	23.9 ± 1.2	12.9 ± 1.9

Table A.3: The results of estimation for the spallation events in the present study and the experiment by estimation Hagner et al. [57].

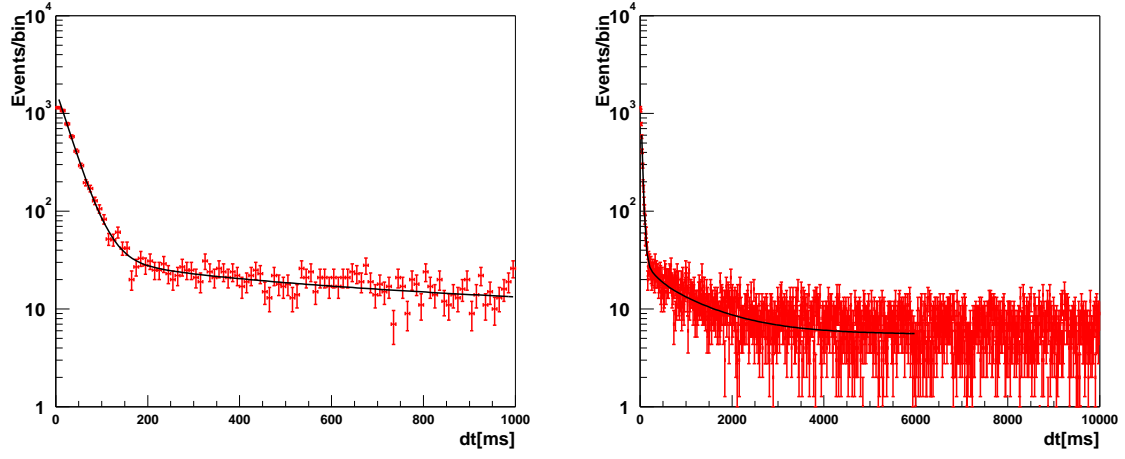
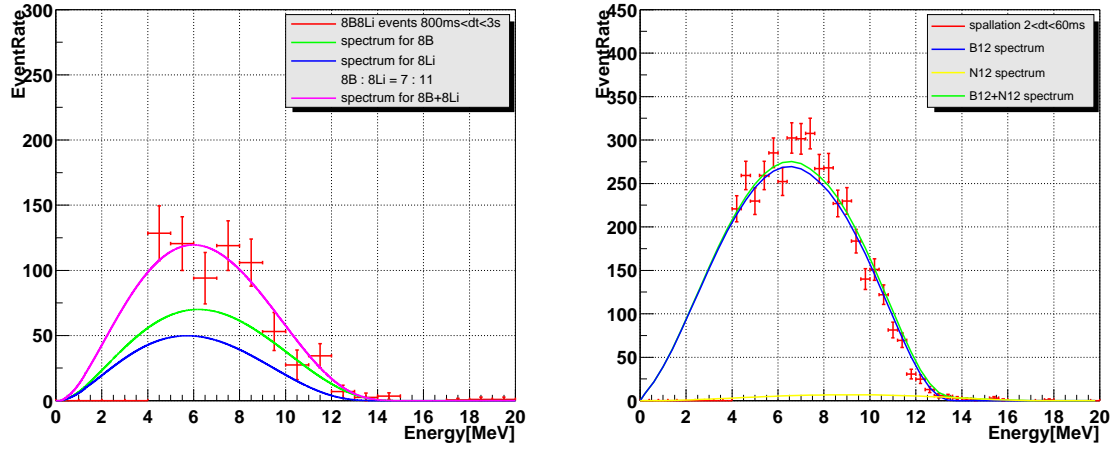


Figure A.12: The decay time fitting result for the spallation events

Figure A.13: The left figure shows energy distribution for ^8B and ^8Li with calculated spectrum. The right figure shows for ^{12}B and ^{12}N .

Bibliography

- [1] Ahmad, Q. R. et al., Phys. Rev. Lett. 89 (2002) 011301
- [2] K. Eguchi et al., Phys. Rev. Lett. 90 (2003) 021802
- [3] W. Pauli, Letter to L. Meitner and her colleagues (letter open to the participants of the conference in Tübingen) (1930)
- [4] F. Reines and C. L. Cowan, Nature 178 (1956) 446
- [5] M. L. Perl et al., Phys. Rev. Lett. 35 (1975) 1489
- [6] The LEP Collaborations and LEP Electroweak Working Group, as reported by J. Dress at XX International Symposium on Lepton and Photon Interactions at High Energy, Rome, Italy (2001)
- [7] Kodama, K. et al., Phys. Lett. B504 (2001) 218-224
- [8] R. Davis, Jr. et al., Phys. Rev. Lett. 20 (1968) 1205
- [9] K. Hirata et al., Phys. Rev. Lett. 58 (1987) 1490-1493
- [10] J. Bahcall et al., Astro. J. 555 (2001) 990
- [11] C. E. Ortiz et al., Phys. Rev. Lett. 85 (2000) 2909
- [12] B. T. Cleveland et al., Ap. J. 496 (1998) 505
- [13] Y. Fukuda et al., Phys. Rev. Lett. 77 (1996) 1683
- [14] J. N. Abdurashitov et al., Phys. Rev. C60 (1999) 0055801
- [15] W. Hampel et al., Phys. Lett. B447 (1999) 127
- [16] S. Fukuda et al., Phys. Lett. B539 (2002) 179-187
- [17] Mikheev, S. P., Smirnov, A. Yu., Nuovo Cim. C9 (1986) 17-26
Mikheev, S. P., Smirnov, A. Yu., Sov. J. Nucl. Phys. 42 (1985) 913-917
Wolfenstein, L., Phys. Rev. D17 (1978) 2369
- [18] S. J. Parke, Phys. Rev. Lett. 57 (1986) 1275-1278

- [19] G. L. Fogli et al., Phys. Rev. D66 (2002) 053010
- [20] H. Murayama, <http://hitoshi.berkeley.edu/neutrino/> (2002)
- [21] K. Fujikawa and R. E. Shrock, Phys. Rev. Lett. 45 (1980) 963
- [22] Z. Daraktchieva et al., hep-ex/0304011
- [23] D.A. Krakauer , R.L. Talaga , R.C. Allen , H.H. Chen, et al., Phys. Lett. B252 (1990) 177
- [24] L. B. Auerbach et al., Phys. Rev. D63 (2001) 112001
- [25] R. Schwienhorst et al., Phys. Lett. B513 (2001) 23
- [26] J. A. Morgan, Phys. Lett. B102 (1981) 247-250
- [27] G. G. Raffelt, Phys. Rept. 320 (1999) 319-327
- [28] R. Barbieri et al., Phys. Rev. Lett. 61 (1988) 27
- [29] R. Davis et al., Prog. Nucl. Part. Phys. 32 (1994) 13
- [30] A. Cisneros, Astrophys. Space Sc. 10 (1971) 87
M. Voloshin et al., Sov. J. Nucl. Phys. 44 (1986) 440
E. Kh. Akhmedov, Phys. Lett. B213 (1988) 64
- [31] C. S. Lim and W. J. Marciano, Phys. Rev. D37 (1988) 1368
- [32] Y. Fukuda et al., Phys. Rev. Lett. 77 (1996) 1683-1686
- [33] C. S. Lim et al., Phys Lett. B243 (1990) 389
R. S. Raghavan et al., Phys. Rev. D44 (1991) 3786
E. Kh. Akhmedov and J. Pulido, Phys. Lett. B553 (2003) 7
- [34] R. S. Raghavan et al., Phys. Rev. D38 (1988) 1317
A. Joshipura et al., Phys. Rev. D66 (2002) 113008
J. F. Beacom and N. Bell, Phys. Rev. D65 (2002) 113009
- [35] A. Acker et al., Phys. Lett. B285 (1992) 371
- [36] A. Acker and S. Pakvasa, Phys. Lett. B320 (1994) 320
- [37] V. Barger, W. Y. Keung and S. Pakvasa, Phys. Rev. D25 (1982) 907
- [38] S. Petcov, Sov. J. Nucl. Phys. 24 (1977) 340
W. Marciano and A. Sanda, Phys. Lett. B67 (1977) 303
- [39] F. Reines et al., Phys. Rev. Lett. 32 (1974) 180
- [40] D. A. Krakauer et al., Phys. Rev. D44 (1991) R6
- [41] E. L. Chupp et al., Phys. Rev. Lett. 62 (1989) 505

- [42] G. G. Raffelt, Phys. Rev. D31 (1985) 3002
- [43] Y. Gando et al., Phys. Rev. Lett. 90 (2003) 171302
- [44] P. Vogel and J. F. Beacom, Phys. Rev. D60 (1999) 053003
- [45] J. B. Birks, Proc. Phys. Soc. A64 (1951) 874
- [46] T. K. Gaisser et al., Phys. Rev. D38 (1988) 85
- [47] M. Honda et al., Phys. Rev. D52 (1995) 4985-5005
- [48] G. Battistoni et al., Astropart. Phys. 12 (2000) 315-333
- [49] J. Pulido, hep-ph/0106201
- [50] O. G. Miranda et al., Nucl. Phys. B595 (2001) 360-380
- [51] V. A. Kutvitskii and L. S. Solov'ev, JETP 78 (1994) 456
- [52] S. Chandrasekar and E. Fermi, Astrophys. J. 118 (1953) 116
- [53] A. Friedland and A. Gruzinov, astro-ph/0211377
- [54] H. M. Antia et al., astro-ph/0005587
- [55] M. Apolonio et al., Phys. Lett. B466 (1999) 415
- [56] F. Boehm et al., Phys. Rev. D64 (2001) 112001
- [57] T. Hagner et al., Astropart. Phys. 14 (2000) 33-47